

**IN-SITU ELECTROCHEMICAL GENERATION OF SUPEROXIDE ION FOR THE
CONVERSION OF CO₂ AND CHLORINATED COMPOUNDS IN IONIC LIQUID AND
NANOHYBRID-IONIC LIQUID MEDIA**

AHMED HALILU

**FACULTY OF ENGINEERING
UNIVERSITI MALAYA
KUALA LUMPUR**

2021

**IN-SITU ELECTROCHEMICAL GENERATION OF
SUPEROXIDE ION FOR THE CONVERSION OF CO₂ AND
CHLORINATED COMPOUNDS IN IONIC LIQUID AND
NANOHYBRID-IONIC LIQUID MEDIA**

AHMED HALILU

**THESIS SUBMITTED IN FULFILMENT OF THE REQUIREMENTS
FOR THE DEGREE OF
DOCTOR OF PHILOSOPHY**

**FACULTY OF ENGINEERING
UNIVERSITI MALAYA
KUALA LUMPUR**

2021

UNIVERSITI MALAYA
ORIGINAL LITERARY WORK DECLARATION

Name of Candidate: AHMED HALILU

Matric No: 17014127/2

Name of Degree: Doctor of Philosophy (PhD.)

Title of Thesis ("this Work"): IN-SITU ELECTROCHEMICAL GENERATION OF SUPEROXIDE ION FOR THE CONVERSION OF CO₂, AND CHLORINATED COMPOUNDS IN IONIC LIQUID AND NANOHYBRID-IONIC LIQUID MEDIA

Field of Study: CHEMICAL ENGINEERING (REACTION ENGINEERING)

I do solemnly and sincerely declare that:

- (1) I am the sole author/writer of this work;
- (2) This work is original;
- (3) Any use of any work in which copyright exists was done by way of fair dealing and for permitted purposes and any excerpt or extract from, or reference to or reproduction of any copyrighted work has been disclosed expressly and sufficiently and the title of the work and its authorship have been acknowledged in this work;
- (4) I do not have any actual knowledge nor do I ought reasonably to know that the making of this work constitutes an infringement of any copyrighted work;
- (5) I hereby assign all and every right in the copyright to this work to the University of Malaya ("UM"), who henceforth shall be the owner of the copyright in this work and that any reproduction or use in any form or by any means whatsoever is prohibited without the written consent of UM having been first had and obtained;
- (6) I am fully aware that if in the course of making this work I have infringed any copyright whether intentionally or otherwise, I may be subject to legal action or any other action as may be determined by UM.

Candidate's Signature

Date: 18/9/2021

Subscribed and solemnly declared before,

Witness's Signature

Date: 22/8/2021

Name:

Designation:

ABSTRACT

Pollution remediation is one of the 21st-century global environmental concerns that need to be sustainable. As such, the conversion of pollutants such as CO₂ or chlorinated organics to useful products is a judicious strategy to achieve sustainability of their remediation processes as it provides an opportunity to generate economic profit. Conversion of pollutants can be achieved using superoxide ions (O₂^{•-}) as demonstrated in this research in the case of CO₂ and selected chlorinated organics. The conversion of pollutants using O₂^{•-} relies heavily on media with low nucleophilic susceptibility. This study successfully generated stable O₂^{•-} at $-\pm 1.0$ V vs Ag/AgCl in ammonium [Amm⁺], pyrrolidinium [Pyrr⁺], piperidinium [Pip⁺] and morpholinium [Mor⁺] based ILs that satisfy the low nucleophilic criterion. The study further pioneered the development of IL-nanofluid media using fully characterized novel pseudocapacitive Fe/Ru-SiMWCNT nanohybrid. The nanofluid has low nucleophilic susceptibility and suitable as media for stable O₂^{•-} generation at -0.445 V vs Ag/AgCl. Moreover, the interfacial and mass transfer parameters therein were determined using cyclic voltammetry (CV), chronoamperometry (CA) and electrochemical impedance spectroscopy (EIS) analysis. Long-term stability of the O₂^{•-} was determined in ILs and the nanofluid media using UV/Vis spectrometry. The kinetic parameter indicated that O₂^{•-} stays longer in some ILs; [MOEMPyrr⁺][PFTP⁻] (3.82 % decay, 0.34×10^{-5} s⁻¹), [MOEMMor⁺][TFSI⁻] (4.81 % decay, 1.71×10^{-5} s⁻¹), [BTMAmm⁺][TFSI⁻] (8.38 % decay, 0.82×10^{-5} s⁻¹). Second, O₂^{•-} decayed by only 2.24 % in Fe/Ru-SiMWCNT-[MOEMPyrr⁺][PFTP⁻] nanofluid with a rate constant of 0.423×10^{-5} s⁻¹ after at least 1 day. These long-term stability results validated the media for at least 60 min in-situ O₂^{•-} mediated electrolysis. The CV technique was used in the second part of the analysis to investigate selective CO₂ conversion to peroxy-dicarbonate anion (C₂O₆²⁻) by O₂^{•-} at -0.54 V vs Ag/AgCl. The C₂O₆²⁻ was identified by O-O (peroxy-bridge) symmetric stretching harmonic at 853 cm⁻¹

using DFT-IR and ATR-IR spectroscopy. The energy efficiency of $C_2O_6^{2-}$ production in the nanofluid was 97.6 %, higher than that in $[MOEMPyrr^+][PFTP^-]$ (50 %). This study postulated that the pseudocapacitance of Fe_3O_4 and RuO_2 phase of the nanofluid implicated a low overpotential required for CO_2 conversion by $O_2^{\bullet-}$ unlike ordinary ILs. Moreover, the CO_2 conversion mechanism followed direct nucleophilic addition of $O_2^{\bullet-}$ to CO_2 since the charge transfer resistance of the CO_2 saturated media is extremely high (6.86×10^{18} k Ω). In the third part of the study, in-situ $C_2O_6^{2-}$ further carboxylated diethanolamine to produce methyl (2-hydroxyethyl) (methyl) carbamate. In the fourth part of this research, dechlorination of CH_2Cl_2 and C_6H_5Cl by $O_2^{\bullet-}$ was investigated in $[BMPip^+][TFSI^-]$. The dechlorination process produced non-dioxin product distribution, achieving 100 % dechlorination after 2 h of electrolysis. In all these accomplishments, quantum chemical calculations were conducted to support the results. The final part of the research entailed analysis of product distribution from the electrolysis of either CO_2 or CH_2Cl_2 and C_6H_5Cl using GCMS, 1D (1H and ^{13}C), 2D (COSY, HSQC and HMBC) nuclear magnetic resonance analysis. Overall, this research contributed by conceptualizing the development of stable nanofluid media for reactive oxygen species, energy storage and conversion applications.

Keywords: Quantum chemical calculation, Reaction Engineering, CO_2 conversion, CO_2 capture, Superoxide Ion, Peroxydicarbonate anion, Nanotechnology, Climate engineering.

ABSTRAK

Pemulihan pencemaran merupakan salah satu isu alam sekitar global yang perlu diberikan penekanan secara berterusan di abad ke-21. Maka, penukaran bahan pencemar seperti karbon dioksida (CO_2) atau organik berklorin kepada produk yang berguna adalah strategi yang bijaksana untuk mencapai keberlanjutan proses pemulihan mereka kerana ia memberi peluang untuk menjana keuntungan ekonomi. Penukaran bahan pencemar dapat dicapai dengan menggunakan ion superoksida ($\text{O}_2^{\bullet-}$) seperti yang ditunjukkan dalam penyelidikan ini menggunakan CO_2 dan organik berklorin terpilih. Penukaran bahan pencemar menggunakan ion superoksida ($\text{O}_2^{\bullet-}$) bergantung sepenuhnya kepada media dengan kerentanan nukleofilik yang rendah. Maka, kajian ini telah berjaya menghasilkan $\text{O}_2^{\bullet-}$ yang stabil dalam ammonium [Amm^+], pyrrolidinium [Pyrr^+], piperidinium [Pip^+] dan morpholinium [Mor^+] berasaskan IL pada $\pm 1.0 \text{ V vs Ag/AgCl}$ yang dapat memenuhi kriteria nukleofilik rendah. Kajian ini seterusnya merintis pembangunan media IL-cecair nano dengan menggunakan pencirian penuh novel kapasitif pseudo Fe/Ru-SiMWCNT hibrid nano. Cecair nano mempunyai kerentanan nukleofilik yang rendah dan media yang sesuai untuk penghasilan $\text{O}_2^{\bullet-}$ yang stabil pada $-0.445 \text{ V vs Ag/AgCl}$. Tambahan lagi, parameter antara muka dan pemindahan jisim telah ditentukan menggunakan voltametri siklik (CV), kronoamperometri (CA) dan analisis spektroskopi impedan elektrokimia (EIS). Kestabilan jangka panjang bagi $\text{O}_2^{\bullet-}$ telah ditentukan dalam ILS dan media cecair nano menggunakan UV/Vis spektrometri. Pertama, parameter kinetik menunjukkan bahawa $\text{O}_2^{\bullet-}$ berada lebih lama dalam ILS berikut: [MOEMPyrr^+][PFTP^-] (3.82% pereputan, $0.34 \times 10^{-5} \text{ s}^{-1}$), [MOEMMor^+][TFSI^-] (4.81% pereputan, $1.71 \times 10^{-5} \text{ s}^{-1}$), [BTMAmm^+][TFSI^-] (8.38% pereputan, $0.82 \times 10^{-5} \text{ ms}^{-1}$). Kedua, hanya 2.24% pereputan $\text{O}_2^{\bullet-}$ telah diperhatikan dalam Fe/Ru-SiMWCNT-[MOEMPyrr^+][PFTP^-] cecair nano dengan pekali malar $0.423 \times 10^{-5} \text{ s}^{-1}$ sekurang-kurangnya selepas satu hari. Keputusan kestabilan jangka panjang mengesahkan media

ini bagi sekurang-kurangnya 60 min $O_2^{\bullet-}$ elektrolisis bermedia in-situ. Di bahagian kedua analisis ini, penentuan selektif untuk penukaran CO_2 kepada peroxy-dikarbonat ($C_2O_6^{2-}$) oleh $O_2^{\bullet-}$ pada -0.54 V vs Ag/AgCl menggunakan teknik CV. Melalui kombinasi DFT-IR dan spektroskopi ATR-IR, $C_2O_6^{2-}$ telah dikenalpasti melalui regangan harmonik simetri O-O (peroxybridge) unik pada 853 cm^{-1} . Kecekapan tenaga bagi penukaran CO_2 oleh $O_2^{\bullet-}$ dalam cecair nano adalah 97.6 % iaitu lebih tinggi dari ~ 50 % kecekapan tenaga dalam [MOEMPyrr⁺][PFTP⁻]. Kajian ini membuktikan bahawa kapasitif pseudo fasa Fe_3O_4 dan RuO_2 bagi cecair nano menunjukkan pengurangan potensi yang diperlukan untuk penukaran CO_2 oleh $O_2^{\bullet-}$, tidak seperti IL biasa. Mekanisma penukaran CO_2 mengikuti penambahan nukleofilik langsung $O_2^{\bullet-}$ kepada CO_2 kerana rintangan pemindahan cas media tepu CO_2 sangat tinggi (6.86×10^{18} k Ω). Di bahagian ketiga kajian ini, $C_2O_6^{2-}$ in-situ telah digunakan lebih lanjut untuk karboksilasi dietanolamin untuk menghasilkan metil (2-hidroksietil) (metil) karbamat. Di bahagian keempat kajian ini, penyahklorinan CH_2Cl_2 dan C_6H_5Cl oleh $O_2^{\bullet-}$ telah dikaji dalam [BMPip⁺][TFSI⁻]. Proses penyahklorinan menghasilkan pengedaran produk bukan dioksin, mencapai 100% penyahlorinasi selepas elektrolisis selama 2 jam. Melalui kesemua pencapaian ini, pengiraan kimia kuantum telah dijalankan untuk menyokong hasil kajian. Bahagian akhir kajian memerlukan analisis pengedaran produk dari elektrolisis sama ada CO_2 atau CH_2Cl_2 dan C_6H_5Cl menggunakan GCMS, 1D (1H dan ^{13}C) dan analisis resonan magnetik nuklear 2D (COZY, HSQC dan HMBC). Rumusannya, kajian ini menyumbang dengan berkonsepkan pengembangan media cecair nano stabil untuk spesies oksigen reaktif, penyimpanan tenaga dan aplikasi penukaran.

ACKNOWLEDGEMENTS

All appreciation goes to Allah (SWT) who guide and give us the ability to carry out this study right from the onset.

During this study's progression, most of the experiments were carried out chiefly using Chemical Engineering state-of-the-art facilities, Universiti Malaya (UM). Other analyses were conducted at the Institute of Research Management and Services UM, Chemistry Department UM, Physics Department UM, Department of Mechanical Engineering UM, Nanotechnology and Catalysis Research Center (NANOCAT) UM and MIMOS, Malaysia. The Newton Funds Institutional Links (IF013-2015) and GP058A-2020 (RU) funded the research. Therefore, I am grateful for all the provided supports.

I am highly grateful to my supervisory team, Asst Prof. Dr Maan Hayyan, Prof. Dr Mohamed Kheireddine Aroua, Prof. Dr Rozita Yusoff, and Dr Hanee Farzana Hizaddin for the guide, insightful supports and encouragements in various aspects and capacities right from the onset to the cessation of the research.

I am also grateful to the Head of the Chemical Engineering Department, Prof. Dr Ngoh Gek Cheng, for all the administrative enablement.

I appreciate the efforts of Dr Adeeb Hayyan during the study. I also appreciate the gesture from Emeritus Prof. Dr Mohammad Hashim for availing me to use the laboratory work station. Many thank again goes to Prof. Dr Azlan for the togetherness.

Many thanks go to Messrs; Rizman A Lateef, Suhana Mat Idris, Mohamed Hamdi Zainal-Abidin, Hurun Ein Suhaimi, Shiqin, the chemical engineering postgraduate club committee, the technical staffs of chemical engineering; Rustan, Kamaruddin, the staffs of faculty of engineering and many others.

I reserved the last part of my family's acknowledgement for being an asset. To my beloved and deceased father Khalil bn Ahmad, I pray that Allah reunites us in Jannah. To mother Ruqayyah bint Uthman; a rare gem for being the substance of my upliftment.

Special appreciation goes to my brothers, sisters, nephew, nieces, aunties, and fiancée for their prayers all through, I appreciate you all.

Universiti Malaya

Table of Contents

Abstract	iii
Abstrak	v
Acknowledgements	vii
List of Figures	xvi
List of Tables	xx
List of Symbols and Abbreviations	xxii
List of Appendices	xxv
CHAPTER 1: INTRODUCTION	1
1.1 General Overview	1
1.2 Problem Statement and Significance of the Study	5
1.3 Research Philosophy and Scope	7
1.4 Research Objectives	9
1.5 Research Methodology	9
1.6 Thesis Outline	11
CHAPTER 2: LITERATURE REVIEW	12
2.1 Superoxide Ion	12
2.2 Methods of $O_2^{\bullet-}$ Generation	13
2.2.1 The electrochemical generation of $O_2^{\bullet-}$	13
2.2.2 Chemical generation of $O_2^{\bullet-}$	14
2.3 Media for Generation of $O_2^{\bullet-}$	15
2.3.1 Aprotic solvents as media	15
2.3.2 Ionic liquid as media	16
2.3.2.1 General outlook on ionic liquids	18

2.3.2.2	Physicochemical properties of ionic liquids	20
2.3.2.3	Effect of impurities on ionic-liquid properties	23
2.4	Reactions of $O_2^{\bullet-}$	25
2.4.1	One-electron transfer	25
2.4.2	Nucleophilic substitution	27
2.4.3	Proton abstraction	28
2.4.4	Disproportionation	29
2.4.5	Applications of $O_2^{\bullet-}$ in organic synthesis	31
2.5	Detection of $O_2^{\bullet-}$	33
2.6	Outlook on CO_2 Emission, Capture and Utilization	35
2.6.1	Non- $O_2^{\bullet-}$ mediated CO_2 utilization	36
2.6.2	CO_2 utilization by $O_2^{\bullet-}$	38
2.7	Outlook on Dechlorination of Chlorinated Compounds	40
2.7.1	Non- $O_2^{\bullet-}$ mediated dechlorination	43
2.7.2	Mediation of dechlorination by $O_2^{\bullet-}$	43
2.8	Electrochemical Process	44
2.8.1	Electrode system	44
2.8.2	Chronoamperometry	45
2.8.3	Cyclic voltammetry	46
2.8.3.1	Reversible systems	47
2.8.3.2	Irreversible and quasi-reversible systems	48
2.8.3.3	Mass transfer parameter from CV analysis	50
2.9	Electrochemical Impedance Spectroscopy	51
2.9.1	Nyquist plot	53

CHAPTER 3: EXPERIMENTAL METHODOLOGY	55
3.1 Softwares, Instruments, Equipment, Fixtures, Gases, Chemicals	55
3.3 Computational Calculations	60
3.3.1 Molecular geometry optimization	60
3.3.2 Calculating the chemical reactivity descriptor	60
3.3.3 Theoretical UV-Vis analysis for $O_2^{\bullet-}$	62
3.3.4 COSMO-RS based calculations	62
3.4 Experimental Procedures	63
3.4.1 Development of Fe/Ru-SiMWCNT nanohybrid	63
3.4.2 Characterization of Fe/Ru-SiMWCNT nanohybrid	63
3.4.2.1 Physiochemical surface and textural properties	63
3.4.2.2 CO_2 temperature-programmed desorption	64
3.4.2.3 Temperature programmed oxidation	65
3.4.3 Synthesis of Fe/Ru-SiMWCNT-ILs nanofluid	65
3.4.4 Characterization of Fe/Ru-SiMWCNT-IL nanofluid	65
3.4.4.1 Drying	65
3.4.4.2 The electrochemical potential window of the ILs and Fe/Ru-SiMWCNT-IL nanofluid	66
3.4.4.3 Electrochemical impedance spectroscopy study	67
3.4.5 Cleaning of the electrochemical cell	68
3.4.5.1 Polishing of electrodes	68
3.4.6 Electrochemical active surface area	68
3.4.7 The electrochemical generation of $O_2^{\bullet-}$ in ILs and nanofluid	69
3.4.8 Long-term stability of $O_2^{\bullet-}$ in ILs and nanofluid	70
3.4.9 Electrolysis of CO_2 in ILs or Fe/Ru-SiMWCNT-IL nanofluid containing $O_2^{\bullet-}$	72

3.4.10	Electrolysis of C ₆ H ₅ Cl and CH ₂ Cl ₂ in IL containing O ₂ ^{•-}	73
3.4.11	Gas chromatography-mass spectroscopy analysis	76
3.4.12	Nuclear magnetic resonance analysis	78
3.5	Safety and Heuristics	79
CHAPTER 4: RESULTS AND DISCUSSION		81
4.1	Computational Analysis	81
4.1.1	COSMO-RS analysis	81
4.1.2	Chemical reactivity descriptor	86
4.2	Characterization of Fe/Ru-SiMWCNT Nanohybrid, ILs and Nanohybrid-ILs Nanofluid	90
4.2.1	X-ray diffraction analysis of Fe/Ru-SiMWCNT nanohybrid	90
4.2.2	Surface properties of Fe/Ru-SiMWCNT nanohybrid	92
4.2.2.1	Temperature-programmed desorption	92
4.2.2.2	XPS analysis of Fe/Ru-SiMWCNT nanohybrid	93
4.2.2.3	Raman analysis of Fe/Ru-SiMWCNT nanohybrid	95
4.2.2.4	Morphology and textural property of Fe/Ru-SiMWCNT nanohybrid	97
4.2.3	Electrochemical potential windows of ILs and Fe/Ru-SiMWCNT-ILs nanofluids	100
4.2.4	Electrochemical impedance spectroscopy	104
4.2.4.1	EIS parameter for ILs	104
4.2.4.2	EIS Parameter for Fe/Ru-SiMWCNT-ILs nanofluid	107
4.3	Generation of Superoxide Ion (O ₂ ^{•-}) in ILs	109
4.3.1	The electrochemical generation of stable O ₂ ^{•-}	109
4.3.1.1	Mass transfer phenomena of O ₂ in IL	110
4.3.1.2	Interfacial phenomena for O ₂ ^{•-} generation in IL	112

4.3.1.3	The electrochemical generation of unstable $O_2^{\bullet-}$	115
4.3.1.4	Effect of IL-cation substituents	116
4.3.2	Chemical generation of stable $O_2^{\bullet-}$	118
4.3.2.1	Long-term stability of $O_2^{\bullet-}$	118
4.3.2.2	Kinetics of $O_2^{\bullet-}$ in ILs	119
4.4	Conversion of CO_2 to Peroxydicarbonate ($C_2O_6^{2-}$) Using IL Media	122
4.4.1	Using ILs as media	123
4.4.1.1	Spectroscopic identification of $C_2O_6^{2-}$	126
4.4.2	Mechanism of CO_2 conversion by $O_2^{\bullet-}$ to $C_2O_6^{2-}$ in IL	129
4.5	Conversion of CO_2 by $O_2^{\bullet-}$ in Fe/Ru-SiMWCNT-IL Nanofluid as Media	135
4.5.1	Potential dependence of R_{ct} and σ in nanofluid	136
4.5.2	Detection of $O_2^{\bullet-}$ in Fe/Ru-SiMWCNT/[MOEMPyrr ⁺][PFTP ⁻] nanofluid	141
4.5.2.1	Electrochemical active surface area	141
4.5.2.2	Generation of $O_2^{\bullet-}$ in Fe/Ru-SiMWCNT/[MOEMPyrr ⁺][PFTP ⁻]	142
4.5.2.3	Mass transfer phenomena	145
4.5.2.4	Interfacial phenomena	146
4.5.2.5	Long-term stability of $O_2^{\bullet-}$	147
4.5.2.6	Conversion of CO_2 to $C_2O_6^{2-}$	148
4.6	Carboxylation of Diethanolamine by $C_2O_6^{2-}$ to Carbamate	154
4.6.1	Using ILs as media	155
4.6.1.1	Effect of time on product distribution	155
4.6.1.2	Effect of IL electrolyte on product distribution	157
4.6.2	Using Fe/Ru-SiMWCNT/[MOEMPyrr ⁺][PFTP ⁻] nanofluid as media	159
4.6.2.1	Effect of an applied potential	159

4.6.3	Proposed mechanism for methyl (2-hydroxyethyl) (methyl) carbamate formation	162
4.6.3	GCMS analysis	163
4.6.4	NMR analysis	164
4.7	Dechlorination of CH ₂ Cl ₂ and C ₆ H ₅ Cl by O ₂ ^{•-} in [BMPip ⁺][TFSI ⁻]	168
4.7.1	DFT frontier molecular orbital analysis	169
4.7.2	COSMO-RS benchmarking on dechlorination process	173
4.7.3	Electrochemical active surface area	178
4.7.4	Evidence of O ₂ ^{•-} in [BMPip ⁺][TFSI ⁻] containing CH ₂ Cl ₂ or C ₆ H ₅ Cl	179
4.7.5	Tafel analysis	182
4.7.6	Normalized exchange current density	184
4.7.7	Electrolytic dechlorination of CH ₂ Cl ₂ and C ₆ H ₅ Cl using O ₂ ^{•-} in [BMPip ⁺][TFSI ⁻]	186
4.7.8	NMR analysis	191
CHAPTER 5: CONCLUSION AND RECOMMENDATION		194
5.1	Conclusions	194
5.2	Recommendations	200
	References	202
APPENDICES		233
	Appendix A	233
	Appendix B	243
	Appendix C	249
	Appendix D	251
	Appendix E	261
	Appendix F	265

Appendix G	267
Appendix H	269
Appendix I	270
Appendix J	271
Appendix K	272
Appendix L	278

Universiti Malaya

LIST OF FIGURES

- Figure 2.1: Molecular orbital diagram for (a) superoxide ion ($O_2^{\bullet-}$), (b) dioxygen (Miao et al., 2019; Zaichenko et al., 2020; Kumar, A., & Sevilla, M. D. 2018) EC= Electron configuration BO = Bond order 13
- Figure 2.2: (a) Relative density as a function of the water mole fraction and (b) Relative viscosity as a function of the water mole fraction for five different ILs at 101 kPa (Andanson et al., 2016), Copyright (2016) Elsevier 25
- Figure 2.3: The cyclic voltammograms (CVs) in dimethylformamide containing 0.1 M of tetraethylammonium perchlorate. (a) $O_2^{\bullet-}$ generation and (b) CO_2 conversion by $O_2^{\bullet-}$ at the platinum working electrode and a scan rate of 100 mV/s (Roberts et al., 1984), Copyright (1984) American chemical society 39
- Figure 2.4: The cyclic voltammograms (CVs) in 1-n-butyl-3-methylimidazolium hexafluorophosphate $[BMIm^+][HFP^-]$ at ambient pressure. (1) = N_2 background, (2) = after sparging with CO_2 , (3) = after sparging with O_2 , (4) = after sparging with O_2 and CO_2 simultaneously at glassy-carbon disk working electrode and a scan rate of 100 mV/s (AlNashef et al., 2002), Copyright (2002) American chemical society 40
- Figure 2.5: Cyclic voltammograms for the electrode reaction; $Ox + ne^-$. Curve 1 is reversible, and curve 2 is quasi-reversible, curve 3 is irreversible and accompanied by a conversion of reduced species to an inactive electro species (Bard et al., 1980), Copyright (1980) Wiley 49
- Figure 2.6: General representation of the Nyquist plot (Mei et al., 2018), Copyright (2018) American chemical society. EDL = electrochemical double layer 54
- Figure 3.1: General process flow diagram of the research. Appendix L presents pictures of the major equipment 58
- Figure 3.2: (a) Schematic of the experimental set-up; feasibility analysis of the gas cylinder based on the international organization for standardization (ISO) confirmed the storage technique to be appropriate. No leakages throughout while the valves and flow meters are in good condition, (b) Illustration of the apparatus used to conduct electrochemical investigations. (1) Electrochemical cell, (2) GC-microelectrode, (3) Counter electrode, and (4) Ag/AgCl reference electrode 59
- Figure 4.1: COSMO-RS profile for (a) $[EDMPAm^+][TFSI^-]$, (b) $[BMPyrr^+][TFSI^-]$, (c) $[MOEMPyrr^+][PFTP^-]$, (d) $[MOEMMor^+][TFSI^-]$, (e) $[BMIm^+][TFSI^-]$, (f) $[PMIm^+][TFSI^-]$, (g) $[BMPip^+][TFSI^-]$, (h) $[TBMAm^+][TFSI^-]$, (i) $[BMAm^+][TFSI^-]$, (j) $[MTOAm^+][TFSI^-]$, and (k) $[DEMAm^+][TF^-]$. The COSMO-RS profiles ILs were compared with $O_2^{\bullet-}$, CO_2 and O_2 85

Figure 4.2: Mulliken atomic charges of carbon and nitrogen atoms in (a) [TMHAm⁺], (b) [BMPyr⁺], (c) [EMIm⁺], (d) [DMPIIm⁺] (Katayama et al., 2004a). This study; (e) [TBMAm⁺], (f) [BMAm⁺], (g) [EDMPAm⁺], and (h) [BMPip⁺] 89

Figure 4.3: X-ray diffraction pattern of Fe/Ru-SiMWCNT calcined at different temperatures such as; 400, 500, and 600 °C 91

Figure 4.4: (a) Temperature programmed oxidation and (b) CO₂ temperature programmed desorption for Fe/Ru-SiMWCNT nanohybrid 92

Figure 4.5: (a) The full survey-scan XPS spectra, (b) The O 1s core-level XPS spectrum (c) The Si 2p core-level XPS spectrum (d) The C 1s or Ru 3d core-level XPS spectrum (e) The Fe 2p core-level XPS spectrum for Fe/Ru-SiMWCNT nanohybrid heterostructures. Deconvoluted spectra are in dotted lines, while the experimental spectra are thick continuous black line indicated by an arrowhead 95

Figure 4.6: (a) Raman spectrum of Fe/Ru-SiMWCNT nanoparticles (b) Raman mapping spectrum of Fe/Ru-SiMWCNT nanoparticles 97

Figure 4.7: (a) FESEM/EDS (i-iv) at 500 nm resolution, (b) HRTEM at 20 nm resolution, (c) HRTEM at 200 nm resolution, (d) HRTEM at 2 nm resolution and (e) Fast Fourier transform at 2 nm resolution for Fe/Ru-SiMWCNT nanohybrid 99

Figure 4.8: CVs of O₂^{•-} generated in (a) [EDMPAm⁺][TFSI⁻], (b) [BMPyr⁺][TFSI⁻], (c) [MOEMPyrr⁺][PFTP⁻], (d) [MOEMMor⁺][TFSI⁻], (e) [BMIm⁺][TFSI⁻], (f) [PMIm⁺][TFSI⁻], (g) [TBMAm⁺][TFSI⁻], (h) [BMAm⁺][TFSI⁻], (i) [MTOAm⁺][TFSI⁻], and (j) [BMPip⁺][TFSI⁻]. All the measurements were performed after sparging the IL with N₂ (background) at 25 °C. This is necessary to ensure that ILs are free from impurities as recommended 114

Figure 4.9: CVs of unstable generation of O₂^{•-} in (a) [BMIm⁺][TCM⁻] and (b) [BMIm⁺][DCA⁻]. This profile was obtained after saturating the ILs with N₂ followed by O₂ 116

Figure 4.10 Absorbance spectra of O₂^{•-} based on TD-DFT calculation on Gaussian 09 software package. This is a theoretical estimation that guides the experimental observation of water-free O₂^{•-}. The analysis was done in a vacuum where external influence, such as water, is absent 118

Figure 4.11: Cyclic voltammograms (CVs) of CO₂ conversion by O₂^{•-} in (a) [EDMPAm⁺][TFSI⁻], (b) [MOEMPyrr⁺][PFTP⁻], (c) [MOEMMor⁺][TFSI⁻], (d) [TBMAm⁺][TFSI⁻], (e) [BMAm⁺][TFSI⁻], (f) [MTOAm⁺][TFSI⁻] and (g) [BMPip⁺][TFSI⁻] after continuously sparging the ILs with N₂ (Background), or O₂ or simultaneously sparging the ILs with CO₂/O₂. Measurement were recorded at 9 mV/s 126

Figure 4.12: Nyquist plots detected in (a) O₂-saturated-[BM⁺][TFSI⁻], (b) O₂/CO₂-saturated-[BM⁺][TFSI⁻] and (c) CO₂-saturated-[BM⁺][TFSI⁻]. Bode plots detected in (d) O₂-saturated-[BM⁺][TFSI⁻], (e) O₂/CO₂-saturated-[BM⁺][TFSI⁻] and (f) CO₂-saturated-[BM⁺][TFSI⁻] 133

Figure 4.13: Typical Nyquist plot at a bias voltage of -1.564 V vs Ag/AgCl for (a) N₂ saturated (b) O₂ saturated, (c) CO₂ saturated and (d) O₂/CO₂ saturated Fe/Ru-SiMWCNT/[MOEMPyrr⁺][PFTP⁻] nanofluid. Typical bode plot detected in (e) N₂ saturated (f) O₂ saturated, (g) CO₂ saturated, and (h) O₂/CO₂ saturated Fe/Ru-SiMWCNT/[MOEMPyrr⁺][PFTP⁻] 139

Figure 4.14: Potential-dependent (a) charge-transfer resistance and (b) Warburg impedance coefficient of Fe/Ru-SiMWCNT/[MOEMPyrr⁺][PFTP⁻] nanofluid in contact with GC 141

Figure 4.15: Cyclic voltammograms of N₂ saturated (a) Fe/Ru-SiMWCNT/[MOEMPyrr⁺][PFTP⁻] nanofluid, (b) [MOEMPyrr⁺][PFTP⁻] and (c) Charging difference vs. scan rates stripping in N₂ saturated Fe/Ru-SiMWCNT/[MOEMPyrr⁺][PFTP⁻] nanofluid and [MOEMPyrr⁺][PFTP⁻] 142

Figure 4.16: CVs of O₂^{•-} electrochemically generated in Fe/Ru-SiMWCNT/[MOEMPyrr⁺][PFTP⁻] nanofluid (a) In terms of applied potential (b) In terms of over-potential (c) Amount of O₂^{•-} in terms of activation overpotential. All measurements were done at 25 °C 145

Figure 4.17: (a) Absorbance spectra of O₂^{•-} chemically generated and (b) Kinetics of O₂^{•-} decay in Fe/Ru-SiMWCNT/[MOEMPyrr⁺][PFTP⁻] nanofluid. Measurements and chemical generation of O₂^{•-} were achieved at room temperature 148

Figure 4.18: Cyclic voltammogram (CVs) of C₂O₆²⁻ generation in Fe/Ru-SiMWCNT/[MOEMPyrr⁺][PFTP⁻] nanofluid (a) In terms of applied potential (b) In terms of activation overpotential (c) In terms of overpotential in [MOEMPyrr⁺][PFTP⁻] (d) Amount of C₂O₆²⁻ detected in Fe/Ru-SiMWCNT/[MOEMPyrr⁺][PFTP⁻] nanofluid and [MOEMPyrr⁺][PFTP⁻] vs activation overpotential (e) Energy efficiency of CO₂ conversion to C₂O₆²⁻ by O₂^{•-}. Measurements were done at room temperature 153

Figure 4.19: (a) Electrolysis of O₂/CO₂ in Fe/Ru-SiMWCNT/[MOEMPyrr⁺][PFTP⁻] nanofluid containing diethanolamine (b) Electrolysis of O₂/CO₂ in Fe/Ru-SiMWCNT/[MOEMPyrr⁺][PFTP⁻] nanofluid afterwards, Diethanolamine was added 161

Figure 4.20: Summary of the proposed mechanism for the formation of methyl (2-hydroxyethyl) (methyl) carbamate 163

Figure 4.21: (a) GC chromatogram for methyl (2-hydroxyethyl) methylcarbamate as the product resulting from the reaction of C₂O₆²⁻ and diethanolamine, (b) Mass spectrum for

methyl (2-hydroxyethyl) methylcarbamate in Ru/Fe-SiMWCNT/[MOEMPyrr⁺][PFTP⁻] nanofluid 164

Figure 4.22: (a) ¹H NMR spectrum and (b) ¹³C H NMR spectrum of methyl 2-hydroxyethyl (methyl) carbamate 165

Figure 4.23: 2D-NMR analysis profiles for detected methyl (2-hydroxyethyl) (methyl) carbamate (a) COSY/400MHz, (b) HSQC/400mHz and (C) HMBC/600MHz 168

Figure 4.24: (a) Mulliken atomic charges on [BMPip⁺]-cation, (b) Frontier molecular orbital showing 3-D rendered iso-valued surfaced for [BMPip⁺]-cation. The green colour coding represents a negative iso-surface, while the brown colour coding signifies the positive iso-surface computed at the DFT/B3LYP/6-31G level of theory 172

Figure 4.25: (a) σ -surface/ σ -profile of [BMPip⁺][TFSI⁻] and H₂O in comparison with σ -profile of C₆H₅Cl and CH₂Cl₂, (b) σ -potential of [BMPip⁺][TFSI⁻], H₂O, C₆H₅Cl, and CH₂Cl₂, (c) Activity coefficient of C₆H₅Cl, or CH₂Cl₂ in H₂O, (d) Activity coefficient of C₆H₅Cl, or CH₂Cl₂ in [BMPip⁺][TFSI⁻] at infinite dilution 177

Figure 4.26: Charging difference (Δj) vs. scan rates stripping in N₂/O₂ saturated; (a) [BMPip⁺][TFSI⁻], (b) [BMPip⁺][TFSI⁻]/CH₂Cl₂, (c) [BMPip⁺][TFSI⁻]/C₆H₅Cl, (d) Comparing the ECSA of GC electrode in O₂ saturated [BMPip⁺][TFSI⁻], [BMPip⁺][TFSI⁻]/CH₂Cl₂, and [BMPip⁺][TFSI⁻]/C₆H₅Cl 179

Figure 4.27: CV of O₂^{•-} generation in (a) [BMPip⁺][TFSI⁻] containing 2.5 mM CH₂Cl₂ (b) [BMPip⁺][TFSI⁻] containing 2.5 mM C₆H₅Cl 181

Figure 4.28: Tafel plot of Log (j) versus overpotential (η) region in (a) O₂-saturated [BMPip⁺][TFSI⁻], (b) O₂-saturated [BMPip⁺][TFSI⁻] containing CH₂Cl₂ and (c) O₂-saturated [BMPip⁺][TFSI⁻] containing C₆H₅Cl. The scan rate was used at 9 mV/s. Linear Tafel plot detected in region in (d) O₂-saturated [BMPip⁺][TFSI⁻], (e) O₂-saturated [BMPip⁺][TFSI⁻] containing CH₂Cl₂ and (f) O₂-saturated [BMPip⁺][TFSI⁻] containing C₆H₅Cl 183

Figure 4.29: Normalized exchange current density (i_0 . ECSA) for O₂^{•-} generation in (a) [BMPip⁺][TFSI⁻], (b) [BMPip⁺][TFSI⁻] containing CH₂Cl₂ and (c) [BMPip⁺][TFSI⁻] containing C₆H₅Cl. (d) The Ln(i_0) versus T⁻¹ for O₂^{•-} generation in [BMPip⁺][TFSI⁻], [BMPip⁺][TFSI⁻] containing CH₂Cl₂, and [BMPip⁺][TFSI⁻] containing C₆H₅Cl 186

Figure 4.30: Dechlorination activity of C₆H₅Cl and CH₂Cl₂ by O₂^{•-} in [BMPip⁺][TFSI⁻] (a) Conversion of C₆H₅Cl and CH₂Cl₂ by O₂^{•-} (b) Product selectivity from CH₂Cl₂ conversion by O₂^{•-} (c) Product selectivity from C₆H₅Cl conversion by O₂^{•-} and (d) Degree of dechlorination of CH₂Cl₂ or C₆H₅Cl by O₂^{•-} 191

LIST OF TABLES

Table 2.1: Some ionic liquids used for long-term stability study of $O_2^{\bullet-}$	15
Table 2.2: Some ILs used for generating stable $O_2^{\bullet-}$	17
Table 2.3: Cathodic and anodic potential vs Ag/AgCl for ECW of ILs at cut-off current density 0.5 mA/cm^2 using GC macro-electrode ($25 \text{ }^\circ\text{C}$)	
Table 2.4: Diffusion coefficients and solubility of electrochemical reduction of O_2 in IL media by CV technique using Au electrode	51
Table 2.5: Circuit elements for modelling EIS data	52
Table 3.1: Specifications of the ionic liquids (ILs) *	56
Table 3.2: Structure of ions in the ILs comprising of cation and anion ends	57
Table 4.1: Energetic and reactivity descriptor of ILs, CO_2 and $O_2^{\bullet-}$	88
Table 4.2: Cathodic and anodic potentials vs Ag/AgCl for ECWs of ILs at cut-off current density 0.5 mA/cm^2 using GC macro working electrode*	103
Table 4.3: Electrochemical window of Fe/Ru-SiMWCNT-ILs nanofluid at cut-off current density 0.5 mA/cm^2 using GC macro working electrode*	103
Table 4.4: Parameter values of elements in the equivalent circuit model for ILs	106
Table 4.5: EIS parameter in the equivalent circuit model for Fe/Ru-SiMWCNT-ILs*	108
Table 4.6: Comparing the specific capacitance with literature at $25 \text{ }^\circ\text{C}$	108
Table 4.7: Mass transfer and interfacial parameter of O_2 reduction to $O_2^{\bullet-}$ in ILs*	115
Table 4.8: Rate constant of $O_2^{\bullet-}$ chemically generated in ILs	122
Table 4.9: Total consumption percentage and consumption rate of $O_2^{\bullet-}$ in ILs	122
Table 4.10: Comparing DFT/B3LYP/6-31G-IR and ATR-IR for $C_2O_6^{2-}$ in [TBM Am^+][TFSI $^-$]	129
Table 4.11: EIS parameter from the Randle equivalent circuit model	133
Table 4.12: Effect of time on carboxylation reaction between diethanolamine and $C_2O_6^{2-}$	156
Table 4.13: Chemical symbols	156

Table 4.14: Effect of ILs electrolyte on product distribution 157

Table 4.15: Reactivity of electrogenerated $O_2^{\bullet-}$ in O_2/CO_2 -saturated Fe/Ru-SiMWCNT/[MOEMPyrr⁺][PFTP⁻] nanofluid containing 1.0 mM diethanolamine; effect of the over-potential on product distribution 161

Table 4.16: Reactivity of electrogenerated $O_2^{\bullet-}$ in O_2/CO_2 -saturated [MOEMPyrr⁺][PFTP⁻] containing 1.0 mM diethanolamine; effect of over-potential on product distribution 162

Universiti Malaya

LIST OF SYMBOLS AND ABBREVIATIONS

[EDMPAmm ⁺][TFSI ⁻]	Ethyl-dimethyl-propylammonium bis(trifluoromethylsulfonyl)imide
[MOEMMor ⁺][TFSI ⁻]	N-Methoxyethyl-N-methylmorpholinium bis(trifluoromethylsulfonyl)imide
[BMPyrr ⁺][TFSI ⁻]	1-Butyl-1-methylpyrrolidinium bis (trifluoromethylsulfonyl)imide
[MOEMPyrr ⁺][TFSI ⁻]	1-(2-Methoxyethyl)-1-methylpyrrolidinium bis(trifluoromethylsulfonyl)imide
[BIMm ⁺][TFSI ⁻]	1-Butyl-3-methylimidazolium bis(trifluoro-methylsulfonyl)imide
[EMIm ⁺][TFSI ⁻]	1-Ethyl-3-methylimidazolium bis(trifluoromethylsulfonyl)imide
[PMIm ⁺][TFSI ⁻]	1-Propyl-3-methylimidazolium bis(trifluoromethylsulfonyl)imide
[TBMA ⁺][TFSI ⁻]	Tributylmethylammonium bis(trifluoromethylsulfonyl)imide
[BTMA ⁺][TFSI ⁻]	Butyltrimethylammonium bis(trifluoromethylsulfonyl)imide
[MTOA ⁺][TFSI ⁻]	Methyltrioctylammonium bis(trifluoromethylsulfonyl)imide
[Ch ⁺][TFSI ⁻]	Choline bis(trifluoromethylsulfonyl)imide
[TES ⁺][TFSI ⁻]	Triethylsulfonium bis(trifluoromethylsulfonyl)imide
[BIMm ⁺][DCA ⁻]	1-Butyl-3-methylimidazolium dicyanamide
[BIMm ⁺][TFMS ⁻]	1-Butyl-3-methylimidazolium trifluoromethanesulfonate
[BIMm ⁺][TCM ⁻]	1-Butyl-3-methylimidazolium tricyanomethane
[BIMm ⁺][HFP ⁻]	1-Butyl-3-methylimidazolium hexafluorophosphate
[BIMm ⁺][HCDA ⁻]	1-Butyl-3-methylimidazolium heptachlorodialuminate
[DEMA ⁺][TF ⁻]	Diethylmethylammonium triflate
[BIMm ⁺][TFB ⁻]	1-butyl-3-methylimidazolium tetrafluoroborate
[EMIm ⁺][TFB ⁻]	1-ethyl-3-methylimidazolium tetrafluoroborate
[DMIm ⁺][TFB ⁻]	1-decyl-3-methylimidazolium tetrafluoroborate
[BIMm ⁺][HFB ⁻]	1-butyl-3-methylimidazolium hexafluorophosphate
[BIMm ⁺][MS ⁻]	1-butyl-3-methylimidazolium methylsulfate
[HMPyrr ⁺][TFSI ⁻]	N-(3-Hydroxypropyl) pyridinium bis (trifluoromethylsulfonyl) imide
[BMPyrr ⁺][TFA ⁻]	1-butyl-1-methylpyrrolidinium bis(trifluoromethanesulfone)imide
[HMPyrr ⁺][TFSI ⁻]	N-(3-Hydroxypropyl) pyridinium bis (trifluoromethylsulfonyl) imide
[MPiper ⁺][TFSI ⁻]	1-(3-methoxypropyl)-1-methylpiperidinium bis (trifluoromethylsulfonyl) imide
[TBMAMm ⁺][TFSI ⁻]	Tributylmethylammonium bis(trifluoromethylsulfonyl)imide

[BTMAmm ⁺][TFSI ⁻]	Butyltrimethylammonium bis(trifluoromethylsulfonyl)imide
[MTAmm ⁺][TFSI ⁻]	Methyltrioctylammonium bis(trifluoromethylsulfonyl)imide
[OTAm ⁺][TFMS ⁻]	Octyltriethylammonium bis(trifluoromethylsulfonyl)imide
[DEMAmm ⁺][TFSI ⁻]	N,N-diethyl-N-methyl-N-(2-methoxyethyl)ammonium bis (trifluoromethylsulfonyl)imide
[EDMEAmm ⁺][PFFP ⁻]	N-Ethyl-N,N-dimethyl-2-methoxy-ethylammoniumtris(pentafluoroethyl) trifluorophosphate
[TMAmm ⁺][TFSI ⁻]	Trimethyl-N-hexylammonium bis(trifluoromethanesulfone)imide
COSMO-RS	Conductor like screening model for realistic solvents
C _o	Bulk concentration of O ₂ (mol/mL)
D _o	Diffusion coefficient of O ₂ (m ² /s)
D	Diffusion coefficient of the electroactive species (m ² /s)
E _{a,D}	The activation energy for diffusion of the electroactive species
v	Potential sweep rate (V/s)
E _p	Peak potential for cathodic current (V)
E ^o	Formal potential of the reaction
k ^o	Standard heterogeneous rate constant (cm/s)
n	Number of electrons
r _o	Radius of ultra-microelectrode (cm)
j _c	Current density (A/cm ²)
i _p	Cathodic peak current of cyclic voltammetry (A)
i _{ss}	Steady-state current of chronoamperometry (A)
α	Charge transfer coefficient
A	Surface area of the macro-working electrode (cm ²)
C _o	Bulk concentration of O ₂ (mol/mL)
D _o	Diffusion coefficient of O ₂ (m ² /s)
E _p	Peak potential for cathodic current (V)
E ^o	Formal potential of the reaction
R	Universal gas constant (J/mol. K)
T	Absolute temperature (K)
F	Faraday's constant (96485 C/mol)
k ^o	standard heterogeneous rate constant (cm/s)
n	number of electrons
r _o	radius of ultra-microelectrode (cm)
CE	Columbic efficiency

M	Mole of product
$O_2^{\bullet-}$	Superoxide ion
$C_2O_6^{2-}$	Peroxydicarbonate anion
R_{ct}	Charge transfer resistance (Ohm)

Universiti Malaya

LIST OF APPENDICES

Appendix A: Frontier molecular orbital of IL	233
Appendix B: Mulliken atomic charges of ILs	243
Appendix C: Electrochemical window	249
Appendix D: Electrochemical impedance spectroscopy	251
Appendix E Cathodic and anodic separation	261
Appendix F: Absorbance spectra of $O_2^{\bullet-}$ chemically generated	265
Appendix G: CV of CO_2 reduction by $O_2^{\bullet-}$	267
Appendix H: Gas chromatography-mass spectrometry (GCMS) spectrums	269
Appendix I: Nuclear magnetic resonance (NMR)	270
Appendix J: Non-Faradaic cyclic voltammogram	271
Appendix K: Lists of achievements	272
Appendix L: Some major equipment	278

CHAPTER 1: INTRODUCTION

1.1 General Overview

Strengthening resilience and adaptive capacity to control environmental-related pollutants such as carbon dioxide (CO₂) or chlorinated substances is part of the sustainable development goals (SDGs). This SDG is realizable through CO₂ capture and utilization (CCU). The focus of SDG is resolving large-scale CO₂ emissions from anthropogenic point sources mainly power plants, automobile and production industries (Hunt et al., 2010; Markewitz et al., 2012). However, the CCU consumes high energy inputs, both upstream, during CO₂ capture and downstream, during subsequent reactions (Appel et al., 2013). For instance, the capture of CO₂ from coal-fired plants and its regeneration back to the gas phase amount to ~ 30 % reduction in the plant's power output (Boot-Handford et al., 2014).

Similarly, the SDG is feasible through the dechlorination of chlorinated substance that constitutes environmental concern. Chlorinated substances are valued pharmaceutical building blocks (Wilcken et al., 2013) or precursors for producing speciality chemicals (Jeschke, 2010). The occurrences of chlorinated organics in our environment are in the form of by-products of chemical processes or unregulated incinerations and disposals (Keppler et al., 2002; Miyake et al., 2017). Therefore, societies tend to be oblivious to their existence, making them potentially harmful. So, transforming chlorinated compounds into a less toxic substance is the SDG expectations towards environmental remediation.

Meanwhile, the electrochemical conversion-widely proposed as a downstream transformation of CO₂ to speciality chemicals, fuels, or drop-in fuels, requires high activation overpotentials (Kuhl et al., 2012). This high activation overpotential increases the CO₂ conversion energy. Converting CO₂ at low overpotential plea on the need to design a new electrochemical reaction system by relaxing critical constraints common

with the classical electrochemical CO₂ conversion technique. Given the high overpotential in CO₂ reduction, e.g., >1.0 V for CO₂ conversion to CH₄ on Cu vs Ag/AgCl electrocatalyst (Kuhl et al., 2012), the focus now is lowering the reduction intermediate's free-energy (e.g. CO₂^{•-}). Therefore, the design of an electrochemical system that can reduce kinetic barriers by promoting this high-energy species' stabilization can typically accomplish low overpotential. Although a recent investigation confirmed a low overpotential of ~ 0.285 V for CO₂ conversion to CH₄ on Cu-Se electrocatalyst (Yang et al., 2019), there is less attention to modify the reactant state of CO₂ as a means to improve the conversion kinetics. Modifying the reactant state of CO₂ means activating it at low overpotential to an anion. For that reason, AlNashef et al. (2002) activated CO₂ with superoxide ion (O₂^{•-}) to peroxy-dicarbonate anion.

Apart from CO₂, the classical conversion of chlorinated environmental pollutant often yields poisonous dioxin substances (Field & Sierra-Alvarez, 2008; McKay, 2002). Producing dioxin undermines the dechlorination process's purpose of establishing a safe environment particular for SDGs. Given this challenge, research interests emphasize converting chlorinated compound to non-dioxin-based compounds. For example, O₂^{•-} mediated conversion of CH₃Cl and CHBr to non-dioxin products (Johnson, Nidy, & Merritt, 1978; Merritt & Sawyer, 1970; Ryding et al., 2015). Towards O₂^{•-} mediated conversion of CO₂ or chlorinated pollutants, the major constraint is developing an electrolyte medium to sustain O₂^{•-} for utilization.

Usually, aprotic solvents (dimethyl sulfoxide, acetonitrile and dimethylformamide) and ionic liquids (ILs) media can retain O₂^{•-} (Roberts Jr. & Sawyer, 1983; Maan Hayyan, Hashim, & AlNashef, 2016). However, the dimethyl sulfoxide (DMSO), is renowned for rendering ~3 % decay of the O₂^{•-} (Chin et al., 1982; Che et al., 1996; Roberts, Calderwood, & Sawyer, 1984; Chin et al., 1982; Casadei et al., 1996). This phenomenon is similar to other aprotic solvents such as acetonitrile (ACN) and

dimethylformamide (DMF). On the other hand, Hayyan et al. (2016) reviewed research studies that indicated different ILs media capability to sustain the $O_2^{\bullet-}$. The ILs have a non-volatile profile and could retain $O_2^{\bullet-}$, rendering low decay (Evans et al., 2004). The rate constant for $O_2^{\bullet-}$ decay in ILs is low and falls within the range of 10^{-5} - $10^{-3} \text{ m}^{-1}\text{s}^{-1}$ (Hayyan et al., 2012; Schwenke et al., 2015; Hayyan et al., 2017). This kinetic parameter approves $O_2^{\bullet-}$ long-term stability in ILs. Exceptionally, imidazolium-cation undergo ion-pairing with $O_2^{\bullet-}$ to form imidazolones (AlNashef et al., 2010; Hayyan et al., 2013). In contrast, aliphatic and alicyclic IL-cations have a low tendency to interact with $O_2^{\bullet-}$ (Katayama et al., 2004). Thus, the $O_2^{\bullet-}$ /IL couple offers a promising opportunity for radical driven electrochemical processes. Along the timeline for $O_2^{\bullet-}$ generation and utilization by CO_2 or chlorinated substance, for instance, finding stable ILs electrolyte are essential.

ILs electrolytes are pivotal for the design of industrially scalable electrochemical processes (Zhigang Lei Orcid, 2017; Zhang et al., 2019). Their application, especially in electrochemical conversion of substrates (e.g. CO_2), has received much attention due to their high gas sorption capacity (Zhao et al., 2014; Oh & Hu, 2015; Wang et al., 2020). Moreover, the restructuring of interfacial multilayer between ILs and electrodes initiates a tendency for low activation overpotential in ILs (Motobayashi, Shibamura, & Ikeda, 2020). This low activation overpotential property further inspires the sustainable CO_2 conversion by $O_2^{\bullet-}$ in ILs even at the expense of CO_2 chemical inertness. Therefore, it is indispensable to improve ILs electrolyte media (nanofluid) to further have practically low overpotential (Aman et al., 2017).

Concerning the conversion of the chlorinated compound using $O_2^{\bullet-}$ through an electrochemical technique in ILs media, there is no report until now. The available report on the dechlorination process using $O_2^{\bullet-}$ only focused on the aprotic solvents (Johnson, Nidy, & Merritt, 1978; Merritt & Sawyer, 1970; Ryding et al., 2015). Therefore, the use

of IL, in this case, serves three unique purposes; 1) as media for sustainable generation of $O_2^{\bullet-}$, 2) inducement of high spin density that increase charge redistribution during the electrochemical process and 3) capacity for absorption of chlorinated compounds thereby improving their coverage around the electrode to facilitate their electrochemical dechlorination by $O_2^{\bullet-}$.

This present research focused on the conversion of two major substrates; CO_2 and chlorinated substances (CH_2Cl_2 and C_6H_5Cl) using in-situ electrochemically generated $O_2^{\bullet-}$. The study considered IL for converting chlorinated pollutants and ILs or nanofluid for CO_2 conversion. In the first part of the work, quantum chemical calculation using COSMOthermX19 software estimated the capacity of the ILs for CO_2 and O_2 sorption and chlorinated substance. Also, quantum chemical calculation using Gaussian 09 software estimated the chemical reactivity prospective of $O_2^{\bullet-}$ with CO_2 or chlorinated substances. The second part of the study focused on characterizing the ILs and novel nanofluid media using cyclic voltammetry and electrochemical impedance spectroscopy. The third part of the study focused on the generation of stable $O_2^{\bullet-}$ electrochemically in structurally new ILs or ILs based nanofluid. Meanwhile, the ILs nanofluid contains novel Fe/Ru-SiMWCNT nanohybrid component prepared from a one-pot process with the hybridization of each atomic orbitals, thereby forming newly hybridized orbitals. Therefore, the Fe/Ru-SiMWCNT nanohybrid differs in terms of physicochemical, structural and bonding properties compared to other nanoparticles such as $Fe_3O_4-SiO_2$ (Ding et al., 2012), $Ru-SiO_2$ (Cui et al., 2016), and $Fe_3O_4-MWCNT$ (Kletetschka, et al., 2019; Liu et al., 2018). Interestingly, the Fe/Ru-SiMWCNT nanohybrid is important by contributing a pseudocapacitive attribute during $O_2^{\bullet-}$ synthesis or CO_2 conversion. Moreover, through a systematic temperature program desorption experiment in the CO_2 and O_2 environment, the Fe/Ru-SiMWCNT nanohybrid have CO_2/O_2 sorption capacity. Many analytical techniques characterize the physicochemical and morphological

properties of the Fe/Ru-SiMWCNT nanohybrid for approving the prowess of the Fe/Ru-SiMWCNT-ILs nanofluid. Spectroscopy and electrochemical means indicated that both ILs and Fe/Ru-SiMWCNT nanohybrid-IL (nanofluid) are suitable media for the possible generation of stable $O_2^{\bullet-}$. The study also establishes the charge transport phenomena in ILs and their Fe/Ru-SiMWCNT nanohybrid-IL. The fourth part of this study focused on investigating and validating the long-term stability of $O_2^{\bullet-}$ in IL or nanofluid media. In the progression of this part, UV-Vis spectroscopy was employed. The fifth part of the study focused on utilizing $O_2^{\bullet-}$ by CO_2 using the CV technique before proceeding with electrolysis. Also, this part of the study utilized $O_2^{\bullet-}$ by the chlorinated compound in a suitable IL using the CV technique before proceeding with dechlorination electrolysis. In the sixth part of the work, GCMS, 1-D NMR (1H and ^{13}C), and 2-D NMR (COSY, HSQC and HMBC) experiment elucidated resultant speciality chemical product from the reaction between $O_2^{\bullet-}$ and CO_2 , CH_2Cl_2 , C_6H_5Cl . The study in this part also used electrochemical impedance spectroscopy to describe the mechanism guiding $O_2^{\bullet-}$ utilization by CO_2 , CH_2Cl_2 , and C_6H_5Cl . The results of each of these parts were reported in the appropriate section of this report. The breakthrough of this study is the pioneering of ionic liquid-based nanofluids for stable $O_2^{\bullet-}$ generation and utilization. Another advance of this study is the utilization of peroxy-dicarbonate from CO_2 reaction with $O_2^{\bullet-}$ to carboxylate diethanolamine then producing structurally new carbamate. Besides, this is the first study that utilizes IL as a media to dechlorinate chlorinated pollutants using electrochemically generated $O_2^{\bullet-}$. Throughout the thesis, American English style was adopted.

1.2 Problem Statement and Significance of the Study

Though ILs could function as media for $O_2^{\bullet-}$ generation using cyclic voltammetry (CV), the CV technique is limited to examining only the short-term stability of $O_2^{\bullet-}$. This implied that CV cannot give quantitative approval of the longer time it takes $O_2^{\bullet-}$ to reside

in the ILs. The CV technique of $O_2^{\bullet-}$ generation only account for a stability duration of ≤ 60 seconds. Therefore, generating and utilizing $O_2^{\bullet-}$ in the conversion of CO_2 or chlorinated compounds (CH_2Cl_2/C_6H_5Cl) requires evaluation of $O_2^{\bullet-}$ long-term stability in ILs as a first criterion. This is an important pre-requisite before approval of $O_2^{\bullet-}$ utilization in a media for typical reactions that span at ≥ 30 min.

In cumulative, ~ 300 studies on the short-term and long-term stability of $O_2^{\bullet-}$ in ILs concluded that IL-cation could be susceptible to $O_2^{\bullet-}$ nucleophilic attack. The $O_2^{\bullet-}$ nucleophilic tendencies amidst ILs electrophilic potential using reactivity descriptor (e.g. global electrophilicity index, Mulliken charges) is unfamiliar and necessary. Consequently, understanding and adequately interpreting the mediated reaction (e.g. the conversion of CO_2 or chlorinated compounds) by $O_2^{\bullet-}$ is lacking in the literature.

There is no doubt that the rise in CO_2 emission increases global temperatures and induces climate change. Therefore, for a promising carbon economy, an energy-efficient CO_2 utilization mediated by $O_2^{\bullet-}$ to produce speciality chemicals is necessary. However, the conventional approach of CO_2 utilization suffers from high overpotential requirement because of inherent CO_2 chemical stability. The media that would assure CO_2 conversion by $O_2^{\bullet-}$ at low overpotential is highly desired and yet to be reported previously.

Similarly, chlorinated organic compounds from industrial processes and many unregulated incinerations are abundant and harmful to our environment. Their presence in the environment undermines one of the 24 principles of green engineering and chemistry. Moreover, the conventional means of dechlorination produce highly poisonous dioxins. Producing dioxins while attempting to solve environmental issue undermines the overall objective of rendering the chlorinated compound less toxic in line with the SDG. Therefore, the goal is to dechlorinate these pollutants into non-dioxin products.

1.3 Research Philosophy and Scope

This study demonstrates proof of concepts for the electrochemical technology of generating and utilizing stable $O_2^{\bullet-}$ in new structurally distinct ILs and novel nanohybrid-IL (nanofluid) media. The study's focus is to investigate the viability of $O_2^{\bullet-}$ mediating conversion of substrates such as CO_2 in ILs or nanofluid. Another priority of this study is to examine the viability of $O_2^{\bullet-}$ promoting dechlorination of CH_2Cl_2 and C_6H_5Cl as model chlorinated pollutants in IL. The study eliminated CO_2 capture constrain by using ILs with renown CO_2 sorption capacity, thereby focusing on CO_2 conversion by $O_2^{\bullet-}$. Moreover, instead of using water to promote dechlorination, ILs could serve the purpose as $O_2^{\bullet-}$ will disproportionate in water, unlike ILs. The electrochemical technique detects the generated $O_2^{\bullet-}$ at a synchrony condition with the substrates' electrolysis. This technique is unlike the detection of $O_2^{\bullet-}$ using electron paramagnetic resonance (EPR) or electron spin resonance (ESR) techniques. These techniques employ the paramagnetic or electron spin property of $O_2^{\bullet-}$ (Bolojan et al., 2012; Ye et al., 2021). The detection of $O_2^{\bullet-}$ using EPR or ESR does not synchronize with the $O_2^{\bullet-}$ mediated electrolysis of the substrates (CO_2 , CH_2Cl_2 and C_6H_5Cl). As such, this work's scope does not cover the investigation of the paramagnetic property or spin property of $O_2^{\bullet-}$ in the generating media. Therefore, the electrochemical detection of $O_2^{\bullet-}$ was maintained throughout the study.

Moreover, the CO_2 and chlorinated organic compounds (CH_2Cl_2 a C_6H_5Cl) were selected as the substrates because they are among the top environmental pollutants that have drawn global attention. Also, selecting ILs for the conversion of CO_2 is particularly interesting due to dual purposes; 1) serve as CO_2 sorption media, and 2) serve as $O_2^{\bullet-}$ generation media. The use of $O_2^{\bullet-}$ /IL system to treat these pollutants is an option that is promising because ILs can extract these pollutants and can be regenerated afterwards. Also, though, ILs are unlike other solvents, the cost and value of the product produced in

ILs justify the use of ILs. Moreover, the reduction in pollutants and regeneration of the ILs will compensate for the cost of procuring ILs. Noteworthy, the regeneration of IL is not part of this study's scope mainly due to the number of objectives to focus on. Future endeavour could consider regeneration. Considering that this is the first study that discovered and conceptualized the generation of $O_2^{\bullet-}$ in IL-nanofluid media, and some structurally new ILs, a benchmark was employed to characterize these media using quantum chemical calculations, spectroscopy and electrochemical techniques. The quantum chemical calculations used three essential software, Gaussian-09, COSMOthermX and Tmolex.

The utilization of $O_2^{\bullet-}$ by CO_2 , CH_2Cl_2 and C_6H_5Cl in ILs or IL-nanofluid media can reduce the overall cost implication of environmental remediation using this technique. Moreover, the data for CO_2 conversion or the dechlorination mediated by $O_2^{\bullet-}$ was gathered through mainly electrochemical and spectroscopic means.

This study has established original findings concerning nanohybrid-IL (nanofluid) conceptualization and development. The nanofluid contains Fe_3O_4 and RuO_2 phases with pseudocapacitance attribute, which collectively promote a reduction in the overpotential of the electrochemical process. The study investigates the long-term stability of $O_2^{\bullet-}$ in ILs media or nanofluid, reactions between $O_2^{\bullet-}$ and CO_2 to selectively yield $C_2O_6^{2-}$, reaction between $C_2O_6^{2-}$ and amines to produce new valuable chemicals, e.g. methyl (2-hydroxyethyl) (methyl) carbamate. The novel nanofluid medium could sustainably capture CO_2 through the adsorption process, adding to the CO_2 absorption capacity of the ILs. This study is the first that reports the generation of stable $O_2^{\bullet-}$ in carefully developed nanofluid with ILs as the base fluid. Largely, these developments can spur industrial interest to design reactors towards an energy-efficient and sustainable CO_2 conversion by $O_2^{\bullet-}$ in ionic liquids or nanohybrid-ILs. The mechanistic insight into CO_2 transformation by $O_2^{\bullet-}$ in the IL or nanofluid was found and described. The study also conceptualizes the

kinetics of $O_2^{\bullet-}$ stability in the IL or nanofluid. Therefore, the study provided an avenue for understanding the mechanism of $O_2^{\bullet-}$ in different media that can serve a multi-task purpose.

1.4 Research Objectives

The objectives of this research are:

1. **To investigate the quantum chemical properties of ionic liquids (ILs) media components, gases, and ions using computational packages.** Gaussian 09 COSMOthermX19 and Tmolex software were used. Global electrophilicity index (ω) and sigma profiles of molecules were investigated.
2. **To develop nanofluid with transition metals functionalized on modified multi-walled carbon nanotubes and ILs base fluid using the one-pot synthesis technique.** HRTEM, XRD, FESEM, XPS, and Raman will characterize the nanohybrid component. Also, electrochemical impedance spectroscopy (EIS) will characterize the nanohybrid-IL and IL media.
3. **To examine the electrochemical generation of $O_2^{\bullet-}$ in the ILs and nanofluid media using cyclic voltammetry.** The diffusion coefficient, the solubility of O_2 and charge transfer coefficients will be determined.
4. **To test the long-term stability of $O_2^{\bullet-}$ in ILs and selected nanofluid.** The kinetics parameter such as rate constant, the total consumption rate of $O_2^{\bullet-}$ will be determined.
5. **To examine the electrolysis of CO_2 , CH_2Cl_2 , and C_6H_5Cl by $O_2^{\bullet-}$.** GCMS and NMR will be used to elucidate their possible product distributions.

1.5 Research Methodology

The specific research methodologies are as follows:

1. Investigation of realistic non-covalent interactions between ILs, $O_2^{\bullet-}$, O_2 and CO_2 .
These theoretical calculations confirm the suitability of ILs for stable generation and subsequent utilization of $O_2^{\bullet-}$.
2. Synthesis of novel nanohybrid and formulation of nanofluid-ILs for possible $O_2^{\bullet-}$ generation and utilization.
3. Determination of electrochemical potential windows of ILs and nanofluid-ILs using cyclic voltammetry (at a sweep rate of 100 mV/s).
4. Electrochemical impedance spectroscopy analysis of ILs and their nanoparticle-based derivatives were also measured.
5. The $O_2^{\bullet-}$ was generated electrochemically in ILs and nanofluid using cyclic voltammetry technique.
6. Chronoamperometry analysis was carried out at open circuit potential (OCP) to estimate steady-state currents of the ILs and nanofluid-ILs media after sparging them with N_2 and O_2 sparged at a mild condition.
7. Long-term stability of $O_2^{\bullet-}$ in suitable ILs and nanofluid-ILs was conducted using UV/VIS spectrophotometer after chemically generating $O_2^{\bullet-}$ from KO_2 precursor.
8. Electrolysis of CO_2 and $O_2^{\bullet-}$ was investigated in selected ILs and nanofluid-ILs at mild condition. This reaction was preceded by involving other organic substrates to produce carbamate. Also, electrolysis of CH_2Cl_2 , and C_6H_5Cl by $O_2^{\bullet-}$ in selected IL was conducted at the mild condition to produce non-dioxin compounds. The study proposed the reaction mechanism between $O_2^{\bullet-}$ and the mentioned substrates.
9. Reaction product elucidations were determined using GCMS and supported by detailed 1D/2D NMR experiments.

1.6 Thesis Outline

The layouts of the thesis are organized into five chapters, as follows:

Chapter 1 – The first chapter comprised a general introduction that gave a detailed research overview. This research overview entails the research scope and objectives, perspective and rationale, value proposition of the study, novelty, and question addressed by the research.

Chapter 2 – The second chapter presents a literature review on superoxide ion ($O_2^{\bullet-}$) concepts ranging from fundamental properties to its generation and potential applications. The chapter also covers the suitable medium for $O_2^{\bullet-}$ generation. It went further to discuss the types of reactions that are mediated by $O_2^{\bullet-}$. The chapter also evaluated outlooks on CO_2 emission, capture and utilization. Also, an outlook on the dechlorination of chlorinated compounds was discussed. The electrochemical process and concepts were also discussed in this chapter.

Chapter 3 – This chapter presents all materials with their level of purity. The chapter also outlined the detailed methods used throughout the study. The chapter also sets out all the equipment used with their specifications and brands.

Chapter 4 – This chapter presents results and discussion with the electrochemical activity studies in line with all the study's objectives.

Chapter 5 – The chapter presents the overall conclusions drawn from the study and gave future research recommendations.

CHAPTER 2: LITERATURE REVIEW

2.1 Superoxide Ion

Superoxide ion ($O_2^{\bullet-}$) is a derivative of O_2 which undergoes a single-electron reductive electrochemical process (AlNashef et al., 2002; Donald T. Sawyer & Valentine, 1981). Several researchers have identified $O_2^{\bullet-}$ as a Brønsted base, a hydrogen atom abstractor, a strong nucleophile and a primary precursor for generating other reactive oxygen species (ROS) such as hydrogen peroxide (H_2O_2), singlet oxygen (1O_2) or hydroxyl radicals ($\bullet OH$) (Sawyer et al., 1985; Dickinson & Chang, 2011). These properties rationalize $O_2^{\bullet-}$ susceptible to utilization by varieties of organic molecules. $O_2^{\bullet-}$ exists in a doublet electronic state with a spin component of $-\frac{1}{2}$ and $+\frac{1}{2}$. The spin component implies that $O_2^{\bullet-}$ possesses an intrinsic form of angular momentum associated with its atomic nuclei (Hensen et al., 2020; Pan et al., 2020). Moreover, the doublet electronic state of $O_2^{\bullet-}$ implies that it has an unpaired electron that can give two orientation in space, especially when it is in a magnetic field's vicinity, thereby exerting different energy to a chemical system (Neese et al., 2019). These orientations necessitate rotational symmetry and allow spin component values $-\frac{1}{2}$ and $+\frac{1}{2}$.

Furthermore, when $O_2^{\bullet-}$ is in the presence of a magnetic pole, it shows a paramagnetic attribute with limited magnetic susceptibility, inadequate attractive force, and a dipole moment (Neese et al., 2019). These properties are due to the one unpaired electron in $O_2^{\bullet-}$ as indicated from the molecular orbital diagram in Figure 2.1a (Miao et al., 2019; Zaichenko et al., 2020). Therein, $O_2^{\bullet-}$ have an odd number of electrons so that at least one of these electrons is unpaired. This property is contrary to O_2 , which have two unpaired electrons as indicated by its molecular orbital (Figure 2.1b). Therein, O_2 have an even number of electrons to pair all of these electrons.

The $O_2^{\bullet-}$ is also active to ultraviolet and visible (UV-Vis) light irradiation, mostly at ~ 255 nm excitation wavelength (Maan Hayyan, Hashim, & AlNashef, 2016).

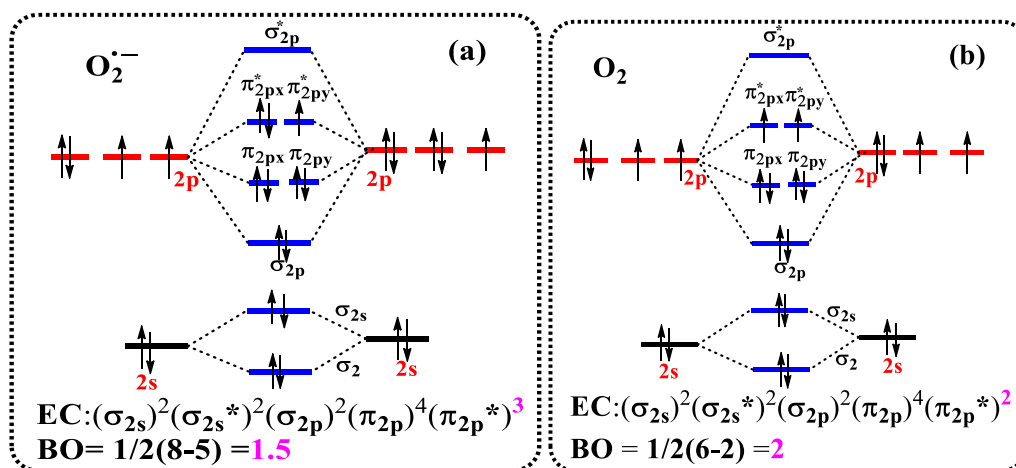


Figure 2.1: Molecular orbital diagram for (a) superoxide ion ($\text{O}_2^{\bullet-}$), (b) dioxygen (Miao et al., 2019; Zaichenko et al., 2020; Kumar, A., & Sevilla, M. D. 2018) EC= Electron configuration, BO = Bond order.

2.2 Methods of $\text{O}_2^{\bullet-}$ Generation

2.2.1 The electrochemical generation of $\text{O}_2^{\bullet-}$

Cyclic voltammetry is the typical electrochemical technique of producing $\text{O}_2^{\bullet-}$ due to its simplicity (AlNashef et al., 2002). The method is convenient, fast, no by-product, and viable for studying the kinetics of $\text{O}_2^{\bullet-}$ possible reactivity (Mohammad et al., 2001). The first report on electrochemical $\text{O}_2^{\bullet-}$ generation was more than five decades ago (Maricle and Hodgson, 1965). This study investigated the one-electron electrolytic reduction of O_2 in aprotic solvents and established the method through electron spin resonance (ESR) identification of $\text{O}_2^{\bullet-}$.

The electrochemical generation of $\text{O}_2^{\bullet-}$ has the advantage of preparing the reagent *in-situ* in the presence of a substrate as long as the substrate is not electroactive or reactive with $\text{O}_2^{\bullet-}$ (Winterbourn, 2020). The concentration of $\text{O}_2^{\bullet-}$, electroactive reagents, intermediates, and products are determinable by the electrochemical method during the electrochemical reaction and after its completion. However, the disadvantages of the electrochemical process for the generation of $\text{O}_2^{\bullet-}$ (Winterbourn, 2020) are:

- 1- Low $O_2^{\bullet-}$ concentrations (≤ 10 mM),
- 2- Possible interference from electroactive substrate reactions at the surface of the electrode,
- 3- Limited stability of the solution (half-life for ~ 5 mM $O_2^{\bullet-}$ is ~ 7 h),
- 4- Possible interferences due to the presence of an electroactive supporting electrolyte.

The current study uses electrochemical means of $O_2^{\bullet-}$ generation/detection and utilization. Therefore, the electrochemical process took note of the disadvantage and ameliorate any possible challenge.

2.2.2 Chemical generation of $O_2^{\bullet-}$

The chemical generation of $O_2^{\bullet-}$ employ KO_2 as precursor (Hayyan et al., 2012). The KO_2 is the most common commercial salt of O_2 known for more than six decades (Jackson and Werner, 1957). Many studies are using KO_2 for the long-term stability study of the chemically generated $O_2^{\bullet-}$ through UV-Vis irradiation (Maan Hayyan, Hashim, & AlNashef, 2016). This practice emerged because the electrochemical generation of $O_2^{\bullet-}$ is short-lived and cannot get information on the medium's viability for long-term electrolysis. On this account, reports investigated various media on the $O_2^{\bullet-}$ long-term stability summarized in Table 2.1. The long-term stability is estimated using the total percentage consumption of chemically generated $O_2^{\bullet-}$. Generally, the entire percentage span from 0 to 100 % and the ILs with higher percentage consumption of $O_2^{\bullet-}$ is not suitable for radical driven catalysis.

Table 2.1: Some ionic liquids used for long-term stability study of $O_2^{\bullet-}$

Abbreviation*	Total $O_2^{\bullet-}$ % Consumption after 120 min	Reference
[S222 ⁺][TFSI ⁻] [DMIm ⁺][MS ⁻]	92.50 47.50	(Hayyan et al., 2012) (Maan Hayyan, Hashim, & AlNashef, 2014)
[BDMIm ⁺][TfO ⁻] [EMIm ⁺][TFSI ⁻] [EMIm ⁺][MS ⁻] [P14,666 ⁺][TPTP ⁻] [P14,666 ⁺][TFSI ⁻] [MOPMPip ⁺][TFSI ⁻] [BMPyrr ⁺][DCA ⁻]	11.40 11.40 11.20 10.90 7.90 5.40 4.60	(Hayyan et al., 2014)
[BMPyrr ⁺][TFSI ⁻] [BMPyrr ⁺][TfO ⁻] [HMPyrr ⁺][TFSI ⁻]	4.10 3.70 3.30	(Hayyan et al., 2013) (Hayyan et al., 2014)
[MOEMPip ⁺][TPTP ⁻] [BMPyrr ⁺][TFA ⁻] [N112,102 ⁺][TFSI ⁻] [MOEMMor ⁺][TFSI ⁻]	2.40 2.40 0.69 0.65	(Hayyan et al., 2012) (Hayyan et al., 2015)
[EDMPAmm ⁺][TFSI ⁻]	9.00	(Hayyan et al., 2017)
[MO1,102 ⁺][N(Tf) ₂ ⁻] [N112,102 ⁺][N(Tf) ₂ ⁻] [S222 ⁺][N(Tf) ₂ ⁻]	2.60 2.80 92.50	(Hayyan et al., 2012)
[MOEMPip ⁺][TPTP ⁻] [P14,666 ⁺][N(Tf) ₂ ⁻]	28.30 40.00	(M. Hayyan et al., 2017) (M Hayyan et al., 2010)

*The abbreviations are interpreted in the list of abbreviation

2.3 Media for Generation of $O_2^{\bullet-}$

Since the inception of research on $O_2^{\bullet-}$, only two types of media have been evidence for its generation, and they include; 1) aprotic solvents and 2) ionic liquids (Maan Hayyan, Hashim, & AlNashef, 2016).

2.3.1 Aprotic solvents as media

Aprotic solvents such as acetonitrile (AcN), dimethylformamide (DMF) and dimethylsulfoxide (DMSO) are viable as media for the generation of $O_2^{\bullet-}$ (Che et al., 1996). Generally, aprotic solvents were found to sustain $O_2^{\bullet-}$ but they are not only highly volatile and unsuitable, but consumed a high amount of the $O_2^{\bullet-}$ with rate constant of

$\sim 10^3$ - 10^7 $\text{m}^{-1}\text{s}^{-1}$ and second-order mechanism (Bauer et al., 2019; Mohammad et al., 2001; Maria et al., 1997; Claude P Andrieux, Philippe Hapiot, & Jean Michel Saveant, 1987; Maricle and Hodgson, 1965; Peover and White, 1966). This rate constant implied that the consumption rate of $\text{O}_2^{\bullet-}$ in aprotic media is fast.

2.3.2 Ionic liquid as media

Unlike the aprotic solvents, ionic liquid (ILs) are renowned with low kinetic rate constant, which lies in the range of $\sim 10^{-5}$ - 10^{-3} s^{-1} , and serve as suitable media for the generation and utilization of $\text{O}_2^{\bullet-}$ (Hayyan et al., 2012; Schwenke et al., 2015; Maan Hayyan, Hashim, & AlNashef, 2016; Hayyan et al., 2017). The $\text{O}_2^{\bullet-}$ can exhibit long-term stability in ILs (Hayyan et al., 2012). In retrospect, imidazolium chloride-aluminium chloride was the first IL used for the generation of $\text{O}_2^{\bullet-}$ (Carter et al., 1991). Unfortunately, the $\text{O}_2^{\bullet-}$ was unstable due to the irreversible reaction of $\text{O}_2^{\bullet-}$ with the protic impurities in the imidazolium chloride-aluminium chloride. After a decade of pioneering effort of generating $\text{O}_2^{\bullet-}$ in IL, the first evidence for stable generation of $\text{O}_2^{\bullet-}$ was in 1-butyl-3-methylimidazolium hexafluorophosphate $[\text{BMIm}^+][\text{HFP}^-]$ (AlNashef et al., 2001). Later, studies indicate that the $\text{O}_2^{\bullet-}$ undergoes ion-pairing with imidazole IL-cation to produce 2-imidazolones (AlNashef et al., 2010; Hayyan et al., 2013). This ion-pairing means that IL-cation is a determinant for the general electrochemistry of stable $\text{O}_2^{\bullet-}$ generation and utilization (Doblinger, Lee, & Silvester, 2019).

On the contrary, the ammonium cations are exceptional for a stable generation of $\text{O}_2^{\bullet-}$. For instance, trimethyl-n-hexyl-ammonium $[\text{TMHAMm}^+]$ cation stability to $\text{O}_2^{\bullet-}$ the nucleophilic attack was attributed to the negative charge of its C (sp) atom (Sun, Forsyth, & Macfarlane, 1998; Buzzeo et al., 2003; Katayama et al., 2004; Ashassi-Sorkhabi, Kazempour, & Salehi-Abar, 2018). The methoxy functionalized piperidinium cation based ILs such as 1-(3-methoxy propyl)-1-methyl-piperidinium $[\text{MOPMPip}^+]$ (Hayyan et al., 2012), 1-(3-Methoxypropyl)-1-methyl-piperidinium (Hayyan et al., 2017),

or 1-(2-Methoxyethyl)-1-methyl-piperidinium (Neale et al., 2016) were also viable as media for stable $O_2^{\bullet-}$ generation and utilization. However, in consideration of their methoxy (-OCH₃) functionality, the presence of O-atom could exacerbate the electron-donating potential of the alkyl group (-CH₃) (Burie et al., 1997). Consequently, this tempts an electron-withdrawing tendency by the methoxy functionality in the piperidinium cation, thereby inducing susceptibility to $O_2^{\bullet-}$ nucleophilicity effect. A nucleophilic attack's vulnerability could halt piperidinium-based IL's capacity for sustainable, stable $O_2^{\bullet-}$ generation and utilization. The ILs used for the generation of stable $O_2^{\bullet-}$ are summarized in Table 2.2 and the review published by Hayyan et al. (2016).

Table 2.2: Some ILs used for generating stable $O_2^{\bullet-}$

Ionic Liquid*	Reference
[BmIm ⁺][TFB ⁻] [EMIm ⁺][TFB ⁻] [DMIm ⁺][TFB ⁻] [BmIm ⁺][HFB ⁻] [BmIm ⁺][I ⁻] [BmIm ⁺][MS ⁻]	(Feroci et al., 2011) (Rogers et al., 2009)
[BmIm ⁺][HFB ⁻]	(AlNashef et al., 2002)
[EMIm ⁺][TFSI ⁻] [BmIm ⁺][TFSI ⁻] [BmIm ⁺][TFSI ⁻] [BmIm ⁺][TFB ⁻] [BmIm ⁺][HFP ⁻]	(Buzzeo et al., 2003) (Rogers et al., 2009)
[BmIm ⁺][TFES ⁻]	(Switzer et al., 2013)
[BmIm ⁺][TFB ⁻]	(Feroci et al., 2007)
[BmIm ⁺][TFB ⁻] [BmIm ⁺][HFB ⁻]	(Gu et al., 2005) (AlNashef et al., 2010)
[EMIm ⁺][ES ⁻] [EMIm ⁺][TFSI ⁻] [HMIm ⁺][Cl ⁻] [DMIm ⁺][TFS ⁻] [BmIm ⁺][HFP ⁻] [HMIm ⁺][HFP ⁻] [BmIm ⁺][HFP ⁻] [EMIm ⁺][ES ⁻]	(Sethupathy et al., 2012)
[EMIm ⁺][TFSI ⁻]	(Buzzeo et al., 2004)
[EMIm ⁺][TFSI ⁻] [BmIm ⁺][TFSI ⁻]	(Villagrán et al., 2006) (René et al., 2009)
[DMPIm ⁺][TFSI ⁻] [BmIm ⁺][TFMS ⁻] [EMIm ⁺][TFSI ⁻] [HMPyrr ⁺][TFSI ⁻]	(Hayyan et al., 2013) (Islam et al., 2009)

[BMPyr ⁺][TFA ⁻]	(Hayyan et al., 2012)
[TM ⁺][TFSI ⁻]	(Katayama et al., 2004)
[BTM ⁺][TFSI ⁻] [MT ⁺][TFSI ⁻] [OT ⁺][TFMS ⁻] [TBM ⁺][TFSI ⁻] [DEM ⁺][TFSI ⁻] [BTM ⁺][TFSI ⁻]	(AlSaleem et al., 2019)

*Definition of the ILs are given under the list of abbreviation section

2.3.2.1 General outlook on ionic liquids

Ionic liquids (ILs) are salts composed of ions and have a melting point below 100 °C (Zhigang Lei 2017). They are also called neoteric solvents, designer solvents, ionic fluid or molten salts. The first IL was ethyl ammonium nitrate, featuring a melting point of ~ 12 °C as reported in 1914 by Paul Walden (Zhigang Lei 2017). Since the past two decades, different ILs categories have received wide attention according to the trend in the web of science (WOS) database. The number of scientific contributions on ILs has exponentially risen from a few (587) in 1970-1996 range to 49,818 in 2021, exceeding other popular scientific areas' annual growth rates (web of science, access date 2/4/2021; 11:10 am, GMT). The information shows that many researchers are engaged in studying this exciting research field, yielding tremendous outcomes. There is a multidisciplinary emergence of ILs involvement in chemistry, materials science, chemical engineering, and environmental science (Lei et al., 2017; Dong et al., 2017; Wang et al., 2020). Some significant fundamental opinions are emerging, different from the original concepts, as insights into the nature of ILs. These entail the physicochemical properties of ILs recognized to range from renowned terms such as "non-volatile, non-flammable, and air and water stable" (Hallett & Welton, 2011). These attributes originate from various mixtures of cations and anions that coincide with the definition of ILs, resulting in a different collection of behaviour. Regardless, ILs remains more desirable than conventional volatile solvents for radical driven catalysis, often exhibiting "green" and

"designer" properties to an armful useful degree. Owing to the enormous growth in a chemical variety of ILs, their classification includes:

1. Room-temperature ILs (RTILs) (Hallett & Welton, 2011; Chatel & MacFarlane, 2014; Wickramanayake et al., 2014; Mai and Koo, 2016; Dhatarwal, Remsing, & Kashyap, 2020).
2. Task-specific ILs (Gurkan et al., 2010; Ruckart et al., Glover, 2015; Qian, Texter, & Yan, 2017;).
3. Polyionic liquids (Rojas et al., 2014),
4. Supported ILs (Scovazzo et al., 2009; Wickramanayake et al., 2014).

These classifications of ILs includes the composites of ILs kept on metal-organic frameworks (Khan, Hasan, & Jhung, 2014; Luna et al., 2013). Considering the ILs molecular structure, there are a complex set of phenomena taking place due to their organic-ionic nature and intermolecular interactions. This intrinsic association creates a fascinating and challenging field of study with the desire to first screen ILs quickly for specific purposes. Due to this reason, the elucidation of structure-performance relationships unravelling the synergy among ILs, solutes, supports, and the components in the mixture becomes necessary and requires an integration of experimental and theoretical methods.

The general disposition on IL is that a proper understanding of their behaviour at the microscopic scale will help elucidate macroscopic fluid phenomena and promote their laboratory or industrial applications (Wang et al., 2020). In this regard, the multiscale aspects of ILs, ranging from the molecular level to the industrial level, was recently reported (Dong et al., 2017). Besides, Izgotodina et al. (2017) gave an insight into predicting the energetic, physical, and spectroscopic properties of ILs through quantum chemical methods and empirical approaches. Usually, the COSMO-RS (conductor-like screening model for real solvents) model was used (Eckert & Klamt, 2013). Accordingly,

COSMO-RS is the most widely used predictive model in the IL community, enabling theoretical calculations to elucidate the thermochemical properties of ILs.

The advances in IL research are associated with characterization techniques. Infrared (IR) and Raman spectroscopies have proven to provide fundamental insight into ionic interactions and the resulting liquid structure in ILs (Paschoal, Faria, & Ribeiro, 2017). Therefore, the application of IR and Raman spectroscopies in the mid-and low-frequency in the bulk liquid could help understand the structural modifications of ILs accompanying phase transitions induced by variable temperature or pressure. A review by Wang et al. (2017) explains whether ILs is chemically stable. The study covers the chemical stability and reactivity of popular imidazolium-based ILs, thermal decomposition, hydrolysis, and nucleophilic reactions of anions under actual operating conditions like high temperature, and water presence, air, or other gases. The nanoconfined scale in ILs and the interactions between ILs and the pore walls inside porous materials reveals the ILs distinctly modified physicochemical properties.

2.3.2.2 Physicochemical properties of ionic liquids

The conductivity of ILs could be understood either through thermal (Daisuke Tomida, 2018) or electrical inducement (Salazar et al., 2014). Valkenburg et al. (2005) reported the early known thermal conductivity of ILs (Valkenburg et al., 2005). The thermal conductivity value for various IL range from ~ 0.106 to ~ 0.238 W/(m. K) at 25 °C. The thermal conductivities of ILs were classified to be about the same order with some organic solvents such as methanol and toluene (Daisuke Tomida, 2018). However, 1, 3-dimethyl imidazolium dimethyl phosphate's thermal conductivity was ~ 0.238 W/(m. K) as the highest reported value so far (Chen et al., 2013). The lowest value of thermal conductivity for ILs is ~ 0.107 W/(m. K) for 1-butyl-1-methyl-pyrrolidinium tris (Penta-fluoroethyl) trifluoro-phosphate as the lowest value (Ge et al., 2007). The IL's thermal

conductivity depends on temperature and pressure but independent of IL-moiety's alkyl chain length (Tomida et al., 2013; Tomida et al., 2007).

Another type of ILs conductivity is driven by electricity, as demonstrated using IL/H₂O and IL/nonaqueous solvents (Jarosik et al., 2006). They founded that the maximum electrical conductivity for IL/H₂O couples was ~ 92–98 mS/cm, while in the case of IL/nonaqueous solvents, the maximum electrical conductivity is much lower (~ 18–30 mS/cm). Comparing these two couples with pure ILs and their mixtures, the temperature dependence of conductivity over the 288–368 K range follows the Arrhenius law. This pattern's activation energy for combinations of ILs decreases with an increase in diluent amount. Also, they observed that the activation energy varies with IL form. The typical corresponding activation energy value for the diluted IL solution in the molecular solvent is ~ 12 kJ/mol.

The viscosity (η) of IL is a physiochemical property that arises from non-covalent interactions such as hydrogen bonding, Van der Waals and columbic forces (Bhattacharjee et al., 2015). The size and shape of IL can affect the magnitude of viscosity since interfacial phenomena (conductivity or charge transfer coefficient) and mass transfer phenomena (diffusion coefficient) prevail therein (Seki et al., 2010; Řehák, Morávek, & Strejc, 2012). In general, these studies showed that IL's viscosity is higher than commonly used conventional organic solvents. Therefore, it is noteworthy that high viscosity may deter IL applicability. For instance, simple unit operations such as stirring and pumping could become difficult; in other applications such as those in the field of tribology, high viscosity may be desirable (Aparicio, Atilhan, & Karadas, 2010).

Overall, ILs viscosity ranged in the 1-3 orders of magnitude higher than conventional solvents (Yao & Anderson, 2009). Takuda et al. (2005) showed that increasing the length of alkyl substituents could result in IL's corresponding high viscosity (Tokuda et al., 2005). They varied alkyl chain length of 1-alkyl-3-alkyl-1-methyl-

imidazolium bis (trifluoromethanesulfonyl) imide [RMI^{m+}][TFSI⁻] (R is methyl, ethyl, butyl, hexyl or octyl substituents). The increase in viscosity was due to stronger Van der Waals interactions between larger cations from the incorporation of higher alkyl chain lengths.

The density of ILs is higher than H₂O, and it is in the range of 1-1.6 g/mL (Santos et al., 2016; Sas et al., 2018). Besides, the density of piperidinium, ammonium, pyrrolidinium and morpholinium cations-based ILs paired with bis (trifluoromethylsulfonyl) imide anion were investigated to be ~ 1.45 g/cm³ (Ibrahim et al., 2016). The ILs molecular weight does not correlate with the density values. However, the nature of the IL molecular structure relates to the density value. Specifically, for morpholinium cations, the observed density was similar to the literature (Gaciño et al., 2011; Marciniak & Wlazło, 2012). Similarly, they also compared the density value of ammonium-based IL and found a correlation (Řehák et al., 2012).

The melting point (M.pt) of ILs is an import gauge for purity levels of ILs (Zhigang Lei 2017). Accordingly, the M.pt also aids in determining solubility, phase equilibrium properties and vapour pressure and other physicochemical properties of ILs. Generally, ILs has a low melting point levelling below 100 °C and predominantly liquid at room temperature. The IL cation structure and anion affect the melting point; if the anion's size increases, the IL's melting point decreases, and if the cation is large and asymmetric, the melting point will reduce.

The electrochemical window (ECW) is a connotation used to describe an electrolytic medium (Chen et al., 2019). The ECW originate by subtracting the reduction-potential range (cathodic limit) from the oxidation potential (anodic limit). The test substance does not get oxidized or reduced around these two extreme limits. The ECW of ILs is crucial as it indicates an enhancement in the cathodic limiting potential of the ILs.

The general methods used for estimating ECW are linear sweep voltammetry (LSV) and cyclic voltammetry (Elgrishi et al., 2018). Accordingly, Table 2.3 shows some ECW for different ILs and their cathodic and anodic limits.

Table 2.3: Cathodic and anodic potential vs Ag/AgCl for ECW of ILs at cut-off current density 0.5 mA/cm² using GC macro-electrode (25 °C).

ILs*	E _{CL}	E _{AL}	ECW	Reference
[MPDIm ⁺][Br ⁻]	-2.13	1.26	3.39	(Lerch & Strassner, 2019)
[MPBIm ⁺][DCA ⁻]	-2.42	4.75	7.17	
[4MPDIm ⁺][Br ⁻]	-2.47	3.46	5.93	
[C ₂ MIm ⁺][TFSI ⁻]	-3.11	1.13	4.50	(Kazemiabnavi et al., 2016)
[C ₃ MIm ⁺][TFSI ⁻]	-3.12	1.09	4.30	
[P14666 ⁺][TPTP ⁻]	-3.64	2.17	5.81	(Hayyan et al., 2013)
[N122,102 ⁺][TFSI ⁻]	-3.47	2.52	5.99	
[HMPyrr ⁺][TFSI ⁻]	-3.06	2.61	5.67	
[BMPyrr ⁺][TfO ⁻]	-2.95	1.88	4.83	
[BMPyrr ⁺][DCA ⁻]	-2.95	1.67	4.62	
[BMPyrr ⁺][TFSI ⁻]	-2.92	2.28	5.20	
[BMPyrr ⁺][TFA ⁻]	-2.85	1.35	4.20	
[EMIm ⁺][TFSI ⁻]	-2.07	2.12	4.19	
[MOEMMor ⁺][TPTP ⁻]	-1.95	2.03	3.98	
[MOPMPip ⁺][TFSI ⁻]	-1.94	2.37	4.31	
[MOEMMor ⁺][TFSI ⁻]	-1.93	2.75	4.68	
[MOEMPip ⁺][TPTP ⁻]	-1.75	2.12	3.87	
[S222 ⁺][TFSI ⁻]	-1.30	2.21	3.51	
[BMPy ⁺][DCA ⁻]	-1.25	1.71	2.96	
[HPy ⁺][TFSI ⁻]	-1.22	2.74	3.96	
[HPPy ⁺][TFSI ⁻]	-1.12	2.69	3.81	

*Definition of the IL are provided in the lists of abbreviation

2.3.2.3 Effect of impurities on ionic-liquid properties

Pure ILs are usually essential for various applications. Unfortunately, some ILs contain certain impurities, such as water or active organic or inorganic substances. Considering an electrochemical process, water as an impurity in ILs can narrow their property such as ECW (O'Mahony et al., 2008). However, the presence of ~ 50 ppm water as an impurity in hydrophobic dried IL; 1-Butyl-3-methylimidazolium Bis (trifluoromethylsulfonyl) imide [C₁C₄Im][NTf₂], does not affect its density or viscosity values (Andanson et al., 2016). This was different in case of hydrophilic ILs such as 1-Butyl-4-methyl pyridinium Bis (trifluoromethylsulfonyl) imide [C₁C₄Pyri][NTf₂],

Butyltrimethylammonium Bis (trifluoromethylsulfonyl)imide [C_1C_4Im][BF_4], and 1-Butyl-3-methylimidazolium Tetrafluoroborate [C_1C_4Im][OTf] whose water quantity after drying was 34, 70, < 10, and 50 ppm respectively. In these ILs for $xH_2O = 0.02$ (less than 1000 ppm), the density was decreased by $\sim 0.05\%$ while for $xH_2O = 0.001$ (50 ppm) the density decreases by $\sim 0.0025\%$ (Figure 2.2a). They considered these effects on the density to be relatively small, and in other words, a quantity of 1000 ppm of water has an impact on the 4th digit of the density. This scenario is the amount of H_2O found in highly hydrophilic ILs even after subjecting them to drying pretreatment procedures. Similarly, the viscosities of the hydrophilic ILs are decreasing with the addition of a small amount of H_2O (Figure 2.2b). Although there is an observable decrease in the viscosity with the addition of H_2O , it cannot be generalized for all ILs according to suggestions from the literature (Rilo et al., 2010; Yu et al., 2012; Andanson, Traïkia, & Husson, 2014). There are also additional impurities in ILs, such as halides-based ones, which can affect the chemical and physical properties of ILs (Hoogerstraete et al., 2014). These findings showed that the presence of unwanted impurities in ILs affects their physicochemical properties.

The presence of water in ILs as an impurity can increase the reduction potential for O_2 to $O_2^{\bullet-}$ (Doblinger, Lee, & Silvester, 2019). This study investigated the effect of water impurity in ILs using different IL-cations such as imidazolium, ammonium, pyrrolidinium, pyridinium, sulfonium, and phosphonium. The IL-cations associate with anions such as [BF_4^-], [PF_6^-], [NTf_2^-], and [FAP^-]. The study found that even at a low humidity value of $\sim 65\%$ RH, the IL-cation significantly affects the O_2 reduction current. Mechanistically, the results suggest that there is a significant amount of water incorporated at the electrode-hydrophilic IL ([C_2mim][NTf_2] and [$N_{4,1,1,1}$][NTf_2]) interface. This result is absent in the more hydrophobic IL such as [$P_{14,6,6,6}$][NTf_2]. Besides, they suggested that moisture can significantly affect O_2 reduction currents, for

instance, in $[\text{C}_2\text{mim}][\text{NTf}_2]$. Therefore, as a recommendation, hydrophobic and large IL-cations and anions were recommended for O_2 reduction, especially in humidified conditions. Thus, in this research, we have taken measures to use ultra-pure ILs. Where necessary, the ILs were analyzed to confirm their purity using spectroscopic techniques before use.

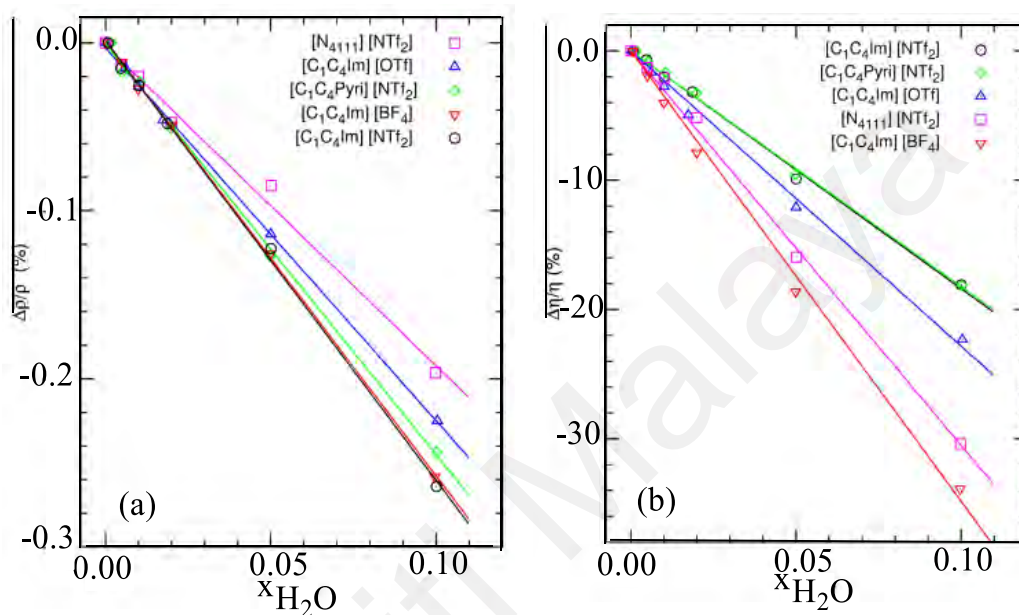


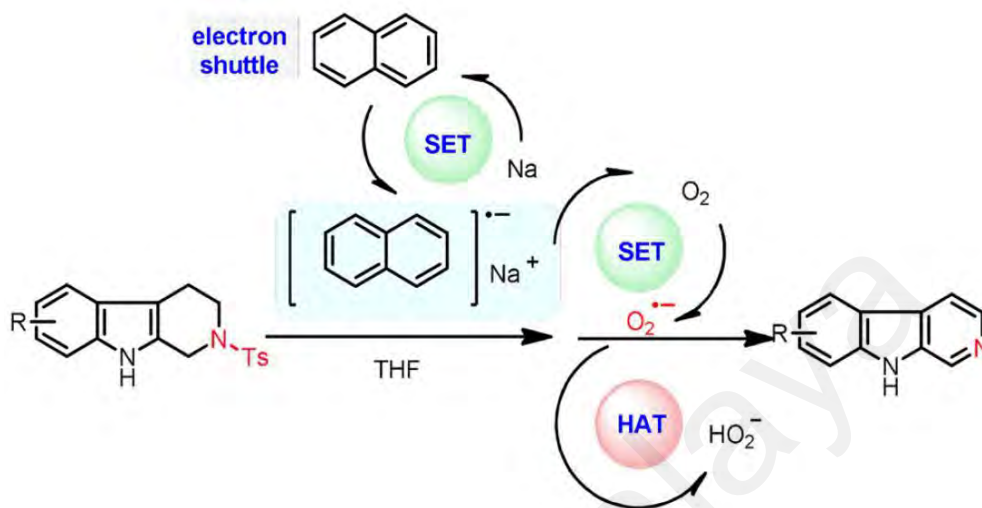
Figure 2.2: (a) Relative density as a function of the water mole fraction and (b) Relative viscosity as a function of the water mole fraction for five different ILs at 101 kPa (Andanson et al., 2016), Copyright (2016) Elsevier.

2.4 Reactions of $\text{O}_2^{\bullet-}$

2.4.1 One-electron transfer

One electron transfer reaction is the relocation of an electron from any chemically active species, an atom or molecule, to another chemical entity (Rohe et al., 2020). The one-electron transfer by $\text{O}_2^{\bullet-}$ mechanistically accounts for a redox process that usually changes the reactant's oxidation state and the product (Maan Hayyan, Hashim, & AlNashef, 2016). This attribute is the $\text{O}_2^{\bullet-}$ mediation of one-electron transfer process for dehydrogenation of N-heterocycles into N-heteroarenes (Huang et al., 2018). As shown in Scheme 2.1, the dehydrogenation process occurred at redox potentials of $E^{\circ} = -0.75 \text{ V}$

vs SCE for $O_2/O_2^{\bullet-}$ couples and $E^\circ = -2.5$ V vs Ag/AgCl for N-heteroarenes/N-heterocycles. The equilibrium constant (K) of the electron shuttle process is 0.8×10^6 $M^{-1}S^{-1}$.



Scheme 2.1: Dehydrogenation of N-heterocycles to N-heteroarenes by one-electron transfer process from $O_2^{\bullet-}$ (Huang *et al.*, 2018), Copyright (2018) Wiley.

In the biological context, the Mn_2^{II} complex, which served as a biomimetic of class Ib Mn_2 -Ribonucleotide reductase could react with $O_2^{\bullet-}$ through the one-electron transfer process (Magherusan *et al.*, 2018). The Ribonucleotide reductases (RNRs) are essential enzymes that transform ribonucleotides to deoxyribonucleotides (Thomas *et al.*, 2019). This study indicated that the deoxyribonucleotides could be a required precursor for DNA synthesis and repair, especially in all living cell.

Recently, $O_2^{\bullet-}$ was reported to undergo one-electron transfer with SO_2 , thereby forming SO_2^- with an equilibrium constant of $K = \sim 1.1 M^{-1}S^{-1}$ (Carroll *et al.*, 2018; Lundgren *et al.*, 2018; Muñoz-Rugeles, Galano, & Alvarez-Idaboy, 2018; Zabik *et al.*, 2019). According to these studies, the reaction goes to completion because the SO_2^- got complexed by SO_2 and dimerizes to dithionite ion ($S_2O_4^{2-}$).

Generally, the $O_2^{\bullet-}$ engaging in one-electron transfer reactions process with organic compounds such as heterocyclic and nitro-derivative, inorganic compounds such as nonmetal, inorganic compounds or even metal ion/complexes, is based on $O_2^{\bullet-}$ acting as a moderate reducing agent (Afanas 1991; Donald T Sawyer, Chiericato Jr, & Tsuchiya, 1982; Donald T Sawyer, Sobkowiak, & Roberts, 1995). These studies suggested that the process follow either outer-sphere one-electron transfer without forming an intermediate ($O_2^{\bullet-} + A \rightleftharpoons O_2 + A^{\bullet-}$) or inner-sphere one-electron transfer where the $O_2^{\bullet-}$ adducts forms an intermediate ($O_2^{\bullet-} + A \rightleftharpoons A - O_2^{\bullet-} \rightarrow O_2 + A^{\bullet-}$).

2.4.2 Nucleophilic substitution

The super reactivity of $O_2^{\bullet-}$ could be gauged in nucleophilic substitution reactions (Sawyer & Valentine, 1981). Over four decades ago, a nucleophilic substitution (S_N2) reaction involved an electron-pair donor (for instance, $O_2^{\bullet-}$) with an electron pair acceptor otherwise referred to as electrophile (Newton & Warren, 1980). If the electrophile has a sp^3 -hybridized carbon, it must have a leaving group (X) for the nucleophilic substitution reaction to occur. The first evidence of $O_2^{\bullet-}$ application in nucleophilic substitution reactions was five decades (Merritt & Sawyer, 1970). This reaction involves several alkyl halides that serve as electrophiles. This study investigated chlorine's nucleophilic displacement from n-butyl chloride, sec-butyl chloride, and t-butyl chloride by $O_2^{\bullet-}$ (1:1 $O_2^{\bullet-}$ /alkyl halide) to yield peroxide radical. The reactions concerning series of alkyl halides proceed with pseudo-first-order kinetics with a rate constant of $3.2 \times 10^{-1} s^{-1}$ (n-butyl chloride), $0.6 \times 10^{-1} s^{-1}$ (sec-butyl chloride) and $0.4 \times 10^{-1} s^{-1}$ (t-butyl chloride) at ambient condition. They observed that the halide's reaction rates are too fast. In general terms, the reactivity of the alkyl halide substrate with $O_2^{\bullet-}$ follows the order; benzyl > primary > secondary > tertiary > aryl and I > Br > Cl (San Filippo, Chern, & Valentine, 1975). About six decades ago, the $O_2^{\bullet-}$ mediated nucleophilic reaction depend on α -effect,

solvation, basicity, and polarizability (Bunnett, 1963). The α -effect accounts for an improved reactivity of nucleophiles like $\text{O}_2^{\bullet-}$ (Edwards & Pearson, 1962). The α -effect is also a positive deviation from a Brønsted plot (Hoz & Buncl, 1985). Afterwards, IUPAC incorporated this definition into their Glossary of terms (Muller, 1994).

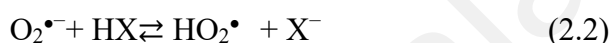
Besides, the nucleophilic substitution by $\text{O}_2^{\bullet-}$ at the O-alkyl carbon as a usual mechanism of decomposition of organic carbonates, sulfonates, aliphatic carboxylic ester was demonstrated recently (Bryantsev *et al.*, 2011). They found that nucleophilic substitution with phenol esters or carboxylic acids and O-alkyl fluorinated aliphatic lactones proceed through the carbonyl carbon attack.

The nucleophilic substitution reaction between hydrated $\text{O}_2^{\bullet-}$ and alkyl halides (CH_3Cl and CH_3Br) are feasible (Mauritz *et al.*, 2015). The study found that the reaction rate decreases when the number of water molecules in the cluster increases. This study used mass spectrometric experiments coupled with quantum chemical calculations to acquire all the results.

2.4.3 Proton abstraction

The $\text{O}_2^{\bullet-}$ reacts with a proton, diverse organic and inorganic compounds as proton source to form per-hydroxyl radical (HO_2^{\bullet}) as shown in Eq 2.1 and Eq 2.2 (Roberts Jr. & Sawyer, 1983). The deprotonation process by $\text{O}_2^{\bullet-}$ was also observed using phenol (Zabik *et al.*, 2019). This deprotonation process advances previous studies that followed $\text{O}_2^{\bullet-}$ reaction with H_2O , alcohol, sucrose, and glucose (Singh & Evans, 2006). In these studies, the results showed that $\text{O}_2^{\bullet-}$ was less reactive in the examined media; $\text{O}_2^{\bullet-}$ reacted rapidly with H_2O with a pseudo-second-order rate constant of $1.0 \times 10^5 \text{ M}^{-1} \text{ s}^{-1}$. The reaction is faster with methanol at a scale of $10^7 \text{ M}^{-1} \text{ s}^{-1}$ rate constant. In the case of ethanol, the pseudo-second-order rate constant involving the reaction with $\text{O}_2^{\bullet-}$ was $10^2 \text{ M}^{-1} \text{ s}^{-1}$ and $<0.1 \text{ M}^{-1} \text{ s}^{-1}$ with 2-propanol. An essential observation in these studies is that; no response between $\text{O}_2^{\bullet-}$ and sugars. They showed that $\text{O}_2^{\bullet-}$ was stable to a great extent in pyridine,

acetone, and various other aprotic solvents. Therefore, the generated $O_2^{\bullet-}$ did not react with glucose but react catalytically with fructose and sucrose. In a different aprotic solvent such as DMF, they suggested that both glucose and fructose reacted relatively rapidly with $O_2^{\bullet-}$ with a pseudo-second-order rate constant of the order of $10^5 M^{-1} s^{-1}$. From a general perspective, the aprotic solvents such as DMF to which $O_2^{\bullet-}$ was stable in, could not afford a proton for $O_2^{\bullet-}$ to abstract. These collectively render the aprotic solvent a medium used for $O_2^{\bullet-}$ reaction with other substrates even though they are less favorable than ILs.

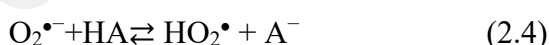


2.4.4 Disproportionation

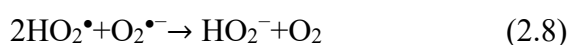
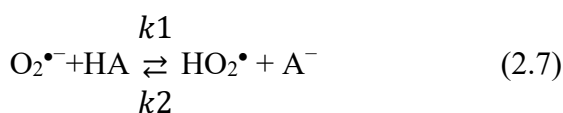
There are two perspectives on the disproportionation of $O_2^{\bullet-}$. The water-induced and aprotic-induced disproportionation of $O_2^{\bullet-}$. The former implies water acting as Brönsted acid and disproportionate $O_2^{\bullet-}$ ($O_2^{\bullet-} + H_2O \rightleftharpoons HO_2^{\bullet} + OH^-$) to form hydroperoxyl radical and hydroxyl anion (Che et al., 1996). This $O_2^{\bullet-}$ disproportionation was investigated in aprotic solvents such as acetonitrile, dimethylformamide and dimethylsulfoxide media. The aprotic media contain various water concentrations such as $0.04 \pm 0.002 M$, to $0.02 \pm 0.001 M$ and $0.02 \pm 0.001 M$. The disproportionation of $O_2^{\bullet-}$ in these aprotic media followed second-order reaction with rate constants of $8.90 \pm 0.4 \times 10^3 M^{-1} s^{-1}$, $2.20 \pm 0.1 \times 10^3 M^{-1} s^{-1}$, and $0.07 \pm 0.003 \times 10^3 M^{-1} s^{-1}$ respectively. Irrespective of these scenarios, the generated $O_2^{\bullet-}$ was short-lived and transformed into hydroperoxyl radical (HO_2^{\bullet}) or hydroperoxide anion (OH^-) in either aprotic solvent or hydrated aprotic solvent, unlike ionic liquids (ILs).

According to the definition since five decades ago, $O_2^{\bullet-}$ disproportionation is a phenomenon describing the oxidation of $O_2^{\bullet-}$ back to O_2 (Bielski & Allen, 1977). This case implied that disproportionation of $O_2^{\bullet-}$ in aqueous media results in the formation of

molecular oxygen in the ${}^1\Delta_g$ electronically excited states (Barlow, Bisby, & Cundall, 1979). Another perspective reported that a factor such as a proton source presence could disproportionate $O_2^{\bullet-}$ to H_2O , HO_2 , and O_2 due to its strong basicity (Mauritz Johan Ryding, Fernández, & Uggerud, 2016). These results indicated that aside from molecular oxygen, the disproportionation of $O_2^{\bullet-}$ can form other product such as water. The underlying $O_2^{\bullet-}$ disproportionation dynamics in aqueous solutions is required (Gibian et al., 1979). They found that the rate-limiting step for the process was a second-order relative to the concentration of $O_2^{\bullet-}$. In line, when the rate reached a maximum, the pH is equivalent to the pKa of HO_2^- and it decreased monotonically with a decrease in the concentration of the H^+ source. This scenario prompted the assertion that the disproportionation equilibrium of $O_2^{\bullet-}$ in H_2O at a neutral pH favors the forward reaction, and the response reached completion at a pH of 14. By implication, the disproportionation of $O_2^{\bullet-}$ follows the same mechanism in water and aprotic solvent (Claude et al., 1987). The general disproportionation mechanism of $O_2^{\bullet-}$ is represented in Eqs 2.3-2.9. The mechanism involving the H-atom disproportionation of two $HO_2^{\bullet-}$.

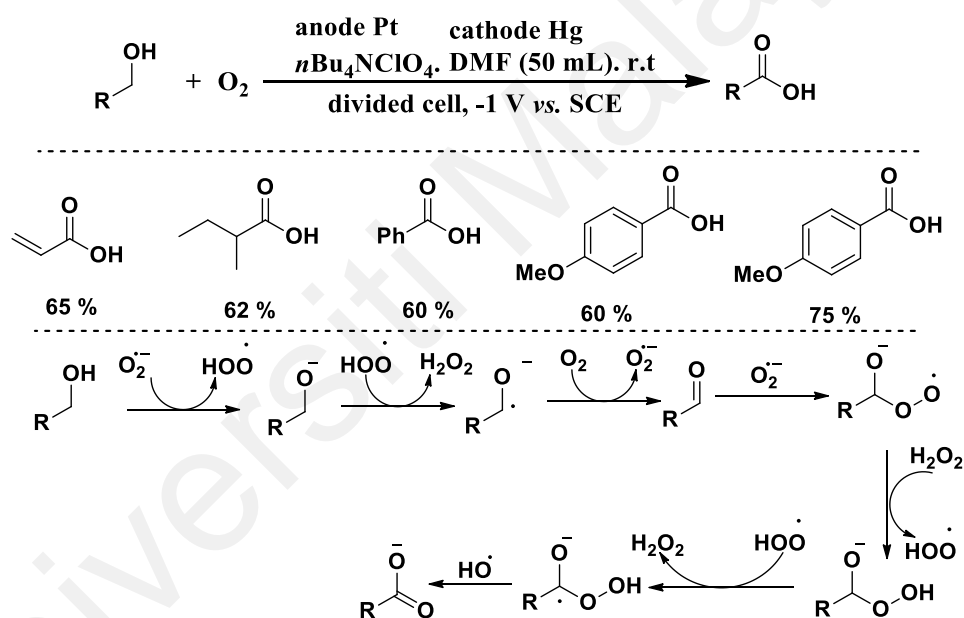


The mechanism involving the electron-transfer reduction of $2HO_2^{\bullet}$ by $O_2^{\bullet-}$



2.4.5 Applications of $O_2^{\bullet-}$ in organic synthesis

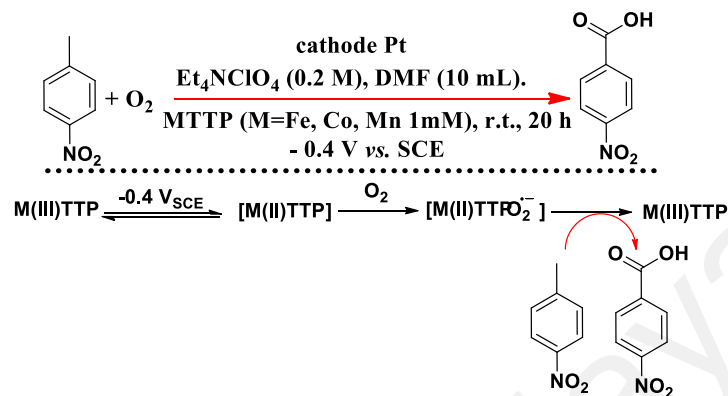
In terms of organic synthesis, as illustrated in Scheme 2.2, more than two decades ago, $O_2^{\bullet-}$ mediated oxidation of primary alcohols to yield carboxylic acids (Singh et al., 1991). They performed the primary alcohols' electrolysis at -1 V vs SCE and observed the aldehyde's oxidation as intermediate molecules through the cyclic voltammograms. According to the study, $O_2^{\bullet-}$ acted as a Brønsted base and oxidant sequentially delivering the desired carboxylic acid from the alcohol. The production of aldehyde intermediate is fast and highlighted the advantage of the $O_2^{\bullet-}/O_2$ system in the selectivity. This process is a complementary method for facile alcohol oxidation.



Scheme 2.2: The $O_2^{\bullet-}$ assisted electro-oxidation of a primary alcohol to a carboxylic acid (M. Singh et al., 1991), Copyright (1991) Wiley.

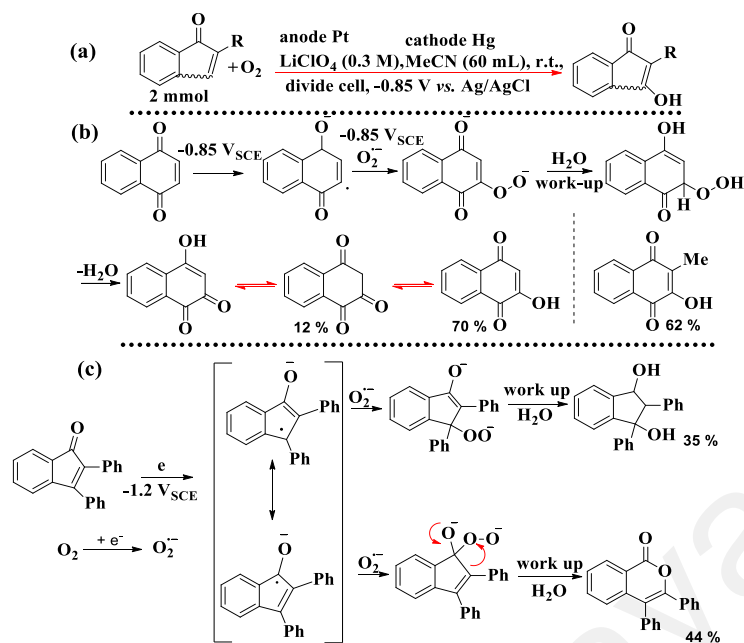
Similarly, as shown in Scheme 2.3, Chuban et al. (1991) investigated electrochemical oxidation of para-nitrotoluenes to yield para-nitrobenzoic acid by metalloporphyrin catalysts in the presence of $O_2^{\bullet-}$. They showed that the electrolysis happened under the potentiostat mode at -0.4 V vs SCE, a much less negative-potential value than that required for the electroactive starting material, product, and O_2 . In an earlier study, the reaction was initiated by the reduction of metalloporphyrin to M(II)TTP

at -0.4 V vs SCE; then M(II)TTP interacts with $O_2^{\bullet-}$ forming intermediate $[M(III)TTPO_2^{\bullet-}]$ (Chuban, Dong, & Shufang, 1991). Subsequent oxidation of starting material accomplished the eventual product through several steps.



Scheme 2.3: The $O_2^{\bullet-}$ -assisted and metal-catalyzed electro-oxidation of nitrotoluenes (Chuban et al., 1991), Copyright (1991) Wiley.

Barba, Batanero, & Barba (2017) reported $O_2^{\bullet-}$ mediating coupling reaction, as shown in Scheme 2.4. They investigated the radical coupling reaction of electrogenerated radical anion of 1, 4-naphthoquinone, 2-methyl-1, 4-naphthoquinone, 2, 3-diphenyl-1-Hinden-1-one or phenylacetylene with simultaneously electrogenerated $O_2^{\bullet-}$. These reactions produced essential products such as 2-Hydroxy-1, 4-naphthoquinone, 2-hydroxy-3-methyl-1, 4-naphthoquinone, 3-hydroxy-2, 3-di-phenylindan-1- one, 3, 4-diphenyl-1H-iso-chromen-1-one and benzoic acid.



Scheme 2.4: The $\text{O}_2^{\bullet-}$ assisted formation of hydroxynaphthoquinones (Barba et al., 2017), Copyright (1991) Wiley.

2.5 Detection of $\text{O}_2^{\bullet-}$

The typical detection techniques for $\text{O}_2^{\bullet-}$ include electrochemistry, UV-vis, Luminescence, vibrational spectroscopy, and Electron spin resonance (Maan Hayyan, Hashim, & AlNashef, 2016). The $\text{O}_2^{\bullet-}$ redox properties, absorption of electromagnetic wave attributes, or any timely accumulation of $\text{O}_2^{\bullet-}$ derived product enables most of these detection techniques. Notably, the electron spin resonance (ESR) detection procedure exploits the $\text{O}_2^{\bullet-}$ spin property. The detection methods are either in the spectrophotometric or nonspectrophotometric category and depend on $\text{O}_2^{\bullet-}$ generation routes. More than four decades ago, ideal $\text{O}_2^{\bullet-}$ is detectable with a pulse at $\sim \geq 1$ mM concentration (Ozawa & Hanaki, 1977).

There is growing interest in detecting $\text{O}_2^{\bullet-}$ since it can further form way reactive species such as singlet oxygen and peroxy radicals. Suggestively, $\text{O}_2^{\bullet-}$ magnetic characteristic permits its detection by electron paramagnetic resonance (EPR) spectroscopy (Rigo et al., 1979). Unfortunately, it is not easy to measure its concentration

in aqueous media because it can dismutate rapidly to H_2O_2 and O_2 ($k = \sim 10^8 \text{ M}^{-1}\text{s}^{-1}$ at a pH of ~ 5). Therefore, this study used N-halopiperidines as specific spin-trappers of the $\text{O}_2^{\bullet-}$ to detect the radical through the spin trapping technique. This technique transforms short-lived radicals into long-lived radicals by reaction with particular spin trappers. They investigated the $\text{O}_2^{\bullet-}$ detection through the method of $\text{O}_2^{\bullet-}$ consecutive reaction with piperidinoxyl.

A chemiluminescent compound such as 5-amino 2, 3-dihydroxy-1, 4-phthalayineidone can detect various ROS (M nzel et al., 2002). The study focused on seeing $\text{O}_2^{\bullet-}$ in vascular tissue so, they suggested that using two or more different techniques that yield similar results provides a reliable approach for studying ROS in vascular tissues.

Gao et al. (2007) reported the detection of nanomolar-micromolar levels of $\text{O}_2^{\bullet-}$ using 2-chloro-1, 3,-dibenzothiazolinecyclohexene fluorescent probe coupled with a spectra character-signaling. They suggested that the fluorescent probe image of $\text{O}_2^{\bullet-}$ present in living cells. According to their observation, the fluorescent probe has better selectivity for $\text{O}_2^{\bullet-}$ over competing for cellular ROS and some biological compound.

Nauseef et al. (2014) reported that fluorescence and chemiluminescent probes for both extracellular and intracellular $\text{O}_2^{\bullet-}$ have shortcomings that may limit their use; hence, non-redox sensitive investigations can provide spatial and temporal detection of $\text{O}_2^{\bullet-}$.

Li et al. (2011) reported the detection of $\text{O}_2^{\bullet-}$ released from cancer cells using potassium-doped multi-walled carbon nanotubes (KMWNTs)-1-butyl-3-methylimidazolium hexafluorophosphate $[\text{BMIm}^+][\text{PF}_6^-]$ ionic liquid composite gels as an electrochemical biosensor. They showed that the KMWNTs- $[\text{BMIm}^+][\text{PF}_6^-]$ could

induce O_2 reduction to generate a robust current signal in a neutral solution. They compared KMWNTs without $[BMIm^+][PF_6^-]$ or MWNTs- $([BMIm^+][PF_6^-])$ composites and deduced that KMWNTs- $([BMIm^+][PF_6^-])$ could enhance the O_2 reduction peak current by 6.2 folds and 2.8 fold. Consequently, this significantly increases the detection sensitivity of ROS. The $O_2^{\bullet-}$ biosensor was fabricated by coupling superoxide dismutase (SOD) in the KMWNTs- $([BMIm^+][PF_6^-])$ gel by observing the O_2 produced by an enzymatic reaction between SOD/ $O_2^{\bullet-}$ without the assistance of electron mediators.

2.6 Outlook on CO₂ Emission, Capture and Utilization

The 1887-1987 data on global CO₂ levels showed that the amount of CO₂ in the atmosphere was less than 350 ppm (Allen, 2009; Mathias, Anderies, & Janssen, 2017). At that time, the level of CO₂ was in equilibrium, and it balances the carbon cycle by erasing the likelihood of global temperature increase. Unfortunately, increasing industrialization since 1987 to meet the 30 to 50 per cent increase in energy demand has increased the CO₂ emission above the 350-ppm equilibrium threshold (van Ruijven, De Cian, & Sue Wing, 2019). Accordingly, recent projection confirmed that the future level of CO₂ from the high anthropogenic activity exceeded the terrestrial abundance of ~550 ppm in the next 3-8 decades (Smith & Myers, 2018). In congruence, the NASA report relates that previous and present atmospheric CO₂ levels are at ~ 300 ppm and ~ >400 ppm, respectively (Kuhns & Shaw, 2018; Ussiri & Lal, 2017).

The current CO₂ capture method, such as precombustion and post-combustion capture of CO₂ from large point sources, is viable to reduce the CO₂ concentration in the atmosphere (Sanz-Pérez et al., 2016). However, direct removal of CO₂ from the air is feasible to reduce the concentration of CO₂ from the global atmosphere (Lackner, Ziock, & Grimes, 1999). Some solvents and solid sorbents with sorption capacity with CO₂ are suitable CO₂ capture medium. Some of these solvents or solid sorbents include supported amine and ammonium materials, glycerol and metal-organic frameworks (MOFs). For

instance, linear amines grafted over PAF-1 (porous polymer networks) with 4023 m²/g surfaces recorded CO₂ uptake of 1.3 mmol/g at 22 °C, at 1 bar (Lu et al., 2012). The PAF-1 functionalized with diethylenetriamine gave direct air capture sorbing attribute of 3.6×10¹⁰ mmol/g (Lu et al., 2013). Another more suitable medium for CO₂ capture is the use of ILs because;

- 1- Low energy required for regenerating ILs after capture CO₂ (Earle & Seddon, 2000).
- 2- ILs low vapour pressure makes their regeneration comes with no losses into the gas stream (Gordon, 2001).
- 3- ILs have a high thermal and chemical stability, making them passive to impurity, reactions to cause any corrosion to process equipment (Gan, Rooney, & Zou, 2006).

2.6.1 Non-O₂^{•-} mediated CO₂ utilization

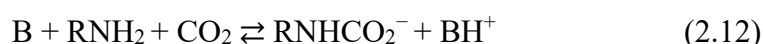
The utilization of CO₂ is concerned with its transformation to useful products such as fuel, commodity chemicals and materials. The classical approach to CO₂ utilization is the Sabatier reaction which produces CH₄ from CO₂ and H₂ feedstock (Vogt et al., 2019). Sabatier's process later inspired the growth of CO₂ catalysis regardless of the challenge of activating an unreactive molecule such as CO₂ (Kleij, 2019). Sabatier's reaction and any other CO₂ catalysis are efforts to mimic the ingenious complex mechanism of nature's capability to create carbon-derived materials using chiefly CO₂, water, and sunlight as a feedstock (Artz et al., 2018). The CO₂ as chief feedstock have been utilized with an amine to yield carbamates which are important peptide bond surrogates usually found in modern drug discovery and medicinal chemistry (De Simone et al., 2018; Ghosh and Brindisi, 2015). The CO₂ based carbamate could serve as an immunotherapeutic target for molecule drug design (Vanneman and Dranoff, 2012). Carbamate production from CO₂ and amine is a reaction that centres on C-N bond formation chemistry. However, the type

of carbamate produced depends on the type of amine molecule used as feedstock (Honda et al., 2011). The carbamate production by this means proceeds via an empirical mechanism guiding the interaction of CO₂ from the gas phase with amine solution (Ion et al., 2008). The investigations so far do not primarily attempt to consider a molecular reaction that describes all reaction in solution after the absorption of CO₂ from the gas phase to produce carbamate (McCann et al., 2009). The most popular reaction mechanism is in Eqs 2.10 and 2.11 (Caplow, 1968). The reaction involves forming the carbamate's zwitterionics form in the first step, then a slow proton exchange reaction with a base in the second step.



The amides are weak bases that are not known to protonate in an aqueous solution. Thus, the zwitterion concentration is insignificant compared with the tautomeric, neutral form of the carbamic acid. The structural question of this carbamic acid is not mechanistically important. However, the second step is known to be diffusion controlled and instantaneous for any possible observation.

Another suggested mechanism for carbamate formation, as presented in Eq 2.12, includes building a termolecular reaction between CO₂ and amine and a base (Crooks & Donnellan, 1989). This mechanism is weak for empirically describing observations. On a molecular level, they are renowned for combining sequential lower-order reactions.



The mechanism in Eq. 2.13 and 2.14 is realistic and proceeds via amine and CO₂'s direct reaction, followed by the carbamic acid's deprotonation in a normal protonation equilibrium (Cullinane & Rochelle, 2006; McCann et al., 2009).





In an earlier study, acetylenic amines and CO₂ reacted to form different molecules such as 5-methylene-1, 3-oxazolidin-2-ones (Feroci et al., 2005). Similarly, this kind of CO₂ utilization was through reacting amines with CO₂ in the presence of alcohol (Heyn, Jacobs, & Carr, 2014). These reaction concepts are not the ones adopted in this current research study. Our approach is different by utilizing O₂^{•-} and the mechanism differs from these conventional ones.

2.6.2 CO₂ utilization by O₂^{•-}

The CO₂ utilization by O₂^{•-} in 2-bromomethanol saturated media have mediated carbonates formation (Casadei et al., 1997). This utilization process is another proof that electrochemically generated O₂^{•-} in an aprotic solvent to convert primary and secondary alcohols bearing leaving groups into the corresponding cyclic carbonate. The report suggested that the leaving-group in the starting material allows the intermediate to evolve to cyclic carbonate's high yields directly. However, when there is no leaving-group in the starting material, an external electrophile is required to direct the carboxylation process to completion. After a short while, the external electrophile must be added to the electrolysis mixture to initiate the carboxylation agent's reaction. They also suggested that the surviving intermediate amount thus establishes the dialkyl carbonate yield. In turn, the monoalkyl carbonate concentration depends on both steric factors and nucleophilicity of the substrate or its anion. They assert that the higher the steric hindrance, the lower yield of carbonate from alcohol. This scenario shows why tertiary alcohols and phenols do not react towards the carboxylation reaction. This kind of study was also reported by Maria et al. (2001), where the reactivity of alcohols/O₂^{•-} in aprotic dipolar solvents and the presence of CO₂ was examined.

The production of the peroxy-dicarbonate anion (C₂O₆²⁻) from CO₂ utilized by O₂^{•-} (Figure 2.3a) in acetonitrile, dimethylformamide and dimethyl sulfoxide is also

viable (Roberts et al., 1984). Moreover, Figure 2.3b shows the reverse oxidative CV wave's disappearance for peroxy-dicarbonate production.

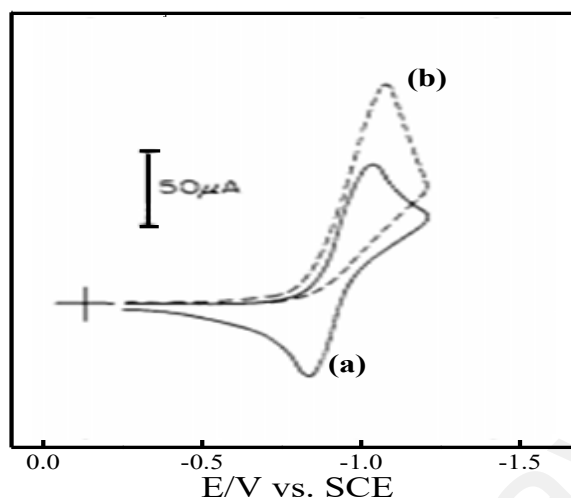


Figure 2.3: The cyclic voltammograms (CVs) in dimethylformamide containing 0.1 M of tetraethylammonium perchlorate. (a) $\text{O}_2^{\bullet-}$ generation and (b) CO_2 conversion by $\text{O}_2^{\bullet-}$ at the platinum working electrode and a scan rate of 100 mV/s (Roberts et al., 1984), Copyright (1984) American chemical society.

The $\text{C}_2\text{O}_6^{2-}$ is IR-active at $\sim 851 \text{ cm}^{-1}$ in $\text{K}_2\text{C}_2\text{O}_6$ (Jones & Griffith, 1980). The detailed kinetics of $\text{C}_2\text{O}_6^{2-}$ formation was investigated by Buzzeo et al. (2004) in an ionic liquid. According to their studies, the rate constants for the $\text{O}_2^{\bullet-}$ reaction with CO_2 in 1-Ethyl-3-methylimidazolium Bis (trifluoromethylsulfonyl) imide was estimated around $1.4 \pm 0.4 \times 10^3 \text{ M}^{-1}\text{s}^{-1}$. The $\text{O}_2^{\bullet-}$ generation in 1-n-butyl-3-methylimidazolium hexafluorophosphate, as shown by AlNashef et al. (2002), inspired this study. They generated $\text{O}_2^{\bullet-}$ from electrochemical reaction of O_2 dissolved in two different solvents such as acetonitrile containing tetraethylammonium perchlorate (TEAP) room-temperature ionic liquid at atmospheric pressure. The study, as shown in Figure 2.4, affirmed that subsequent addition of CO_2 enhances the rate of O_2 reduction in both systems but inhibits the reverse oxidation reaction of $\text{O}_2^{\bullet-}$ to O_2 ; indicating the utilization of CO_2 therein to form $\text{C}_2\text{O}_6^{2-}$.

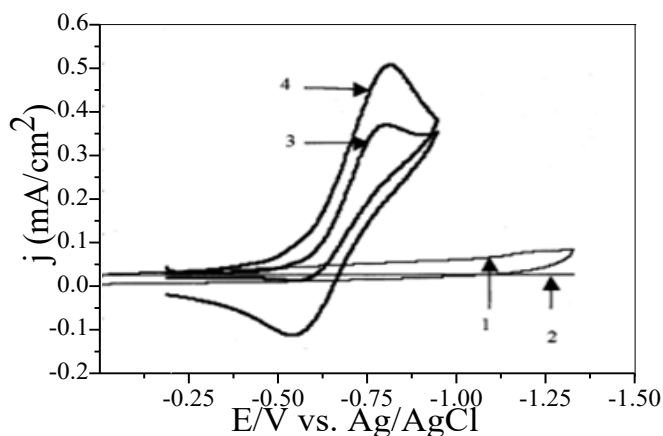


Figure 2.4: The cyclic voltammograms (CVs) in 1-n-butyl-3-methylimidazolium hexafluorophosphate [BMIm⁺][HFP⁻] at ambient pressure. (1) = N₂ background, (2) = after sparging with CO₂, (3) = after sparging with O₂, (4) = after sparging with O₂ and CO₂ simultaneously at glassy-carbon disk working electrode and a scan rate of 100 mV/s (AlNashef et al., 2002), Copyright (2002) American chemical society.

The carboxylation of amine from O₂^{•-}/CO₂ (C₂O₆²⁻) can produce carbamate (Casadei et al., 1997). According to the report, if an electron-withdrawing group activates the C-H adjacent to the N-H group, the C-H's competitive deprotonation can occur. Consequently, this hampers the carboxylation process due to strong electron-withdrawing nitrogen-based substituents. Non-protic medium sustainably retains nucleophilic radicals for reaction (AlNashef et al., 2002). Accordingly, this recommendation applies in carbamate production using O₂^{•-}/CO₂ couples, non-volatile, toxic medium and catalysts during electrolysis (Feroci et al., 2011; Feroci, Inesi, & Rossi, 2000).

2.7 Outlook on Dechlorination of Chlorinated Compounds

Contemporarily, chlorinated hydrocarbons are useful as significant designer pharmaceutical molecules (Wilcken et al., 2013) and agrochemicals (Jeschke, 2010) found in various industrial-based processes. Chlorinated hydrocarbons could originate through industrial processes and many unregulated incineration practices. They have become nearly ubiquitous to our environment. Their effect becomes somewhat inherently

hazardous to the environmental ecosystem and undermines one of the 24 principles of green engineering and chemistry (Tang et al., 2008; Zimmerman et al., 2020).

For instance, chlorobenzene (C_6H_5Cl) and dichloromethane (CH_2Cl_2) have recently gained recognition because of their importance as precursors used in the manufacture of valuable products, but they are still harmful to the environment. C_6H_5Cl does not occur spontaneously but as a by-product released to the environment from the production of substances like degreasing agents, adhesives, rubber, paint, or fibre-swelling agent in textile processing or fibre-swelling agents. It can readily evaporate into the environment as a 6th airborne or landfills contaminant (Mohan, K.V, & C, 2017). The typical route of body contact with C_6H_5Cl from the environment is through inhalation or dermal route. The C_6H_5Cl invoke epoxide's biochemical production, which binds to proteins in the liver, kidney, lungs, ribonucleic acid (RNA), and deoxyribonucleic acid (DNA), causing severe medical complications (Krewet, er, & Norpoth, 1989). Other studies confirmed that exposure to C_6H_5Cl in the environment could cause problems with the immune system, the blood, the heart, and the respiratory system in animals (Von Burg, 1981; Willhite, 1990). Several epidemiological studies have established the relationship between indoor exposure to C_6H_5Cl and respiratory diseases (Diez et al., 2000; G Wieslander et al., 1994; Wieslander et al., 1996). The indoor air concentrations of C_6H_5Cl which usually amount from the usage of C_6H_5Cl -derived products, ranging from 1 to $3.5\mu g/m^3$ in Leipzig, Germany (Herbarth et al., 2000; Herbarth, M 1998), and about $72.2\mu g/m^3$ in various cities in the USA (Búa et al., 1991). The amount of C_6H_5Cl in workplaces ranges between $18.7\text{ mg}/m^3$ and $488\text{ mg}/m^3$ (Kusters, Lauwerys, & health, 1990).

Also, CH_2Cl_2 is another toxic compound that is not miscible with water and readily evaporates into the environment. CH_2Cl_2 is a solvent for plastics, cellulose esters, insecticides, and paints in terms of application. It is also used as a solvent for liquid-liquid

extractions, cleaning fluids, extraction of essential oils, and polyurethane foam blowing applications. The CH_2Cl_2 is a precursor for pharmaceutical and other chemical intermediates applications. In principle, the CH_2Cl_2 gets into the environment from these different applications as B-2 carcinogen, in which case; a minimum concentration of ~ 150 mg/Kg body weight is lethal (Goullé et al., 1999; Schlosser et al., 2015). The primary environmental exposure to CH_2Cl_2 exposure is mainly by inhalation or dermal contact and eventually becomes metabolized to CO, causing CO poisoning (Yang, 2014).

Concerns over the toxicity and environmental persistence of $\text{C}_6\text{H}_5\text{Cl}$ and CH_2Cl_2 have motivated an increase in environmental investigations. These primarily speculate means of rendering them passive or non-toxic via a dechlorination process before discharging them into waste streams. The $\text{C}_6\text{H}_5\text{Cl}$ and CH_2Cl_2 have an acceptable daily intake (ADI) of ~ 0.004 and a 0.5 mg/Kg body (Council, 2012; Guengerich, Kim, & Iwasaki, 1991; Gut et al., 1996). The dechlorination process reaching these ADI levels implies that their presence in the environment will not be lethal. Notwithstanding, it is challenging to regulate this amount and enforce that the ADI level as many process disposals and discharges are on-going. Generally, chlorinated compounds (e.g. $\text{C}_6\text{H}_5\text{Cl}$ and CH_2Cl_2) are inherently hazardous and undermining some of the 24 principles of green engineering and chemistry (Tang et al., 2008; Zimmerman et al., 2020). Therefore, this is a tremendous environmental problem that impedes their relevance as chemical precursors unless authority enforces their disposal to their respective ADI, which is not realistic.

The electrochemical reductive dechlorination process is one of the most promising approaches for the dechlorination of organic chlorides (Lei et al., 2019; Shu et al., 2019; Zheng et al., 2019). Nevertheless, the process's mechanism depends on the molecular structures and chlorine substituents (Costentin, Robert, & Savéant, 2003; Huang et al., 2012; Lei et al., 2019; Martin et al., 2016). This dechlorination is research on-going to improve our environmental integrity. As conventional techniques produce dioxin that is

another poisonous substance (Field & Sierra-Alvarez, 2008; McKay, 2002), it is necessary to use a more feasible approach that produces no dioxin as a by-product. Therefore, developing a strategy for their degradation is essential, especially under the auspices of enforcing our sustainable green engineering environment.

2.7.1 Non- $O_2^{\bullet-}$ mediated dechlorination

Recently, the electrochemical reductive dechlorination of chlorinated volatile organic compounds (Cl-VOCs) has become more thermodynamically favoured (Lei et al., 2019). This study found that the substituent in the Cl-VOCs toward dehalogenation reactivity follows a unique pattern. Accordingly, the degree of chlorination of Cl-VOCs increases in the order of their substituents such as; alkyl group \ll β -chlorine $<$ double bond $<$ α -chlorine. The electron transfer process accompanying the dechlorination process usually follows a concerted and stepwise dissociative mechanism. Another study investigated the dechlorination of 4-chlorophenol on Pd/MWCNT nanoparticle-based electrode to yield chiefly phenol and Cl^- (Miao et al., 2019). Nearly all the 4-chlorophenol was dechlorinated, and the dechlorination efficiency of the Pd/MWCNT nanoparticle-based electrode after five cycles was close to 100 %. Zheng *et al.* (2019) investigated the reductive dechlorination of 2, 4 dichlorophenol on Ni/Fe bimetallic surface (Zheng et al., 2019). Irrespective of the electrode used, related studies established that the organic chlorides' dechlorination mechanisms depend on their molecular structures and the solvent condition (Contentin et al., 2003; Huang et al., 2012; Lei et al., 2019; Martin et al., 2016). Therefore, the need to score the importance of dechlorination of organic hydrocarbons using suitable solvents to offset the dechlorination process's expense is still impeding, mainly when using conventional techniques.

2.7.2 Mediation of dechlorination by $O_2^{\bullet-}$

In another promising technique, $O_2^{\bullet-}$ which was electrogenerated from cheap O_2 to dechlorinate organic chlorides through mechanistic nucleophilic substitution (S_N2) of

their halide functionality (Johnson, Nidy, & Merritt, 1978; Merritt & Sawyer, 1970; Ryding et al., 2015). Presently, no study has used IL to dechlorinate chlorinated organic compounds using this method until now.

2.8 Electrochemical Process

2.8.1 Electrode system

An electrochemical cell contains two electrodes immersed in an electrolyte medium (Bard et al., 1980). These electrodes immersed in an electrolyte medium (for instance, IL) create an interface with the electrolyte, thereby building up an electrode-electrolyte junction. As a result, every typical electrochemical cell has two electrode-electrolyte interphases. Two electrodes serve for a scenario where the cell properties are required. Contrarily, to measure the pure electrolyte characteristics or analytes in the electrolyte, a third electrode is inserted, which referred to as the reference electrode (Ni et al., 2018).

The three-electrode system could study analytes' behaviour at the electrode/electrolyte interface, where both potential and current are required. The three-electrode system is composed of a working electrode (WE), the counter electrode (CE) and a reference electrode (RE). Accordingly, the current flow between the two electrodes. The voltage drop in each electrode originates from the potential between one electrode and the reference electrode.

Considering analytes/electrolyte with WE electrode immersed, when the system is perturbed by applying potential/current to WE cathodically or anodically, it is taken away from equilibrium. The general method to apply potential/current uses a standard RE, whose potential is almost constant. After the perturbation, recording the current developed across the WE and some other electrode prevails. A third electrode, CE, is used to complete the circuit to carry current. Therefore, to determine any analytes' electrochemical behaviour, three-electrode systems are used rather than the two-electrode

system. There are transient electrochemical techniques such as chronoamperometry (CA), cyclic voltammetry (CV), and electrochemical impedance spectroscopy (EIS) that uses the electrode system.

2.8.2 Chronoamperometry

Chronoamperometry is a dynamic technique where a square-wave potential applies to the WE (Bard et al., 1980). This technique is otherwise known as constant potential bulk electrolysis, controlled potential amperometry, and potential pulse electrolysis.

In simple term, $O + e \rightleftharpoons R$ with a formal potential E^0 , in the CA, the potential step applied to the WE should be sufficiently more negative than E^0 to promote O reduction to R on the WE surface. Accordingly, the current is diffusion-limited, and the current-time response by the Cottrell Eq 2.15 (Cottrell, 1903);

$$i(t) = \frac{nFAD_0^{1/2}C_0^*}{\pi^{1/2}t^{1/2}} \quad (2.15)$$

Where $i(t)$ is current, n is the number of electrons transferred in the half-reaction, F is Faraday's constant (96,485 C/mol), A is the electrode area, D_0 the diffusion coefficient, C_0^* is the initial concentration, and t is time. Three variables (n , c and D) in the Cottrell equation are unknown when investigating redox reaction involving the n -electron-transfer system. Therefore, other beneficial approaches using microelectrode determine nC and D values simultaneously. Microelectrodes are widely used and demonstrate high mass transport rates, right signal-to-noise ratios and low uncompensated resistances (Bard et al., 1980; Compton & Banks, 2018). When conducting electrochemistry in ILs with high viscosity, these features are essential (Buzzeo, Evans, & Compton, 2004).

Many numerical models could describe the chronoamperometry responses or time-current transients, especially observed at a microelectrode (Buzzeo, Evans, & Compton, 2004; Klymenko et al., 2004). Shoup and Szaba Eq 2.16 and 2.17 are popular

while describing the current response with time values within an error of 0.5 % (Shoup & Szabo, 1982). Accordingly, considering an n electron process, the CA response at a microelectrode is as follows;

$$i = 4nFrDcf(t) \quad (2.16)$$

$$f(t) = 0.7854 + 0.8862\sqrt{\frac{r^2}{4Dt}} + 0.2146 \exp\left(-0.7823\sqrt{\frac{r^2}{4Dt}}\right) \quad (2.17)$$

Eq 2.17 applies to all solvent regardless of their viscosity. Where r is the electrode radius. Combining experimental CA with the fitting of the dynamic current responses to the Shoup and Szabo Eq. 2.18 results in a powerful electroanalytical technique that facilitate the determination of both the product (nc) and the diffusion coefficient (D) of electroactive analytes (Ikeuchi, 2005; Paddon et al., 2007). This scenario is possible because, at short times, the response is Cottrellian and depends on $ncD^{1/2}$. On the contrary, at long times, the steady-state current is recorded, which scales with ncD according to the steady-state current equation describe below,

$$i_{ss} = 4nFD_0C_0r_0 \quad (2.18)$$

Where i_{ss} is the steady-state current, r is the electrode radius other parameters (D , F and n) are in Eq 2.16 and 2.17. It is possible to analyze the transient to give (nc) and D . At longer transient times, the current approaches a steady-state value where ncD is constant (Evans et al., 2003).

2.8.3 Cyclic voltammetry

Cyclic voltammetry (CV) has been notable for its flexibility in various fields that involve the electron transport process. Usually, in CV analysis, the working electrode potential (E/V) is linearly scanned or stripped forward from E_1 to E_2 and then backward from E_2 to E_1 , given rising to a resultant current which is measurable (Elgrishi et al., 2018). Figure 2.5 shows CVs' general instances for the electrochemical conversion of electroactive species in an electrolyte solution. The CV method is applicable to study electrode processes, even when the products or intermediates are short-lived, about <10 s

(Liedtke et al., 2019). The CV can check the electrochemical pattern of different substances because it can give an insight into the relationship of structure, potential, and specific activities. The method is noticeable with its points of interest of straightforwardness, sensitivity, speed, and low expenses, among others, which brings about a broad scope of utilizations up until this point (Kumar & Dhaliwal, 2020; Puthongkham & Venton, 2020).

2.8.3.1 Reversible systems

In Figure 2.5, Curve 1 indicates when the process is reversible. Usually, in the forward scan (E_1 to E_2), a cathodic peak is obtained by reducing an electroactive specie (Elgrishi et al., 2018). In the backward scan (E_2 to E_1), an anodic peak appears due to the re-oxidation of the reduced electroactive specie. Therefore, the essential criteria for reversing an electrochemical process are that the cathodic and anodic peak currents should be equal in magnitude albeit, the cathodic peak potential is $58/n$ more-negative than the anodic peak (Bard et al., 1980). This criterion indicates that the reversibility decreases when the difference between the two peak potentials (E_{pc} and E_{pa}) increases.

Moreover, the half-wave potential used to obtain the formal redox potential is obtained by $E_{1/2} = (E_{pc} + E_{pa})/2$. The theoretical expression of peak current for a reversible CV is a function of the scan rate, and it is called Randles-Sevcik expression. This expression shows the dependence of peak current i_p on scan rate ν . The number of electrons for this kind of system can also be determined by anodic and cathodic peak potentials in the equation (Bard et al., 1980).

$$i_p = 2.69 \times 10^5 n^{3/2} AD^{1/2} C \nu^{1/2} \quad (2.19)$$

$$\Delta E_p = \frac{E_{pa} - E_{pc}}{n} \approx 0.059 \quad (2.20)$$

Where i_p = peak current (A), n = electron stoichiometry involves in charge transfer, A = electrode area (cm^2), D = diffusion coefficient (cm^2s^{-1}), C = concentration (molcm^{-3}), ν

= scan rate (Vs^{-1}), ΔE_p = potential separation (v), E_{pa} = anodic peak potential (v) and E_{pc} = cathodic peak potential (v).

2.8.3.2 Irreversible and quasi-reversible systems

Considering an irreversible system represent by curve 3 in Figure 2.5, individual reduction and oxidation peak are reduced in magnitude and widely separated (Espinoza et al., 2019). Compared with the reversible process shown by curve 1, the cathodic peak usually appears at much more negative potential while the anodic peak occurred at much more positive potential. The entirely irreversible process has an anodic peak in the potential region that is not measurable. Therefore, the potential-peak shift with the scan rate stripping characterizes an irreversible system.

$$E_p = E^{0'} - \frac{RT}{\alpha F} \left[0.782 + \ln \left(\frac{D_o^{1/2}}{k^0} \right) + \ln \left(\frac{\alpha F}{RT} \right)^{1/2} \right] \quad (2.21)$$

$$E_p - E_{p/2} = \frac{1.857RT}{\alpha F} = \frac{47.7}{\alpha} \text{ mV at } 25 \text{ }^\circ\text{C} \quad (2.22)$$

Where α is the transfer coefficient and the potential E_p occurs at a higher value than E_0 with the overpotential related to k_0 and α .

Figure 2.5, curve 2 shows another case in which an electroactive species, say A, is reduced to a product, say B. The B can be reoxidized back to A although, before the reoxidation of B to A, some part of B gets converted to no-electroactive specie, say C. Usually, the cathodic peak appears similar to the one illustrated in curve 1, the anodic peak is much smaller. This pattern is the case of a quasi-reversible system (Avaca et al., 1993; Mann, Helfrick, & Bottomley, 2014; Myland & Oldham, 2005). Nicholson and Shain's equations could elucidate quasi-reversible or irreversible systems. The Nicholson and Shain peak current for the analysis is given by;

$$i_p = 2.69 \times 10^6 n(n\alpha)^{1/2} ACD^{1/2}V^{1/2} \quad (2.23)$$

The peak current is proportional to bulk concentration. However, specifically for quasi-reversible systems, the current is controlled by mass transfer and charge transfer. The standard heterogeneous rate constant range for quasi-reversible systems is; $10^{-1} > k_0 > 10^{-5}$ cm/s. Also, the peak separation is larger than those observed in reversible systems. The electrochemical reduction of O_2 to $O_2^{\bullet-}$ in aprotic or ILs media is renowned for following the quasi-irreversible pattern (AlNashef et al., 2002).

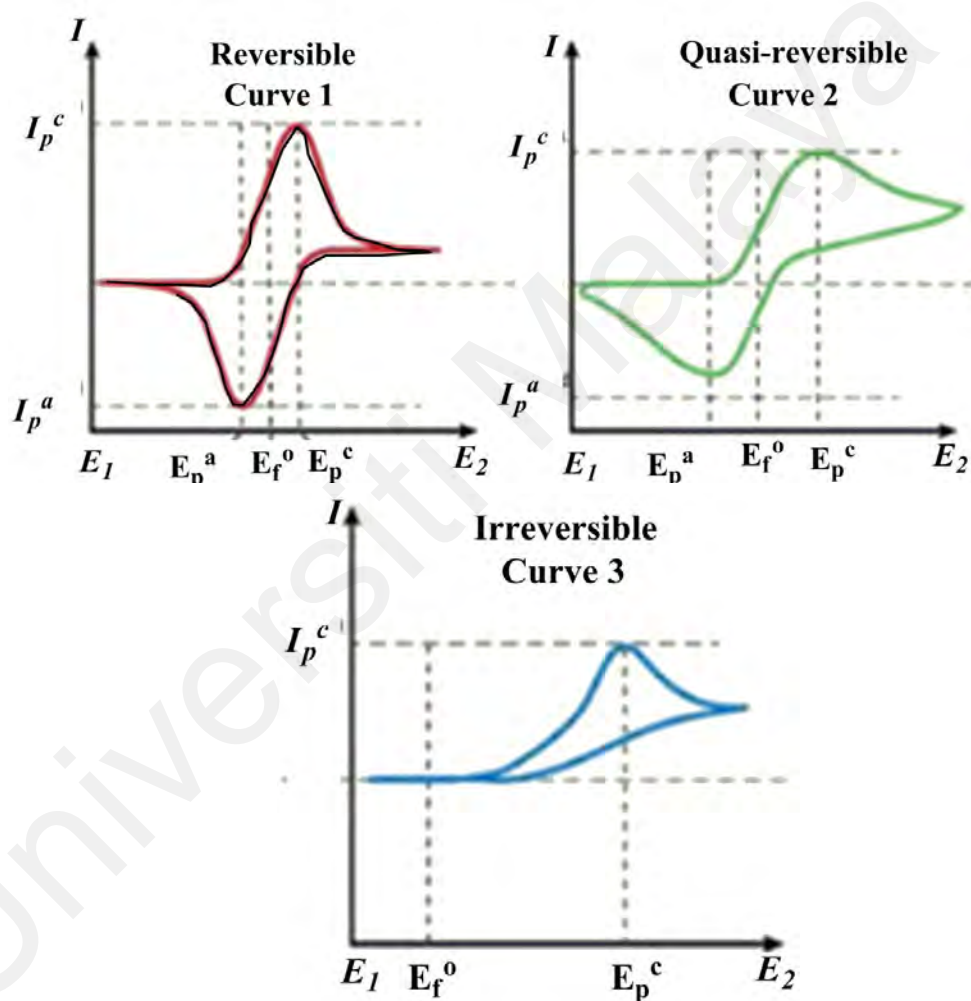


Figure 2.5: Cyclic voltammograms for the electrode reaction; $Ox + ne^-$. Curve 1 is reversible, and curve 2 is quasi-reversible, curve 3 is irreversible and accompanied by a conversion of reduced species to an inactive electro species (Bard et al., 1980), Copyright (1980) Wiley.

2.8.3.3 Mass transfer parameter from CV analysis

Peculiar to the $O_2^{\bullet-}$ generation via CV analysis, the mass transfer parameters include diffusion coefficient (D_o), solubility (C_o) (Hayyan et al., 2012). For instance, the D_o -values and C_o -values of O_2 in some ILs have are shown in Table 2.4. According to the review and other new studies, the D_o -values $\sim 10^{-10}$ magnitude. In commonly used IL, the D_o for $O_2^{\bullet-}$ was reported to be 0.02 to 0.03 of the O_2 values and the solvated $O_2^{\bullet-}$ diffusion in the IL resulting in a large entity (Zigah et al., 2008). Base on the Stoke-Einstein relationship (Pandolfi et al., 2017), this variation would correspond to a solvated $O_2^{\bullet-}$ that is 10,000 times heavier compared to neutral O_2 in the same IL (René et al., 2009). Certainly, $O_2^{\bullet-}$ in IL is different from $O_2^{\bullet-}$ in conventional solvents, so does this affects their mass transfer phenomena in general (René et al., 2009; Zigah et al., 2008). Evans et al. (2004) have shown that $O_2^{\bullet-}$ diffusion coefficients in ammonium base IL are higher in magnitude and lower than those of O_2 in the same media. They claimed this was likely due to the difference in the Coulombic forces' strength between these highly ionic solvents, neural O_2 and $O_2^{\bullet-}$ radical, respectively.

Table 2.4: Diffusion coefficients and solubility of electrochemical reduction of O₂ in IL media by CV technique using Au electrode

ILs	D _o (× 10 ⁻¹⁰ m ² /s)	C _o (mM)	Type of electrode	Reference			
[EMIm][TFSI ⁻]	7.3	3.9	10µm Au	(Buzzeo et al., 2003) (Buzzeo et al., 2004)			
[HTAmm ⁺][MS ⁻]	1.48	11.60	10µm Au	(Buzzeo et al., 2003) (Buzzeo et al., 2004) (Rogers et al., 2009)			
	4.6	3.90					
	5.3	3.90					
	6.0	3.80					
	7.0	3.70					
	8.0	3.90					
	4.25	3.90					
	4.55	3.90					
	5.29	3.90					
	6.00	3.8					
	7.02	3.70					
	7.98	3.90					
		4.1			4.50	10µm Pt	(Rogers et al., 2009)
		4.9			4.40		
5.6		4.40					
6.5		4.30					
7.4		4.40					
[BMIm ⁺][TFSI ⁻]	8.3	3.60	10µm Au	(Rogers et al., 2009)			
	9.0	3.80					
	4.3	3.40					
	5.1	3.60					
	5.7	3.70					
	6.8	3.70					
		4.7	4.40	10µm Pt	(Rogers et al., 2009) (Barnes et al., 2008)		
		5.7	4.30				
		7.0	4.30				
		8.6	4.20				
9.8		4.40					
[MPMPipm ⁺][HFP ⁻]	1.0	14.30	11µm CF, 3mm GC	(Hayyan et al., 2011)			
	1.4	11.70					
	2.2	9.40					
[BMPyrr ⁺][TFA ⁻]	0.42	14.78	11µm CF, 3mm GC				
	2.34	7.46					
	2.81	7.39					

2.9 Electrochemical Impedance Spectroscopy

Electrochemical impedance spectroscopy (EIS) analysis evaluates a series of heterogeneous systems with unique structural and electrical properties using the

equivalent circuit as models. EIS is an alternating current (AC) technique in which an applied potential $E(t)$ modulated over a time with a small amplitude $|E_0| \sim 5 - 10 \text{ mV}$ at a controlled frequency (ω) according to Eq 2.24. Where ω is an angular frequency defined by $\omega = 2\pi f$, and f is the frequency measured in Hz.





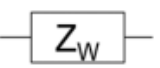
$$E(t) = |E_0| \sin(\omega t) \quad (2.24)$$

Usually, a small perturbation in potential ($|E_0|$) is required to ensure the current linear behaviour in an EIS system following the Butler–Volmer model (Bard et al., 1980). The current response $I(t)$ according to Eq 2.25 is matched in frequency but offset by a phase angle (φ) depending on the parameters of the electrochemical circuit. Therefore, impedance expressed in ohms (Ω) units is the AC analogue to resistance and is thus related to the alternating potential and current through Ohm’s law, as indicated in Eq 2.26. An equivalent circuit fitting model (ECM) is required to gain insightful information from the EIS data. The ECM combines fundamental elements such as resistors, capacitors, inductors, constant phase elements, and diffusion elements as EIS parameters. Table 2.5 shows the EIS parameters for a typical EIS system.

$$I(t) = |I_0| \sin(\omega t + \varphi) \quad (2.25)$$

$$Z(\varphi) = E(t)/I(t) \quad (2.26)$$

Table 2.5: Circuit elements for modelling EIS data

EIS element	Circuit	Formular
Resistor (R)		$Z_R = R$
Capacitor (c)		$Z_c = 1/j\omega C = -j/\omega C$
Inductor (L)		$Z_L = -j\omega L$
Constant Phase Element (CPE)		$Z_{CPE} = 1/(j\omega)^\beta Q$
Warburg Diffusion (W)		$Z_w = \frac{\sigma\sqrt{2}}{(j\omega)^{1/2}}$

2.9.1 Nyquist plot

The Nyquist plot of electrochemical systems represents the imaginary part of an impedance ($-Z_{im}$) as a function of the real part (Z_{Re}) of an impedance (Figure 2.6). In general, the Nyquist plot is described by a semicircle at high frequencies, a non-vertical line or another semicircle at an intermediate frequency, and a nearly vertical line at low frequencies.

Nyquist plot fitting with an equivalent circuit extracts the possible EIS elements (Table 2.5) or EIS parameters (Mei et al., 2018). The resistors are essential elements that describe Faradaic charge transfer reactions across interfacial layers (Bard et al., 1980; Orazem & Tribollet, 2011). As one of the elements, the capacitance describes the non-faradaic charge accumulated at the interface (Bard et al., 1980; Orazem & Tribollet, 2011). The inductors as one of the EIS elements often need to be included in EIS models due to metallic contacts or leads being too close to one another (Bard et al., 1980; Orazem & Tribollet, 2011).

Heterogeneity at the electrodes' surface amounts to non-ideal capacitance in the double-layer, usually at the solid/electrolyte interface (Orazem & Tribollet, 2011). Consequently, CPEs as an EIS element are customarily employed instead of pure capacitors to model this kind of interfacial layer (Bard et al., 1980; Orazem & Tribollet, 2011). Accordingly, diffusion of roaming charges within metal oxide electrodes and solution is an essential factor in EIS data analysis. There is also an impedance of diffusion (Z_w) called Warburg diffusion (Bisquert, 2000; Bisquert & Fabregat-Santiago, 2010).

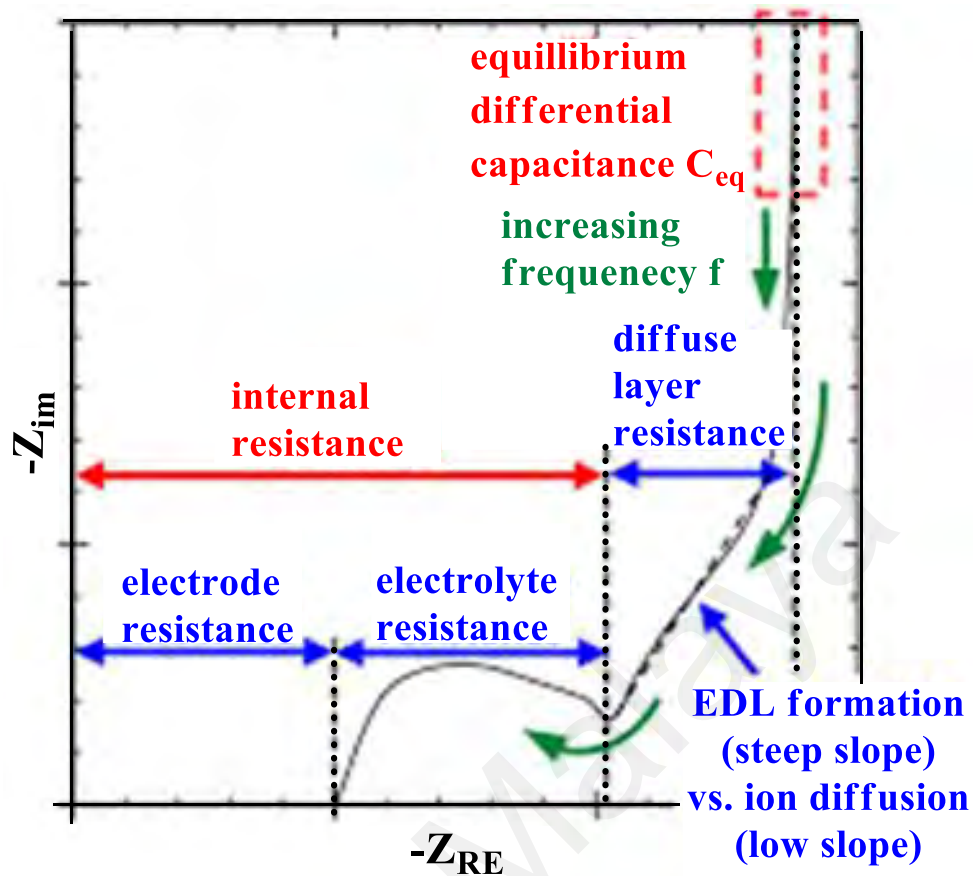


Figure 2.6: General representation of the Nyquist plot (Mei et al., 2018), Copyright (2018)

American chemical society. EDL = electrochemical double layer.

CHAPTER 3: METHODOLOGY

3.1 Softwares, Instruments, Equipment, Fixtures, Gases, Chemicals and Ionic Liquids

This study's software is a licensed version of Gaussian 09, COSMOthermX thermodynamic suite, Turbo-Molex suite, EC-lab, Topspin, Chemdraw, and NOVA 2.1.4 installed on Acer Computer Intel Core i5/2.53 GHz processor.

The equipment used for this study for electrochemical or spectroscopic data acquisition includes Potentiostat (model PGSTAT302N) and Biologic. For the spectroscopic data acquisition, the instruments are GC/MS (Schimadzu QP 2010/RTX5ms column), NMR (Bruker Avance III 400 HD), FESEM (FEI Quanta 400 machine), HRTEM (JEOL JEM-3010), XPS Thermo Scientific ESCA Lab 250Xi, and TPDRO 1100, Raman (Renishaw), UV/Vis spectrophotometer (PerkinElmer-Lambda 35) and XRD (Bruker D8 advance instrument). Along with this equipment, the instruments include a vacuum oven (Mettler VO500), Hot water circulator (Model HC-10), Hotplate wisestire (MSH 20D), Branson 2800 sonicator, Digital balance (AG204 Metler Toledo), Vacuum pump rocker 300, Refrigerator (TOSHIBA GR-R72MD), Water bath with thermomix UB heater and Frigomix U-1 cooler.

The fixtures used in this study are electrodes (Glassy carbon micro-electrode BASi, 3 mm, Platinum macro-electrode BASi, Ag/AgCl reference electrode BASi, 5.7 mm), Polishing kit (BASi PK-4) (Base Plates: heavy glass plates, Substrates: Fine grit pad, brown texmet/alumina pad, and nylon/diamond pad) and Polishing suspensions (2 ml of 15 μm coarse diamond polish, 2 ml of 3 μm fine diamond polish, 2 ml of 1 μm fine diamond polish and 7 ml of 0.05 alumina polish).

The gases used for this study are ultra-pure 99.999 % purity level, and they include; Ultra-high pure CO₂, Ultra-high pure O₂ (99.999 %), Ultra-high pure Ar (99.999 %), and Ultra-high pure N₂ (99.999 %). Feasibility study on the gas storage is done in the

department, ensuring no leakage could unforeseen contamination. A feasibility study on the gases confirms that the valve does not discharge more than the set point volumetric flowrate.

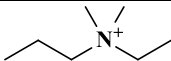
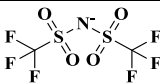
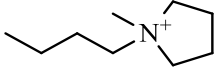
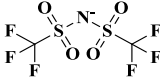
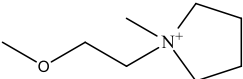
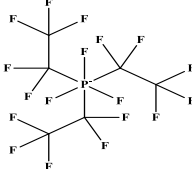
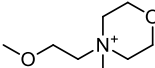
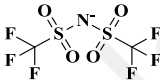
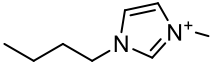
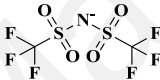
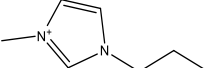
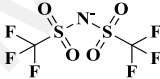
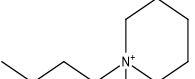
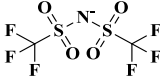
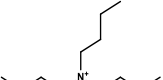
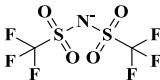

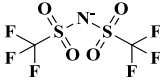
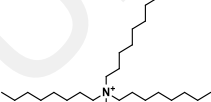
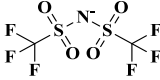
Chemicals used for this study include; Potassium superoxide (Sigma Aldrich, > 99.9 %), $\text{FeCl}_3 \cdot 6\text{H}_2\text{O}$ (R&M Chemicals > 98 wt. %) and $\text{FeCl}_2 \cdot 4\text{H}_2\text{O}$ (Merck Millipore > 98 wt. %), Multiwall carbon nanotube (US Research Nanomaterials, Inc. Houston Texas, > 95 %), Dimethyl sulfoxide (Fisher scientific 99.98 %), Alkylating agent such as ethyl iodide (Fisher Scientific; $\text{C}_2\text{H}_5\text{I}$ > 98 %) Deionized water (pH ~ 7), Ammonia (NH_3 aq.), Diethanolamine (> 99 % pure), dichloromethane (> 99 % pure), and chlorobenzene (> 99 % pure), Tetraethyl orthosilicate (Merck Millipore > 98 % pure), and Ruthenium chloride hexahydrate (Merck Millipore > 98 % pure). Potassium superoxide (KO_2), HCl, acetone, ethanol and diethanolamine were obtained from Merck Millipore. The Ionic liquids (ILs) used for this study was synthesis grade, and their molecular formulae and weight, CAS number, pH, and melting point are shown in Table 3.1, while their structure is present and Table 3.2.

Table 3.1: Specifications of the ionic liquids (ILs) *.

Ionic liquid abbreviation	Mt. pt. (°C)	pH	Formula	CAS Number
[EDMPAmm ⁺][TFSI ⁻]	-11	-	$\text{C}_9\text{H}_{18}\text{F}_6\text{N}_2\text{O}_4\text{S}_2$	258273-77-7
[BMPyr ⁺][TFSI ⁻]	-18	8-9	$\text{C}_{11}\text{H}_{20}\text{N}_4$	223437-11-4
[MOEMPyrr ⁺][PFTP ⁻]	-	-	$\text{C}_{14}\text{H}_{18}\text{F}_{18}\text{NOP}$	1195983-48-2
[MOEMMor ⁺][TFSI ⁻]	-	-	$\text{C}_{10}\text{H}_{18}\text{F}_6\text{N}_2\text{O}_6\text{S}_2$	796039-07-1
[BMIm ⁺][TFSI ⁻]	2	7	$\text{C}_{10}\text{H}_{15}\text{F}_6\text{N}_3\text{O}_4\text{S}_2$	174899-83-3
[PMIm ⁺][TFSI ⁻]	-20	5-6	$\text{C}_9\text{H}_{13}\text{F}_6\text{N}_3\text{O}_4\text{S}_2$	216299-72-8
[BMPip ⁺][TFSI ⁻]	-	6-7	$\text{C}_{12}\text{H}_{22}\text{F}_3\text{N}_2\text{O}_4\text{S}_2$	623580-02-9
[TBMA ⁺][TFSI ⁻]	<RT	-	$\text{C}_{15}\text{H}_{30}\text{F}_6\text{N}_2\text{O}_4\text{S}_2$	405514-94-5
[BMAmm ⁺][TFSI ⁻]	17	-	$\text{C}_9\text{H}_{18}\text{F}_6\text{N}_2\text{O}_4\text{S}_2$	258273-75-5
[MTOA ⁺][TFSI ⁻]	<RT	-	$\text{C}_{27}\text{H}_{54}\text{F}_6\text{N}_2\text{O}_4\text{S}_2$	375395-33-8

*Specifications are obtained from Sigma Aldrich and Merck datasheet for the individual ILs. Mt.pt. = melting point, CAS = chemical abstract service. The ILs have < 1% moisture content from the Karl Fischer titration.

Table 3.2: Structure of ions in the ILs comprising of cation and anion ends

S/N	Cation	Anion
1	 Ethyl-dimethyl-propylammonium	 bis(trifluoromethylsulfonyl)imide
2	 1-Butyl-1-methyl pyrrolidinium	 bis(trifluoromethylsulfonyl)imide
3	 1-(2-Methoxyethyl)-1-methylpyrrolidinium	 tris(pentafluoroethyl)trifluorophosphate
4	 N-Methoxyethyl-N-methyl morpholinium	 bis(trifluoromethylsulfonyl)imide
5	 1-Butyl-3-methylimidazolium	 bis(trifluoromethylsulfonyl)imide
6	 1-Propyl-3-methylimidazolium	 bis(trifluoromethylsulfonyl)imide
7	 1-Butyl-1-Methylpiperidinium	 bis(trifluoromethylsulfonyl)imide
8	 Tributylmethylammonium	 bis(trifluoromethylsulfonyl)imide
9	 Butyltrimethylammonium	 bis(trifluoromethylsulfonyl)imide
10	 Methyltrioctylammonium	 bis(trifluoromethylsulfonyl)imide

3.2 Project Flow Diagram

The research strictly followed the steps elucidated in the Figure 3.1, to achieve all the stated objectives. The flow diagram spans three work packages such as, W-1, W-2 and W-3. The W-1 involved theoretical calculations, W-2 involved the development of nanofluid and generation of $O_2^{\bullet-}$, and W-3 involve $O_2^{\bullet-}$ long-term stability and utilization

for CO_2 , CH_2Cl_2 and $\text{C}_6\text{H}_5\text{Cl}$ conversion. The decision involving yes (Y)/no (N) informed whether to proceed with the experiment/computational calculations or repeat the task repeatedly until the appropriate result is achieved. The detailed description of each work package of the research flow diagram is in section 3.3 and 3.4.

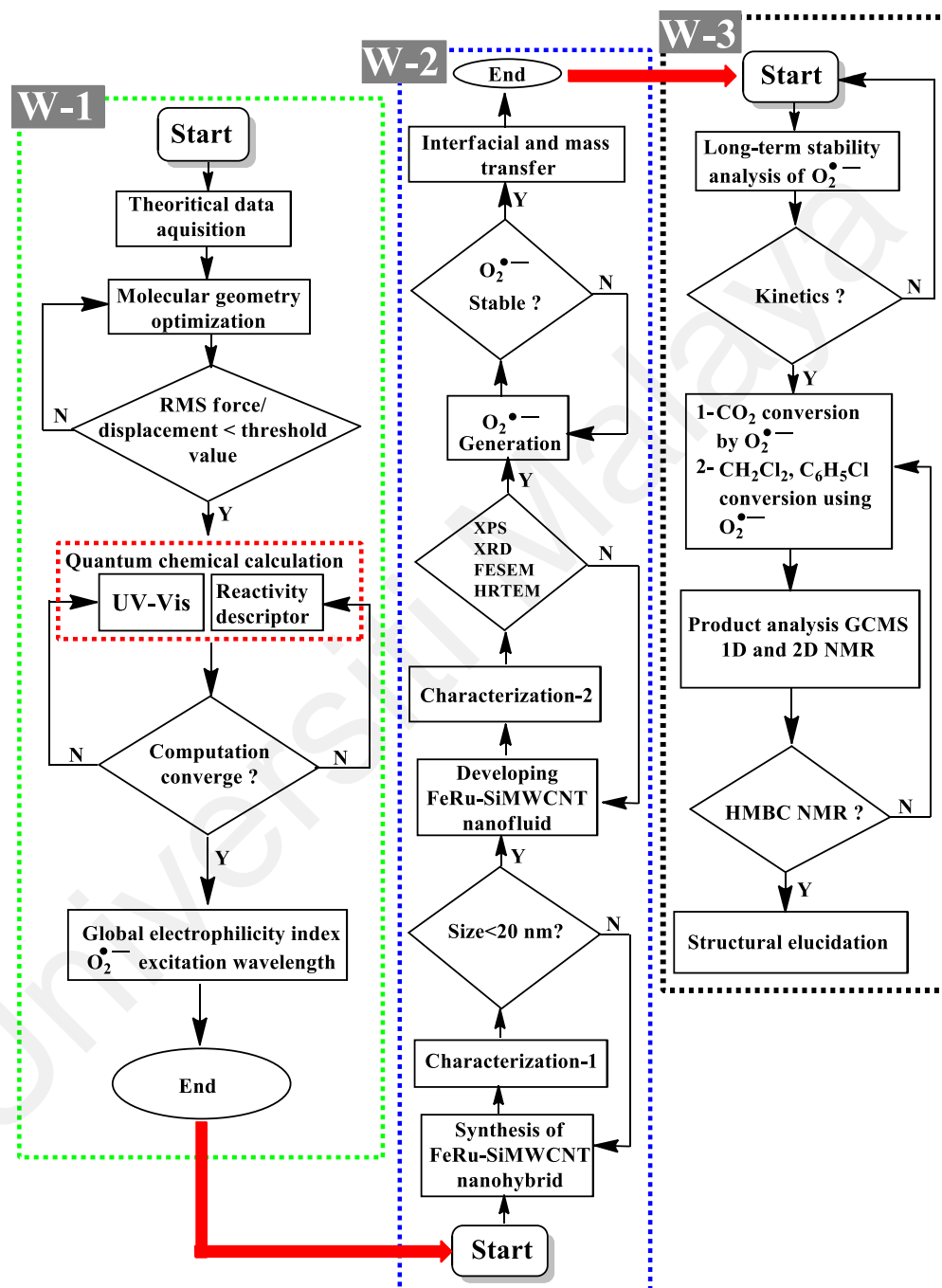


Figure 3.1: General process flow diagram of the research.

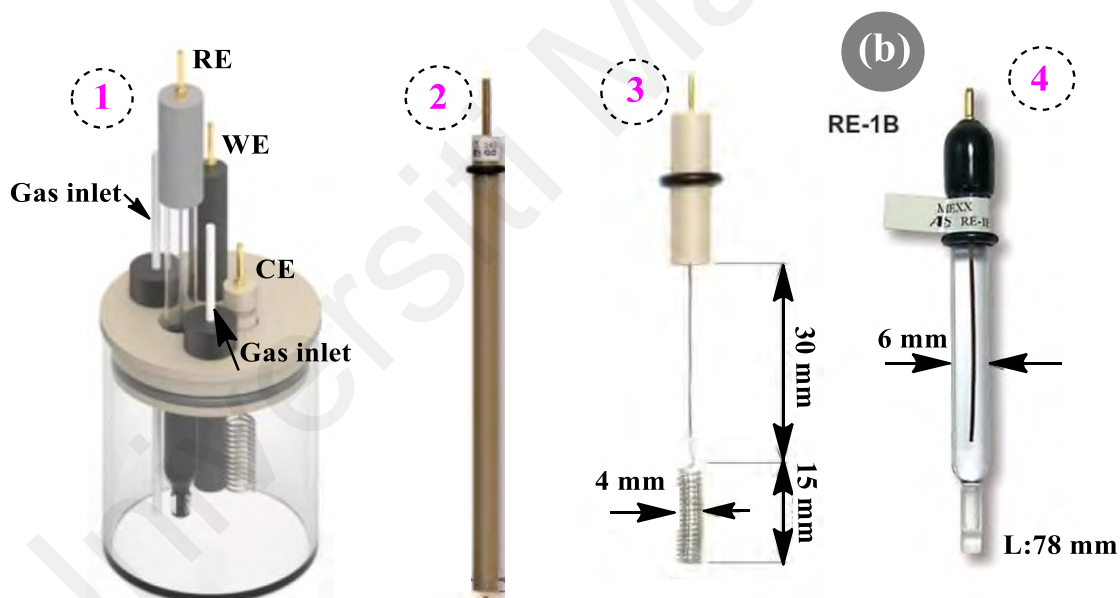
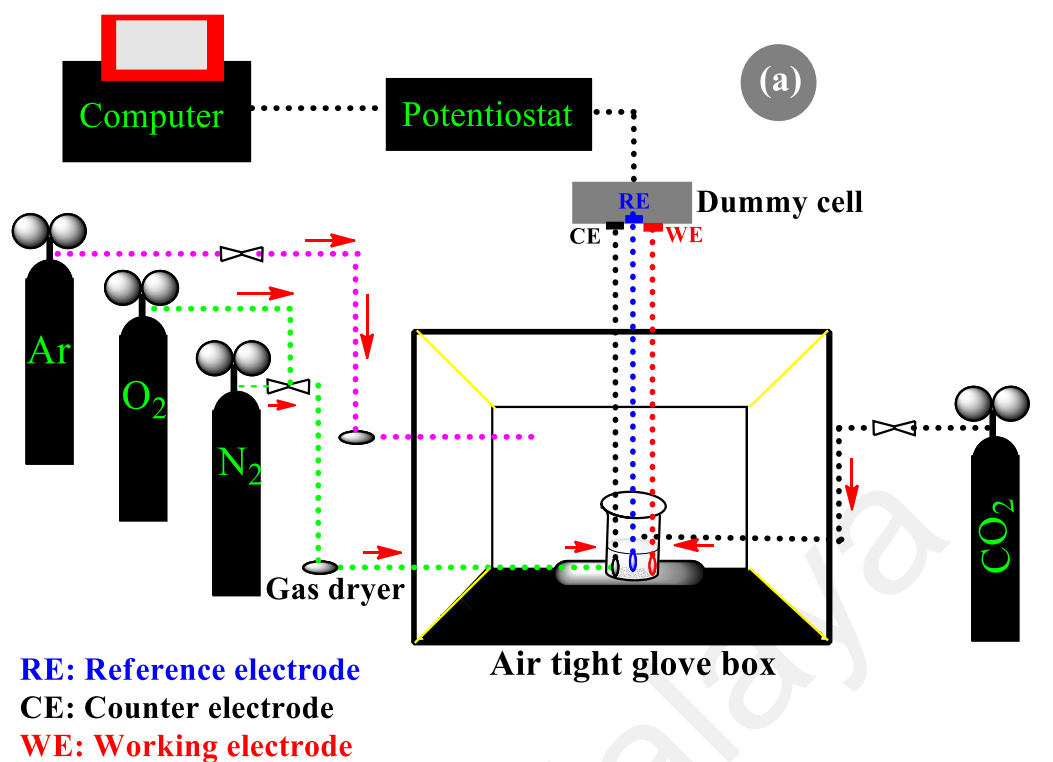


Figure 3.2: (a) Schematic of the experimental set-up, (b) Illustration of the apparatus used to conduct electrochemical investigations: (1) Electrochemical cell, (2) GC-microelectrode, (3) Counter electrode, and (4) Ag/AgCl reference electrode.

3.3 Computational Calculations

3.3.1 Molecular geometry optimization

Gaussian 09 and Turbomole platform conducted computational geometry optimization of molecules. Considering Gaussian 09, the structure of water-free superoxide ion ($[\text{O}_2(\text{H}_2\text{O})_n]^{\bullet-}$, $n=0$) were optimized in vacuum using Gaussian 09 software at DFT level of theory and 3-21G basis set (Frisch et al., 2009; Gaussian 09, 2009), without additional symmetry constraints. The 3-21G basis set handle the three-dimensional periodic boundary conditions. Similarly, the optimized molecular structure of ILs in Table 3.1, CO_2 , chemicals such as CH_2Cl_2 , $\text{C}_6\text{H}_5\text{Cl}$ according to the level of theory. The optimization achieved convergence criterion where maximum force/displacement or RMS force/displacement are less than threshold values. Consequently, the optimized geometries have their potential energy surface at their local minimum. This optimization strategy preceded all the data acquisition by the Gaussian 09 software.

Similarly, Turbomole software optimized the molecular geometries of the ILs, $\text{O}_2^{\bullet-}$, O_2 and CO_2 using def-SV (P) basis set for all atoms at the Hartree-Fock (HF) (Steffen et al., 2010). This optimization is significant for building COSMO-file before estimating sigma profiles on COSMOthermX19 using a conductor-like screening model for real solvent (COSMO-RS) method. The COSMO-file contain all the back end source information on all the quantum chemical and thermodynamic signature for a molecule in question. Therefore, COSMO-RS on the latest COSMOthermX19 software extracts the sigma profile data for a particular molecule in question.

3.3.2 Calculating the chemical reactivity descriptor

Gaussian 09 software can estimate the quantum chemical reactivity descriptor of optimized molecular geometries. The chemical reactivity using a descriptor such as the global electrophilicity indices (ω) can describe the reaction involving $\text{O}_2^{\bullet-}$ and CO_2 or

chlorinated substance (CH₂Cl₂, C₆H₅Cl) in ILs. The global electrophilicity index (ω) provide information about non-covalent interaction in O₂^{•-}/IL/CO₂ multicomponent system. Also, the (ω) depends on quantum chemical energetics of molecules estimated from the energy of their highest occupied molecular orbital (HOMO) and lowest unoccupied molecular orbital (LUMO). Therefore, Gaussian 09 (Frisch et al., 2009; Gaussian 09, 2009), which is a quantum chemical suite, coupled with Gauss View (Dennington, Keith, & Millam, 2009), estimated the global electrophilicity indices of all the ILs listed in Table 3.1, O₂^{•-}, O₂, CO₂ and chlorinated substance (CH₂Cl₂, C₆H₅Cl) with the aid of Eq 3.1, 3.2 and 3.3 (Jupp et al., 2018; Wu et al., 2017). Energy of HOMO (E_H) and LUMO (E_L) for each of the ILs in Table 3.1, O₂, CO₂, O₂^{•-} and chlorinated substance (CH₂Cl₂, C₆H₅Cl) were evaluated from their respective frontier molecular orbitals approximations based on PM6 optimized geometry in vacuum. Additionally, based on DFT level of theory (Parr, 1982), B3LYP exchange-correlation functional (Becke, 1996), and 6-314 basis set, the cutout plane of C₂O₆²⁻, a product of CO₂ reaction with O₂^{•-} in IL, was built and optimized likewise the method used for ILs, CO₂ and O₂^{•-}. Frequency analysis was done at the same theory level to enable computation of the theoretical FTIR of C₂O₆²⁻.

$$\eta = \frac{1}{2}(E_{\text{LUMO}} - E_{\text{HOMO}}) \quad (3.1)$$

$$\mu = \frac{1}{2}(E_{\text{HOMO}} + E_{\text{LUMO}}) \quad (3.2)$$

$$\omega = \frac{\mu^2}{2\eta} \quad (3.3)$$

Where η = Chemical hardness (eV), μ = Global electronic chemical potential (eV), and ω = Electrophilicity index (eV).

3.3.3 Theoretical UV-Vis analysis for $O_2^{\bullet-}$

The time-dependent density functional theory (TD-DFT) single-point calculations using Gaussian 09 software (Carsten, 2019; Runge & Gross, 1984) on the optimized geometry of $[O_2(H_2O)_n]^{\bullet-}$, $n=0$ determined the maximum excitation wavelength (λ_{max}) of $O_2^{\bullet-}$ upon UV-Vis irradiation. Moreover, the ability of the TD-DFT level of theory to accurately estimate the excitation wavelength of the $[O_2(H_2O)_n]^{\bullet-}$, $n=0$, upon UV-Vis irradiation, was investigated by varying the basis set such as double-zeta (Aug-cc-PVDZ), triple-zeta (Aug-cc-PVTZ), and quadruple-zeta (Aug-cc-PVQZ). In the single point TD-DFT calculations, the B3LYP exchange-correlation functional of the optimized geometry of $[O_2(H_2O)_n]^{\bullet-}$, $n=0$ was used (Becke, 1996).

3.3.4 COSMO-RS based calculations

COSMOthermX19 was used to analyze the intrinsic non-covalent interaction of all the ILs listed in Table 3.1, $O_2^{\bullet-}$, O_2 and CO_2 from their COSMO files. The COSMO-RS method was based on BP-TZVP-C30-1401-CTD parameterization (Eckert & Klamt, 2013). The IL-anion such as $[TFSI^-]$ anion was available in the COSMOthermX19 database. Hence, only the COSMO-files of all the IL cations listed in Table 3.1, $[PFTP^+]$ IL-anion, $O_2^{\bullet-}$, O_2 and CO_2 were generated at DFT (Parr, 1982) levels, using Beck-Perdew-86 functional (Perdew, 1986) considering zeta-valence potential basis set (def-TZVP) for all atoms (Schäfer, Huber, & Ahlrichs, 1994), and a resolution of identity standard (RI) approximation. Afterwards, job functional for molecular mixture in COSMOthermX19 software extracted the interaction among $O_2^{\bullet-}$, ILs and CO_2 with their σ -profiles as additional output.

3.4 Experimental Procedures

3.4.1 Development of Fe/Ru-SiMWCNT nanohybrid

Initially, the Fe/Ru-SiMWCNT nanohybrid were prepared at ambient conditions. In a typical procedure, the co-precipitation technique prepared the Fe₃O₄ phase by mixing aqueous ferric hexahydrate (FeCl₃·6H₂O) and ferrous tetrahydrate (FeCl₂·4H₂O) using a 3:2 ratio in a round bottom flask (Umar et al., 2020). The precipitation occurred immediately, promoting a colour change to dark-black, the magnetite's characteristic colour. The mixture was stirred vigorously for 1.0 h, at a stirring rate of 400 rpm, using a magnetic stirrer and adding a stoichiometric amount of aqueous ammonia slowly to adjust the mixture's pH to ~10 (Nkurikiyimfura et al., 2020). Therefore, at 2.0 wt. % tetraethyl orthosilicate TEOS (2 wt. %) was added into the mixture and kept constant for 24 h with the same stirring rate (Xiong et al., 2019). Therefore, 0.5 wt. % aqueous RuCl₃·6H₂O was added drop-wise into the mixture, and the pH adjusted to ~10 (Assadi, Gutierrez Moreno, & Fronzi, 2020). The mixture was also stirred at 600 rpm for 12 h at room temperature. Covalent functionalization of oxidized MWCNT with the nanoparticles proceeds using a similar method described previously (Chinh et al., 2019). Afterwards, washing of the indexed Fe/Ru-SiMWCNT produced preceded with deionized H₂O/HCl solution, acetone, vacuum dried at 50 °C/890 mbar overnight, and calcined in static N₂ environment at 400, 500 and 600 °C for 3.0 h.

3.4.2 Characterization of Fe/Ru-SiMWCNT nanohybrid

3.4.2.1 Physiochemical surface and textural properties

Fe/Ru-SiMWCNT nanohybrid's microstructure was characterized by a field emission scanning electron microscope (FESEM) on model FEI-Quanta 400 machine equipped with energy dispersive spectrometer (EDS). The EDS could detect and confirm elemental composition on different morphological regions of Fe/Ru-SiMWCNT nanohybrid. High-resolution transmission electron microscopy (HRTEM, JEOL JEM-

3010) was employed to understand the Fe/Ru-SiMWCNT nanohybrid's atomic arrangement electrocatalyst enablement. Also, Powder X-ray diffraction (XRD) studies were conducted using the Bruker D8 advanced instrument. The diffraction peaks were obtained at ambient temperature with Cu K α radiation using ~ 0.1541 nm X-ray wavelength (λ) for the Bragg's angle range of 10 to 80°/0.03° step size and 1 s/step acquisition time at 40 kV and 40 mA. The XRD spectra's degree of crystallinity of Fe/Ru-SiMWCNT nanohybrid was estimated using Eq 3.4 (Ahvenainen, Kontro, & Svedström, 2016; Jiang et al., 2016). Crystalline peaks were isolated. The amorphous peaks were also isolated using high-score plus software by uploading the XRD ASCII files. Accordingly, the degree of crystallinity (DOC) using Eq 3.4 was determined. The Fe/Ru-SiMWCNT-IL nanohybrid was also analyzed using X-ray photoelectron spectroscopy (XPS) with 200 W Al-K α radiations on a Thermo Scientific ESCA Lab 250Xi. During the process, the analytical chamber's base pressure containing the sample was maintained at ~ 3 mbar, while the C1s line from adventitious carbon at ~ 284.8 eV was used for energy reference.

$$\text{DOC} = \frac{A_{cp}}{A_{CA}} \times 100 \quad (3.4)$$

Where A_{cp} = Area of crystalline peaks (cm^2), A_{CA} = Area of crystalline and amorphous peak (cm^2).

3.4.2.2 CO₂ temperature-programmed desorption

The CO₂ temperature-programmed desorption (CO₂-TPD) analysis conducted on TPDRO 1100 series setup equipped with a thermal conductive detector confirmed CO₂ sorption capacity of Fe/Ru-SiMWCNT nanohybrid (Weng et al., 2019). Approximately 60 mg of Fe/Ru-SiMWCNT nanohybrid sample was first pretreated through heating up to 120 °C at a rate of 10 °C/min in N₂ (20 mL/min) for 1.0 h to make it water-free. This procedure preceded by switching the sample to 100 % CO₂ and heating commences at 10 °C/min over 40 °C to 600 °C temperature range.

3.4.2.3 Temperature programmed oxidation

The temperature-programmed oxidation (TPO) analysis conducted on the TPDR0 1100 series equipped with a thermal conductivity detector detected and confirmed the O₂ sorption capacity of Fe/Ru-SiMWCNT nanohybrid. Overall, TPO could be used for investigating the O₂ sorption capacity of nanomaterials (Minh et al., 1997). Pretreatment of ~ 60 mg Fe/Ru-SiMWCNT nanohybrid sample was done in N₂ (20 mL/min) environment, heated to 120 °C at 10 °C/min ramped for 1.0 h holding time to remove any available surface or coordinated water. The Fe/Ru-SiMWCNT nanohybrid sample was allowed to cool before ~ 5 % Oxygen in Helium (5 % O₂/He; V/V, 20 mL/min) mixture was introduced to the samples. Measurements were carried out in an O₂ environment at a programmed temperature ramp in the range of 40-600 °C at a rate of 10 °C/min.

3.4.3 Synthesis of Fe/Ru-SiMWCNT-ILs nanofluid

Preparation of Fe/Ru-SiMWCNT-IL was done using a similar procedure reported previously (Mondragón et al., 2018). As-synthesized Fe/Ru-SiMWCNT was added to the ILs listed in Table 3.1 at 30 g/L mass concentration of stock and homogenized by Branson 2800 ultrasound sonicator at ambient condition and sonic speed of 30 mph for 3.0 h 100% duty cycle.

3.4.4 Characterization of Fe/Ru-SiMWCNT-IL nanofluid

3.4.4.1 Drying

The Fe/Ru-SiMWCNT-IL nanofluid were dried in the vacuum oven at 50 °C overnight. This drying practice usually removes any volatile analytes impurities and moisture to evade their negative consequence on O₂^{•-} generation (Doblinger et al., 2019; Pozo-Gonzalo et al., 2016). This scenario is because volatile analytes could be electrochemically active. Therefore, it is a general recommendation that ILs or their analogues and nanofluid should be dried first to eliminate moisture traces.

3.4.4.2 The electrochemical potential window of the ILs and Fe/Ru-SiMWCNT-IL nanofluid

The electrochemical potential window (ECW) measurements for the ILs were achieved by sterilizing them first with N₂ as a pretreatment measure that removes any possible electroactive impurities such as H₂O or its analogues. This pretreatment measure is in accord with the regular practice of cleaning ILs, which many researchers have shown (Doblinger et al., 2019; Maan Hayyan, Hashim, & AlNashef, 2016). The media were first pretreated to eliminate H₂O through drying at 50 °C, 890 bars for 6.0 h to measure the ECWs of ILs and Fe/Ru-SiMWCNT-IL.

In furtherance, saturating the ILs or Fe/Ru-SiMWCNT-IL with N₂ is an additional means of pretreatment that could implicate displacement of any trace amount of H₂O therein. This because H₂O has a lower kinetic diameter (KD) of ~ 0.330 nm compared to N₂ (KD= ~ 0.346 nm) (Wang et al., 2015). The KD estimates the molecule's electron conformer's size as an influencer of scattering (Wang et al., 2015). The KD is different from the ordinary atomic or molecular diameter of a gaseous molecule. However, since KD of N₂ > KD of H₂O, N₂ can lead to scattering events in the vicinity of H₂O. When applied to IL or Fe/Ru-SiMWCNT-IL media, it can be a cleaning means to eliminate H₂O impurity and ensure a sterile media. Eliminating H₂O is vital because the presence of H₂O was reported to narrow ECWs of ILs (O'Mahony et al., 2008; Schröder et al., 2000). In another report, the presence of H₂O in ILs can cause undesired cathodic reactions whose consequence extends to reduce current efficiency of cathodic processes in the ILs; this can minimize the electrochemical cell efficiency (Randström et al., 2007).

Therefore, cyclic voltammetry (CV) performed on auto-lab Potentiostat detected the ECWs of H₂O-free ILs listed in Table 3.1 and their Fe/Ru-SiMWCNT-IL nanofluid counterparts using a three-electrode cell system at a cut-off current density of 0.5 mA/cm² (Hayyan et al., 2011). The cell consisted of a Pt wire (5.7 cm, BASi Inc.) counter

electrode, a glassy carbon (GC) (OD: 6 mm, ID: 3mm) working electrode, and a saturated Ag/AgCl (6 mm) reference electrode. Before each CV measurement, the glove box containing the cell with Fe/Ru-SiMWCNT-IL nanofluid or ILs was deaerated with Ar gas for 20 min and then, followed by priming with N₂ for 30 min. The CV sweep rate of 9 mv s⁻¹ was maintained during each measurement at a constant ambient temperature.

3.4.4.3 Electrochemical impedance spectroscopy study

The electrochemical impedance spectroscopy (EIS) measurement was conducted using Bio-logic Potentiostat (Sp-300) in ILs and Fe/Ru-SiMWCNT/IL media sinus amplitude of 10 mV, 50 kHz to 50 mHz frequency. The EIS measurements were performed on freshly prepared samples enclosed in an aluminium Faraday cage at the suitable potential for O₂^{•-} generation and utilization. The working electrode was polished using alumina slurry (BASi) on micro cloth (Buehler) and sonicated in distilled water before each experiment. This procedure ensured that impurities on the working electrode's surface are absent. The EIS quality was evaluated using the total harmonic distortion (THD) at the glassy carbon (GC); OD: 6 mm, ID: 3 mm, Platinum (Pt); 5.7 cm, BAS Inc., and Ag/AgCl; 6 mm. The THD quantifies the distortion of the input and output signals using Eq 3.5 (Mao, Krewer, & Hanke-Rauschenbach, 2010).

$$\text{THD}_v = 100 \times \frac{\sqrt{\sum_{h=2}^N V_{h,rms}^2}}{V_{1,rms}} \quad (3.5)$$

Where $V_{1,RMS}$ = RMS voltage (V) and $V_{h,RMS}$ = Harmonic voltage (V).

The EIS measurements were conducted in O₂-saturated IL and O₂/CO₂-saturated-IL under potentiostatic mode using the same set of electrodes at 10.0 mV amplitude to investigate the mechanistic radical driven catalysis. The EIS measurements were also conducted in O₂-saturated IL and O₂/(CH₂Cl₂, C₆H₅Cl)-saturated-IL. Overall, the EIS measurements data were fitted and analyzed using the latest EC-Lab 11.31 software.

3.4.5 Cleaning of the electrochemical cell

Cleaning the electrochemical cell is essential to avoid cross contaminations. The electrochemical cell shown in Figure 3.2 contains grooved channels for retrofitting the electrodes. After every experiment, the electrochemical cell was cleaned with isopropanol and dried. This procedure prevented any contamination from reaching the IL from the chemical remnant from previous experiments. The Ag/AgCl reference electrode was also cleaned and placed into a KCl solution. The Pt counter electrode was wiped and placed in an airtight container. The GC working electrode was cleaned after every round of experiments. The clips were cleaned by removing the corroded layer on the connection part to prevent potential overload during the experiments.

3.4.5.1 Polishing of electrodes

The macro-electrode was polished using alumina solution (BASi) and sonicated in distilled water for 10 min before each experiment. This procedure was done to ensure no impurities on the working electrode (WE) surface precipitated during the previous investigation. However, ultra-micro-electrode were polished using a diamond solution (BASi) and then sonicated in distilled water for 10 min.

3.4.6 Electrochemical active surface area

According to the literature's recommendation, the electrochemical active surface area (ECSA) is necessary for ensuring the repeatability of electrochemical measurements (Voiry et al., 2018). A differential capacitance method was adopted to estimate the ECSA. Typically, the ECSA falls at different scan rates ranging from 9, 36, 64, 81, 100, and 144 mV/s in the narrow potential of -0.35 V to -0.8 mV range vs Ag/AgCl showing no faradaic current response. The differential capacitance equals the double layer capacitance (C_{DL}), and it was estimated by plotting $\Delta j (j_a - j_c)$ determined at a suitable non-faradaic potential vs Ag/AgCl against the scan rates. Where j_a and j_c are the anodic and cathodic current density, respectively. The electrochemical active surface area

(ECSA) was obtained from Eq. 3.6 using this capacitance in a different environment (Liu et al., 2019).

$$\text{ECSA} = \frac{C_{DL}}{C_{DLref}} \times \text{geometric area} \quad (3.6)$$

Where C_{DLref} describes the capacitance of an ideal flat surface of the electrode. It is known that the C_{DLref} value is influenced by an oxidation layer on an electrode's surface (Trasatti & Petrii, 1991). Sterilization with N_2 effectively ensured no faradaic current emanating from redox species. Therefore, to estimate the C_{DLref} , CV of N_2 -saturated media was measured in the non-faradaic region. The geometry area of the GC electrode is $\sim 0.0720 \text{ cm}^2$ (computed using πr^2 , where $r = 3\text{mm}$).

3.4.7 The electrochemical generation of $O_2^{\bullet-}$ in ILs and nanofluid

Cyclic voltammetry (CV) analysis was used to detect electrochemically generated $O_2^{\bullet-}$ in the dried ILs and Fe/Ru-SiMWCNT-IL nanofluid. In a typical procedure, $\sim 1\text{-}2 \text{ mL}$ of the ILs (listed in Table 3.1) and their corresponding Fe/Ru-SiMWCNT-IL nanofluid was poured in 10 mL capacity electrochemical cell containing three-electrodes; Pt wire (5.7 cm , BASi Inc.) counter electrode, a glassy carbon (GC) (OD: 6 mm , ID: 3mm) working electrode, and a saturated Ag/AgCl (6 mm) reference electrode clamped in a jacketed gas box. Accordingly, gas lines for O_2 , N_2 , and CO_2 were connected into the cell; the electrodes were clipped to an auto-lab Potentiostat, computer-controlled using the latest Nova 2.1 software for data acquisition. The cell containing the IL and Fe/Ru-SiMWCNT-IL nanofluid with the three electrodes were sparged with N_2 to remove any electrochemically active impurities. Then calibration of the gas (O_2 0.5 L/min) saturation in ILs and nanofluid was done and 10 min was found to be suitable. In this calibration, the current stability was monitored for stripping the scan rate from 144 , 100 , 81 , 64 , 36 , and 9 mV/s using the different sparging time 2 min , 5 min , and 10 min . Accordingly, cyclic voltammetry (CV) measurements were conducted while stripping the

scan rate from 144, 100, 81, 64, 36, and 9 mV/s. The CV measurements were performed in 0.1 to -1.5 vs Ag/AgCl potential range. Different CV waves were recorded in the ILs or Fe/Ru-SiMWCNT-IL nanofluid media. Therefore, the interfacial phenomena in the media were evaluated in terms of charge transfer coefficient (α). The mass transfer phenomena were also estimated in terms of solubility (C_o) and diffusion coefficient (D_o) of O_2 in the media when chronoamperometry (CA) analysis at $\sim 11 \mu\text{m} \pm 2 \mu\text{m}$ dia using Eqs 3.7, 3.8, 3.9, and 3.10 similar to the previous report (Hayyan et al., 2011). Detailed definition of the parameters in Eqs 3.7, 3.8, 3.9, and 3.10 are given under the list of symbols and abbreviations.

$$i_p = (2.99 \times 10^5) \sqrt{\alpha D_o \nu A^2 C_o^2} \quad (3.7)$$

$$E_p = E^{0'} - \frac{RT}{\alpha F} \left[0.782 + \ln \left(\frac{D_o^{1/2}}{k^0} \right) + \ln \left(\frac{\alpha F}{RT} \right)^{1/2} \right] \quad (3.8)$$

$$i_{ss} = 4nFD_oC_o r_o \quad (3.9)$$

$$EE (\%) = \frac{E^0}{V_{cell}} \times FE (\%) \quad (3.10)$$

3.4.8 Long-term stability of $O_2^{\bullet-}$ in ILs and nanofluid

Since CV analysis could only assess short-lived $O_2^{\bullet-}$, the long-term stability of $O_2^{\bullet-}$ in ILs, and Fe/Ru-SiMWCNT-IL nanofluid was investigated through the chemical generation of $O_2^{\bullet-}$ using the method reported previously (Hayyan et al., 2012). In a typical procedure, spectroscopic grade dimethyl sulfoxide (DMSO) was dried overnight in a vacuum oven at $60 \text{ }^\circ\text{C}$ and 890 bar vacuum pressure. Besides, potassium superoxide (KO_2) was stored in an air-tight vial containing molecular sieves. The molecular sieves were also poured into the dried DMSO ensuring the absence of any possible reaction with H_2O , and the mixture was stirred for at least 1.0 h in the fume cupboard. The lack of any moisture was evident by no brownish coloration. Afterwards, KO_2 was introduced into the DMSO, and the $O_2^{\bullet-}$ present therein was calibrated on the UV-Vis device. The long-term stability of $O_2^{\bullet-}$ in the ILs and their corresponding nanohybrids was monitored, and

the pH of the media was always set to be $\sim \geq 7.0$. A ~ 0.05 g blank solution of the IL in ~ 5 mL DMSO was prepared after making ~ 0.05 g stock of IL in a closed vial. This is followed by preparing a fresh solution of KO_2 in DMSO. Calibration of the UV-vis experiment was determined using different concentration points. The UV-vis for the blank and 5 mL of KO_2 in DMSO/ ~ 0.05 g IL solution was measured immediately and differently. The UV-vis scan was repeated for 180 min steps of 30 min. Therefore, the plot of $\text{O}_2^{\bullet-}$ peak height was done against the time. If the height of the peak is small, the superoxide is considered stable in that IL and vice versa. Considering that, the reaction follows a pseudo-first-order pattern (Eq 3.11, 3.12), and then the reaction rate constant was determined by plotting the natural log of the peak height versus the time (s). The negative index of the straight-line slope was taken to be k .

Kinetics of the $\text{O}_2^{\bullet-}$ long-term stability in these media was evaluated, and the reaction rate constant was determined by plotting the natural logarithmic peak height against the time in seconds. The straight-line slope's negative index was taken as a constant rate k . The reaction might follow pseudo-first-order kinetics or second-order kinetics. Therefore, the rate constants serve as an indication for the stability of $\text{O}_2^{\bullet-}$ in the studied ILs. A low rate constant denotes that the $\text{O}_2^{\bullet-}$ is chemically stable in the studied ILs. For pseudo-first-order kinetics (Eq 3.12), it is assumed that the added IL into DMSO is in large excess compared to $\text{O}_2^{\bullet-}$ and the effect of IL concentration is negligible (Hayyan et al., 2014; Hayyan et al., 2017).



$$r = k[\text{O}_2^{\bullet-}]^1 \quad (3.12)$$

Where k is the rate constant, $[\text{A}]$ is the concentration of cation, and Z is either the new product or the ion-pairing of $\text{O}_2^{\bullet-}$ cation. The pseudo-second-order kinetics assumed that either the involvement of cation or the order of $\text{O}_2^{\bullet-}$ is two (Eq 3.13, and Eq 3.14) (Hayyan et al., 2014; Hayyan et al., 2017).

$$r = k[O_2^{\bullet-}]^2 \quad (3.13)$$

$$r = k[A]^1[O_2^{\bullet-}]^1 \quad (3.14)$$

3.4.9 Electrolysis of CO₂ in ILs or Fe/Ru-SiMWCNT-IL nanofluid containing O₂^{•-}

Initially, the conversion of CO₂ by O₂^{•-} was detected using cyclic voltammetry, similar to previously reported experiments (AlNashef et al., 2002). The cell button from the Potentiostat was switched on, and the electrochemical cell was filled with N₂ to keep it inert. The cell containing the ILs/nanohybrid with the three well-polished electrodes; Pt wire (5.7 cm, BASi Inc.) counter electrode, a glassy carbon (GC) (OD: 6 mm, ID: 3mm) working electrode, and a saturated Ag/AgCl (6 mm) reference electrode were sparged with N₂ to expel any remnant of electrochemically active specie that could interfere with the general electrochemical process in the system.

To generate C₂O₆²⁻, calibration of the gas (O₂ 0.5 L/min and 5.95 m³/min CO₂) saturation in ILs and nanofluid was done and 10 min was found to be suitable. After this period, the current generated is stable enough to acquire the CO₂ conversion data. Therefore, O₂ 0.5 L/min and CO₂ (5.95 m³/min), gases were sparged simultaneously for 10 min to saturate the ILs or Fe/Ru-SiMWCNT-IL nanofluid. After cycles of CV experiment, ~ 5 mL stock of post CO₂, O₂^{•-} reaction product was instantly sampled, and ~ 0.1 mL was fetched and immediately analyzed on the attenuated total reflection Bruker optics Fourier transform infrared spectroscopy (ATR-FTIR) IFS 66V/S instrument. The FTIR machine can achieve up to 100 spectra per second, and this is a powerful visible, near IR, mid-IR, far-IR vacuum spectrometer. This measurement implies that it can record several IR spectra from 450 cm⁻¹ to 4000 cm⁻¹ range of molecular vibrational modes within a second, fast enough for identifying unstable species such as the C₂O₆²⁻.

In typical electrolysis, 2.0 mL of Fe/Ru-SiMWCNT/[MOEMPyrr⁺][PFTP⁻] nanofluid containing 1.0 mM diethanolamine was electrolyzed under different ranges of

potentiostat control ($E = -1.366$ to -1.564 V vs Ag/AgCl) under continuous sparging of 0.01 L/min O_2 and 0.01 m³/min CO_2 for 1.0 h. The electrolysis experiments were measured at 60 °C in a three-electrode electrolyzer, comprising of a working electrode (GC), a counter electrode (Pt) and a reference electrode (Ag/AgCl) similar to the previous method (Feroci et al., 2011; Feroci et al., 2007). At the end of the electrolysis, the current flow was switched off, and ~ 2 mM of ethyl iodide was added to the catholyte and stirred for another 3 h. The reaction mixture was separated using diethyl ether in (3×10 mL) for extraction. Before collecting the fraction, the reaction product was dissolved in diethyl ether (3×10 mL) and gradually transferred into the column. The solvent was removed under reduced pressure, and the products were separated by the column chromatography n-hexane/ethyl acetate, 8/2 mobile phase. The stationary phase was a silica sandwich between ~ 0.5 cm layers of fine sand. Diethyl ether was gradually added to enhance the separation and change in polarity down the column. The spectroscopic data from product elucidation are similar to those reported previously in the literature (Feroci et al., 2011; Feroci et al., 2007; Inesi, Mucciante, & Rossi, 1998).

3.4.10 Electrolysis of C_6H_5Cl and CH_2Cl_2 in IL containing $O_2^{\bullet-}$

In this section, [BMPip⁺][TFSI⁻] was selected and used throughout the dechlorination process because only ~ 8.2 % $O_2^{\bullet-}$ therein after 3 h. The rate of $O_2^{\bullet-}$ decay validated the capability of [BMPip⁺][TFSI⁻] for \leq a 3.0 h electrolysis reaction time interval. Before the electrolysis of C_6H_5Cl and CH_2Cl_2 by $O_2^{\bullet-}$ in [BMPip⁺][TFSI⁻], the pre-requisites analysis that was considered include; 1) estimating the electrochemical active surface area (ECSA), and 2) determination of normalized exchange current density in ($i_{0,ECSA}$) and 3) confirming the generation of $O_2^{\bullet-}$ in [BMPip⁺][TFSI⁻] containing C_6H_5Cl or CH_2Cl_2 , These pre-requisites are essential for monitoring the $O_2^{\bullet-}$ mediated electrolysis in [BMPip⁺][TFSI⁻].

In the first pre-requisite involving the determination of ECSA, a procedure already described in section 3.4.6 was adopted. The narrow potential range between -0.35 V to -0.8 mV range vs. Ag/AgCl was used during the CV cycles. This range is characterized to be non-faradaic typical with the differential capacitance method for estimating the ECSA using Eq. 4.

The second pre-requisite involving the determination of $i_{0,ECSA}$, the kinetics of $O_2^{\bullet-}$ driven dechlorination of C_6H_5Cl and CH_2Cl_2 was formulated using current-potential response and Tafel analysis. The current potential response was determined using linear sweep voltammograms (LSVs) similar to the literature method (Li et al., 2014), using biologic Potentiostat SP-300. The current-potential response in O_2 saturated $[BMPip^+][TFSI^-]$ and O_2 saturated $[BMPip^+][TFSI^-]$ containing 2.5 mM CH_2Cl_2 or C_6H_5Cl was measured at 9.0 mV/s scan rate. Also, the Tafel analysis was constructed from the natural logarithm of current density (j /mA/cm²) and activation overpotential (η). The η is the difference between the applied potential (E_p) and the thermodynamic potential (E_p^0) for any reaction of interest (Appel & Helm, 2014). Therefore, from the Tafel analysis, the exchange current density (i_0) that determines the kinetics of $O_2^{\bullet-}$ driven dechlorination of C_6H_5Cl or CH_2Cl_2 was estimated using Butler-Volmer (Eq 3.15) (Bard et al., 1980). Considering the cathodic process for C_6H_5Cl and CH_2Cl_2 dechlorination by $O_2^{\bullet-}$, the activation overpotential (η) is negative. Therefore, the term $\exp\left(-\frac{(1-\alpha)nF}{RT}\eta\right)$ in Eq 3.15 is insignificant then Eq. 3.16 is obtained. By taking the natural log of both sides of Eq 3.16, Eq. 3.17 is obtained and (i_0) can be determined from the intercept to the plot of $\ln(i)$ versus η . The i_0 represents the inherent rate of electron transfer between the analyte and the electrode and is similar to the constant chemical reaction rate (Voiry et al., 2018). Since the surface of the electrode affects the magnitude of i_0 , normalization of the i_0 using the ECSA (Voiry et al., 2018), was done to provide a most discriminating measure for the intrinsic rate of electron transfer during $O_2^{\bullet-}$

generation and utilization. The normalized exchange current density ($i_{0,ECSA}$) was further correlated with temperature for 25, 35 and 45 °C in O₂ saturated [BMPip⁺][TFSI⁻] and [BMPip⁺][TFSI⁻] containing 2.5 mM CH₂Cl₂ or C₆H₅Cl.

$$i = i_0 \left[\exp\left(\frac{-\alpha n F}{RT} \eta\right) - \exp\left(\frac{(1-\alpha)n F}{RT} \eta\right) \right] \quad (3.15)$$

$$i = i_0 \exp\left(\frac{-\alpha n F}{RT} \eta\right) \quad (3.16)$$

$$\ln(i) = \ln(i_0) - \left(\frac{\alpha n F}{RT}\right) \eta \quad (3.17)$$

Where; i_0 = Exchange current density (mA/cm²), α = Charge transfer coefficient (dimensionless), η = Activation overpotential applied to the working electrode (V). Other parameters have been defined accordingly in the list of abbreviation and symbols.

In the third pre-requisite involving the generation of O₂^{•-}, the [BMPip⁺][TFSI⁻] was first purified by drying under a vacuum for ~6 h at a temperature of ~50 °C. The essence of this drying procedure is to expel any available moisture as that could tilt O₂^{•-} to disproportionate. Therefore, ~2 mL of [BMPip⁺][TFSI⁻] was poured into a 10 mL capacity electrochemical cell while holding glassy carbon (GC; OD: 6 mm, ID: 3 mm), Pt (5.7 cm, BAS Inc.), and Ag/AgCl (6 mm) electrodes clamped in a sterile jacketed glove box. The electrodes were connected to an Autolab Potentiostat Model PGSTAT302N. Latest Nova 2.1 controlled the electrochemical process. Accordingly, N₂ was directed to the electrochemical cell through a gas channel where the inert environment was ensured. At this stage cyclic voltammetry (CV) technique as reported previously (Johnson, Nidy, & Merritt, 1978; Merritt & Sawyer, 1970; Ryding et al., 2015) was used for the possibility of O₂^{•-} generation in [BMPip⁺][TFSI⁻] and [BMPip⁺][TFSI⁻] containing CH₂Cl₂ or C₆H₅Cl at -1.3 to 0.1 V vs. Ag/AgCl potential range. The current density of the CV wave of O₂ saturated [BMPip⁺][TFSI⁻] and O₂ saturated [BMPip⁺][TFSI⁻] containing CH₂Cl₂ or C₆H₅Cl were normalized relative to the electrochemical active surface area (ECSA) of the GC electrode (Voiry et al., 2018). The charge transfer coefficient (α) governing the

process, solubility (C_o), and diffusion coefficient (D_o) of O_2 into [BMPip⁺][TFSI⁻] were calculated using Eqs 5-7 (Hayyan et al., 2011). This estimation was after performing chronoamperometry (CA) analysis using $\sim 11 \pm 2 \mu\text{m}$ (dia.) carbon fibre ultra-microelectrode in O_2 saturated [BMPip⁺][TFSI⁻] and O_2 saturated [BMPip⁺][TFSI⁻] containing CH_2Cl_2 or C_6H_5Cl .

Following these pre-requisites, the electrolysis experiments were carried in a membraneless electrochemical glass cell comprising a Pt wire (5.7 cm, BASi Inc.) counter electrode, a glassy carbon (GC) (OD: 6 mm, ID: 3mm) working electrode, and a saturated Ag/AgCl (6 mm) reference electrode). An Autolab PGSTAT302N (Metrohm) Potentiostat was used to control the electrochemical experiment throughout the electrolysis time interval. The test media were prepared from 2 mL [BMPip⁺][TFSI⁻], and 2 mL [BMPip⁺][TFSI⁻] containing 2.5 mM of CH_2Cl_2 or C_6H_5Cl . The 2 mL [BMPip⁺][TFSI⁻] containing 2.5 mM of CH_2Cl_2 or 2.5 mM C_6H_5C were first homogenized to a single phase for 10 minutes each using a magnetic stirrer at 200 rpm. In typical electrolysis, the homogenized media was kept constant at 35 °C and under a continuous flow of 0.01 L/min O_2 at a constant potential of -2 V. The electrolysis time was varied for 0.5, 1.0, 1.5, and 2 h.

3.4.11 Gas chromatography-mass spectroscopy analysis

The work-up product was collected and analyzed on a Shimadzu QP2010 ultra-gas chromatograph-mass spectroscopy (GCMS) equipped with a TCD detector, autosampler, and RTX5ms column (0.25 μm : 30m: 0.25 mm). The instrument is equipped with a TCD detector, an autosampler, and a 30 m and 0.25 mm diameter RTX5ms column as the stationary phase. The helium carrier gas was set at a 50 mL/min flow rate, the inlet and detector temperatures were both set at 150 °C, and the split-less injection option was employed. The mass range of the mass spectrometer was set to 500 (m/z) maximum. In a typical experiment, the oven temperature was initially held at 35 °C for 5 min, and the

temperature was then ramped at 10 °C/min to a maximum oven temperature of 100 °C. At linear speeds of 48.8 cm/s with purge flow, the injection pressure was 150 kPa, column flow was 1.8 mL/min. The conversion of reactant and selectivity to desired product selectivity was estimated using equation Eqs 3.18 to 3.21, respectively (Gadewar, Malone, & Doherty, 2000; Guo et al., 2020; Ni et al., 2018; Periana et al., 1994). Considering that the product obtained is not available in the market, this study could not procure their standards so that a standard external procedure be employed in estimating their yield. However, within this constraint's auspices, the peak area integration method was used to estimate the % yield of each of the products obtained using Eq 3.20. This measurement is because the product's peak area is usually proportional to the amount of the compound produced.

After each electrolysis round, the reaction mixture's workup was dissolved in diethyl ether (3×10 mL) and gradually transferred into the column. The column chromatography n-hexane/ethyl acetate; 8/2 mobile phase. The stationary phase was a silica sandwich between ~0.5 cm layers of fine sand. Diethyl ether was gradually added to enhance the separation and change in polarity down the column. The work-up product (raffinate) was collected and analyzed on a Shimadzu QP2010 ultra-gas chromatograph-mass spectroscopy (GCMS) equipped with a TCD detector, autosampler, and RTX5ms column (0.25 µm: 30m: 0.25 mm). Eqs 3.18 and 3.19 (Gadewar et al., 2000; Guo et al., 2020; Ni et al., 2018; Periana et al., 1994), were used to estimate the activities of the dechlorination process in terms of conversion and selectivity. Also, the degree of dechlorination of CH₂Cl₂ and C₆H₅Cl was determined using Eq. 3.21 (Yoshinaga et al., 2004). To further elucidate the significant dechlorination product's molecular structure, ¹H NMR measurement was conducted on a Bruker Avance III 600 MHz spectrometer in deuterated chloroform (CDCl₃) as NMR solvent, containing tetramethylsilane (TMS) as an internal standard. The NMR spectra were analyzed using Topspin 4.0.7 software.

$$\text{Conversion (X)} = \frac{(m(\text{reactant})_{\text{in}} - m(\text{reactant})_{\text{out}})}{m(\text{reactant})_{\text{in}}} \times 100 \quad (3.18)$$

$$\text{Selectivity (S)} = \frac{mC_p}{\sum mC_p} \times 100 \quad (3.19)$$

$$\text{Yield (Y; \%)} = \frac{\text{Area of Product}}{\text{Total Area of Products}} \times 100 \quad (3.20)$$

$$\text{Degree of dechlorination (DD \%)} = \frac{m}{m+l} \times 100 \quad (3.21)$$

Where; m = dechlorinated product, l = unreacted starting chlorinated material.

The GCMS analysis conditions are presented in Table 3.3.

Table 3.3: GC-MS specifications and analytical condition

Analytical Instruments	
Shimadzu GC/MS	GCMS mass spectrum QP-2010 Controller IG-50 Auto-Injector Autosampler Power supply module Schimadzu GCMS solution software
Column	Size: 30 m (Length) x 0.25 mm (i.d) x 0.25 (Film thickness) Description: RTX5ms Agilent
Analytical Conditions	
Injection Temperature	250 °C
Interface Temperature	280 °C
Carrier Gas	Helium
Column flow	0.6 ml/min
Carrier flow	10 ml/min
Injection Volume	1 µl

3.4.12 Nuclear magnetic resonance analysis

To elucidate the molecular structure of the significant product, ^1H , ^{13}C , correlation spectroscopy (2D $^1\text{H}/^1\text{H}$ COSY NMR), heteronuclear single quantum coherence spectroscopy (2D $^1\text{H}/^{13}\text{C}$ HSQC) analysis and heteronuclear multiple bond correlation spectroscopy (HMBC) was done. A Bruker Avance III 600 MHz spectrometer and deuterated chloroform (CD_3Cl_3) NMR solvent with tetramethylsilane (TMS) as an internal standard was used. Topspin 4.0.7 software was used to analyze the NMR results. The NMR Data acquisition was performed with shimming using automated ^1H shimming routines, followed by manual fine-tuning on Bruker Avance III 600 MHz spectrometer.

The CDCl_3 was degassed by three freeze-pump-thaw cycles and vacuum-transferred before used. The ^1H NMR spectra were recorded with chemical shifts reported relative to the residual CDCl_3 and TMS. During the data acquisition, ^1H selective excitation and ^1H non-selective spectra acquisition were mixed by interchanging between them every 30 seconds for ^1H selective excitation and every 60 seconds for ^1H non-selective spectra. The product identification was determined using a standard 30° pulse sequence. This was with a 1.64 s acquisition time and 1 s relaxation delay time using a single transient. Data processing was performed using the latest Topspin 4.0.7 software. The analysis condition during the NMR analysis is presented in Table 3.4.

Table 3.4: NMR specifications and analytical condition

Analytical Instruments	
Bruker Avance NMR	Magnetic field ~ 600 MHz Controller IG-50 Pulse technique Power supply module Topspin software
NMR Tube	Size: 30 m (Length) x 0.25 mm (i.d) x 0.25 (Film thickness)
Analytical Conditions	
Injection Temperature	25 °C
Carrier Gas	Nitrogen
Number of scans	16
Pulse	15µsec
Power level	15 (W)
Size of FID	65536

i.d = internal diameter, Hz = short form of hertz

3.5 Safety and Heuristics

The electrochemical conversion of CO_2 , $\text{C}_6\text{H}_5\text{Cl}$, and CH_2Cl_2 mediated by $\text{O}_2^{\bullet-}$ in ILs and ILs-based nanofluid media has not been conducted previously in the department. Therefore, as compliance with occupational health and safety, hazard identification, risk assessment, and control (HIRAC) analysis was conducted first. The HIRAC is essential for anyone who intended to use the laboratory or interact with the laboratory facilities and materials. Details of the procedure can be obtained from the University of Malaya faculty of engineering safety and health committee. Moreover, the material safety data sheet (MSDS) of chemicals and precursors were studied before commencing all experiments.

For instance, C_6H_5Cl and CH_2Cl_2 model chlorinated organics have an acceptable daily intake (ADI) of ~ 0.004 and $0-0.5$ mg/kg body respectively (Council, 2012; Guengerich et al., 1991; Gut et al., 1996). In terms of toxicity levels, ~ 150 mg/Kg body weight for CH_2Cl_2 was reported to cause fatal incidence (Goullé et al., 1999). The CH_2Cl_2 is classified as a group B-2 carcinogen by several regulatory agencies on occupational safety and health administration (Schlosser et al., 2015). The CH_2Cl_2 standard route of exposure is through inhalation and dermal route, thereby getting metabolized by the body to carbon monoxide and potentially leading to carbon monoxide poisoning (N. Yang, 2014). C_6H_5Cl is also ranked 6th among environmental pollutants on similar accounts, mostly when the ADI limit is exceeded (Mohan et al., 2017). Therefore the fatal possibilities of C_6H_5Cl or CH_2Cl_2 were taken care of during measurement or utilization. Generally, the use of latex gloves at single-use, avoidance of direct inhalation or skin contact of all chemicals was ensured during the experiment. The CO_2/O_2 gas cylinders were kept outside the laboratory and controlled by a gas meter with a control valve. Base on this strict adherence to the occupational safety Act of 1994 (OSHA 1994), the experiment proceeded without any casualty.

CHAPTER 4: RESULTS AND DISCUSSION

4.1 Computational Analysis

Quantum chemical computational analysis was conducted using the ILs listed in Table 3.1, CO₂, or O₂^{•-}. The essence of this quantum chemical calculation is to properly evaluate their reactivity or stability attributes and possibility. This analysis offers the assurance of ranking the reactivity or stability of molecules in a multiphase system. The computational analysis outcome as described in section 4.1.1 and 4.1.2, would allow proper interpretation of the radically driven catalysis of CO₂ or chlorinated compounds (Aparicio et al., 2011).

4.1.1 COSMO-RS analysis

The conductor-like screening model for the real solvent (COSMO-RS) is a quantum chemistry-based equilibrium thermodynamics technique to predict chemical potentials in liquid (Klamt, 2003). The COSMO-RS has a combination of quantum chemical calculations incorporated with an efficient statistical thermodynamic protocol for estimating quantitative interactions of molecular surfaces (Klamt, Eckert, & Arlt, 2010). In the context of this study, COSMO-RS implementation was used to assess realistic interaction between O₂^{•-}, O₂, CO₂, and the corresponding ILs listed in Table 3.1. According to Eckert & Klamt (2013), these interactions usually map a molecule's surface electron distribution to their potentials and quantifiable by σ -profiles. Also, the σ -profiles are classified into three sections based on charge density; σ ; e/nm². The first section is the hydrogen bond donor (HBD) region occurring at $\sigma \leq -0.820$ e/nm². The HBD section signifies a molecule's capacity to donate hydrogen from functionalities such as O-H, N-H, and S-H (Sessler et al., 2017). The second section is the non-polarity section and occurs at -0.820 e/nm² < σ < $+0.820$ e/nm². In this case, it refers to molecules in which their electrons are distributed symmetrically and do not possess an abundance of charges at their opposite sides, and the charges cancel out each other (Galamba et al., 2019). The

third section is the hydrogen bond acceptor (HBA) region occurring at $\sigma \geq 0.820 \text{ e/nm}^2$. The hydrogen bonding acceptor plays a crucial role in establishing a hydrogen bond with an HBD, which features many catalytic chemicals and biological processes (Pike, Hutchinson, & Hunter, 2017; Schwöbel et al., 2009).

Proceeding from the background given above, Figure 4.1 (a-k) shows the σ -profiles of CO_2 , O_2 , $\text{O}_2^{\bullet-}$ and the ILs listed in Table 3.1. Some of the ILs have HBD, while others do not. The appearance of the HBDs on the ILs (Table 3.1) is due to C-H linkage contribution since they do not contain O-H, N-H, and S-H linkages. The C-H could donate a proton but depend on the preference of any available HBD such as N-H, S-H, and O-H (Sessler et al., 2017; Yoon et al., 2008). According to Figure 4.1 (a-j), the ILs with cations such as $[\text{EDMPAmm}^+]$, $[\text{BMPyrr}^+]$, $[\text{MOEMPyrr}^+]$, $[\text{MOEMMor}^+]$, $[\text{BMIm}^+]$, $[\text{BMPip}^+]$, $[\text{TBMamm}^+]$, $[\text{BMamm}^+]$, $[\text{MTOA}^+]$ have HBDs that may arise from contribution of C-H bond since they do not have N-H, S-H and O-H functionality. However, the HBD end on $[\text{EDMPAmm}^+]$ cation occurred at $\sigma = -0.897 \text{ e/nm}^2$. Accordingly, HBD of $[\text{BMPyrr}^+]$, $[\text{MOEMMor}^+]$, $[\text{BMIm}^+]$, $[\text{BMPip}^+]$, $[\text{TBMamm}^+]$, and $[\text{BMamm}^+]$ centered at $\sigma = -0.881 \text{ e/nm}^2$, $\sigma = -1.112 \text{ e/nm}^2$, $\sigma = -0.864 \text{ e/nm}^2$, $\sigma = -0.897 \text{ e/nm}^2$, $\sigma = -0.914 \text{ e/nm}^2$ and $\sigma = -0.894 \text{ e/nm}^2$ respectively. This study believes that these HBD ends originated from C-H but not limited to other stability issues.

Exceptionally, the IL-cation such as $[\text{PMIm}^+]$ does not have either HBD or HBA. Only three typical polar-repulsive ends centred at $\sigma = -0.757$, -0.497 and -0.001 e/nm^2 are visible on $[\text{PMIm}^+]$. Due to the presence of polar-repulsive end, the $[\text{PMIm}^+]$ potentially involve in any other form of noncovalent interaction with other moieties but hydrogen bonding. Also, IL-cations $[\text{MOEMPyrr}^+]$ and $[\text{MTOA}^+]$ do not have HBD, and this also implicated any one of the noncovalent interactions with other moieties that have hydrogen bonding likewise.

Although C-H could contribute HBD, these ILs have been reported for $O_2^{\bullet-}$ generation (Maan Hayyan, Hashim, & AlNashef, 2016). Since $O_2^{\bullet-}$ could be generated in these ILs, it confirmed that the C-H contribution might not make the ILs protic which may impede the $O_2^{\bullet-}$ generation. Consequently, they could be used as media for stable $O_2^{\bullet-}$ generation. Switzer et al., (2013) confirmed N-H moiety in Diethylmethylammonium triflate [DEMAMM⁺][TF⁻] as a proton source. As a result, this revealed the prospect of a hydrogen bond donor capacity by [DEMAMM⁺][TF⁻], which has *pka* values of 10.6 or 11 in the presence of water or aprotic solvents, respectively. Considering the N-H proton activity from the *pka* values, the generation of $O_2^{\bullet-}$ will be impeded possibly due to hydrogen abstraction as earlier mentioned in the literature (Maan Hayyan, Hashim, & AlNashef, 2016). These explanations confirmed that all the ILs presented in Figure 4.1(a-j) have their HBD not originating from N-H or O-H but likely C-H. As a result, any possible proton abstraction by $O_2^{\bullet-}$ is ruled out. However, the σ -profiles of [DEMAMM⁺][TF⁻] revealed an HBD at $\sigma = -1.070 \text{ e/nm}^2$ originating from N-H contribution, as shown in Figure 4.1k.

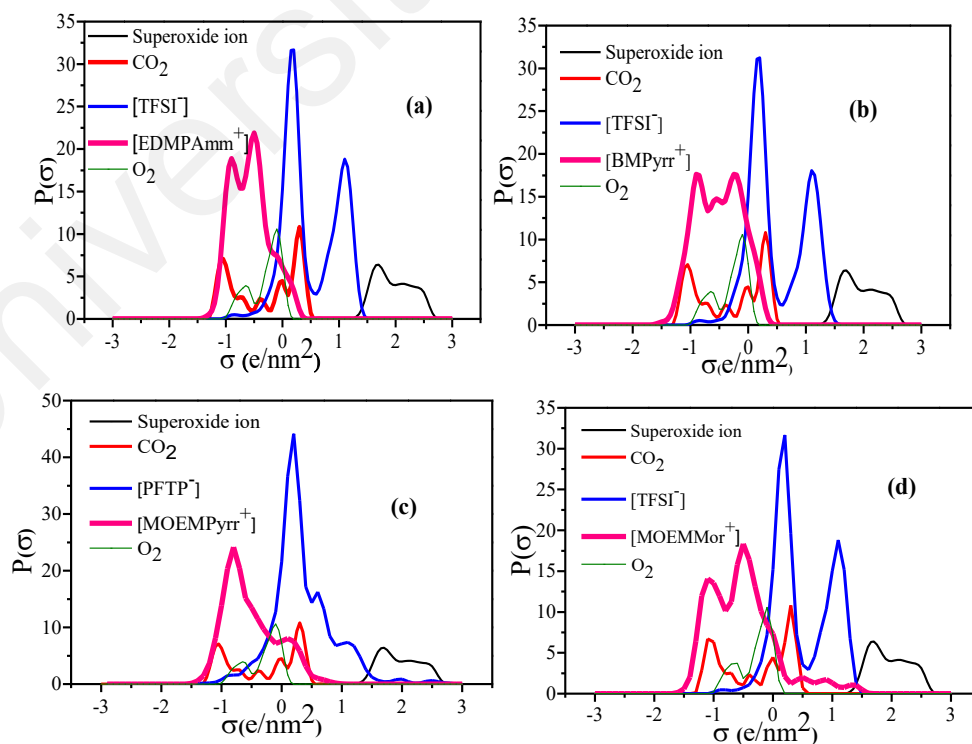
On the other hand, the [TFSI⁻] anion polar end can be observed in the HBA region where $\sigma = 0.1097 \text{ e/nm}^2$. This HBA property of [TFSI⁻] anion was suggested in this study due to its oxygen or fluorine in the molecular structure. This result is because oxygen or fluorine is highly electronegative and will have a strong affinity to a proton. Similarly, other ILs-anions [PFTP⁻] and [TF⁻] also have a polar-repulsive end because one of the σ -profile centres at $\sigma = -0.1998 \text{ e/nm}^2$.

In Figure 4.1 (a-k), the $O_2^{\bullet-}$ has two polar-attractive ends characterized mainly by HBA, which centres at $\sigma = 1.71 \text{ e/nm}^2$ and $\sigma = 2.34 \text{ e/nm}^2$. This result indicates the possibility of $O_2^{\bullet-}$ to interact with the IL-cations via available hydrogen bonding steps that likely originate from C-H. The $O_2^{\bullet-}$ interaction with [PMIm⁺] can be via any other non-covalent-interactions but hydrogen bond. Also, $O_2^{\bullet-}$ can interact with CO₂, whose

charge density is quantified at the HBD region where $\sigma = -1.10 \text{ e/nm}^2$. This observable HBD in CO_2 could be because the sp-carbon in CO_2 has a positive character which is hydrogen-like and avail interaction with $\text{O}_2^{\bullet-}$.

Moreover, the CO_2 COSMO profile whose charge density is in the HBD region at $\sigma = -0.906 \text{ e/nm}^2$ and the IL-anion $[\text{TFSI}^-]$ anion COSMO profile at the HBA region $\sigma = 1.097 \text{ e/nm}^2$, confirmed the stance. Similarly, O_2 only has its charge density centering at the nonpolar regions where $\sigma = -0.102 \text{ e/nm}^2$ and $\sigma = -0.639 \text{ e/nm}^2$. As a result, the absence of any form of non-covalent hydrogen bond interaction between O_2 and ILs was indicated, but Van der Waal interaction with the IL-cation can be possible. In summary, all the ILs presented in Figure 4.1 (a-j) do not have hydrogen bond donors coming from O-H and N-H but likely from C-H which quite challenging to go about if the carbon has a negative Mulliken charge.

The practical significance of this COSMO-RS analysis is in the ability of the IL media to capture CO_2 , O_2 . Also, it measures the ability of the $\text{O}_2^{\bullet-}$ interacting with CO_2 .



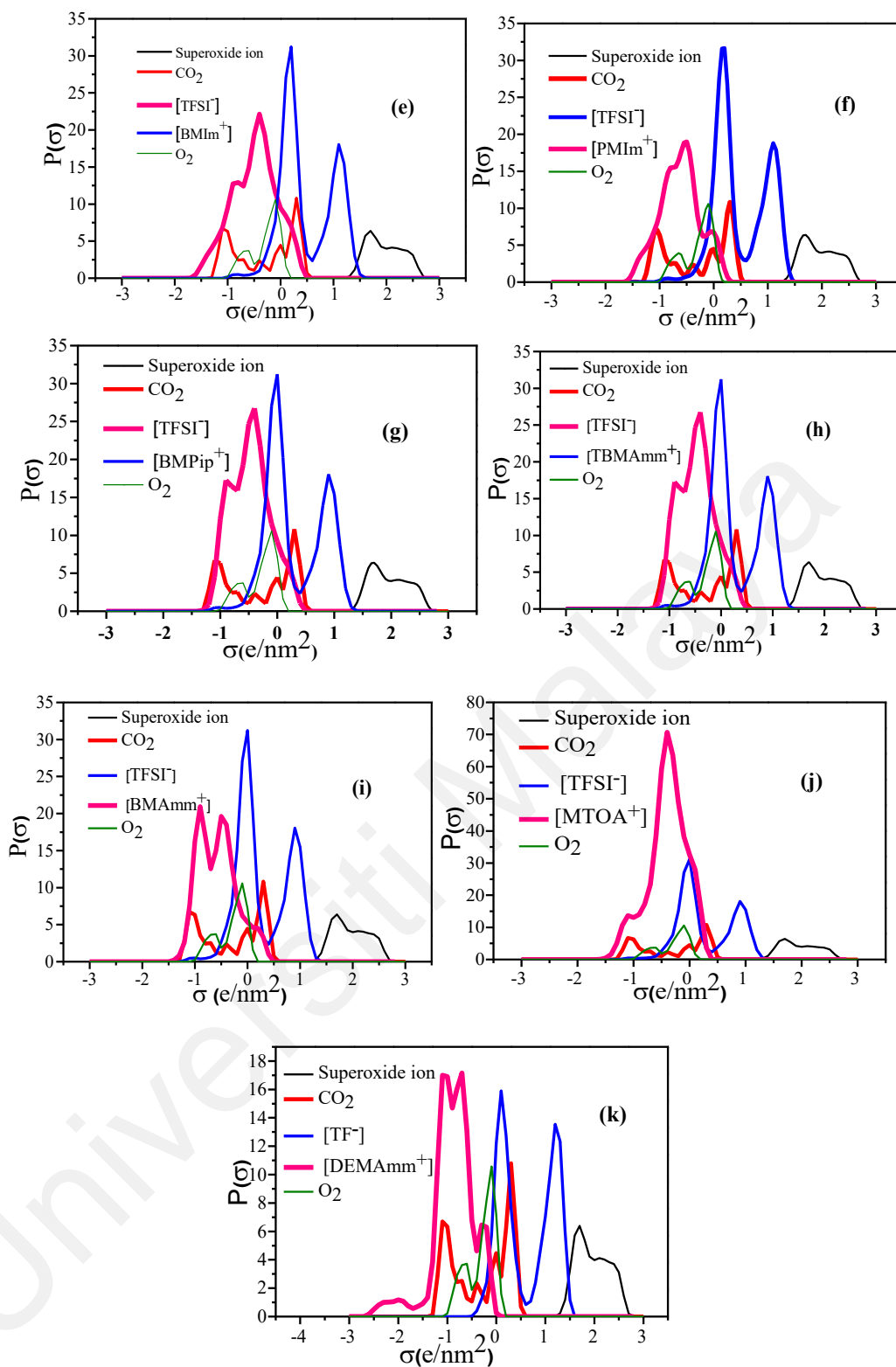


Figure 4.1: COSMO-RS profile for (a) [EDMPAmm⁺][TFSI⁻], (b) [BMPyrr⁺][TFSI⁻], (c) [MOEMPyrr⁺][PFTP⁻], (d) [MOEMMor⁺][TFSI⁻], (e) [BMIm⁺][TFSI⁻], (f) [PMIm⁺][TFSI⁻], (g) [BMPip⁺][TFSI⁻], (h) [TBMAmm⁺][TFSI⁻], (i) [BMAmm⁺][TFSI⁻], (j) [MTOAmm⁺][TFSI⁻], and (k) [DEMAmm⁺][TF⁻]. The COSMO-RS profiles ILs were compared with O₂^{•-}, CO₂ and O₂.

4.1.2 Chemical reactivity descriptor

The chemical reactivity descriptor (CRD) analysis was investigated using the global electrophilicity index (ω) to access and rank the potential reactivity or stability of the ILs listed in Table 3.1, CO₂, and O₂^{•-}. The ω -values were estimated using the frontier molecular orbital (FMO) theory of their highest occupied molecular orbital (HOMO) and lowest unoccupied molecular orbital (LUMO). FMO is one of the best approaches to describe molecules' chemical reactivity or stability (Dannenberg, 1999). The FMO of the ILs listed in Table 3.1, CO₂, and O₂^{•-} are presented in Figure A.1 (**Appendix A**) in terms of 3D renderings of their iso-surfaces for their HOMO and LUMO energy states. These energy states are colour-coded in green representing negative iso-surface, or brown for positive iso-surface. These iso-surfaces define the molecules' geometry according to popular opinion, mostly when their electron densities are rendered in colored 3D representation (Purvis, 1991; Weber et al., 1988).

The CRD for all the ILs listed in Table 3.1, CO₂, and O₂^{•-} was estimated using the method described in section 3.2.1. In this case, the global electrophilicity index (ω) was calculated using the HOMO and LUMO energies of the molecules according to Eq 3.3 (Andrew et al., 2018). The HOMO energy represents their possible ionization potential, while the LUMO energy represents their electron affinity. High HOMO energy corresponds to a more reactive molecule with an electrophile, while low LUMO energy signifies less reactive molecular reaction with nucleophiles (Fukui, 1982). The difference between HOMO and LUMO energies represent the energy gap ($E_{\text{HOMO}} - E_{\text{LUMO}} = \Delta E_g$) which dictates molecules' chemical reactivity and kinetic stability (Proft et al., 2007).

In accordance, the ω -values as shown in Table 4.1 for the ILs listed in Table 3.1 decreased in the following order; [MTOA⁺][TFSI⁻] ($\omega=147.8$ eV) > [TBMAm⁺][TFSI⁻] ($\omega=1.852$ eV) > [BMPip⁺][TFSI⁻] ($\omega=1.659$ eV) > [MOEMPyrr⁺][PFTP⁻] ($\omega=1.559$ eV) > [BMPyrr⁺][TFSI⁻] ($\omega=1.513$ eV) >

$[\text{BMAMm}^+][\text{TFSI}^-]$ ($\omega=1.192$ eV) > $[\text{BMIm}^+][\text{TFSI}^-]$ ($\omega=1.192$ eV) > $[\text{EDMPAMm}^+][\text{TFSI}^-]$ ($\omega=0.212$ eV) > $[\text{MOEMMor}^+][\text{TFSI}^-]$ ($\omega=0.188$ eV) > $[\text{PMIm}^+][\text{TFSI}^-]$ ($\omega=0.036$ eV). The ω -values for $[\text{MTOA}^+][\text{TFSI}^-]$, $[\text{TBMAMm}^+][\text{TFSI}^-]$, $[\text{BMPip}^+][\text{TFSI}^-]$, $[\text{MOEMPyrr}^+][\text{PFTP}^-]$, $[\text{BMPyrr}^+][\text{TFSI}^-]$, $[\text{BMAMm}^+][\text{TFSI}^-]$, and $[\text{BMIm}^+][\text{TFSI}^-]$ are greater than ω -values for CO_2 ($\omega=0.756$ eV). Other ILs such as $[\text{PMIm}^+][\text{TFSI}^-]$, $[\text{MOEMMor}^+][\text{TFSI}^-]$, and $[\text{EDMPAMm}^+][\text{TFSI}^-]$ have their ω -values less than that estimated for CO_2 . Since the ω -values for $\text{O}_2^{\bullet-}$ is -14.764 eV, it indicates that $\text{O}_2^{\bullet-}$ is nucleophilic. Therefore, it is expected that the ILs with ω -values less than CO_2 will potentially be less susceptible to $\text{O}_2^{\bullet-}$ than CO_2 . On the contrary, those ILs with ω -values greater than CO_2 will be more susceptible to $\text{O}_2^{\bullet-}$ than CO_2 . The ω -value is significant for building a probabilistic reaction ranking protocol between at least two substrates, and it can indicate the substrate that is likely to first interact during a chemical process (Chattaraj, Sarkar, & Roy, 2006; Padmanabhan et al., 2007). Estimating the magnitude of ω for ILs or CO_2 is necessary because $\text{O}_2^{\bullet-}$ generation and utilization could participate in a competitive chemical reaction with IL-cations before CO_2 .

For instance, evidence of $\text{C}_2\text{O}_6^{2-}$ formation has been attributed to the doubling effect of faradaic reduction peak from CO_2 conversion by $\text{O}_2^{\bullet-}$ (Maria A. Casadei, 2001; Maria et al., 1997; Casadei et al., 1996; Casadei et al., 1997; Roberts et al., 1984). On estimating the chemical reactivity of tetraethylammonium perchlorate (TEAP) as a medium, it was found that the ω -value is greater than that for CO_2 ; hence, the doubling effect of faradaic reduction peak is not tenable. The ω -value of TEAP is 3.82 eV, and this high ω -value of TEAP would likely make it attractive to be reduced by $\text{O}_2^{\bullet-}$, and subsequently inducing the doubling effect of reduction peak current. This postulation is in line with the observation during CO_2 conversion mediated by $\text{O}_2^{\bullet-}$ in 1-butyl-3-methylimidazolium Hexafluorophosphate; $[\text{BMIm}^+][\text{HFP}^-]$ (AlNashef et al., 2002). The

CO₂ reduction CV wave did not show the reduction current's doubling effect because the ω -value of [BMIm⁺][HFP⁻] is 1.728 eV. This ω -value is less than that for the supporting electrolyte (TEAP). By implication, it can be strongly suggested that the doubling effect may have originated from the electrochemical contribution from TEAP.

Table 4.1: Energetic and reactivity descriptor of ILs, CO₂ and O₂^{•-}.

Ionic Liquid Abbreviation	E _{HOMO}	E _{LUMO}	E _g	ω
[EDMPAmm ⁺][TFSI ⁻]	-11.254	-4.045	15.300	0.212
[BMPyr ⁺][TFSI ⁻]	-9.201	-3.018	6.200	1.513
[MOEMPyr ⁺][PFTP ⁻]	-9.222	-3.119	6.100	1.559
[MOEMMor ⁺][TFSI ⁻]	-9.362	-9.291	12.300	0.188
[BMIm ⁺][TFSI ⁻]	-10.248	-2.073	8.100	1.192
[PMIm ⁺][TFSI ⁻]	-8.550	-1.79	6.800	0.036
[TBMAMm ⁺][TFSI ⁻]	-14.679	-3.512	11.200	1.852
[BMAMm ⁺][TFSI ⁻]	-10.248	-2.173	8.100	1.192
[MTOAMm ⁺][TFSI ⁻]	-8.317	-8.202	0.100	147.812
[BMPip ⁺][TFSI ⁻]	-7.859	-6.926	0.900	0.100
CO ₂	-10.443	-0.534	9.900	0.759
O ₂ ^{•-}	-9.627	0.656	-9.900	-14.659

In this study's viewpoint, ILs with negative Mulliken C (sp) is recommended for O₂^{•-} utilization. The Mulliken atomic charge concept was inspired by Katayama and co-workers (2004) finding who estimated the electron distribution in organic cations that consist of ammonium, imidazolium, and pyrrolidinium moiety from ab initio molecular orbital calculations. They found that the atomic charges at the carbon atoms in trimethyl-n-hexylammonium [TMHAMm⁺] (Figure 4.2a) and 1-butyl-1-methylpyrrolidinium [BMPyr⁺] (Figure 4.2b) were made of negative charges. Their results suggested that the C (sp) atoms in these aliphatic and alicyclic cations were not attacked by nucleophilic reagents such as O₂^{•-} and OH⁻. They also found that the carbon atoms at 2-, 4-, and 5-positions in the heterocycle of 1-ethyl-3-methylimidazolium [EMIm⁺] (Figure 4.2c) and 1, 2-dimethyl-3-propylimidazolium [DMPIIm⁺] (Figure 4.2d) were made of positive charges. By ranking the possible attack of nucleophilic reagents, the 2-position carbon atom got attacked first because it has the largest positive charge. This scenario was confirmed by the nucleophilic addition reaction to various imidazolium cations,

specifically on the 2-position carbon atom (Katayama et al., 2004). Noteworthy, this concept of the study where ILs with negative C (sp) in Table 4.1 and Table A.1 (**Appendix A**) has been published (see Appendix K). Other ILs (as stated in Table 4.1) were used as control, but [BM Amm^+], [BMPip $^+$], [EDMP Amm^+] and [TBM Amm^+] were found to have negative Mulliken charges. The Mulliken atomic charges, shown in Table A.1a (**Appendix A**) indicate that all the carbon atoms in [BM Amm^+] are negative. In Table A.1 (**Appendix A**), the C (Sp 2) in the imidazole ring of [EMIm $^+$] has a +0.642 e/a.u 2 Mulliken atomic charge. Also, in Table A.1, C (Sp) in CO $_2$ has +1.083 e/a.u 2 Mulliken atomic charge. These Mulliken atomic charges are insightful to probe the molecules' chemical process capability (Fogarty et al., 2018; Griffith & Orgel, 1957). This result could rationalize why [BM Amm^+](Figure 4.2f), [EDMP Amm^+](Figure 4.2g) and [BMPip $^+$](Figure 4.2h) has a large negatively charged iso-surface while [EMIm $^+$](Figure 4.2c) has a more positive character, as shown in Figure A.1 h (**Appendix A**) and Figure 4.2.

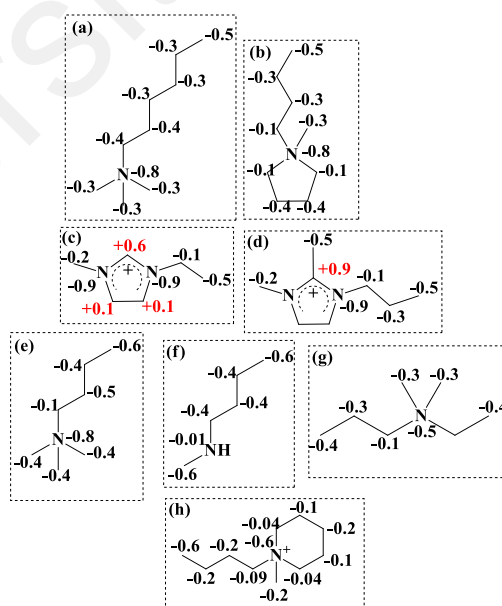


Figure 4.2: Mulliken atomic charges of carbon and nitrogen atoms in ILs; **Literature:** (a) [TMH Amm^+], (b) [BMPyr r^+], (c) [EMIm $^+$], (d) [DMPIIm $^+$] (Katayama et al., 2004a). **This study:** (e) [TBM Amm^+], (f) [BM Amm^+], (g) [EDMP Amm^+], and (h) [BMPip $^+$].

4.2 Characterization of Fe/Ru-SiMWCNT Nanohybrid, ILs and Nanohybrid-ILs Nanofluid

4.2.1 X-ray diffraction analysis of Fe/Ru-SiMWCNT nanohybrid

The crystallinity analysis was used as a screening technique to estimate and isolate the Fe/Ru-SiMWCNT nanohybrid with the highest crystalline phase. Crystallinity is an essential structural parameter in addition to composition, morphology, architecture, facet, size, and dimensionality that determines the properties and functionalities of nanomaterials (Chen et al., 2020). In this context, quantification of the crystalline phase of Fe/Ru-SiMWCNT nanohybrid was first determined using the degree of crystallinity (DOC) shown in Eq. 3.4. Before the DOC analysis, Fe/Ru-SiMWCNT with Fe³⁺/Fe²⁺ compositions of 1.5:1, Ru of 0.5 wt. %, SiO₂ of 19.5 wt. % and 80 wt. % of MWCNT was calcined at 400 °C, 500 °C, and 600 °C. The XRD of these samples was measured, and their corresponding profiles are as presented in Figure 4.3.

Analysis of the XRD profiles on high score plus software confirmed the presence of O₂Ru, Fe₃O₄, CNT, and SiO₂ four-phase mixtures in x-Fe/Ru-SiMWCNT (x = 400, 500, and 600 °C) nanohybrid. The XRD result showed that the O₂Ru phase in these four thermally treated x-Fe/Ru-SiMWCNT formed a tetragonal crystal structure (P42/mnm) with a ~ 0.745 % lattice strain. According to the library matching with reference code 00-040-1290, the lattice parameter of the O₂Ru phase was made of crystallographic indices centre at (110) and (200) planes with their diffraction pattern indexing at ~ 27.9° and ~ 39.4°, respectively. The lattice constant of O₂Ru phase was a₀ = b = 0.4499 nm and c = 0.3101 nm where the d spacing's are: d (110) = 0.318 nm, d (200) = 0.225 nm. Similarly, the Fe₃O₄ phase formed a cubic crystal structure (Fd-3m) with a lattice strain of ~0.639 %, crystallographic planes of (222), (311), (400), (422), (511), and (440). According to the library matching with reference code of 01-0750449, these planes corresponded to the diffraction pattern indexing at 30.6°, 35.7°, 43.4°, 54.2°, 57.5° 63.3°, respectively. There

are two diffraction patterns for the MWCNT phase, which occurred at 23.9° , and 74.7° ; corresponding to the crystallographic planes (002) and (110) (Ref. code: 01-0750449). The SiO_2 phase appeared to be both amorphous when calcined at 400°C and 500°C considering observable hump occurring at the onset of $\sim 21.5^\circ$ towards zero degrees of diffraction. According to library matching with reference code of 01-081-0067, after calcination at 600°C , the SiO_2 amorphous phase disappeared into a hexagonal crystalline phase that features at (110) plane with a diffraction pattern of 26.3° .

According to Eq 3.4, Fe/Ru-SiMWCNT calcined at 400°C , 500°C , and 600°C have the corresponding degree of crystallinity of 60.1 %, 93.800 %, and 98.950 %, respectively. The Fe/Ru-SiMWCNT calcined at 600°C is more crystalline apparent from the amorphous SiO_2 phase's disappearance, and it was selected for further applications.

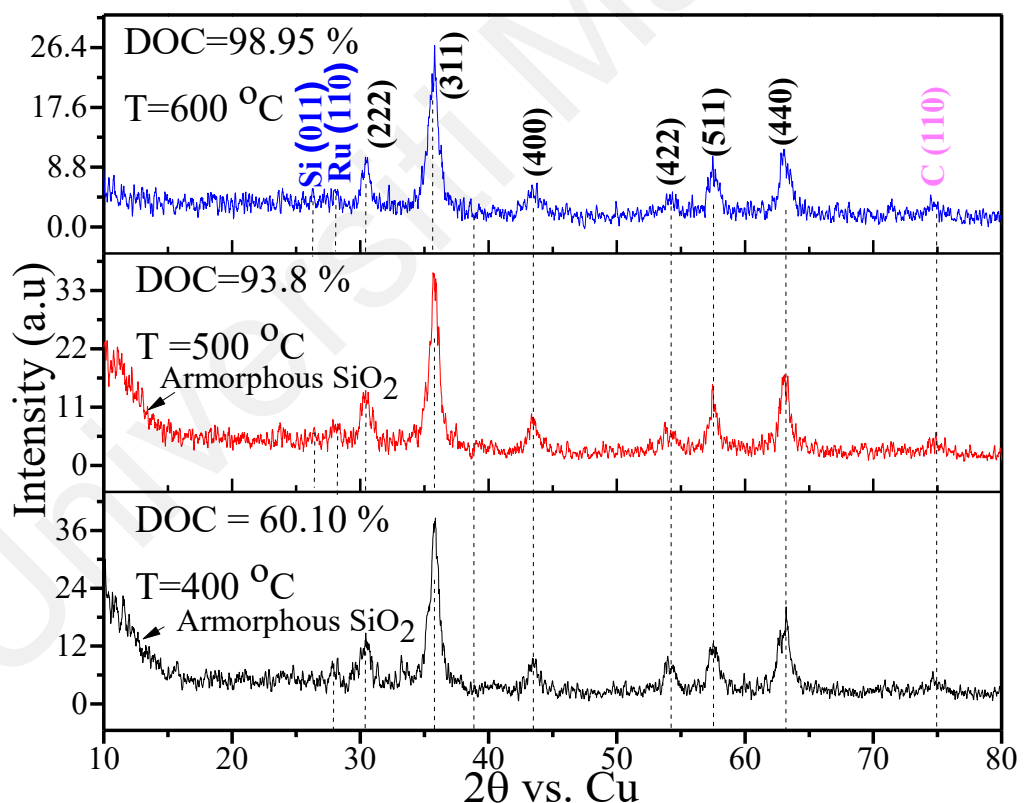


Figure 4.3: X-ray diffraction pattern of Fe/Ru-SiMWCNT calcined at different temperatures such as; 400°C , 500°C , and 600°C .

4.2.2 Surface properties of Fe/Ru-SiMWCNT nanohybrid

4.2.2.1 Temperature-programmed desorption

Figure 4.4a and 4.4b showed the CO₂ temperature-programmed desorption (CO₂-TPD) and temperature-programmed oxidation experiment for determining the intrinsic surface capability of Fe/Ru-SiMWCNT nanohybrid with DOC of 98.950 % to adsorb CO₂ and O₂, respectively. The onset of CO₂ and O₂ adsorption capacity by 0.510 wt. % Fe/Ru-SiMWCNT nanohybrid begins at ~82 °C and ~48 °C, respectively. Eventually, the nanohybrid adsorbed a maximum of ~2.197 μmol of CO₂ and ~131.1 μmol of O₂ at ~252 °C and ~322 °C, respectively. The adsorption of CO₂ can be attributed to the presence of the O₂Ru phase. This result implied that the O₂Ru in Fe/Ru-SiMWCNT nanohybrid could adsorb CO₂ similar to the one reported in the literature at a low temperature as 53 °C/1 mbar Ru (0001) single crystal (Pachecka et al., 2017). Moreover, the CO₂ adsorption capacity by the 0.51 wt. % Fe/Ru-SiMWCNT nanohybrid is higher than ordinary 0.8 wt. % Ru/SiO₂ (0.940 μmol at 213 °C) was reported over three decades ago (Zağlı & Falconer, 1981). Similarly, the presence of O₂-philic Fe₃O₄ in the nanohybrid can be the reason for O₂ adsorption. In a study by Takei et al. 2010, O₂ adsorption on Fe₃O₄ is possible and could be due to the surface oxidation process (Takei et al., 2010).

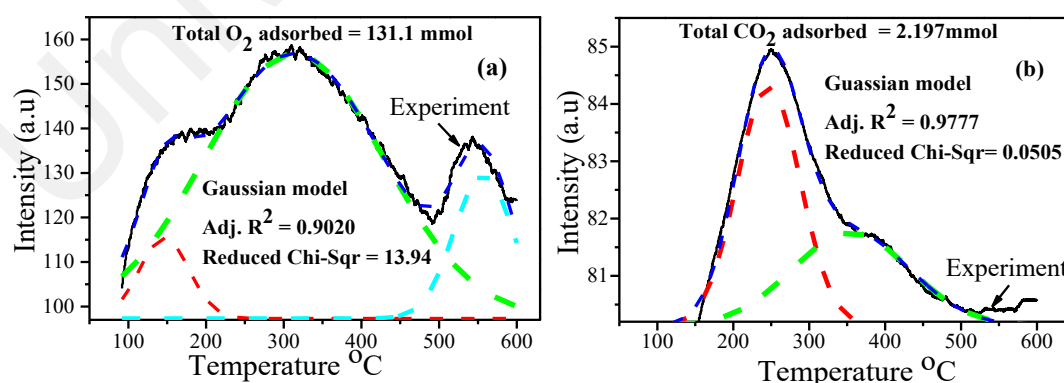


Figure 4.4: (a) Temperature programmed oxidation and (b) CO₂ temperature programmed desorption for Fe/Ru-SiMWCNT nanohybrid.

4.2.2.2 XPS analysis of Fe/Ru-SiMWCNT nanohybrid

To further confirm the coordination of SiO₂, RuO₂, and oxidation of multiwall carbon nanotubes (MWCNT) or Fe₃O₄, the elemental and valence state analysis was performed using XPS as shown in Figure 4.5a-f. Here, the constituent elements' chemical states were calibrated by C1s peak (284.600 eV). Figure 4.5a shows the survey scan XPS spectrum of the Fe/Ru-SiMWCNT nanohybrid with DOC of 98.950 % ranging from 0 eV to 1200 eV binding energy, which contains O 1s, Fe 2p, Si 1s, and 2p, Ru 3p, and C 1s peaks.

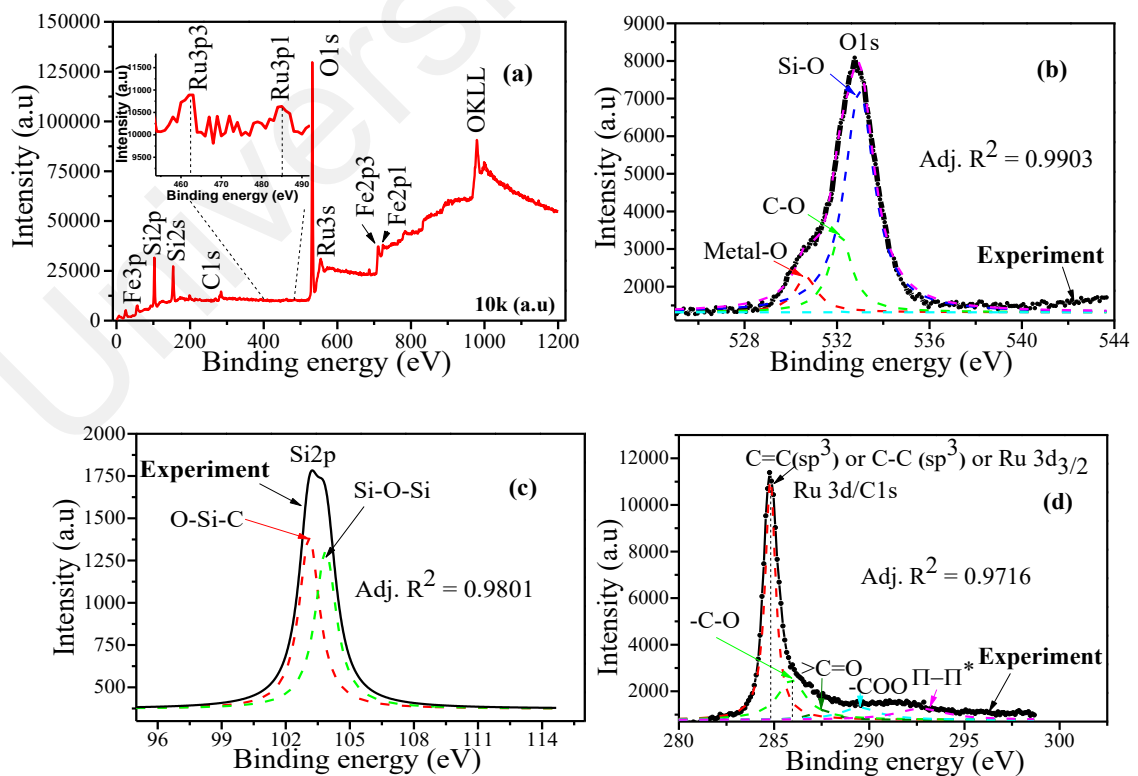
Figure 4.5b shows the core-level XPS spectrum of O1s in Fe/Ru-SiMWCNT. The spectrum reveals three different binding energies as ~ 530.600 eV, ~ 532.200 eV, and ~ 532.900 eV. These binding energies are attributed to O²⁻ point charges coordination to atoms in Fe/Ru-SiMWCNT framework. The ~ 530.600 eV binding energy implies O²⁻ coordination at the either octahedral or tetrahedral site to Fe₃O₄ or O₂Ru. These results align with the general acceptable O 1s binding energies for transition metal oxides which are 530 ± 0.500 eV (Vuković, Valla, & Milun, 1993). The ~ 532.900 eV binding energy implies O²⁻ coordination in the siloxane (Si-O-Si) group. The ~ 532.200 eV binding energy indicates O²⁻ coordination to a carbonaceous phase which mainly originates from the MWCNT.

The O 1s coordination to non-transition metals such as Si or Carbon with 532.900 eV and ~ 532.200 eV binding energies are within the range of previous reports (Oke et al., 2019). By further deconvolution of the Si 2p strong signal, as shown in Figure 4.5c, two binding energies for the Si-O-C and siloxane group (Si-O-Si) were observed at 103 eV 104 eV, respectively. The Si 2p signals for Si-O-C and Si-O-Si as seen here, are similar to the one reported in the literature (Tu et al., 2014). This observation implies that the O²⁻ delocalization at a specific Si node enhances Si-O-C linkage formation because

Si is tetravalent coordinated and confirmed that the SiO₂ phase in Fe/Ru-SiMWCNT was chemically coordinated to MWCNT.

On similar accounts, as shown in Figure 4.5d, the Ru/C phase in Fe/Ru-SiMWCNT overlapped at ~ 284.600 eV binding energy represented for the C1s-Ru3d core levels spectrum was inclusive of Ru 3d_{5/2} and Ru 3d_{3/2}. This result is similar to those reported for C 1s (Bittencourt et al., 2011) and Ru 3d core level (Morgan, 2015).

Figure 4.5e shows the core-level XPS spectra of Fe 2p in the Fe/Ru-SiMWCNT nano hybrid heterostructures. The main peak located at 725.500 eV and 711.600 eV are attributed to Fe³⁺ 2p_{1/2} and Fe³⁺ 2p_{3/2}, respectively, with a significant asymmetry for both of them. A double peak fitting gives peak positions at 709.300 eV and 722.500 eV, which belong to Fe²⁺ 2p_{1/2} and Fe²⁺ 2p_{3/2} core-levels. These results agree with the reported Fe 2p core-level XPS spectrum of the Fe₃O₄ phase (Monti et al., 2012). Interestingly, the absence of any satellite peak at ~718.800 eV binding energy confirmed the absence of free γ -Fe₂O₃ hematite, another iron oxide phase (Monti et al., 2012).



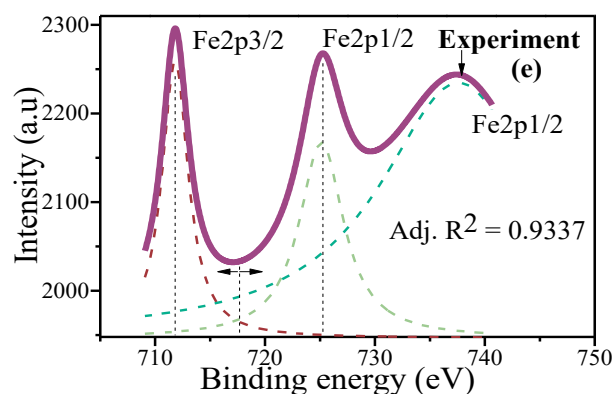


Figure 4.5: (a) The full survey-scan XPS spectra, (b) The O 1s core-level XPS spectrum (c) The Si 2p core-level XPS spectrum (d) The C 1s or Ru 3d core-level XPS spectrum (e) The Fe 2p core-level XPS spectrum for Fe/Ru-SiMWCNT nanohybrid heterostructures. Deconvoluted spectra are in dotted lines, while the experimental spectra are thick continuous black line indicated by an arrowhead.

4.2.2.3 Raman analysis of Fe/Ru-SiMWCNT nanohybrid

The Raman analysis measures the vibrational modes of Fe/Ru-SiMWCNT nanohybrid with DOC of 98.95 % spreading over the $50 \mu\text{m} \times 50 \mu\text{m}$ mapping area.

Figure 4.6a and 4.6b show the Raman spectrum and the Fe/Ru-SiMWCNT nanohybrid mapping area. In the Raman-spectrum for Fe/Ru-SiMWCNT nanohybrid, according to Figure 4.6a, eight Raman active modes correspond to D, G, 2D, $T_{2g}(1)$, $T_{2g}(2)$, A_{1g} , and TO-LO. These modes appeared because of the different components of the Fe/Ru-SiMWCNT that were confirmed earlier during the XPS survey scan (see Figure 4.5a). Each of these compositions has its molecular polarizability changing during the molecular vibration to yield the Raman active modes. According to previous and current popular scientific research opinions, this is otherwise a transition rule (selection rule) which stipulates that for a given Raman transition, molecular polarizability must change during the molecular vibration (Dresselhaus et al., 2010; Hegelund, Rasmussen, & Brodersen, 1973; Mills, 1964; Zhang et al., 2005).

Molecular polarizability is the property of matter that measures its ability to form instantaneous dipoles. It determines the dynamic response of a bound system to an external field, thereby giving an insight into a molecule's internal structure. In the bound system of Fe/Ru-SiMWCNT nanohybrid, the molecular polarizability of MWCNT gave rise to the Raman active mode represented by the D band, which centred at $\sim 1337 \text{ cm}^{-1}$. This result is the attribute of the sp^3 nanocrystalline carbon in the MWCNT. This attribute arises due to the out of plane vibrations because of structural defects in the MWCNT.

Similarly, the G band that centred at 1578 cm^{-1} arises from sp^2 amorphous carbon because of the sp^2 bonded carbon atoms' in-plane vibrations. The ratio of the intensity of D/G peaks was ~ 1.05 and implied that the sp^3 carbon is more than the sp^2 carbon in the Fe/Ru-SiMWCNT framework. In other words, the Fe/Ru-SiMWCNT framework contained less amorphous and more crystalline carbon. These results are in agreement with the D (sp^3 -type), G (sp^2 -type) and D/G ratio reported in the literature for MWCNT (Dong et al., 2020; Tomkiewicz, Cress, & Landi, 2020).

Also, the 2D mode at 2680 cm^{-1} was due to the second-order two-photon process (Wilamowska et al., 2013; Zhang et al., 2016). The $\text{T}_{2g}(1)$ centred at $\sim 546 \text{ cm}^{-1}$ was due to asymmetric stretching of Fe (Ru) and O at octahedral coordination. $\text{T}_{2g}(2)$ mode featured at $\sim 583 \text{ cm}^{-1}$ was asymmetrical stretching of oxygen atoms and Ru-O bonds in octahedral coordination and indicated a high degree of disorder in bond length. The $\text{A}_{1g}/\text{B}_{2g}$ mode at $\sim 743 \text{ cm}^{-1}$ was the symmetric vibration of Fe-O or Ru-O and the tetrahedral coordination.

The longitudinal and transverse optical vibration (LO-TO) centred at 1388 cm^{-1} arose from Si-O-Fe asymmetry vibration, while the silica siloxane (Si-O-Si) bridge has the Raman characteristics at 800 cm^{-1} . This result was also complemented by the wideband occurring at ~ 1018 and 933 cm^{-1} . Accordingly, it is an unusual feature of Si-O- and Si (-O-)² functionality. These observations are consistent with the literature

(Mar et al., 1995; Shebanova & Lazor, 2003). Moreover, these active Raman modes accord with the phases revealed by XRD and XPS results in Figure 4.3 and Figure 4.5, respectively. Considering the $50\ \mu\text{m} \times 50\ \mu\text{m}$ mapping according to Figure 4.6b to yield the spectrum in Figure 4.6a, this can be a bulk analysis that indicated the Fe/Ru-SiMWCNT being a significant phase. As indicated by the red arrow, the mapping area covers many Fe/Ru-SiMWCNT sample micro-regions.

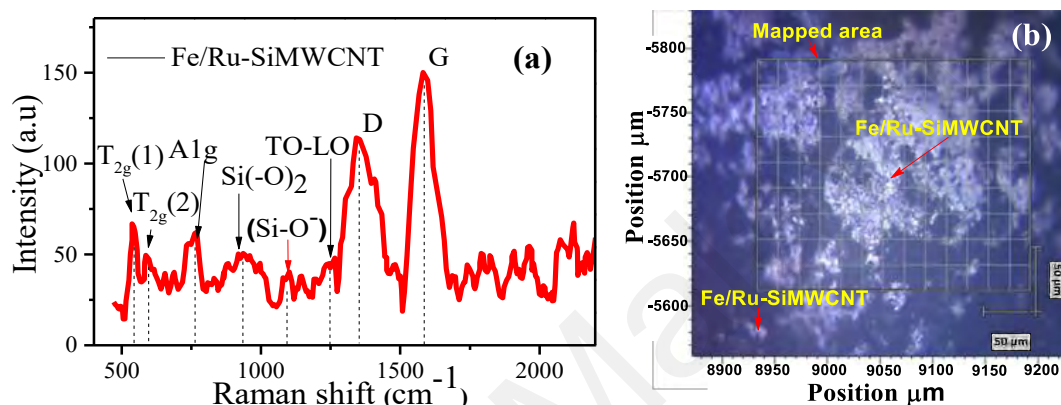


Figure 4.6: (a) Raman spectrum of Fe/Ru-SiMWCNT nanoparticles (b) Raman mapping spectrum of Fe/Ru-SiMWCNT nanoparticles.

4.2.2.4 Morphology and textural property of Fe/Ru-SiMWCNT nano hybrid

This section presents a visualization of the Fe/Ru-SiMWCNT nano hybrid heterostructures with a DOC of 98.95 % to the best possible resolution using FESEM/EDS and HRTEM. In Figure 4.7a, the FESEM image of the Fe/Ru-SiMWCNT at 500 nm resolution shows the interlock of the functionalized MWCNT. The EDS were integrated based on five different spectra on the image (spectrum 1, spectrum 2, spectrum 3, spectrum 4 and spectrum 5). Some of the spectra (spectrum 1, 3 and 4) show edge effect while others (spectrum 5 and 2) did not show edge effect. The edge effects are signatures of more electrons escaping resulting in the bright whitish image. This differentiation on edge effect based on the spectra indicated that the surface of the Fe/Ru-SiMWCNT has a topological difference. The region inclined at high elevation revealed the edge effect (more electron escape) while the region inclined at lower elevation did not

show the edge effect (few electrons escape). The EDS mapping of this same region on the Fe/Ru-SiMWCNT micro-surface confirmed the presence of C (red colored EDS map), Ru (yellow colored EDS map), Si (blue colored EDS map) and Fe (aqua EDS colored map). These compositions also confirmed the XPS and Raman analysis for the Fe/Ru-SiMWCNT.

Also, HRTEM was used at higher atomic resolution further to probe the surface of the Fe/Ru-SiMWCNT nanohybrid as shown in Figure 4.7b (20 nm resolution), Figure 4.7c (200 nm resolution), and Figure 4.7d (2 nm resolution). At 200 nm resolution, the image is not much different from the one seen at 500 nm resolution using FESEM analysis. However, the MWCNT is visible with some dark spot-like features resting on lacey carbon film used to hold the Fe/Ru-SiMWCNT nanohybrid. Increasing the resolution to 20 nm revealed some critical information about the Fe/Ru-SiMWCNT nanohybrid. The lattice fringes of the MWCNT can be seen with ~ 18.270 nm external diameter and 5.4 nm internal diameter when the resolution was further increased to 5 nm, and each fibre of the CNT is at a spacing distance of ~ 0.320 nm. The region which contains the dark spot-like feature was resolved at the highest possible resolution of 2 nm, and that was the maximum limit we could go without destroying the Fe/Ru-SiMWCNT nanohybrid. The dark spot-like feature formed a FeRu phase crater with a grain size of 13.670 nm and showing the binding interface with SiMWCNT. One of the lattice fringe spaces corresponded to 0.210 nm d-space and (311) crystallographic plane for Fe_3O_4 phase in the Fe/Ru-SiMWCNT.

Fast Fourier transformation (FFT) analysis at 2 nm resolution was conducted. The FFT (FFT-1, FFT-2 and FFT-3) patterns shown in Figure 4.7e can be indexed to different sublattice that forms a single a superlattice. The superlattice reflections in the pattern indicated by the yellow arrow in Figure 4.7e suggested the likely formation and reorientation of defects from Ru, which is orthorhombic and coordinated on magnetite,

which is cubic crystal structures. The sublattice with Fd-3m space group observed by the FFT-2 corresponds with the XRD results discussed in section 4.2.1. The FFT-1 revealed that Fe/Ru-SiMWCNT nanohybrid sublattice comprises closely packed cubic Fe_3O_4 ($a=4.684$, $b=3.423$, $c=5.129$) and O_2Ru ($a=4.212$). The FFT-3 revealed the sublattice of SiMWCNT in Fe/Ru-SiMWCNT nanohybrid. Overall, these observations agree with the XRD results and the literature (X. Huang et al., 2019).

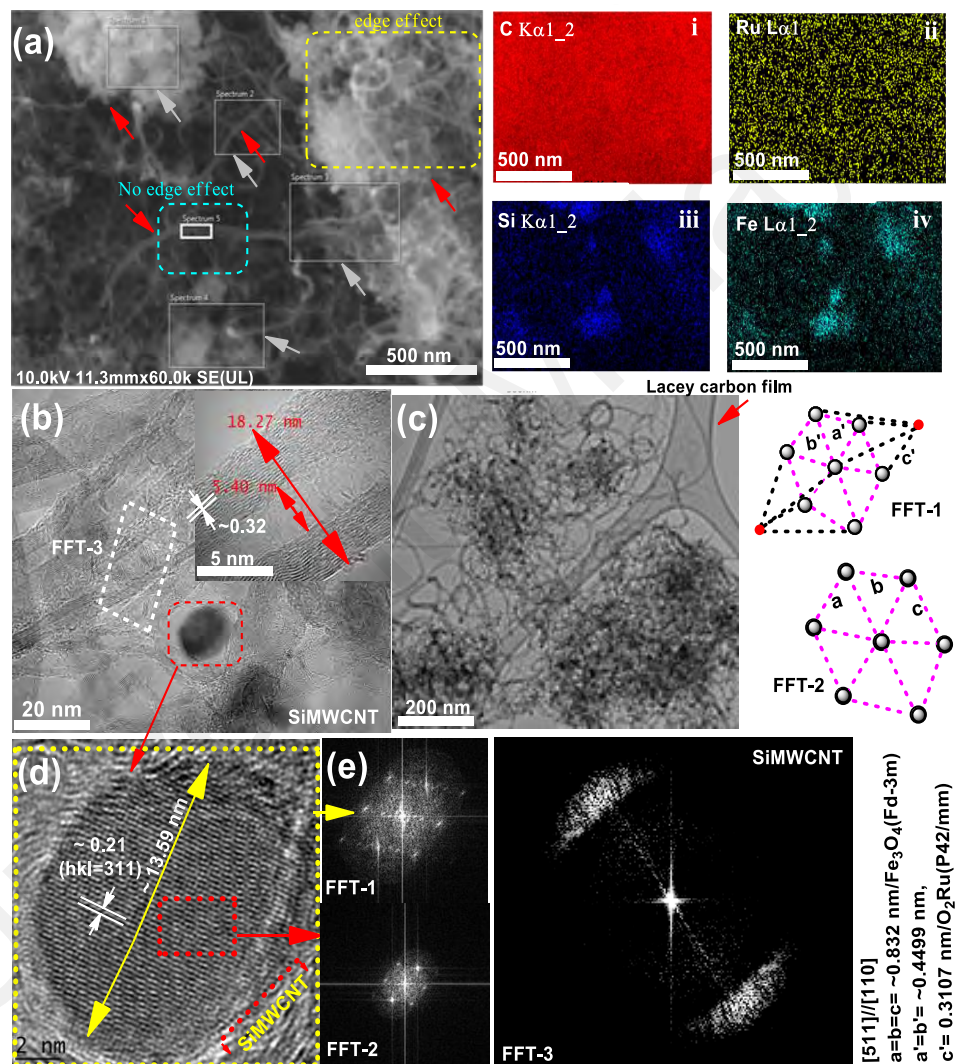


Figure 4.7: (a) FESEM/EDS (i-iv) at 500 nm resolution, (b) HRTEM at 20 nm resolution, (c) HRTEM at 200 nm resolution, (d) HRTEM at 2 nm resolution and (e) Fast Fourier transform at 2 nm resolution for Fe/Ru-SiMWCNT nanohybrid.

4.2.3 Electrochemical potential windows of ILs and Fe/Ru-SiMWCNT-ILs nanofluids

The ECW voltage range between which a medium shows no active reduction or oxidization upon applying electricity (Yoshimura et al., 2002; Zhang et al., 2018). Determining this voltage range is essential, especially when considering ILs or Fe/Ru-SiMWCNT-ILs nanofluids as suitable media for $O_2^{\bullet-}$ generation and utilization in electrochemical reactions. This observation is because radical driven electrochemical reactions require that $O_2^{\bullet-}$ should be generated over a voltage range that has no associated electrochemical activity of the media.

Table 4.2 and Table 4.3 present the ECWs of all the ILs listed in Table 3.1 and their Fe/Ru-SiMWCNT-ILs nanofluids counterparts. In Table 4.2, the ECWs of the ILs increases in this order; [BMPip⁺][TFSI⁻], [MTOAmm⁺][TFSI⁻], [BMAmm⁺][TFSI⁻], [PMIm⁺][TFSI⁻], [MOEMMor⁺][TFSI⁻], [BMIm⁺][TFSI⁻], [TBMAmm⁺][TFSI⁻], [MOEMPyrr⁺][PFTP⁻], and [EDMPAmm⁺][TFSI⁻], [BMPyrr⁺][TFSI⁻]. The ECW of [BMPyrr⁺][TFSI⁻] (6.230 V), [MOEMMor⁺][TFSI⁻] (5.560 V), and [MOEMPyrr⁺][PFTP⁻] (4.990 V) are similar to the literature values; 5.200 V, 4.680 V and 3.980 V respectively (Hayyan et al., 2013). The ECWs CV waves of the ILs are presented in Figure C.1 (a-j) (**Appendix C**). The ECWs CVs wave shows some small humps around the cut-off current density below the value of ~ 0.5 mA/cm². These small humps were negligible since they could emerge from a small increase in the current associated with double-layer charging, mainly due to indeterminate interfacial instability common with the electrochemical process (Xiao et al., 2020). The small hump can also arise from the IL impurities' electrochemical processes (Randström et al., 2007). Since the ILs listed in Table 3.1 are pure, this present study does not envisage that the small hump arises due to impurity in the ILs but due to double-layer charging.

The IL-cation and IL-anion moiety was found to influence the ECWs of the ILs, as shown in Table 4.2. By implication, the IL-cation is responsible for the reductive potentials of the ILs (Sawyer et al., 1995). This reductive potential was found to be different for all the ILs. In general, the reductive potential for all the ILs varied from -1.97 V to -2.890 V. For instance, the reductive potential for $[\text{PMIm}^+][\text{TFSI}^-]$ and $[\text{BMIm}^+][\text{TFSI}^-]$ are -1.970 V and -1.990 V vs Ag/AgCl respectively. These values are close to the electrochemical potential for one-electron reduction of O_2 to $\text{O}_2^{\bullet-}$ which is ~ -1 V vs Ag/AgCl. Although this reductive potential could avail one-electron reduction of O_2 to $\text{O}_2^{\bullet-}$, they are very narrow. This reductive potential signifies how easy $[\text{PMIm}^+]$ and $[\text{BMIm}^+]$ can be electrochemically reduced. By definition, the reductive potential limit arises from reducing IL-cation (Rogers et al., 2009).

Compared with other IL-cation, as in Table 4.2, the reductive potential of $[\text{PMIm}^+]$ and $[\text{BMIm}^+]$ are lower in magnitude. Therefore, the increase in stability of the ILs listed in Table 4.2 in terms of electrochemical reduction are as follows; $[\text{PMIm}^+][\text{TFSI}^-]$, $[\text{BMIm}^+][\text{TFSI}^-]$, $[\text{MOEMMor}^+][\text{TFSI}^-]$, $[\text{BMPip}^+][\text{TFSI}^-]$, $[\text{TBMAm}^+][\text{TFSI}^-]$, $[\text{MOEMPyrr}^+][\text{PFTP}^-]$, $[\text{MTOAm}^+][\text{TFSI}^-]$, $[\text{BMAm}^+][\text{TFSI}^-]$, $[\text{EDMPAm}^+][\text{TFSI}^-]$ and $[\text{BMPyrr}^+][\text{TFSI}^-]$.

The oxidative potential for the ILs-anion moiety establishes the oxidative stability of the ILs to promote many oxidative electrochemical processes. Accordingly, the order of oxidative stability of the ILs is as follows; $[\text{BMPip}^+][\text{TFSI}^-]$, $[\text{MTOAm}^+][\text{TFSI}^-]$, $[\text{BMAm}^+][\text{TFSI}^-]$, $[\text{TBMAm}^+][\text{TFSI}^-]$, $[\text{MOEMMor}^+][\text{TFSI}^-]$, $[\text{PMIm}^+][\text{TFSI}^-]$, $[\text{BMIm}^+][\text{TFSI}^-]$, $[\text{EDMPAm}^+][\text{TFSI}^-]$, $[\text{MOEMPyrr}^+][\text{PFTP}^-]$, $[\text{BMPyrr}^+][\text{TFSI}^-]$. Throughout the determination of ECWs for the ILs, the electrochemical frontiers at the GC working electrode were determined by cyclic voltammetry at 9.0 mV/s scan rate stripping. The scan rate stripping commenced from anodic to cathodic potentials and reversing back to the initial value. At the onset, anodic and cathodic limits were set as the

potential at which the current density reached higher than 0.5 mA/cm^2 for comparison purposes (Rogers et al., 2009). According to the data in Table 4.2 that the tested ILs pose a wide range of voltage to which there is no observable electrochemical activity. These ECWs ranges from $\sim 4.400 \text{ V}$ to 6.230 V , and they are all within a suitable range for electrochemical reactions for instance $\text{O}_2^{\bullet-}$ generation and utilization.

The Fe/Ru-SiMWCNT nanohybrid derived ILs, illustrated in Table 4.3 showed distinctive scenarios of either increase or a decrease in their ECWs relative to those reported in Table 4.2. These developments followed a corresponding increase in their reductive or oxidative potentials (see Table 4.3). For instance, the ECW of $[\text{EDMPAmm}^+][\text{TFSI}^-]$ (see Table 4.2) was 5.96 V , and its nanoparticle-based counterpart such as Fe/Ru-SiMWCNT- $[\text{EDMPAmm}^+][\text{TFSI}^-]$ was found to be $6.210 \text{ V vs Ag/AgCl}$. This result indicates a $\sim 0.250 \text{ V}$ improvement in the overall ECW. Another ammonium-based ILs such for example $[\text{TBMA}^+][\text{TFSI}^-]$, $[\text{BMAmm}^+][\text{TFSI}^-]$, $[\text{MTOAmm}^+][\text{TFSI}^-]$ got their corresponding ECW improved by 1.220 V , 1.270 V , and $1.460 \text{ V vs Ag/AgCl}$ respectively, after adding the FeRu-SiMWCNT nanohybrid. The increase in the ECW could be due to improve the medium's hydrophobicity by adding Fe/Ru-SiMWCNT nanohybrid. This result is in cognisance that the presence of H_2O could narrow the ECWs of ILs (O'Mahony et al., 2008; Schröder et al., 2000).

Comparing the reductive potential of the ordinary ammonium based ILs such as $[\text{EDMPAmm}^+][\text{TFSI}^-]$ (-2.850 V), $[\text{TBMA}^+][\text{TFSI}^-]$ (-2.330 V), $[\text{BMAmm}^+][\text{TFSI}^-]$ (-2.580 V), and $[\text{MTOAmm}^+][\text{TFSI}^-]$ (-2.45 V) with their nanohybrids counterparts such as Fe/Ru-SiMWCNT- $[\text{EDMPAmm}^+][\text{TFSI}^-]$ (-3.600 V), Fe/Ru-SiMWCNT- $[\text{TBMA}^+][\text{TFSI}^-]$ (-3.100 V), Fe/Ru-SiMWCNT- $[\text{BMAmm}^+][\text{TFSI}^-]$ (-3.500 V), and Fe/Ru-SiMWCNT- $[\text{MTOAmm}^+][\text{TFSI}^-]$ (-3.810 V), there is an apparent improvement. Similarly, there are improvement in the ECW of Fe/Ru-SiMWCNT- $[\text{MOEMPyrr}][\text{PFTP}^-]$, Fe/Ru-SiMWCNT- $[\text{MOEMMor}^+][\text{TFSI}^-]$, and Fe/Ru-

SiMWCNT-[BMIm⁺][TFSI⁻] compared to normal [MOEMPyrr⁺][PFTP⁻], [MOEMMor⁺][TFSI⁻], [BMIm⁺][TFSI⁻] (See Figure 4.2 and 4.3). Since the reductive potential signifies the capability of the media to be electrochemically reduced, functionalizing the ILs with Fe/Ru-SiMWCNT nanohybrid can be postulated to further increase the potential at which the medium gets reduced. Also, this cannot be generalized for all ILs because functionalization of Fe/Ru-SiMWCNT nanohybrid did not improve the reductive potentials of other ILs such as [BMPyrr⁺][TFSI⁻], [PMIm⁺][TFSI⁻] and [BMPip⁺][TFSI⁻].

Table 4.2: Cathodic and anodic potentials vs Ag/AgCl for ECWs of ILs at cut-off current density 0.5 mA/cm² using GC macro working electrode*.

Ionic Liquid Abbreviation	Ec.L.	Ea.L.	ECW
[EDMPAmm ⁺][TFSI ⁻]	-2.850	3.110	5.960
[BMPyrr ⁺][TFSI ⁻]	-2.890	3.340	6.230
[MOEMPyrr ⁺][PFTP ⁻]	-2.420	3.140	5.560
[MOEMMor ⁺][TFSI ⁻]	-2.120	2.870	4.990
[BMIm ⁺][TFSI ⁻]	-1.990	3.010	5.000
[PMIm ⁺][TFSI ⁻]	-1.970	2.990	4.960
[TBMAmm ⁺][TFSI ⁻]	-2.330	2.800	5.130
[BMAmm ⁺][TFSI ⁻]	-2.580	2.350	4.930
[MTOAmm ⁺][TFSI ⁻]	-2.450	2.320	4.770
[BMPip ⁺][TFSI ⁻]	-2.150	2.250	4.400

*Measurements were conducted at 25 °C

Table 4.3: Electrochemical window of Fe/Ru-SiMWCNT-ILs nanofluid at cut-off current density 0.5 mA/cm² using GC macro working electrode*.

Nanohybrid-Ionic Liquid Abbreviation	Ec. L.	Ea.L.	ECW
Fe/Ru-SiMWCNT-[EDMPAmm ⁺][TFSI ⁻]	-3.600	2.610	6.210
Fe/Ru-SiMWCNT-[BMPyrr ⁺][TFSI ⁻]	-1.100	1.200	2.300
Fe/Ru-SiMWCNT-[MOEMPyrr ⁺][PFTP ⁻]	-2.960	0.860	3.680
Fe/Ru-SiMWCNT-[MOEMMor ⁺][TFSI ⁻]	-2.720	2.170	4.890
Fe/Ru-SiMWCNT-[BMIm ⁺][TFSI ⁻]	-1.800	1.100	2.910
Fe/Ru-SiMWCNT-[PMIm ⁺][TFSI ⁻]	-1.860	1.760	3.620
Fe/Ru-SiMWCNT-[TBMA ⁺][TFSI ⁻]	-3.100	3.250	6.350
Fe/Ru-SiMWCNT-[BMAmm ⁺][TFSI ⁻]	-3.500	2.400	6.200
Fe/Ru-SiMWCNT-[MTOAmm ⁺][TFSI ⁻]	-3.810	2.400	6.230
Fe/Ru-SiMWCNT-[BMPip ⁺][TFSI ⁻]	-1.820	1.190	3.010

*Measurements were conducted at 25 °C

4.2.4 Electrochemical impedance spectroscopy

4.2.4.1 EIS parameter for ILs

The EIS parameters detected for ILs listed in Table 3.1 were determined from their Nyquist plots presented in Figure D.1 (Appendix D). During the EIS measurement process, the overall THD of the ILs media, as illustrated in Figure D.1a (Appendix D), did not exceed 19.880 %. This THD result implied that the flow of electricity through the ILs media was at least 80.120 % linear. According to research opinions, this degree of linearity validates the accuracy of the EIS data detected during the data acquisition (Alhafadhi & Teh, 2020; Mao et al., 2010).

The Nyquist spectra detected in [EDMPAmm⁺][TFSI⁻], [BMPyrr⁺][TFSI⁻], [MOEMPyrr⁺][PFTP⁻], [MOEMMor⁺][TFSI⁻], [BMIm⁺][TFSI⁻], [PMIm⁺][TFSI⁻], [TBMAMm⁺][TFSI⁻], [BMAMm⁺][TFSI⁻], [MTOAMm⁺][TFSI⁻], and [BMPip⁺][TFSI⁻] media using GC electrode vs. Ag/AgCl is shown in Figure D.1 (b-j) (Appendix D). The Nyquist spectra contain one semi-circle and a straight line. An equivalent circuit (EC) for the Nyquist spectra was derived by a modified Randle's model which accounted for mixed kinetics and charge transfer control element (Torresi et al., 2013). Accordingly for the Nyquist spectra, the EC is described by five elements for the ILs systems which all have one time-constants. Detail explanation of these five elements are given in the following paragraph.

First, the R_e corresponds to the ILs electrolyte resistance, which describes the overall electric resistance of ILs electrolyte layer with the electrode. This parameter should not strongly depend on the potential applied if a dielectric medium's resistance is constant in the case of ILs (Huang et al., 2018). In the ILs media, the semicircle's presence indicates a single time constant associated with a resistor-capacitor (RC) circuit (Lates et al., 2014). The semi-circle impedance parameters (R_e , R_{ct} and C_2) were used to characterize the electrochemical property of the ILs. Accordingly, the R_e -values as shown

in Table 4.4, increase as follows; [BMIm⁺][TFSI⁻], [PMIm⁺][TFSI⁻], [BMPyrr⁺][TFSI⁻], [EDMPAmm⁺][TFSI⁻], [BMPip⁺][TFSI⁻], [MOEMPyrr⁺][PFTP⁻], [TBMamm⁺][TFSI⁻], [BMAmm⁺][TFSI⁻], and [MTOamm⁺][TFSI⁻]. It was found that the [MTOamm⁺][TFSI⁻] have the highest R_e -value while [BMIm⁺][TFSI⁻] has the lowest R_e value.

Second, the R_{ct} corresponds to the charge-transfer resistance, which characterizes the faradaic charge transfer process involving the ions of the ILs. This element can describe many different reactions that occur at different potential values but will always primarily describe the fastest process taking place at a fixed potential. Although the electrolyte resistances (R_e) are high for all ILs except for [BMIm⁺][TFSI⁻] (~204 Ω), their charge transfer resistances (R_{ct}) are very small relative to R_e within. This approves them to be suitable for the electrochemical process. The R_{ct} -values detected in the ILs as shown in Table 4.4 decrease in the order such as [MTOamm⁺][TFSI⁻] (32357 m Ω), [BMPyrr⁺][TFSI⁻] (89.5 m Ω), [BMAmm⁺][TFSI⁻] (0.655 m Ω), [TBMamm⁺][TFSI⁻] (0.424 m Ω), [EDMPamm⁺][TFSI⁻] (0.405 m Ω), [BMPip⁺][TFSI⁻] (0.400 m Ω), [MOEMPyrr⁺][PFTP⁻] (0.325 m Ω), [BMIm⁺][TFSI⁻] (0.204 m Ω), and [PMIm⁺][TFSI⁻] (0.136 m Ω). Generally, the charge transfer resistance (R_{ct}) is far lower than the electrolyte resistance, (R_e) excluding [MTOamm⁺][TFSI⁻].

Third, the C_3 was added in series with the R_{ct} to estimate the faradaic reaction's energy storage capacity for a reversible or quasi-reversible, as a pseudocapacitive term.

Fourth, C_2 was added in parallel with R_{ct} as the double-layer capacitance between the GC electrode and the ILs. Also, the double-layer capacitance (C_2) associated with the R_e was lower in [MTOamm⁺][TFSI⁻] and higher in [BMIm⁺][TFSI⁻]. However, the C_2 increase in the ILs as follows; [MTOamm⁺][TFSI⁻], [BMAmm⁺][TFSI⁻], [EDMPamm⁺][TFSI⁻], [TBMamm⁺][TFSI⁻], [BMPyrr⁺][TFSI⁻], [BMPip⁺][TFSI⁻], [MOEMPyrr⁺][PFTP⁻], [BMIm⁺][TFSI⁻]. Based on the EC, as shown in Figures D.1

(Appendix D), the ILs showed a capacitive coating on the GC electrode's surface. This study's viewpoint shows that the capacitive coating formed a thin film on the GC electrode surface. Also, C_2 represents the double-layer capacitance which the ILs could offer. According to the EC, the double-layer capacitance associated with the ion diffusion was indexed as C_3 .

Fifth, the Warburg impedance (W_3) was associated with the C_3 which is also a double-layer capacitance.

Following the ILs media, the Nyquist plots in Figure D.1 b-j (Appendix D) show similar pattern:

- 1) a semi-circle at the high-frequency region. This semi-circle was assigned to the R_e associated with the electron transfer process (Huang et al., 2018).
- 2) a linear profile mainly at the low-frequency region assigned to the diffusion-limited process (Bredar et al., 2020).

Noteworthy, W_3 as one of the EIS parameter could not be quantified within the whole frequency ranges measured likely because the role of the process that it corresponds to is too small. However, the W_3 correspond to the linear region on the Nyquist spectra.

Table 4.4: Parameter values of elements in the equivalent circuit model for ILs

Media	R_e (Ω)	C_2 ($\mu\text{F}/\text{cm}^2$)	R_{ct} ($\text{m}\Omega$)	C_3 ($\mu\text{F}/\text{cm}^2$)
[EDMPAmm ⁺][TFSI ⁻]	1036	3.333	0.405	18.077
[BMPyrr ⁺][TFSI ⁻]	663	3.547	89.500	18.291
[MOEMPyr ⁺][PFTP ⁻]	2780	5.627	0.325	29.601
[BMIm ⁺][TFSI ⁻]	204	7.023	0.204	24.872
[PMIm ⁺][TFSI ⁻]	642.8	5.427	0.136	24.074
[TBMAm ⁺][TFSI ⁻]	4071	3.248	0.424	21.368
[BMAm ⁺][TFSI ⁻]	9926	2.892	0.655	20.826
[MTOAm ⁺][TFSI ⁻]	13944	1.880	32357	23.105
[BMPip ⁺][TFSI ⁻]	1563	4.843	0.400	18.020

4.2.4.2 EIS Parameter for Fe/Ru-SiMWCNT-ILs nanofluid

The Nyquist plot detected in Fe/Ru-SiMWCNT-ILs nanofluids (Fe/Ru-SiMWCNT-[EDMPAmm⁺][TFSI⁻], Fe/Ru-SiMWCNT-[BMPyrr⁺][TFSI⁻], Fe/Ru-SiMWCNT-[MOEMPyrr⁺][PFTP⁻], Fe/Ru-SiMWCNT-[MOEMMor⁺][TFSI⁻], Fe/Ru-SiMWCNT-[BMIm⁺][TFSI⁻], Fe/Ru-SiMWCNT-[PMIm⁺][TFSI⁻], Fe/Ru-SiMWCNT-[TBMAMm⁺][TFSI⁻], Fe/Ru-SiMWCNT-[BMAMm⁺][TFSI⁻], Fe/Ru-SiMWCNT-[MTOAMm⁺][TFSI⁻], and Fe/Ru-SiMWCNT-[BMPip⁺][TFSI⁻] are shown in Figure D.2 a-g. In terms of percentage reduction, the *Re*-value for ordinary ILs (see section 4.2.4.1) compared with the Fe/Ru-SiMWCNT-ILs, increases in the following order; [BMPyrr⁺][TFSI⁻] (56 %), [PMIm⁺][TFSI⁻] (62 %), [EDMPAmm⁺][TFSI⁻] (67 %), [BMIm⁺][TFSI⁻] (72 %), [MOEMPyrr⁺][PFTP⁻] (75 %), [BMPip⁺][TFSI⁻] (79 %), [TBMAMm⁺][TFSI⁻] (83 %), [MTOAMm⁺][TFSI⁻] (93 %), and [BMAMm⁺][TFSI⁻] (95 %). These result implied that the *Re*-value is lower in Fe/Ru-SiMWCNT-ILs nanofluids compared to ordinary ILs.

Consequently, functionalizing Fe/Ru-SiMWCNT on ILs has the effect of reducing the *Re* values. This is also an indication of the chemical interaction of Fe/Ru-SiMWCNT nanohybrid with ILs. The reduction in *Re*-value upon Fe/Ru-SiMWCNT nanohybrid functionalization on IL is highest in [BMAMm⁺][TFSI⁻]. Similarly, the percent increase in *C*₂ for ordinary ILs and Fe/Ru-SiMWCNT-ILs follows this order: [BMIm⁺][TFSI⁻] (36 %), [MOEMPyrr⁺][PFTP⁻] (50 %), [PMIm⁺][TFSI⁻] (53 %), [BMPip⁺][TFSI⁻] (57 %), [EDMPAmm⁺][TFSI⁻] (69 %), [BMPyrr⁺][TFSI⁻] (71 %), [TBMAMm⁺][TFSI⁻] (71 %), [BMAMm⁺][TFSI⁻] (72 %), and [MTOAMm⁺][TFSI⁻] (78 %).

These results also indicate that Fe/Ru-SiMWCNT has an additional effect of boosting the double layer capacitance. The results were compared with the capacitance of some nanoscale ionic fluids as shown in Table 4.6 (Dutta, Deb, & Bhattacharya, 2018;

Lucio et al., 2018). The Fe/Ru-SiMWCNT-ILs provided more double layer capacitance than the ordinary ILs counterpart as shown in Table 4.5.

Table 4.5: EIS parameter in the equivalent circuit model for Fe/Ru-SiMWCNT-ILs*.

Media	R_e (Ω)	C_2 ($\mu\text{F}/\text{cm}^2$)	R_{ct} (Ω)	C_3 ($\mu\text{F}/\text{cm}^2$)
Fe/Ru-SiMWCNT-[EDMPAmm ⁺][TFSI ⁻]	343	10.783	0.166	21.766
Fe/Ru-SiMWCNT-[BMPyrr ⁺][TFSI ⁻]	290	12.094	0.213	26.966
Fe/Ru-SiMWCNT-[MOEMPyrr ⁺][PFTP ⁻]	675	11.382	0.205	23.860
Fe/Ru-SiMWCNT-[BMIm ⁺][TFSI ⁻]	351	11.026	0.200	23.803
Fe/Ru-SiMWCNT-[PMIm ⁺][TFSI ⁻]	242	11.581	95.140	25.570
Fe/Ru-SiMWCNT-[TBMAm ⁺][TFSI ⁻]	709	11.168	0.393	22.578
Fe/Ru-SiMWCNT-[BMAmm ⁺][TFSI ⁻]	524	10.214	0.118	21.496
Fe/Ru-SiMWCNT-[MTOAm ⁺][TFSI ⁻]	1023	8.561	0.209	20.783
Fe/Ru-SiMWCNT-[BMPip ⁺][TFSI ⁻]	322	11.292	0.127	23.148

*Measured under potentiostatic (-1.564 V vs Ag/AgCl) mode at 10 mV amplitude

Table 4.6: Comparing the specific capacitance with literature at 25 °C

S/N	Media	C_2 ($\mu\text{F}/\text{cm}^2$)	Reference
1	Fe/Ru-SiMWCNT-[EDMPAmm ⁺][TFSI ⁻]	10.783	This study
2	Fe/Ru-SiMWCNT-[BMPyrr ⁺][TFSI ⁻]	12.094	
3	Fe/Ru-SiMWCNT-[MOEMPyrr ⁺][PFTP ⁻]	11.382	
4	Fe/Ru-SiMWCNT-[BMIm ⁺][TFSI ⁻]	11.026	
5	Fe/Ru-SiMWCNT-[PMIm ⁺][TFSI ⁻]	11.581	
6	Fe/Ru-SiMWCNT-[TBMAm ⁺][TFSI ⁻]	11.168	
7	Fe/Ru-SiMWCNT-[BMAmm ⁺][TFSI ⁻]	10.214	
8	Fe/Ru-SiMWCNT-[MTOAm ⁺][TFSI ⁻]	8.561	
9	Fe/Ru-SiMWCNT-[BMPip ⁺][TFSI ⁻]	11.292	
10	PORC17 ACF1	7.200 2.200	(Urita et al., 2014)
11	[BMIm ⁺][BF ₄ ⁻]	9.300	(Lucio et al., 2018)
	[BMIm ⁺][PF ₆ ⁻]	8.500	
12	SnO ₂ -NHIF	4.700	(Dutta et al., 2018)

PorC17 = An indexed mesoporous carbon material (SiO₂-opal/carbon nanocomposite), ACF1 = Activated carbon fibre, NHIF = Nanoscale ionic fluids ([SnO₂⁻-IL]⁺ [(CF₃SO₂)₂N]; herewith, the IL was 1-ethyl-3-(3-trimethoxysilylpropyl)-imidazolium bis (trifluoromethanesulfonyl) imide).

4.3 Generation of Superoxide Ion ($O_2^{\bullet-}$) in ILs

4.3.1 The electrochemical generation of stable $O_2^{\bullet-}$

Figure 4.8 (a-j) present CV waves for one-electron reduction of O_2 to $O_2^{\bullet-}$ in the ILs listed in Table 3.1. The CV waves were accompanied by background voltammograms (blank) for these ILs media. The blank CV wave arose after sparging them with N_2 , indicating that the IL were electrochemically stable for the generation of $O_2^{\bullet-}$. In these ILs, the reduction potential of O_2 occurred at $\sim \pm -1.0$ V vs Ag/AgCl, similar in range with previous reports (Hayyan et al., 2016). Noteworthy, Figure 4.8 (f) showed a pre-cathodic hump at ~ -0.68 V vs Ag/AgCl in addition to the O_2 reduction peak, which occurred at -0.9158 V vs Ag/AgCl. This result is usually prevalent when the ILs contain inactive impurity when saturated with N_2 but active in the O_2 environment. The hump might arise due to the IL's adsorption on the GC electrode surface resulting in the onset of micro electrochemical activity (Islam et al., 2005). In this study's viewpoint, the pre-cathodic hump originating from impurity could be unlikely because the ILs used are pure. According to another opinion, the hump could arise from a double layer charging due to interfacial instability (Xiao et al., 2020). This study believed that this could likely be the reason for the appearance of the pre-cathodic hump.

From Figure 4.8 (i) the reduction potential of O_2 in $[MTOAmm^+][TFSI^-]$ occurred at -1.290 V for 9 mV/s scan rate and -1.9714 V for 144 mV/s. This $[MTOAmm^+][TFSI^-]$ medium avails the highest potential for O_2 one-electron reduction to $O_2^{\bullet-}$. Apart from the fact that $[MTOAmm^+][TFSI^-]$ is highly viscous (237.675 mPa.S, Table 4.7, column 2, entry 9) and diffusion of O_2 through it is very low ($0.029 \times 10^{-10} m^2/s$, Table 4.7, column 3, entry 9). Moreover, $[MTOAmm^+][TFSI^-]$ has the lowest double-layer capacitance ($\sim 1.880 \mu F/cm^2$, Table 4.4, C_2 , entry 8 column 1) and the highest charge transfer resistance (R_{ct}) of $32,357$ m Ω . The $[MTOAmm^+][TFSI^-]$ is different from the

ammonium-based ILs listed in Table 3.1 which are ideal for $O_2^{\bullet-}$ generation and utilization.

The entire CV waves (Figure 4.8 a-j) showed cathodic and anodic separations in multiples of 100 mV and the data is shown in Table E.1 (Appendix E). This result is in line with Nicholson suggestion of an irreversible electrochemical process (Nicholson & Shain, 1965). Therefore, this study deduced that $O_2^{\bullet-}$ generation in the ILs is irreversible and available for subsequent utilization. Similarly, the difference between the cathodic peak potential (E_{pC}) and the half peak potential ($E_{pC}/2$) was any number but 56.5 mV, also concurring with Nicholson suggestion. According to Figure F.1 (a-j) (Appendix F), the linearity of current densities to scan rate stripping during the $O_2^{\bullet-}$ generation confirmed a possible scenario of a diffusion-controlled process for reducing O_2 in the IL bulk phase (Islam et al., 2005).

4.3.1.1 Mass transfer phenomena of O_2 in IL

The mass transfer phenomena associated with O_2 reduction in the ILs media were determined by investigating the diffusion coefficient (D_o) and solubility (C_o). According to the data in Table 4.7, the D_o of O_2 in the [EDMPAmm⁺][TFSI⁻], [BMPyrr⁺][TFSI⁻], [MOEMPyrr⁺][PFTP⁻], [MOEMMor⁺][TFSI⁻], [BMIm⁺][TFSI⁻], [PMIm⁺][TFSI⁻], [TBMAMm⁺][TFSI⁻], [BMAMm⁺][TFSI⁻], [MTOAMm⁺][TFSI⁻], and [BMPip⁺][TFSI⁻] are 19.600×10^{-10} , 1.770×10^{-10} , 0.500×10^{-10} , 0.133×10^{-10} , 1.830×10^{-10} , 34.400×10^{-10} , 0.048×10^{-10} , 0.062×10^{-10} , 0.029×10^{-10} and 5.668×10^{-10} m²/s respectively. These D_o values defined a pattern with the ILs viscosities (η ; Table 4.7 column 1 entry). When the viscosities of ILs increase, the D_o of electroactive O_2 through the ILs decreases. This pattern is similar to the previous report in the literature (Ibrahim et al., 2016; Neale et al., 2016). The viscosity values were measured at 25 °C by setting the immersed spindle's speed to 5 rpm, at 6.6 s⁻¹ shear rates on the DV-II⁺ Pro Extra Brookfield viscometer. Comparing the D_o of O_2 to IL's viscosity, for a constant flux of O_2 into IL, diffusion of

O₂ can be influenced by a concentration gradient. For instance, [BMIm⁺][TFSI⁻] experienced the lowest concentration gradient of O₂ because it has the lowest viscosity. Equally, the concentration gradient of O₂ was slightly increased in [EDMPAm⁺][TFSI⁻] because the magnitude of its D_o < magnitude of O₂ D_o in [PMIm⁺][TFSI⁻]. This is considering that the viscosity of [EDMPAm⁺][TFSI⁻] > [PMIm⁺][TFSI⁻]. The concentration gradient of O₂ becomes highest in [MOEMMor⁺][TFSI⁻] whose O₂ D_o is far less than that for [EDMPAm⁺][TFSI⁻] and [PMIm⁺][TFSI⁻]. This result is because [MOEMMor⁺][TFSI⁻] has a relatively high viscosity.

The second mass transfer phenomena are C_o of O₂ in the ILs, as presented in Table 4.7. Unlike D_o, the C_o values did not define a pattern with IL viscosity; hence, it was strongly suggested to be influenced by the nature of IL-cation. For instance, O₂ C_o in [MOEMMor⁺][TFSI⁻] is 14.135 mM (Table 4.7) because the IL-cation has an ether-like functionality (R-O-R) that can create hydrogen bond with dissolved O₂, thereby increasing its solubility values. In accordance, the increasing O₂ solubility in 1-alkyl-3-methylimidazolium cations based ILs were suggested to be due to the occurrence of C-F and C-H bond that induces hydrogen bond with O₂ (Chrobok, Baj, & Swadzba-Kwasny, 2007). There are C-O and C-F bonds in the [MOEMMor⁺] IL-cation, and either O or F is a strong electronegative point charge capable of creating local dipole in the IL-cation ends as a rationale for hydrogen bonding with O₂. Therefore, the absence of C-O or rather ether-like groups in [EDMPAm⁺], [BMPyrr⁺], [BMIm⁺], [PMIm⁺], [BMPip⁺], [TBMA⁺], [BMAm⁺] and [MTOA⁺] IL-cations strongly suggest the reason why the magnitude of their O₂ solubility are less than those observed in [MOEMPyrr⁺] and [MOEMMor⁺] based IL-cations. These results indicate that the distinctive differences between O₂ diffusion and solubility among the ILs listed in Table 3.1 were brought about by the role of ILs viscosity and the presence of ether-like functionality on the IL-cation (Kumelan et al., 2005; Neale et al., 2016). However, the magnitudes of the O₂ diffusion

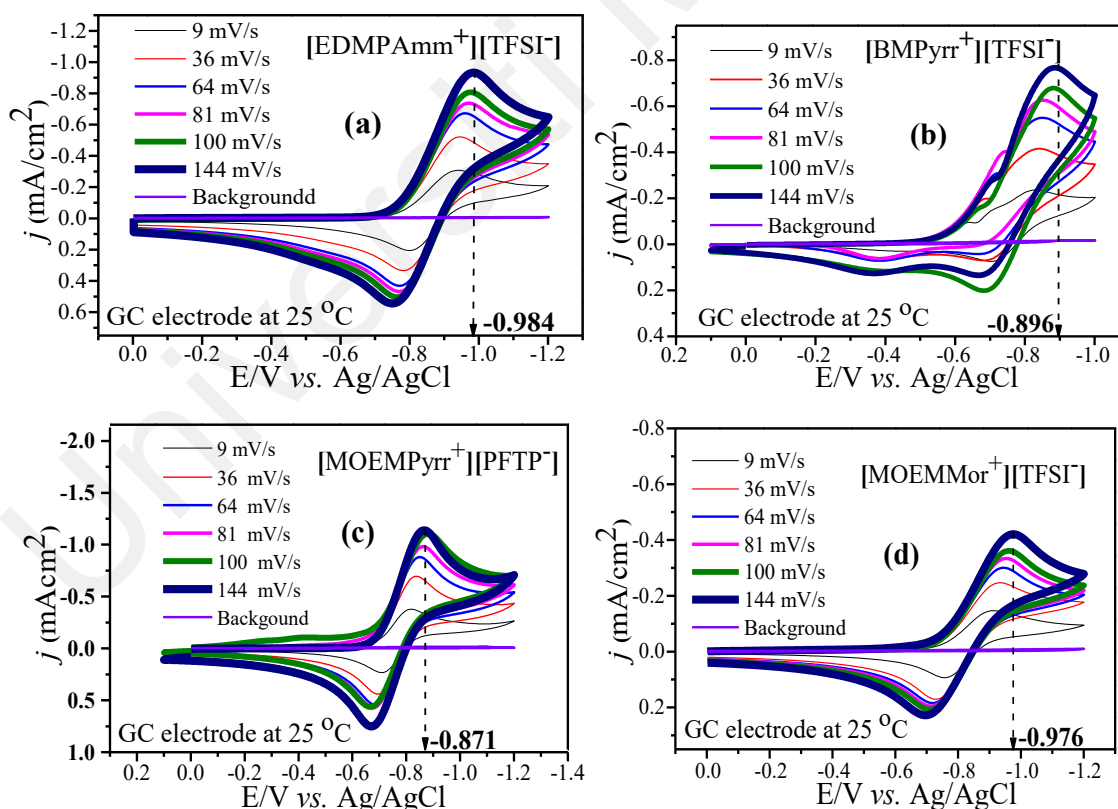
and solubility confirmed molecular transport of O₂ in the ILs system and the absence of eddy diffusion that may arise due to turbulence (Guidelli et al., 2014; He et al., 2006; Molina et al., 2013).

4.3.1.2 Interfacial phenomena for O₂^{•-} generation in IL

The interfacial phenomena during O₂ reduction to O₂^{•-} in ILs was investigated using charge transfer coefficient (α) according to a previous collection of studies (Hayyan et al., 2016). Accordingly, Table 4.7 shows that the charge transfer coefficients for O₂ reduction increase in the following order; [MTOAmm⁺][TFSI⁻]/0.118, [BMPyrr⁺][TFSI⁻]/0.405, [MOEMMor⁺][TFSI⁻]/0.414, [PMIm⁺][TFSI⁻]/0.425, [EDMPAmm⁺][TFSI⁻]/0.441, [BMIm⁺][TFSI⁻]/0.461, [MOEMPyr⁺][PFTP⁻]/0.499, [TBMAmm⁺][TFSI⁻]/0.503, [BMPip⁺][TFSI⁻]/0.535 and [BMAmm⁺][TFSI⁻]/0.544. The numbers beside the IL acronyms are the charge transfer coefficient values (α -value). The α -value that is either < 0.5 implied that the transition state of O₂ reduction to O₂^{•-} as influenced by the variation of applied voltage did not behave midway (Bard et al., 1980). In the case where $\alpha > 0.5$, the transition state of O₂ reduction to O₂^{•-} behave midway on an energy/reaction coordinate profile. Similarly, as Bard et al. (1965) described when $\alpha = 0.5$, there is the symmetry of the energy barrier for the electrochemical reaction where the transition state behaves midway between reactant and product.

All α -values in Table 4.7 have a magnitude that is not zero because of a driving force between the GC electrode material and the O₂ molecule in the ILs. The driving force is ~ 7.6845 eV base on DFT calculations by considering -6.958 eV LUMO energy of O₂ and 0.727 eV HOMO energy of the GC electrode material. In this case, the principal interaction of the molecular orbitals resulting from the GC electrode material to O₂ was based on GC electrode HOMO and O₂ LUMO. In summary, these results indicate that all the ILs can allow favorable transport of charge except [MTOAmm⁺][TFSI⁻]. However, O'Toole et al. (2007) reported that [BMIm⁺] deprotonation by electrogenerated organic

radical anions is feasible. In comparison with AlNashef (2001, 2002) reports on the stability of $O_2^{\bullet-}$ in imidazolium-based ILs, they showed that the rate of $[BMIm]^+$ deprotonation was governed by the basicity of the electrogenerated radical anion (O'Toole, Pentlavalli, & Doherty, 2007). Consequently, they report that the pK_a of the $O_2^{\bullet-}$ was significantly small to promote an unobservable $[BMIm]^+$ deprotonation even at a lower time scale of 9 mV/s. This places imidazolium ILs less desirable for $O_2^{\bullet-}$ utilization. Barnes et al. (2008) reported that a strong association between $O_2^{\bullet-}$ and BDMIm most likely originate from electrostatic interaction of $O_2^{\bullet-}$ and BDMIm, and hydrogen bonding was not possible due to the absence of Brønsted acidity on the 2-position carbon in the BDMIm IL. The formation of the complex impeded the back-electron transfer, and the oxidation peak shifted to a more positive potential than would be expected if this follow-up chemical step (Rogers et al., 2009).



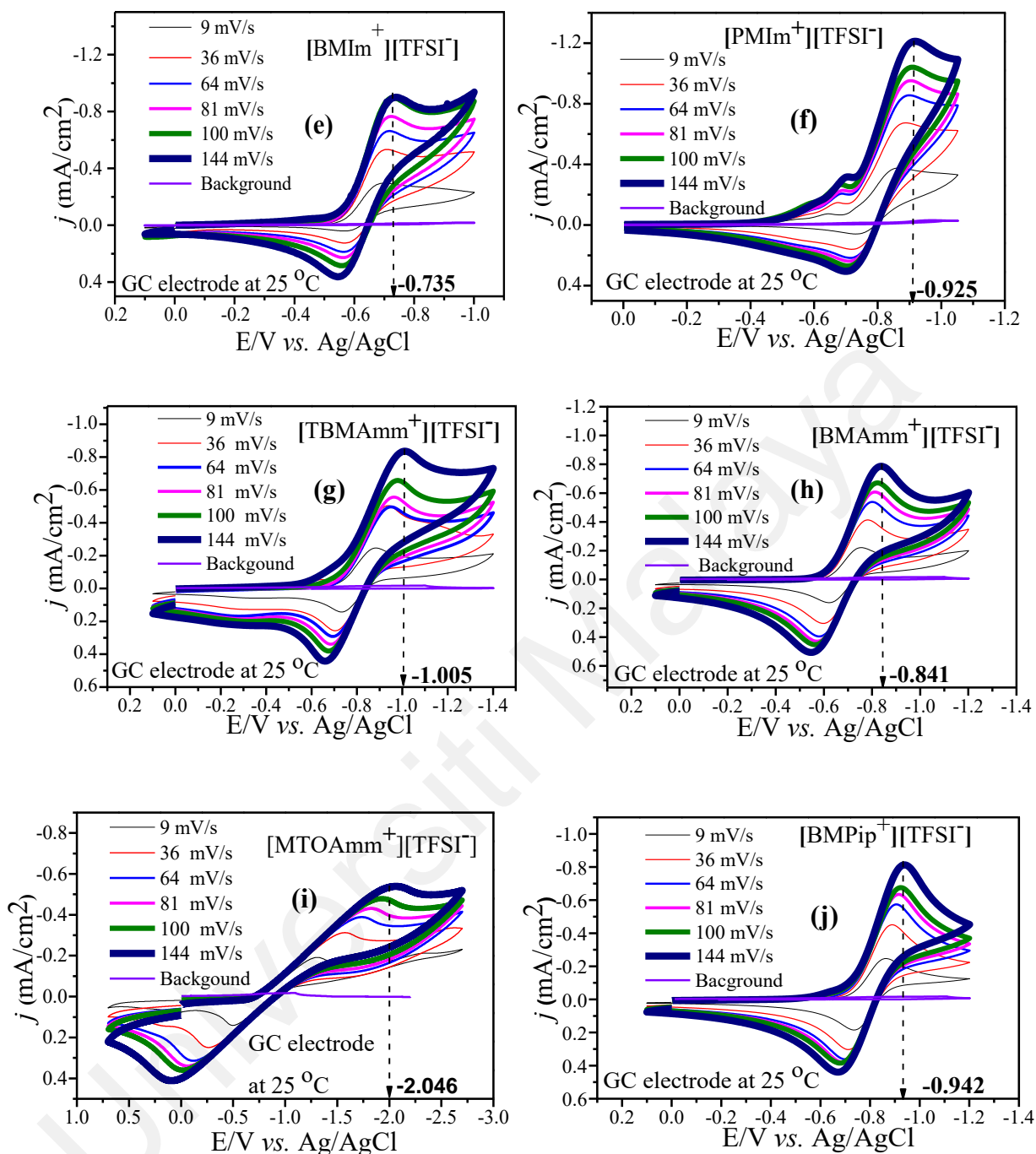


Figure 4.8: CVs of $\text{O}_2^{\bullet-}$ generated in (a) $[\text{EDMPAmm}^+][\text{TFSI}^-]$, (b) $[\text{BMPyrr}^+][\text{TFSI}^-]$, (c) $[\text{MOEMPyrr}^+][\text{PFTP}^-]$, (d) $[\text{MOEMMor}^+][\text{TFSI}^-]$, (e) $[\text{BMIm}^+][\text{TFSI}^-]$, (f) $[\text{PMIm}^+][\text{TFSI}^-]$, (g) $[\text{TBMAMm}^+][\text{TFSI}^-]$, (h) $[\text{BMAMm}^+][\text{TFSI}^-]$, (i) $[\text{MTOAMm}^+][\text{TFSI}^-]$, and (j) $[\text{BMPip}^+][\text{TFSI}^-]$. All the measurements were performed after sparging the IL with N_2 (background) at 25 °C. This is necessary to ensure that ILs are free from impurities as recommended.

Table 4.7: Mass transfer and interfacial parameter of O₂ reduction to O₂^{•-} in ILs*.

IL Abbreviation	η (mPa.S)	$D_o \times 10^{-10}/m^2/s$	C_o/mM	α	CA (nA)
[EDMPAmm ⁺][TFSI ⁻]	63.590	19.600	3.220	0.441	13.400
[BMPyrr ⁺][TFSI ⁻]	11.260	1.770	5.590	0.405	2.100
[MOEMPyrr ⁺][PFTP ⁻]	14.190	0.500	19.020	0.499	2.000
[MOEMMor ⁺][TFSI ⁻]	183.350	0.130	14.140	0.414	0.400
[BMIm ⁺][TFSI ⁻]	7.010	1.830	10.200	0.461	4.000
[PMIm ⁺][TFSI ⁻]	32.990	34.400	2.902	0.425	21.200
[TBMAmm ⁺][TFSI ⁻]	41.180	0.048	0.610	0.503	61.900
[BMAmm ⁺][TFSI ⁻]	78.350	0.062	0.514	0.544	68.000
[MTOAmm ⁺][TFSI ⁻]	237.675	0.029	0.807	0.118	50.000
[BMPip ⁺][TFSI ⁻]	74.460	5.668	2.660	0.535	3.200

* Measurements were done at room temperature.

4.3.1.3 The electrochemical generation of unstable O₂^{•-}

Apart from the fact that some ILs may have a low charge transfer coefficient for O₂ reduction to stable O₂^{•-}, some ILs as media facilitated the generation of unstable O₂^{•-}. All the ILs presented in Table 4.7 in cognisance to Figure 4.8 can be used to generate stable O₂^{•-} with different degree of O₂^{•-} stability. However, since not all the ILs are efficient for stable O₂^{•-} generation, we investigated other ILs such as [BMIm⁺][TCM⁻] and [BMIm⁺][DCA⁻] to demonstrate the unstable generation of unstable O₂^{•-}. Thus, Figure 4.9 show the CV waves corresponding to O₂ reduction to O₂^{•-} but unlike the ones shown in Figure 4.8, the reverse oxidation wave is absent. There are reasons for this kind of observation;

1. O₂^{•-} reversing back to O₂,
2. O₂^{•-} react with the IL-cation or any impurity.

This kind of pattern is usual for generating unstable O₂^{•-} in N-(3-Hydroxypropyl) pyridinium bis (trifluoromethylsulfonyl) imide [HPPy⁺][N(Tf)₂⁻] at -0.780 V vs Ag/Ag/Cl (Hayyan et al., 2011). The O₂^{•-} was found to interact with the [HPPy⁺] cation

consequently making the radical generation unstable. This result is also a confirmation that the ILs interfacial and mass transfer data presented in Table 4.7 in cognisance to CV profiles in Figure 4.8 can generate stable $O_2^{\bullet-}$ for possible utilization. However, the data does not show the viability of the ILs for long-term utilization of the $O_2^{\bullet-}$. Hence the need to further evaluate the long-term stability of the $O_2^{\bullet-}$ in the ILs (e.g. presented in Table 4.7).

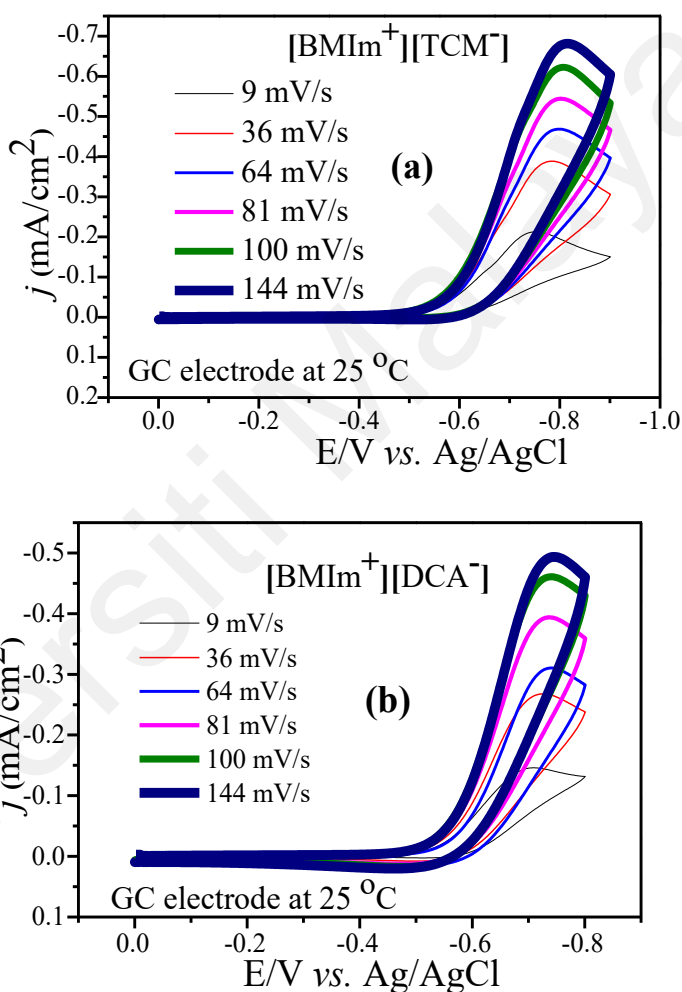


Figure 4.9: CVs of unstable generation of $O_2^{\bullet-}$ in (a) $[BMIm^+][TCM^-]$ and (b) $[BMIm^+][DCA^-]$. This profile was obtained after saturating the ILs with N_2 followed by O_2 .

4.3.1.4 Effect of IL-cation substituents

The substituent nature of IL-cations can influence ILs, such as viscosity (Moosavi et al., 2016). This scenario extends to influence the interfacial and mass transfer data for

$O_2^{\bullet-}$ generation in IL (see Table 4.7). For example, the [MTOAmm⁺][TFSI⁻] (Table 4.7, column 1, entry 9) has the highest viscosity (237.675 mPa.S). Considering [MTOAmm⁺] cation in [MTOAmm⁺][TFSI⁻] compared with other IL-cations in Table 4.7, the high viscosity in [MTOAmm⁺] could be due to the length of alkyl group substituent. In principle, when the length of alkyl substituent is high, Vander Waal interacting centres increases and this attribute is reflected in the media's high viscosity. Consequently, this high viscosity further lowers O_2 diffusion therein. The O_2 diffusion in [MTOAmm⁺][TFSI⁻] is 0.029 m²/s. By comparing with other ILs ([TBMAmm⁺][TFSI⁻], and [BMAmm⁺][TFSI⁻]; Table 4.7, column 1, entries 7 and 8 respectively) O_2 diffusion therein is high (0.048 m²/s and 0.062 m²/s; Table 4.7, column 2 entries 7 and 8). In furtherance, the alkyl group of [PMIm⁺][TFSI⁻] is less than the alkyl chain length in [BMIm⁺][TFSI⁻]. Consequently, the viscosity of [PMIm⁺][TFSI⁻] (7.010 mPa.S) is less than the viscosity of [BMIm⁺][TFSI⁻] (32.990 mPa.S).

Moreover, since these ILs contain no methoxy functionality, their O_2 solubility is low compared with O_2 solubility in [MOEMPyrr⁺][PFTP⁻] and [MOEMMor⁺][TFSI⁻] (Table 4.7). The same comparison applies to [TBMAmm⁺][TFSI⁻] and [BMAmm⁺][TFSI⁻] (Table 4.7); they contain no methoxy functionality; hence, the solubility of O_2 therein is low compared with O_2 solubility in [MOEMPyrr⁺][PFTP⁻] and [MOEMMor⁺][TFSI⁻] (Table 4.7). However, the alkyl chain length of [TBMAmm⁺][TFSI⁻] is higher than the alkyl chain length in [BMAmm⁺][TFSI⁻], and consequently, [TBMAmm⁺][TFSI⁻] has a higher viscosity (Table 4.7). Besides, [BMPip⁺][TFSI⁻] which contain no methoxy group, was correlated with methoxy functionalized piperidinium cation based ILs such as 1-(3-methoxypropyl)-1-methylpiperidinium [MOPMPip⁺] (Hayyan et al., 2012), 1-(3-Methoxypropyl)-1-methylpiperidinium (Hayyan et al., 2017), or 1-(2-Methoxyethyl)-1-methylpiperidinium (Neale et al., 2016). It was found that O_2 has low solubility compared to the family, as

mentioned above of IL. Interestingly, [MOEMPyrr⁺][PFTP⁻] has the highest O₂ solubility (19.020 mM) among all the IL used. Therefore, this study postulate using this particular IL by taking advantage of this solubility attribute.

4.3.2 Chemical generation of stable O₂^{•-}

4.3.2.1 Long-term stability of O₂^{•-}

The Long-term stability of O₂^{•-} can be estimated using UV-visible (UV-vis) analysis. Accordingly, DMSO served as supporting medium for [EDMPAmm⁺][TFSI⁻], [BMPyrr⁺][TFSI⁻], [MOEMPyrr⁺][PFTP⁻], [MOEMMor⁺][TFSI⁻], [BMIm⁺][TFSI⁻], [PMIm⁺][TFSI⁻], [TBMAmm⁺][TFSI⁻], [BMAmm⁺][TFSI⁻], [MTOAmm⁺][TFSI⁻], and [BMPip⁺][TFSI⁻] media for the O₂^{•-} long-term stability study. Initially, the O₂^{•-} UV-Vis excitation wavelength was computed based on time-dependent density functional theory (TD-DFT), as shown in Figure 4.10. Accordingly, wavelengths of water-free O₂^{•-} was estimated to be 255.8 nm and 280.8 nm, respectively. Considering the triple- ζ and double- ζ basis sets, the O₂^{•-} excitation wavelengths upon UV-Vis irradiation were estimated to be 255.8 nm and 280.8 nm, respectively.

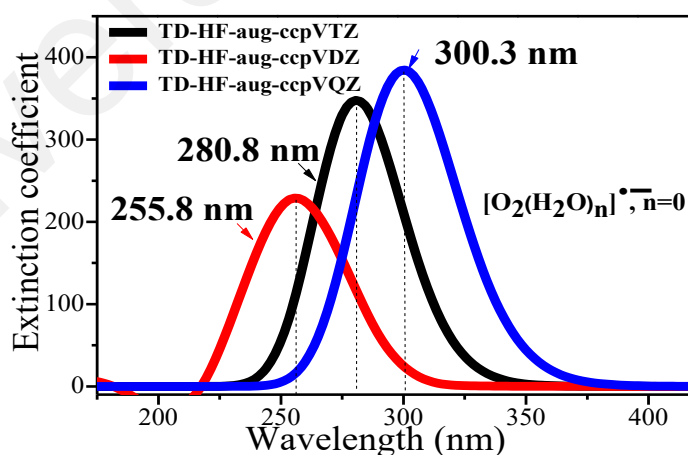


Figure 4.10 Absorbance spectra of O₂^{•-} based on TD-DFT calculation on Gaussian 09 software package. This is a theoretical estimation that guides the experimental observation of water-free O₂^{•-}. The analysis was done in a vacuum where external influence, such as water, is absent.

In cognisance to Figure G.1(c-l) (**Appendix G**), the experimental absorbance spectra of $O_2^{\bullet-}$ generated in [EDMPAmm⁺][TFSI⁻], [BMPyrr⁺][TFSI⁻], [MOEMPyr⁺][PFTP⁻], [MOEMMor⁺][TFSI⁻], [BMIm⁺][TFSI⁻], [PMIm⁺][TFSI⁻], [TBMAMm⁺][TFSI⁻], [BMAMm⁺][TFSI⁻], [MTOAMm⁺][TFSI⁻], and [BMPip⁺][TFSI⁻] appeared at ~ 255-259 nm. These wavelength range for $O_2^{\bullet-}$ is within the value obtained theoretically (see Figure 4.10). The implication of this result is that the $O_2^{\bullet-}$ detected in the ILs are water free or non-solvated. This is an excitation after irradiation and it is within 250-270 nm range of literature reports (Islam et al., 2009; Hayyan et al., 2012; Ahmed et al., 2015).

4.3.2.2 Kinetics of $O_2^{\bullet-}$ in ILs

Figure G.1 (Appendix G) show the effect of time on the maximum absorbance of $O_2^{\bullet-}$ chemically generated in the ILs supported by DMSO (Table 3.1). The absorbance peak of $O_2^{\bullet-}$ reduce with time.

The rate constant associated with the reduction of $O_2^{\bullet-}$ absorbance in the ILs is shown in Table 4.8. By implication, the decrease in absorbance of $O_2^{\bullet-}$ signifies the reaction between $O_2^{\bullet-}$ and the ILs-cation. Therefore, the rate constants in Table 4.8 were calculated based on the first and second-order reaction kinetics described by equation 3.11 to 3.16. In these cases, using the equations to fit the data, the rate constants for $O_2^{\bullet-}$ decay in the ILs either follow first or second order.

The ILs in which $O_2^{\bullet-}$ follows first-order are; [BMIm⁺][TFSI⁻], [PMIm⁺][TFSI⁻], [MTOAMm⁺][TFSI⁻], and [BMPip⁺][TFSI⁻]. This shows that only the concentration of one component affects the decay of $O_2^{\bullet-}$ therein. According to the rate constants for these IL, the $O_2^{\bullet-}$ decay in [PMIm⁺][TFSI⁻] is faster because the rate constant was determined to be $6.730 \times 10^{-5} \text{ s}^{-1}$. This can be affirmed by comparing the rate constants of $O_2^{\bullet-}$ decay in the ILs. Accordingly, the rate constants varied in the increasing order of [BMPip⁺][TFSI⁻] ($0.610 \times 10^{-5} \text{ s}^{-1}$), [MTOAMm⁺][TFSI⁻] ($0.820 \times 10^{-5} \text{ s}^{-1}$),

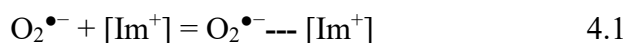
[BMIm⁺][TFSI⁻] ($1.910 \times 10^{-5} \text{ s}^{-1}$), [PMIm⁺][TFSI⁻] ($6.730 \times 10^{-5} \text{ s}^{-1}$). By general comparison, these values are lower than the ones reported for O₂^{•-} decay in [EMI⁺][BF₄⁻] supported by DMSO supporting solvent, which was $2.5 \times 10^{-3} \text{ s}^{-1}$ (Islam et al., 2009). In specific comparison for imidazolium cation, the values for [BMIm⁺][TFSI⁻] ($1.910 \times 10^{-5} \text{ s}^{-1}$) is close to [BMIm⁺][HFP⁻] and 1-ethyl-3-methylimidazolium ethyl sulfate, which are $2.1 \times 10^{-5} \text{ s}^{-1}$ and $1.7 \times 10^{-5} \text{ s}^{-1}$ respectively (AlNashef et al., 2010).

The ILs in which O₂^{•-} follows second order are [EDMPAmm⁺][TFSI⁻], [BMPyrr⁺][TFSI⁻], [MOEMPyrr⁺][PFTP⁻], [MOEMMor⁺][TFSI⁻], [TBMAMm⁺][TFSI⁻], [BMAMm⁺][TFSI⁻] (Table 4.8). This also shows that the concentration of two components affects O₂^{•-} decay therein. Along with these observation the rate constant shows that O₂^{•-} decay in [MOEMMor⁺][TFSI⁻] is faster. Accordingly, the rate constants for O₂^{•-} decay in the ILs following second order kinetics varied in the following increasing order; [MOEMPyrr⁺][PFTP⁻] ($0.080 \text{ M}^{-1}\text{s}^{-1}$), [BMAMm⁺][TFSI⁻] ($0.100 \text{ M}^{-1}\text{s}^{-1}$), [TBMAMm⁺][TFSI⁻] ($0.240 \text{ M}^{-1}\text{s}^{-1}$), [EDMPAmm⁺][TFSI⁻] ($0.330 \text{ M}^{-1}\text{s}^{-1}$), [BMPyrr⁺][TFSI⁻] ($0.740 \text{ M}^{-1}\text{s}^{-1}$) and [MOEMMor⁺][TFSI⁻] ($4.900 \text{ M}^{-1}\text{s}^{-1}$). Particularly, the value for O₂^{•-} in DMSO solvent containing [BMAMm⁺][TFSI⁻] was close to the value for O₂^{•-} in DMSO solvent containing [EDMPAmm⁺][TFSI⁻] which was estimated to be $0.006 \text{ M}^{-1}\text{s}^{-1}$ after 3 h (Hayyan et al., 2017). Similarly, the second order kinetic rate constant for O₂^{•-} decay in [BMPip⁺][TFSI⁻] which is $0.140 \text{ M}^{-1}\text{s}^{-1}$ is similar in value $0.150 \times 10^{-5} \text{ M}^{-1}\text{s}^{-1}$ in [MOPMPip⁺][TFSI⁻] (Hayyan et al., 2017).

Table 4.9 shows the total consumption of O₂^{•-} in ILs, which was calculated by comparing the initial concentration of O₂^{•-} with the concentration along 3 h of measurement. The result show that only 3.820 %, 4.810 %, 8.520 %, 14.258 %, 8.380 %, 6.290 %, 8.270 % of the initial O₂^{•-} in [MOEMPyrr⁺][PFTP⁻], [MOEMMor⁺][TFSI⁻], [EDMPAmm⁺][TFSI⁻], [TBMAMm⁺][TFSI⁻], [BMAMm⁺][TFSI⁻], [MTOAmm⁺][TFSI⁻] and [BMPip⁺][TFSI⁻] were consumed after 3 h of reaction time. In comparison,

for instance, the percentage of $O_2^{\bullet-}$ consumption in [BMPip⁺][TFSI⁻] which is 8.270 % is lower than that detected in [MOMPip⁺][TFSI⁻] which is was 27.320 % (Hayyan et al., 2017). This $O_2^{\bullet-}$ consumption difference in the two ILs can be attributed to the presence of methoxy functionality (-OCH₃) in [MOMPip⁺][TFSI⁻]. In the literature, O-atom's presence can exacerbate the alkyl group's electron-donating potential (-CH₃) (Burie et al., 1997). Consequently, this induces an electron-withdrawing tendency by the methoxy functionality, especially in piperidinium cation, thereby inducing the $O_2^{\bullet-}$ nucleophilicity effect. This could potentially halt the methoxy functionalized piperidinium-based IL's capacity to be sustainably used for stable $O_2^{\bullet-}$ generation and utilization. Other ILs such as [BMPyrr⁺][TFSI⁻], [BMIm⁺][TFSI⁻], and [PMIm⁺][TFSI⁻] indicated 16.45 %, 18.19 % and 47.92 % consumption of the generated $O_2^{\bullet-}$.

In general, these results are similar to reports in the literature (Hayyan et al., 2016; Hayyan et al., 2012; Schwenke et al., 2015). However, from this study's viewpoint, imidazolium-based ILs are not recommended for $O_2^{\bullet-}$ utilization since their $O_2^{\bullet-}$ consumption is high. Also, methoxy functionalized piperidinium-based IL are not suitable for $O_2^{\bullet-}$ utilization since O-atom's presence can exacerbate the ILs, making it susceptible to nucleophilic attack. In this case, non-methoxy functionalized piperidinium based IL such as [BMPip⁺][TFSI⁻] is suitable for $O_2^{\bullet-}$ utilization applications. The imidazolium-based ILs are not suitable because of their inherent complexation with $O_2^{\bullet-}$ following the mechanism proposed describing ion-pairing in Eq 4.1 (Katayama et al., 2004; Rogers et al., 2009). The consequence of this complexation is the production of imidazolones (AlNashef et al., 2010; Hayyan et al., 2013; Islam et al., 2009). Therefore, the use of non-imidazolium-based IL for $O_2^{\bullet-}$ utilization applications has eliminated the possibility of ion-pairing commonly reported for imidazolium ILs.



This study's viewpoint considered that methoxy functionalized ILs with [PFTP⁻] anion could have a suitable combination of properties. For instance, [MOEMPyrr⁺][PFTP⁻] has high O₂ solubility (19.020 mM), low O₂^{•-} total consumption (3.820 %/180 min) and low kinetic rate constant (0.08 M⁻¹s⁻¹) for O₂^{•-} reaction with the IL cation (see Table 4.8). As a result, the nanofluid development and usage for CO₂ conversion by O₂^{•-} in this study focused on [MOEMPyrr⁺][PFTP⁻].

Table 4.8: Rate constant of O₂^{•-} chemically generated in ILs.

Abbreviation	1 st Order Rate Constant × 10 ⁵ (s ⁻¹)	R ² of Rate Constant	2 nd Order Rate Constant × 10 ² (M ⁻¹ s ⁻¹)	R ² of Rate Constant
[EDMPAmm ⁺][TFSI ⁻]	0.710	0.910	0.330	0.930
[BMPyrr ⁺][TFSI ⁻]	1.700	0.930	0.740	0.970
[MOEMPyrr ⁺][PFTP ⁻]	0.340	0.912	0.080	0.940
[MOEMMor ⁺][TFSI ⁻]	1.710	0.920	4.900	0.930
[BMIm ⁺][TFSI ⁻]	1.910	0.970	0.320	0.960
[PMIm ⁺][TFSI ⁻]	6.730	0.860	70.250	0.840
[TBMamm ⁺][TFSI ⁻]	1.370	0.906	0.240	0.916
[BTMamm ⁺][TFSI ⁻]	0.820	0.989	0.150	0.991
[MTOamm ⁺][TFSI ⁻]	0.610	0.967	0.170	0.961
[BMPip ⁺][TFSI ⁻]	0.650	0.821	0.140	0.828

Table 4.9: Total consumption percentage and consumption rate of O₂^{•-} in ILs.

Abbreviation	Total Consumption % of O ₂ ^{•-} After 180 min.	Consumption Rate of O ₂ ^{•-} × 10 ³ (mM/min.)
[EDMPAmm ⁺][TFSI ⁻]	8.520	1.600
[BMPyrr ⁺][TFSI ⁻]	16.450	2.300
[MOEMPyrr ⁺][PFTP ⁻]	3.820	0.940
[MOEMMor ⁺][TFSI ⁻]	4.810	0.350
[BMIm ⁺][TFSI ⁻]	18.100	6.700
[PMIm ⁺][TFSI ⁻]	47.920	0.340
[TBMamm ⁺][TFSI ⁻]	8.250	4.960
[BTMamm ⁺][TFSI ⁻]	8.380	3.480
[MTOamm ⁺][TFSI ⁻]	6.290	1.300
[BMPip ⁺][TFSI ⁻]	8.270	2.220

4.4 Conversion of CO₂ to Peroxydicarbonate (C₂O₆²⁻) Using IL Media

To examine the capability of the generated O₂^{•-} in a plausible application, the utilization of O₂^{•-} in converting CO₂ was investigated. The conversion of CO₂ is a crucial

environmental concern and an essential subject of many investigations. Unfortunately, previous studies only explored aprotic solvents or ILs and it was recommended that media that are stable amidst $O_2^{\bullet-}$ environment be developed (AlNashef et al., 2002; Feroci et al., 2011; Maan Hayyan, Hashim, & AlNashef, 2016). Therefore, in this section, other ILs that could suitably retain $O_2^{\bullet-}$ were employed to investigate the CO_2 conversion.

4.4.1 Using ILs as media

The use of ILs to convert CO_2 was motivated by the $O_2^{\bullet-}$ long-term stability, as described in section 4.3.2.1 (see Table 4.8 and Table 4.9). Accordingly, Figure 4.11 (a-g) shows cyclic voltammograms (CV) for the CO_2 conversion by $O_2^{\bullet-}$ in the ILs. These ILs are structurally different from the collections of ILs that were used for CO_2 capture (Babamohammadi, Shamiri, & Aroua, 2015; Ramdin, de Loos, & Vlugt, 2012; Sadeghpour et al., 2017; Torralba-Calleja, Skinner, & Gutiérrez-Tauste, 2013; Zeng et al., 2017). Hence, all the ILs used for CO_2 conversion by $O_2^{\bullet-}$ as presented in Figure 4.11 (a-g) are novel in their application for $O_2^{\bullet-}$ mediated CO_2 conversion. According to the chemical interaction between the captured CO_2 in the ILs with $O_2^{\bullet-}$, the CO_2 conversion process as shown in Figure 4.11 (a-g) was rationalized into three distinct CV waves as follows:

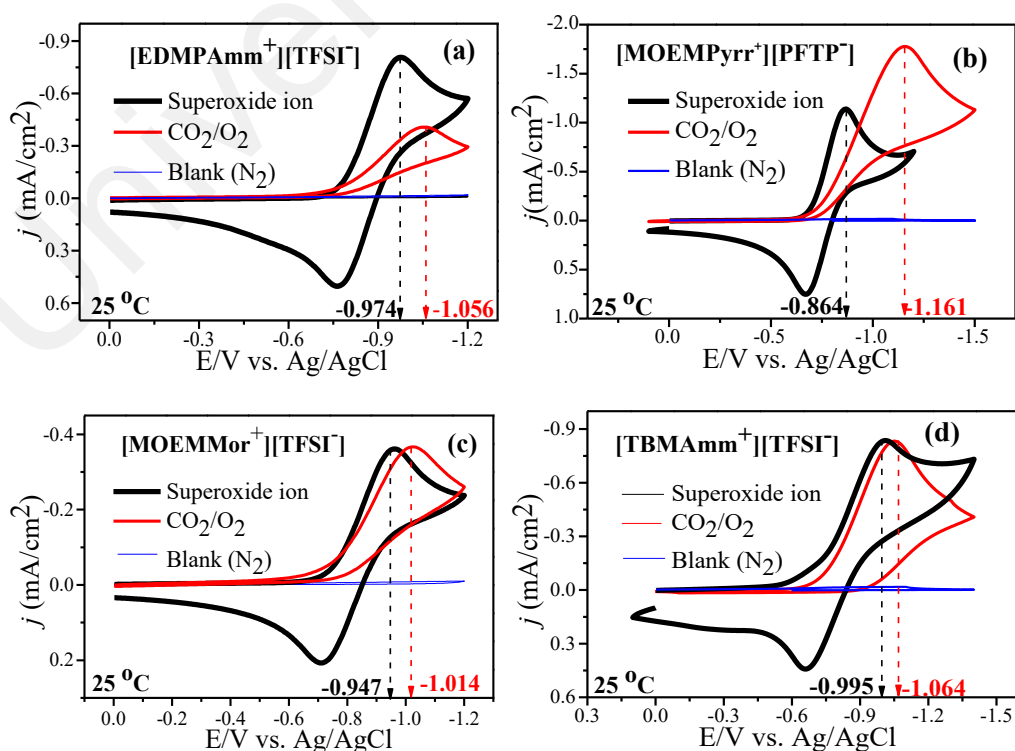
1. The background with no observable faradaic current after saturating the ILs with N_2 .
2. The proof of $O_2^{\bullet-}$ generation due to the presence of redox faradaic currents after saturating the ILs with O_2 .
3. The disappearance of the reverse oxidation wave for $O_2^{\bullet-}$ after saturating the ILs with O_2 and CO_2 .

The indication for CO_2 conversion and $O_2^{\bullet-}$ utilization is by the shift in the potential for $O_2^{\bullet-}$ to a more negative value. In this case, the forward peak in the direct reduction appears at -1.056 , -1.161 , -1.014 , -1.064 , -0.935 , -1.974 and -1.517 V vs

Ag/AgCl. Before CO₂ conversion, the peak potentials were -0.974, -0.864, -0.947, -0.995, -0.822, -1.420, -0.934 V vs Ag/AgCl. These values indicated that the O₂^{•-} mediated conversion of CO₂ to the ILs. Overall, the results show that the ILs contained no electrochemically active impurities and O₂^{•-} is functional to transform CO₂ at the onset. However, the conversion of CO₂ in [MTOAmm⁺][TFSI⁻] is energy-intensive owing to the high potential (-1.974 V vs Ag/AgCl) it takes to transform CO₂ by O₂^{•-} (see Figure 4.11f). Therefore, the CO₂ transformation by O₂^{•-} like other IL media was confirmed by the disappearance of the oxidation faradaic current for the CO₂/O₂^{•-} couple (Figure 4.11a-g). In cognizance to previous reports, the transformation of the CO₂ by O₂^{•-} strongly suggested an in-situ synthesis of peroxy-dicarbonate (C₂O₆²⁻) as the primary product (Casadei et al., 1997; Roberts et al., 1984). These literature reports are different from this study because they conducted the CO₂ conversion by O₂^{•-} in an aprotic solvent, not ILs.

Sawyer et al. (1995) suggested this phenomenon signify a two-step sequence in which O₂^{•-} is formed, followed by irreversible utilization of CO₂ to form C₂O₆²⁻ anion. AlNashef et al., (2002) reconfirmed that the phenomenon also signifies a two-step sequence of O₂^{•-} with irreversible utilization by CO₂ to form C₂O₆²⁻ anion. AlNashef et al., (2002) synthesised C₂O₆²⁻ in 1-n-butyl-3-methylimidazolium hexafluorophosphate ([BMIm⁺][HFP⁻]), and their CV wave is similar to the ones presented in Figure 4.11a-f. For a constant saturated amount of CO₂ and O₂, in the ILs, the peak current in the reduction direction increases. This is the opinion of AlNashef et al., (2002) and Julian et al., (1984). Meaning CO₂ consumption by O₂^{•-} usually have a doubling of the reduction peak as evidence for C₂O₆²⁻ formation. Other studies followed suit by indirectly showing evidence of C₂O₆²⁻ formation by carboxylating other groups directly in addition to the doubling of the reduction peak (Robert et al., 1984; Islam et al., 2005; Casadei et al., 1997).

In cognizance of the global electrophilicity index (ω) described in section 4.2, the doubling effect of the faradaic reduction peak is not tenable, especially when the electrophilicity index of the reacting medium is greater than CO_2 . For instance, the global electrophilicity index of tetraethylammonium perchlorate (TEAP), i.e., the supporting medium usually used for $\text{O}_2^{\bullet-}$ generation (Robert et al., 1984), is $\omega = 3.82$ eV. This value is greater than the combined global electrophilicity index of all the ILs reported in Table 3.1 including CO_2 . Therefore, the high value of TEAP global electrophilicity index would make it attractive for reduction by $\text{O}_2^{\bullet-}$, and subsequently inducing the doubling effect of reduction peak current. On the contrary, when 1-butyl-3-methylimidazolium Hexafluorophosphate; $[\text{BmIm}^+][\text{HFP}^-]$ was used for CO_2 conversion by $\text{O}_2^{\bullet-}$ as evidenced by AlNashef et al., (2002), the CV did not show the doubling effect of reduction current. The $[\text{BmIm}^+][\text{HFP}^-]$ has a global electrophilicity index of $\omega = 1.728$ eV which is roughly doubled that for $[\text{PmIm}^+][\text{TFSI}^-]$ for instance. Hence in this context of ω , the order of $\text{O}_2^{\bullet-}$ increase in susceptibility in IL/ $\text{O}_2^{\bullet-}$ / CO_2 system will be in $[\text{BmIm}^+][\text{HFP}^-]$, $[\text{PmIm}^+][\text{TFSI}^-]$.



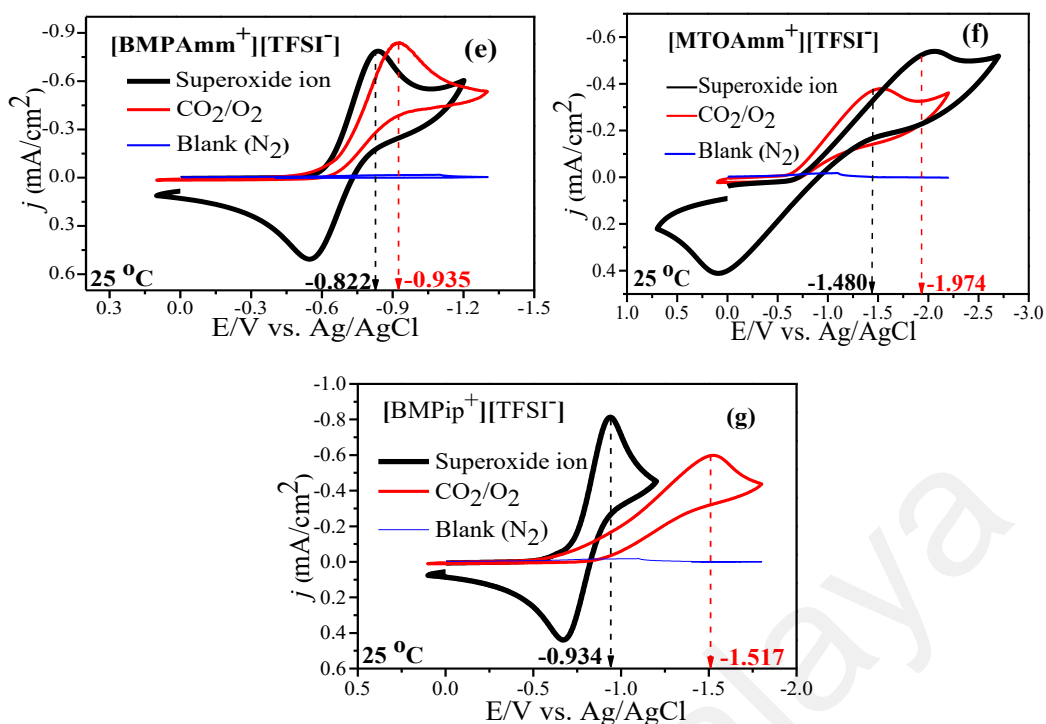


Figure 4.11: Cyclic voltammograms (CVs) of CO₂ conversion by O₂^{•-} in (a) [EDMPAmm⁺][TFSI⁻], (b) [MOEMPyrr⁺][PFTP⁻], (c) [MOEMMor⁺][TFSI⁻], (d) [TBMAmm⁺][TFSI⁻], (e) [BMAmm⁺][TFSI⁻], (f) [MTOAmm⁺][TFSI⁻] and (g) [BMPipm⁺][TFSI⁻] after continuously sparging the ILs with N₂ (Background), or O₂ or simultaneously sparging the ILs with CO₂/O₂. Measurement were recorded at 9 mV/s.

4.4.1.1 Spectroscopic identification of C₂O₆²⁻

In this study, the C₂O₆²⁻ produced in IL from the CO₂ conversion by O₂^{•-} was detected using ATR-IR and supported by theoretical DFT-IR for the first time.

i. Experimental ATR-IR identification of C₂O₆²⁻ anion

The experimental ATR-FTIR shown in Figure B.3a (Appendix B) revealed many vibrations centered at 510 cm⁻¹, 571 cm⁻¹, 608 cm⁻¹, 653.6 cm⁻¹, 742.1 cm⁻¹, 792.7 cm⁻¹, 844 cm⁻¹, 1050.6 cm⁻¹, 1133.03 cm⁻¹, 1175.8 cm⁻¹, 1346 cm⁻¹ and 1577.9 cm⁻¹. The blank ATR-FTIR experiment (Figure B.3a) has additional peaks centred at 885.8 cm⁻¹ and 952.42 cm⁻¹. Among these frequencies, the one of interest herein was the correspondence of O=O symmetric stretching which was centred at 844 cm⁻¹ (Figure

B.3a, measure at 27 °C, 35 °C, and 45 °C). This frequency of vibration for $C_2O_6^{2-}$ generated in $[PMIm^+][TFSI^-]$ at the different temperatures remained similar throughout.

Table 4.10, column 2 also show the frequency of vibrations for experimental ATR-FTIR detection of $C_2O_6^{2-}$ anion generated in $[BMAMm^+][TFSI^-]$ at room temperature. There are ten characteristic vibration centered at 608, 654, 742, 793, 844, 1051, 1133, 1176, 1346 and 1578 cm^{-1} . These vibration frequencies are similar to the blank $[BMAMm^+][TFSI^-]$ which contained no $C_2O_6^{2-}$. The blank peaks are the same with $[BMAMm^+][TFSI^-]$ containing $C_2O_6^{2-}$ except the vibration at 844 cm^{-1} .

ii. DFT-IR identification of $C_2O_6^{2-}$

The Mulliken charges of the $C_2O_6^{2-}$ anion computed at the DFT level of theory confirmed the presence of dipole moments initiators that enable the $C_2O_6^{2-}$ anion to be IR active Table B.2 (Appendix B). The $C_2O_6^{2-}$ anion is an asymmetric top molecule that did not possess an axis of symmetry (Lin et al., 2018). This absence of symmetry axis implied that there was no preferred direction for $C_2O_6^{2-}$ anion to carry out a simple rotation around the total angular momentum. Consequently, the experimental FTIR peak could be broad. However, the DFT-FTIR spectrum of $C_2O_6^{2-}$ anion (Figure B.3b) taking into consideration its symmetry operations, have five visible characteristic harmonics centred at 576.7 cm^{-1} , 730.9 cm^{-1} , 805 cm^{-1} , 1267 cm^{-1} and 1708 cm^{-1} . In specifics, the harmonic which centred at 805 cm^{-1} was attributed to O=O symmetric stretching vibration in $C_2O_6^{2-}$ anion. Other characteristic vibrations mentioned earlier are peculiar to O=C=O rocking and wagging (734 cm^{-1}), and also the scissoring of O=C=O at 1705 cm^{-1} . Comparing the characteristic vibration of $C_2O_6^{2-}$ anion at 734 cm^{-1} and 805 cm^{-1} as much as others, O=C=O harmonic may not have the singularity for $C_2O_6^{2-}$ anion identification in IL. This is owing to the occurrence of more than one particular harmonic at a given wavenumber. This was unlike the vibration at 805 cm^{-1} which only showed O=O

symmetric stretching without another visible harmonic in the $C_2O_6^{2-}$ anion molecular structure.

By comparing between the DFT-FTIR spectrum and the experimental ATR-FTIR spectrum there was an evident blue shift for energy for the O=O harmonics to the tune of 39 cm^{-1} . This blue shift was usual especially as evidence of $C_2O_6^{2-}$ anion coordination on the IL-cation. Otherwise, the blue shift deviation can mainly be brought about by the complexity to involve all influencing factors existing in the ATR-FTIR analysis of post electrosynthesized $C_2O_6^{2-}$ in DFT-FTIR for $[PMIm^+][TFSI^-]/C_2O_6^{2-}$ during the theoretical DFT analysis. Consequently, the energy for harmonics based on DFT-FTIR calculation was less than that of the experimental ATR-IR analysis. Also, the experimental O=O symmetric stretching has a broadband peak, unlike the DFT-FTIR spectrum whose peak was sharp. Usually, electronic transition in liquids or gases is not resolved because it is accompanied by either rotational transition that causes energy fluctuation with the broadband peak as the relic (Larkin, 2017; Perakis et al., 2016; Sathyanarayana, 2015). Resolving this energy fluctuation was complex to be involved in DFT calculation more so, the DFT-FTIR spectrum, which simulated $C_2O_6^{2-}$ anion in an ideal vacuum environment, possessed sharp FTIR peaks as though only vibrational and no rotational transition existed. In a previous study, $C_2O_6^{2-}$ was identified in substances like carbonate and these blue shift observation were a common attribute of $C_2O_6^{2-}$ when coordinated to other groups such as K, $(Me_2N)_2$, Rb, Cs and (Me_4N) . Accordingly, the value of O=O stretching vibration frequency occurring at 844 cm^{-1} in the IL is comparable with the literature value of $\sim 851\text{ cm}^{-1}$ or 868 cm^{-1} IR band assigned to O=O stretching vibration of $C_2O_6^{2-}$ in media involving K, $(Me_2N)_2$, Rb, Cs and (Me_4N) (Chen et al., 2004; Giguère & Lemaire, 1972; Jones & Griffith, 1980; Roberts, Calderwood, & Sawyer, 1984).

Table 4.10: Comparing DFT/B3LYP/6-31G-IR and ATR-IR for $C_2O_6^{2-}$ in $[TBMamm^+][TFSI^-]$

Assignment	Wavenumber (cm^{-1})			Definitions
	DFT-IR	ATR-IR		
		25 °C	Blank	
O=O and O=C=O	620	608	608	O=O and O=C=O rocking,
O=O and O=C=O	661	654	654	O=O and O=C=O rocking,
O=C=O	731	-		O=C=O symmetric stretching
O=C=O	737	742	742	O=C=O symmetric stretching
O=C=O	789	793	793	O=C=O symmetric bending
O=O	805	-	-	O=O symmetric stretching
O=O	846	844	-	O=O asymmetric twisting
O=C=O	-	1051	1051	O=C=O symmetric stretching
O=C=O	1272	1346	1346	O=C=O symmetric stretching

4.4.2 Mechanism of CO_2 conversion by $O_2^{\bullet-}$ to $C_2O_6^{2-}$ in IL

The electrochemical impedance spectroscopy (EIS) analysis in potentiostatic mode can detect the mechanism of $O_2^{\bullet-}$ mediated CO_2 conversion in $[BMamm^+][TFSI^-]$ medium. The EIS measurement was conducted at voltage of -0.773 , -0.360 , and -0.360 V vs. Ag/AgCl for O_2 -saturated- $[BMamm^+][TFSI^-]$, CO_2 -saturated- $[BMamm^+][TFSI^-]$ and O_2/CO_2 -saturated- $[BMamm^+][TFSI^-]$ electrolytes respectively. These voltages are slightly above the equilibrium voltage of the system. At the equilibrium voltage of the system, there would not be any catalytic activity. Therefore, the EIS spectra detected in the O_2 -saturated- $[BMamm^+][TFSI^-]$, CO_2 -saturated- $[BMamm^+][TFSI^-]$ and O_2/CO_2 -saturated- $[BMamm^+][TFSI^-]$ electrolytes above the equilibrium voltage are represented in Figure 4.12. In the O_2 -saturated- $[BMamm^+][TFSI^-]$ and O_2/CO_2 -saturated- $[BMamm^+][TFSI^-]$ electrolyte (Figure 4.12a and 4.12b), the Nyquist plot shows a typical feature:

1. In the high frequency (region-1), there is a small semi-circle, which corresponds to an electron transfer process.
2. By contrast, in the low-frequencies (region-2), a bigger semi-circle was detected, showing a total of two circles that correspond to two-time scales

that are associated with resistor capacitance circuit (EC) (Lates et al., 2014; Torresi et al., 2013).

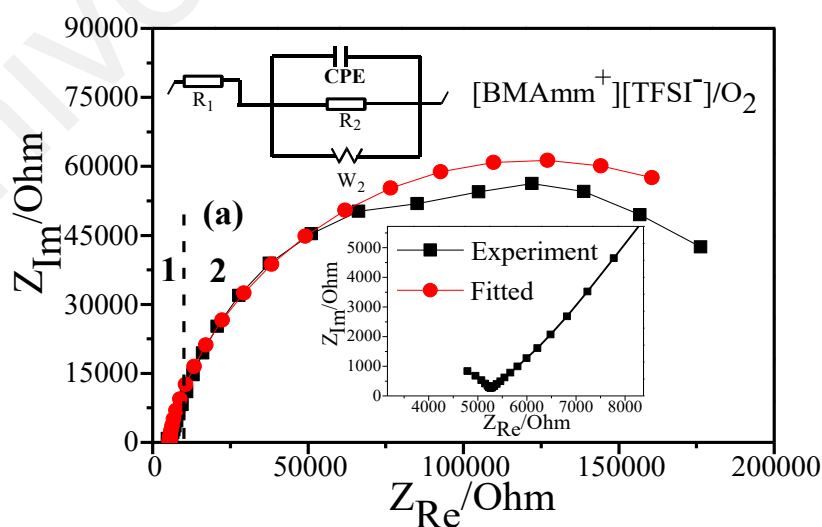
The EIS was modelled by modified Randles EC as illustrated in the inset of Figure 4.12 a-c. $R_1=R_e$ is electrolyte resistance, $R_2=R_{ct}$ is the charge transfer resistance, C_2 is the double-layer capacitance, and W is the Warburg impedance. Therefore, the EC is described by four EIS elements or parameters. As for CO_2 -saturated-[BMAm⁺][TFSI⁻] medium, there is also a small semi-circle at high frequency (region-1) and a straight line at the low-frequency (region-2) (Figure 4.12c). This straight-line pattern is usually associated with the diffusion-limited process.

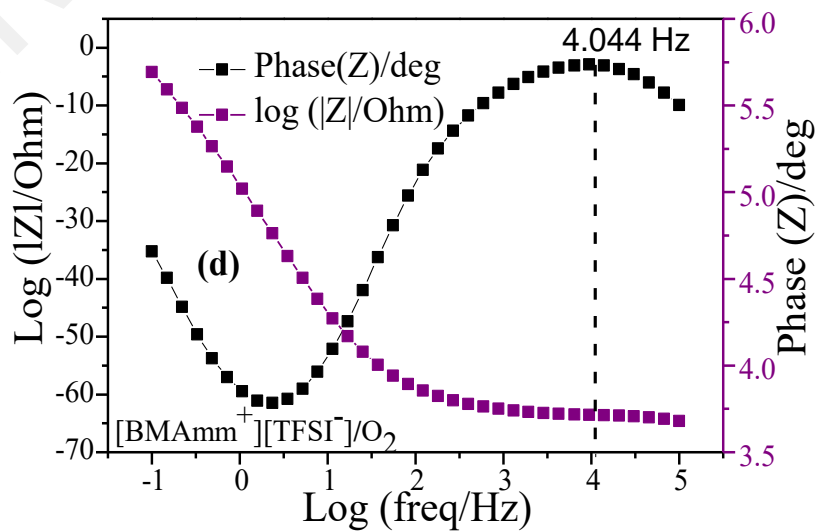
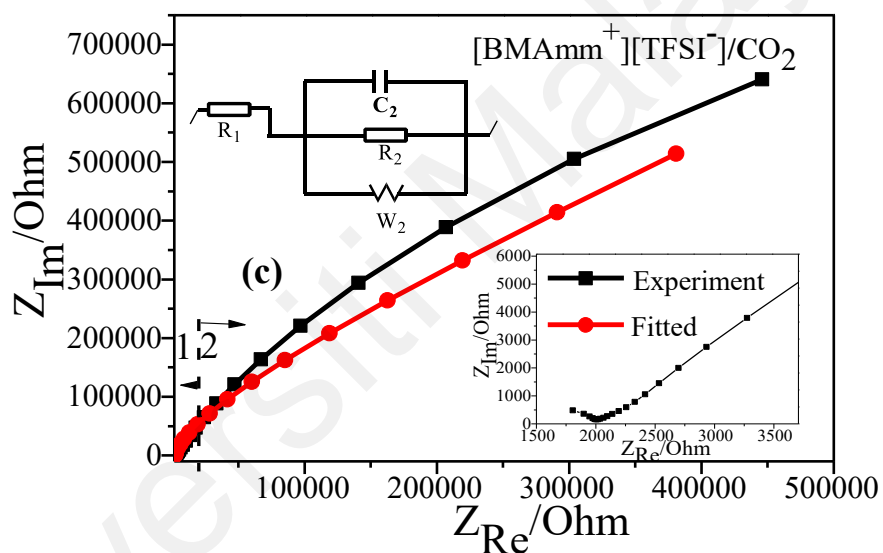
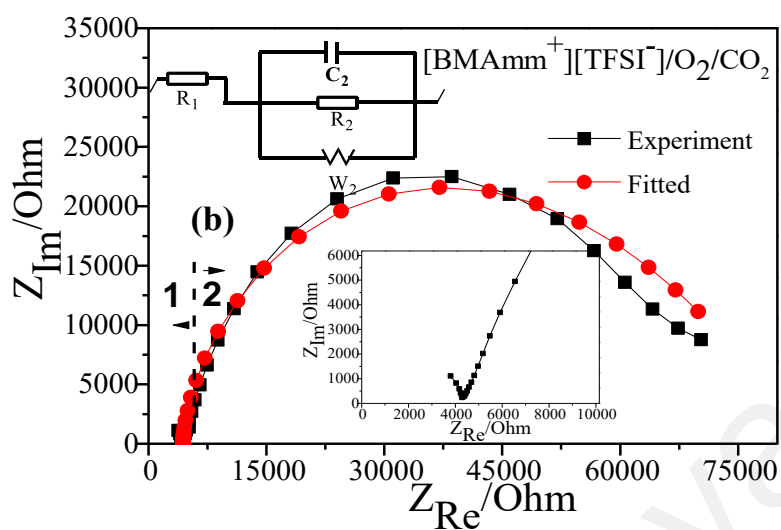
It was found that the R_e according to the high-frequency region-1 in Figure 4.12 a-c, varied in the following order; 5.467, 4.378, and 2.116 k Ω for O_2 -saturated-[BMAm⁺][TFSI⁻], CO_2 -saturated-[BMAm⁺][TFSI⁻], and O_2/CO_2 -saturated-[BMAm⁺][TFSI⁻] electrolytes respectively.

Accordingly, in these media, the double layer capacitance (C_2) also varies in the following order; 5.897, 7.764, and 7.507 $\mu\text{F}/\text{cm}^2$. These C_2 values implied that the mechanism of O_2 reduction to $\text{O}_2^{\bullet-}$ and the subsequent CO_2 utilization by $\text{O}_2^{\bullet-}$ in these media were associated with different charge mobility. The reasonable explanation is that the [BMAm⁺][TFSI⁻] got adsorbed on the GC electrode's surface to form a thin film layer. Therefore, while sparging O_2 , CO_2 or O_2/CO_2 , the gases were absorbed by the [BMAm⁺][TFSI⁻]. Consequently, these contributed to different polarizations that amount to different double layer capacitances. In furtherance, the charge transfer resistance (R_{ct}) revealed that the process is faster in O_2/CO_2 -saturated-[BMAm⁺][TFSI⁻] ($R_{ct} = 79 \text{ k}\Omega$). This R_{ct} is lower than the ones detected in O_2 -saturated-[BMAm⁺][TFSI⁻] ($R_{ct} = 261.467 \text{ k}\Omega$) or CO_2 -saturated-[BMAm⁺][TFSI⁻] ($R_{ct} = 6.86 \times 10^{18} \text{ k}\Omega$). It can be noticed that the R_{ct} value detected in CO_2 -saturated-[BMAm⁺][TFSI⁻] is extremely high. This implied that there is almost no charge

mobility in CO₂-saturated-[BM₄Amm⁺][TFSI⁻]. Therefore, at this condition, the CO₂ conversion would not occur, but the CO₂ will be available for direct nucleophilic oxidation by O₂^{•-}.

The Bode plots detected in O₂-saturated-[BM₄Amm⁺][TFSI⁻], CO₂-saturated-[BM₄Amm⁺][TFSI⁻] and O₂/CO₂-saturated-[BM₄Amm⁺][TFSI⁻] electrolytes are shown in Figure 4.12d, 4.12e, and 4.12f. The phase angles detected in O₂-saturated-[BM₄Amm⁺][TFSI⁻] (Figure 4.11d) and O₂/CO₂-saturated-[BM₄Amm⁺][TFSI⁻] (Figure 4.12f) electrolytes are 3.8 ° and 3.7 °. These phase angles are higher than the one detected in CO₂-saturated-[BM₄Amm⁺][TFSI⁻] electrolyte (Figure 4.12e) which is 3.4 °. The medium with a high phase angle implies the presence of electroactive species such as O₂ reduction to O₂^{•-} or O₂^{•-} utilization by CO₂. However, since the charge transfer resistance in CO₂-saturated-[BM₄Amm⁺][TFSI⁻] electrolyte is high (see Table 4.11 column 2, entry 2) the surface of the GC electrode does not have a readily electroactive species. Consequently, the phase angle remains unchanged or relatively normal. These results indicate that the mechanism of CO₂ utilization by O₂^{•-} and O₂ reduction to O₂^{•-} were different.





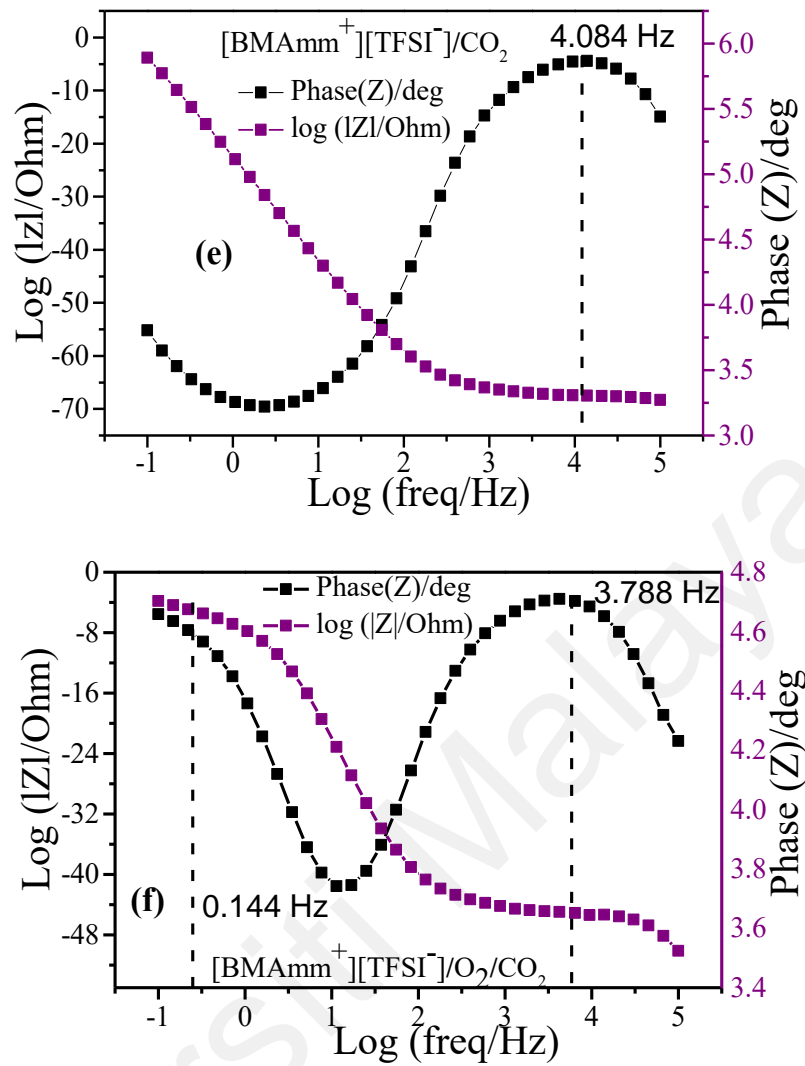


Figure 4.12: Nyquist plots detected in (a) O₂-saturated-[BMAMm⁺][TFSI⁻], (b) O₂/CO₂-saturated-[BMAMm⁺][TFSI⁻] and (c) CO₂-saturated-[BMAMm⁺][TFSI⁻]. Bode plots detected in (d) O₂-saturated-[BMAMm⁺][TFSI⁻], (e) O₂/CO₂-saturated-[BMAMm⁺][TFSI⁻] and (f) CO₂-saturated-[BMAMm⁺][TFSI⁻].

Table 4.11: EIS parameter from the Randle equivalent circuit model

Catholyte	R_e (k Ω)	R_{ct} (k Ω)	C_2 ($\mu\text{F}/\text{cm}^2$)	W ($\Omega \cdot \text{S}^{1/2}\text{cm}^2$)
O ₂ -saturated-[BMAMm ⁺][TFSI ⁻]	5467	261.467	5.897	293191
CO ₂ -saturated-[BMAMm ⁺][TFSI ⁻]	2116	6.86×10^{18}	7.764	426284
O ₂ /CO ₂ -saturated-[BMAMm ⁺][TFSI ⁻]	4378	79.00	7.507	82444

The mechanism guiding $O_2^{\bullet-}$ mediated CO_2 conversion to $C_2O_6^{2-}$ is summarized as follows:

1. Initially, O_2 and CO_2 will diffuse and get absorbed by the $[BMAMm^+][TFSI^-]$. This is possible due to non-covalent interaction from linear σ -profiles of O_2 , CO_2 and $[BMAMm^+][TFSI^-]$ centering at their non-polar ends ranging between $\sigma = -0.791 e/nm^2$ to $\sigma = 0.81 e/nm^2$ (Section 4.1.2; Figure 4.1i).
2. Accordingly, the O_2 -saturated- $[BMAMm^+][TFSI^-]$, O_2/CO_2 -saturated- $[BMAMm^+][TFSI^-]$ or CO_2 -saturated- $[BMAMm^+][TFSI^-]$ further got momentarily adsorbed on the surface of the GC electrode through the participation of the IL moiety to form an IL layer. It was shown that the IL layer could be formed during the electrochemical process (Jänsch, Wallauer, & Roling, 2015).
3. The O_2 will then diffuse through the bulk from being absorbed by the $[BMAMm^+][TFSI^-]$ solution to the GC electrode's vicinity. The O_2 could be transferred through the space between the adsorbed IL layer and the GC electrode surface.
4. Eventually, the O_2 get reduced to $O_2^{\bullet-}$ via a single electron transfer on the GC electrode. Due to the extremely high charge transfer resistance for CO_2 saturated media ($6.86 \times 10^{18} k\Omega$), CO_2 will not be converted but follow a different mechanism. The charge transfer resistance value for O_2/CO_2 -saturated- $[BMAMm^+][TFSI^-]$ was minimal ($79 k\Omega$).
5. Accordingly, the electrochemically generated $O_2^{\bullet-}$ can directly attack the C (Sp) centre of CO_2 . This scenario is highly possible because the C (Sp) centre of CO_2 has a positive Mulliken charge shown in Figure A.1 (Appendix A).

In all these processes, the rate-determining step is the first electron transfer from the GC cathode to the absorbed O_2 to form the high-energetic $O_2^{\bullet-}$ radical. The generated $O_2^{\bullet-}$ thereby interact with CO_2 via nucleophilic addition to induce the formation of $CO_4^{\bullet-}$. Then, $CO_4^{\bullet-}$ further followed consecutive reaction step with CO_2 to form $C_2O_6^{\bullet-}$. Another consecutive reaction between $C_2O_6^{\bullet-}$ and $O_2^{\bullet-}$, $C_2O_6^{2-}$ was formed along with O_2 . These results agree with the CO_2 conversion by $O_2^{\bullet-}$ in aprotic solvents (Roberts, Calderwood, & Sawyer, 1984). The result also revealed a strong advance that $O_2^{\bullet-}$ was undergoing a direct nucleophilic addition to CO_2 .

4.5 Conversion of CO_2 by $O_2^{\bullet-}$ in Fe/Ru-SiMWCNT-IL Nanofluid as Media

This study hypothesised some criteria that must be investigated for a meaningful utilization of $O_2^{\bullet-}$ by CO_2 in nanofluids. Before the process, several verifications were made, and they include:

1. Estimation of charge transport parameters (R_{ct} and σ),
2. Detection of $O_2^{\bullet-}$ in the nanofluid,
3. Mass transport phenomena,
4. Interfacial phenomena,
5. Long-term stability analysis of $O_2^{\bullet-}$ in the nanofluid.

Moreover, this is the first successful demonstration of $O_2^{\bullet-}$ generation and utilization in a nanofluid. Previous studies have reported $O_2^{\bullet-}$ generation and utilization in aprotic solvents or ILs (AlNashef et al., 2002; Feroci et al., 2011; Maan Hayyan, Hashim, & AlNashef, 2016). Also, most renowned studies on nanofluids mainly focused on their thermophysical (Sundar et al., 2014), heat transfer properties (Aman et al., 2017; Barai, Bhanvase, & Sonawane, 2020) for heat transfer applications. There are few other reports on electrical properties of nanofluid (Fal et al., 2016; Fal et al., 2019; Zawrah et al., 2016) but their base fluid is protic in nature and inherently susceptible to nucleophilic

attack (Che et al., 1996). Consequently, this kind of nanofluid could induce disproportionation of $O_2^{\bullet-}$.

Apart from the fact that the base fluid of conventional nanofluids is capable of $O_2^{\bullet-}$ disproportionation, some of their nanoparticle components such as Fe_3O_4/H_2O suspension (Darvanjooghi et al., 2017), suspension of TiO_2/H_2O (Samadi, Haghshenasfard, & Moheb, 2014), $Al_2O_3-SiO_2$ nanofluid (Pineda et al., 2012), and amine-based CNT- SiO_2 nanofluid (Saidi, 2020), could promote O_2 and CO_2 adsorption.

Inspired by nanofluids' capabilities and limitations, this study hypothesised that the development of ILs based nanofluid could further improve $O_2^{\bullet-}$ generation at low overpotential if the nanoparticle has O_2 and CO_2 sorption capacity and pseudocapacitive capabilities. In this regard, fully characterized Fe/Ru-SiMWCNT nanoparticle and IL as base fluid was used to form Fe/Ru-SiMWCNT-IL nanofluid. In particular, Fe/Ru-SiMWCNT/[MOEMPyrr⁺][PFTP⁻] nanofluid following this concept was used for the conversion of CO_2 by $O_2^{\bullet-}$. This has been accepted for publication (Appendix L). The [MOEMPyrr⁺][PFTP⁻] was selected for this purpose because it showed high O_2 solubility and low susceptibility to $O_2^{\bullet-}$ nucleophilic attack as discussed in section 4.3.2.1 during $O_2^{\bullet-}$ long-term stability analysis.

4.5.1 Potential dependence of R_{ct} and σ in nanofluid

These two EIS elements (R_{ct} and σ) are characteristic faradaic parameters used to describe charge transport phenomena across interfaces (Barbero & Lelidis, 2017; Lee & Ryu, 2017; Rudolph & Ratcliff, 2017); for example CO_2 conversion. They were estimated using the EIS analysis. Accordingly, Figure 4.13 (a-h) show the Nyquist and Bode plots detected in Fe/Ru-SiMWCNT/[MOEMPyrr⁺][PFTP⁻] nanofluid that was saturated with N_2 , CO_2 , O_2 , and O_2/CO_2 ultra-pure gases.

The Nyquist plots demonstrated two distinct features in three different frequency domains (regions 1, 2 and 3). There are two semicircles at high and intermediate

frequencies (regions 1 and 2 in Figure 4.13(a-d) and a linear part at a low frequency (region 3 in Figure 4.13b and Figure 4.13c). The semicircles in Figure 4.13(a-d) indicate the interfacial phenomena that are associated with different time constants which are in synchrony with a resistor-capacitor (RC) circuit (Lates et al., 2014).

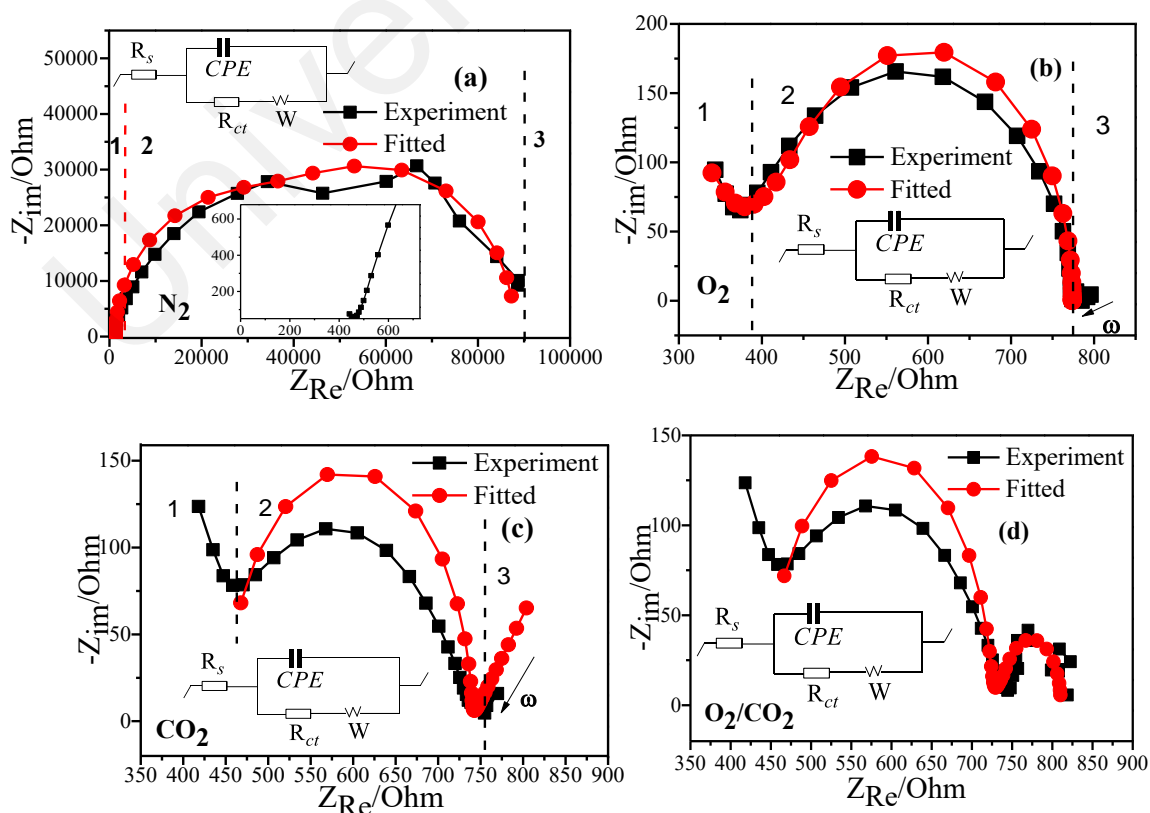
The high-frequencies (region 1 in Figure 4.13a-d) which consists of a small semicircle is typical of a non-faradaic resistance of the Fe/Ru-SiMWCNT/[MOEMPyrr⁺][PFTP⁻] nanofluid medium. The region represents an incomplete capacitive semi-circle arising due to possible non-uniformity of the current distribution on the GC electrode.

The region 2 at intermediate-frequency in Figure 4.13(a-d) contain a larger semicircle typical of a faradaic resistance through the Fe/Ru-SiMWCNT/[MOEMPyrr⁺][PFTP⁻] nanofluid medium. Since there is no electroactive species in Fe/Ru-SiMWCNT/[MOEMPyrr⁺][PFTP⁻] nanofluid medium after its saturation with N₂, region 2 of Figure 4.13a indicates a larger diameter or higher charge transfer resistance.

The second circle's diameter decreases upon saturation of the Fe/Ru-SiMWCNT/[MOEMPyrr⁺][PFTP⁻] nanofluid medium with O₂, CO₂ and O₂/CO₂ electroactive species. This is attributed to the combined impedance arising from charge transfer of the faradaic process, including the double-layer capacitance (C_{dl}) at the GC/Fe/Ru-SiMWCNT/[MOEMPyrr⁺][PFTP⁻] nanofluid interface. From the Nyquist plots, two EIS elements, such as charge transfer resistance (R_{ct}) and the Warburg impedance coefficient (σ) were measure and adopted as the charge transport descriptors in Fe/Ru-SiMWCNT/[MOEMPyrr⁺][PFTP⁻] nanofluid. These two EIS elements (R_{ct} and σ) are essential parameters to describe charge transport phenomena across interfaces in

characteristic faradaic processes (Barbero & Lelidis, 2017; Lee & Ryu, 2017; Rudolph & Ratcliff, 2017).

The Bode plots associated with the Nyquist plots (Figure 4.13a-d) are shown in Figure 4.13(e-h). Irrespective of the gas saturation, the magnitude of the real impedance decreases with the increase in frequency in all media. This indicates better noise immunity of the process and lower output ripples (Rudolph & Ratcliff, 2017). However, the phase angle for N_2 saturated $Fe/Ru-SiMWCNT/[MOEMPyrr^+][PFTP^-]$ nanofluid (Figure 4.13a) is very high (65°), indicating the high pseudocapacitance of the media in the presence of non-electroactive N_2 gas. On sparging O_2 and CO_2 , the pseudocapacitive attribute of the media is gradually being explored through O_2 reduction to $O_2^{\bullet-}$ and CO_2 conversion by $O_2^{\bullet-}$. The O_2 reduction to $O_2^{\bullet-}$ result in lowering the phase angle (Figure 4.13f; 18°), likewise CO_2 conversion to $CO_2^{\bullet-}$ (Figure 4.13g 12°) or by $O_2^{\bullet-}$ to $C_2O_6^{2-}$ (Figure 4.13h; 12°). Consequently, this induces stability of the electrochemical interface. This indicates the interfacial electrochemical process from the saturation with O_2 and CO_2 .



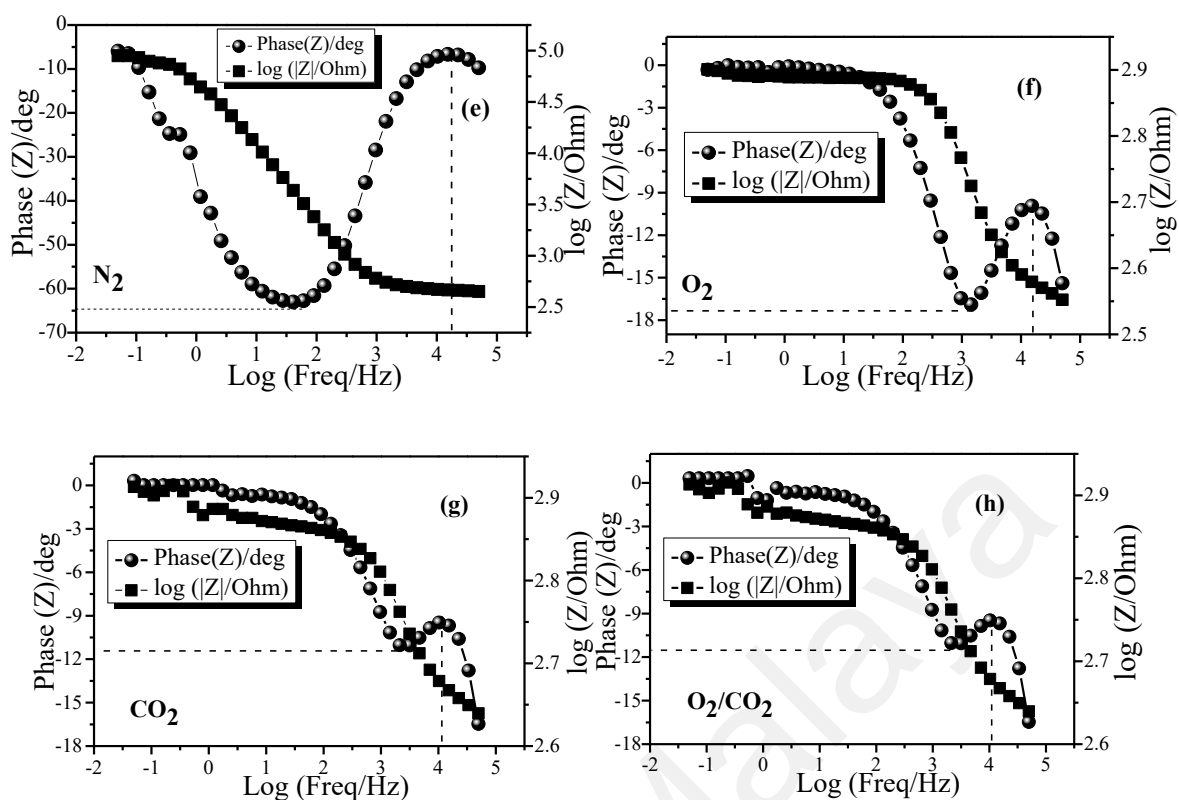


Figure 4.13: Typical Nyquist plot at a bias voltage of -1.564 V vs Ag/AgCl for (a) N₂ saturated (b) O₂ saturated, (c) CO₂ saturated and (d) O₂/CO₂ saturated Fe/Ru-SiMWCNT/[MOEMPyrr⁺][PFTP⁻] nanofluid. Typical bode plot detected in (e) N₂ saturated (f) O₂ saturated, (g) CO₂ saturated, and (h) O₂/CO₂ saturated Fe/Ru-SiMWCNT/[MOEMPyrr⁺][PFTP⁻].

The potential dependence of charge transfer resistance (R_{ct}) and the Warburg impedance coefficient (σ) of the gas saturated Fe/Ru-SiMWCNT/[MOEMPyrr⁺][PFTP⁻] nanofluid is shown in Figure 4.14a and Figure 4.14b respectively. The EIS experimental data (Figure 4.13 a-c) were suitably fitted to the Randles equivalent circuit to estimate the charge transfer resistance (R_{ct}) and Warburg impedance coefficient (σ), (Torresi et al., 2013). Therefore, according to the data in Figure 4.14a, the R_{ct} decreased as the negative potential increased from -1.366 V to -1.564 V vs Ag/AgCl. In the CO₂ saturated Fe/Ru-SiMWCNT/[MOEMPyrr⁺][PFTP⁻] nanofluid, the R_{ct} decreased from 1.728 kOhm at -1.366 V to a local minimum of ~ 0.288 kOhm at -1.564 V. Similarly, for O₂ saturated

Fe/Ru-SiMWCNT/[MOEMPyrr⁺][PFTP⁻] nanofluid, the R_{ct} decreased from 21.969 kOhm at -1.366 V to a local minimum of 4.034 kOhm at -1.564 V. Also, the N₂ saturated Fe/Ru-SiMWCNT/[MOEMPyrr⁺][PFTP⁻] nanofluid, and the R_{ct} decreased from 29.155 kOhm at -1.366 V to a local minimum of 21.062 kOhm at -1.564 V. Comparing these three cases, the charge transfer resistance in N₂ saturated nanofluid is high. This result may be attributed to the absence of an electroactive species in the medium. In either of these cases, the R_{ct} -values at -1.564 V is lower than that detected at -1.366 V. These results confirmed that the applied potential has an inverse relation with the previous report's charge transfer resistance (Memming, 2015).

The impedance over charge diffusion from GC to N₂, O₂, and CO₂ saturated Fe/Ru-SiMWCNT/[MOEMPyrr⁺][PFTP⁻] nanofluid is shown in Figure 4.13a-c. This impedance is quantified by the Warburg impedance coefficient (σ), which is represented mathematically by Eq 4.2 (Bisquert, 2002).

$$\sigma = \frac{RT}{n^2 F^2 A \sqrt{2}} \left(\frac{1}{C_{ox} D_{ox}^{1/2}} + \frac{1}{C_{red} D_{red}^{1/2}} \right) \quad (4.2)$$

Where R is the gas constant, T is temperature, n is the number of electrons transferred, A is the area of the electrode, D is the diffusion of electroactive species, C_{ox} is the concentration of oxidation species, C_{red} is the concentration of reduction species and F is Faraday constant.

The σ can describe the resistance associated with diffusion as a function of the concentration of charge carriers and their diffusion coefficient (Bredar et al., 2020). At -1.564 V from Figure 4.14b, the σ -value for CO₂ saturated Fe/Ru-SiMWCNT/[MOEMPyrr⁺][PFTP⁻] nanofluid is 33.5 Ohm.s^{-1/2}, and at -1.366 V, σ -value is 217.5 Ohm.s^{-1/2}. The result implies that at -1.366 V, there is higher diffusion resistance of CO₂ based radical as an electroactive species within the nanofluid going by equation

4.2. Similarly, the σ -value is $9.163 \text{ Ohm}\cdot\text{s}^{-1/2}$, and $6948 \text{ Ohm}\cdot\text{s}^{-1/2}$ for O_2 and N_2 saturated media operated at -1.564 V . The σ -value is $1075 \text{ Ohm}\cdot\text{s}^{-1/2}$ and $6201 \text{ Ohm}\cdot\text{s}^{-1/2}$ for O_2 and N_2 saturated media performed at -1.366 V . These results indicated that there is no electroactive species after sparging the media with N_2 . This observation is because the σ -value is very high, implying minimal diffusion of electroactive species. However, the σ -value at -1.564 V indicate that diffusion of O_2 is higher than that for CO_2 going by Eq 4.2. Overall, the pattern of σ -value, as shown in Figure 4.14b, is in reminiscence with the variation of σ -value with applied potentials reported previously (Gabrielli et al., 2004).

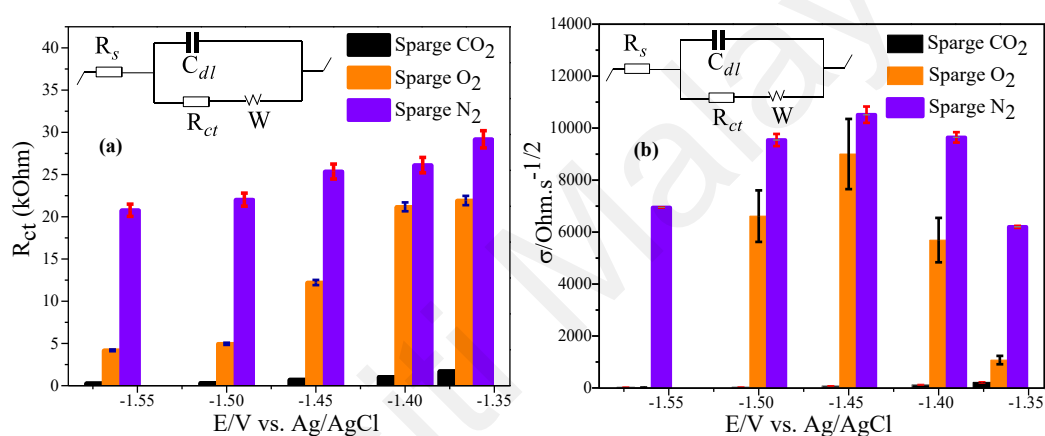


Figure 4.14: Potential-dependent (a) charge-transfer resistance and (b) Warburg impedance coefficient of Fe/Ru-SiMWCNT/[MOEMPyrr⁺][PFTP⁻] nanofluid in contact with GC.

4.5.2 Detection of $\text{O}_2^{\bullet-}$ in Fe/Ru-SiMWCNT/[MOEMPyrr⁺][PFTP⁻] nanofluid

In this section, the electrochemical active surface area (ECSA) was first determined for normalizing the current density during the generation of $\text{O}_2^{\bullet-}$. This is a general recommendation for reporting electrochemical data (Voiry et al., 2018).

4.5.2.1 Electrochemical active surface area

The ECSA of the GC electrode used during the experiment was determined using the differential capacitance measurement method (DCM) with different scan rates of 9, 36, 64, 81 mV/s scan rate stripping at a non-faradaic narrow potential range of -0.4 V to

0.2 V range vs Ag/AgCl (Figure 4.15a-c). The electrical double layer capacitance (C_{dl}) was estimated from the slope of the plots (Figure 4.15c) for the cell with [MOEMPyrr⁺][PFTP⁻] was less and indexed as $C_{dlref} = 0.0584 \text{ mC/cm}^2$. For the cell with Fe/Ru-SiMWCNT/[MOEMPyrr⁺][PFTP⁻] nanofluid, the C_{dl} was $\sim 0.0998 \text{ mC/cm}^2$. Therefore, ECSA was computed using Eq 3.6 to be $\sim 0.123 \text{ cm}^2$.

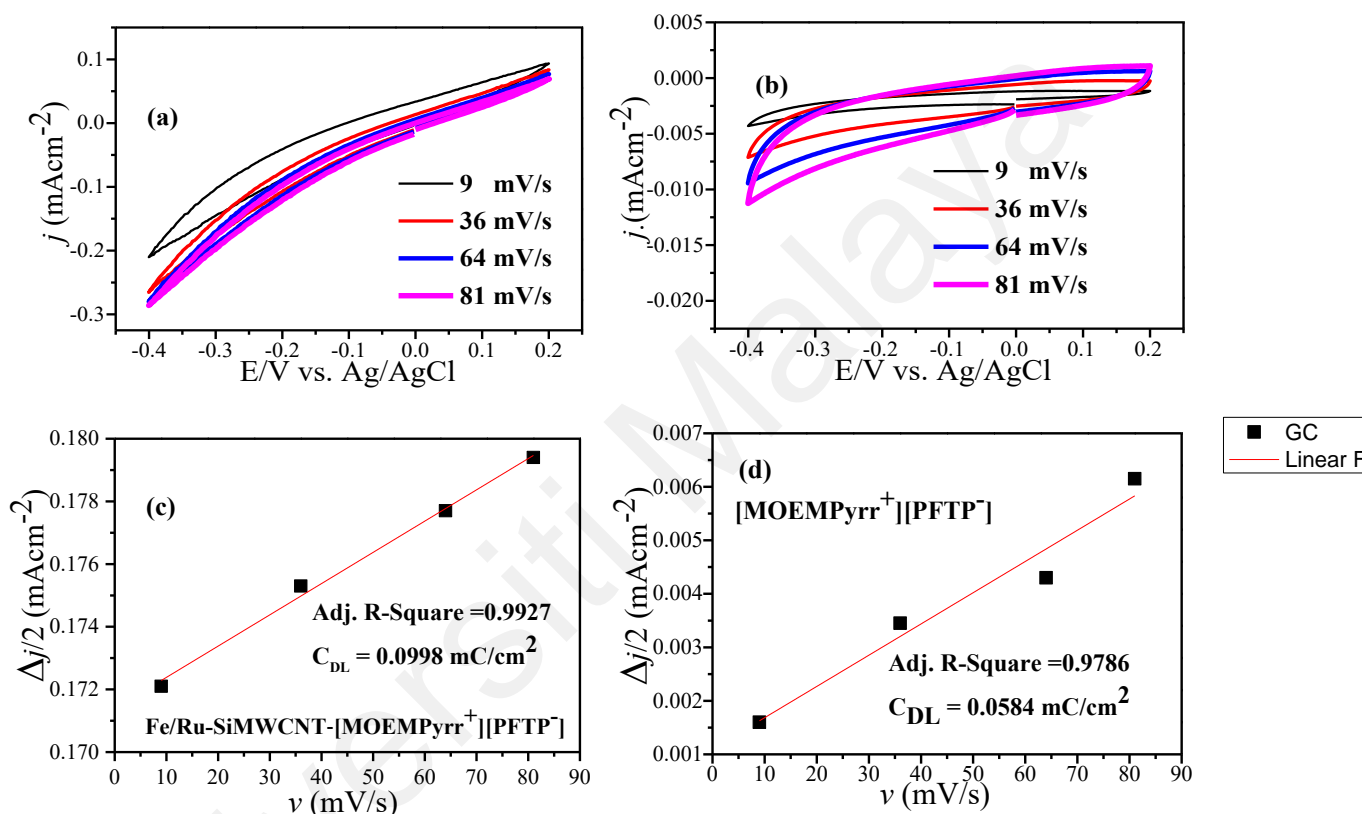


Figure 4.15: Cyclic voltammograms of N_2 saturated (a) Fe/Ru-SiMWCNT/[MOEMPyrr⁺][PFTP⁻] nanofluid, (b) [MOEMPyrr⁺][PFTP⁻] and (c) Charging difference vs. scan rates stripping in N_2 saturated Fe/Ru-SiMWCNT/[MOEMPyrr⁺][PFTP⁻] nanofluid and [MOEMPyrr⁺][PFTP⁻].

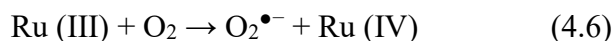
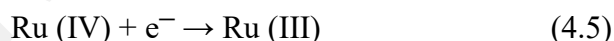
4.5.2.2 Generation of $O_2^{\bullet-}$ in Fe/Ru-SiMWCNT/[MOEMPyrr⁺][PFTP⁻]

Evidence of the one-electron reduction of O_2 to $O_2^{\bullet-}$ in the Fe/Ru-SiMWCNT/[MOEMPyrr⁺][PFTP⁻] nanofluid is shown in Figure 4.16. The measurement was done in terms of applied potential (Figure 4.16a) and the activation overpotential

(Figure 4.16b) required to drive the reaction. Interestingly, the electrochemical generation of $O_2^{\bullet-}$ in the nanofluid at 144 mV/s scan rate occurs at -0.45 V vs Ag/AgCl, which is less negative than the potential of $O_2^{\bullet-}$ generation in $[MOEMPyrr^+][PFTP^-]$ at -0.80 V vs Ag/AgCl. Conventionally, $O_2^{\bullet-}$ generation occurs at ± -1.0 V vs Ag/AgCl (Hayyan et al., 2016). Therefore, the significant shift toward the less negative potential for $O_2^{\bullet-}$ generation in the nanofluid is due to the high O_2 uptake by the Fd3m (311) Fe_3O_4 phase in Fe/Ru-SiMWCNT through adsorption (Figure 3a) and absorption by the $[MOEMPyrr^+][PFTP^-]$ (see Table 4.7, column 4, entry 3). Intrinsically, the lower negative potential for the $O_2^{\bullet-}$ generation in the nanofluid is also aided by Fe (III) in the Fe_3O_4 phase. The Fe (III) mediate reduction of the O_2 to $O_2^{\bullet-}$ according to Eq. 4.3, and 4.4.



Besides, the pseudocapacitance of RuO_2 was shown to occur in protic IL (Rocheffort & Pont, 2006). RuO_2 pseudocapacitance can mediate O_2 reduction into $O_2^{\bullet-}$. Consequently, there are changes in the oxidation state of the Ru according to Eq. 4.5 and 4.6.



These steps rationalize the lower overpotential needed to reduce O_2 in the Fe/Ru-SiMWCNT/ $[MOEMPyrr^+][PFTP^-]$ nanofluid (Figure 4.16a and 4.16b), as compared to the ordinary $[MOEMPyrr^+][PFTP^-]$ (Figure 4.16c). The CV currents densities were normalized using the ECSA value estimated in section 4.5.2.1 (Figure 4.16a, 4.16b and 4.16c).

Therefore, Figure 4.16a and 4.16b show the CV wave for $O_2^{\bullet-}$ detected in Fe/Ru-SiMWCNT/ $[MOEMPyrr^+][PFTP^-]$ nanofluid in terms of potentials applied and the

activation overpotential for O₂ reduction. For instance, at 144 mV/s scan rate, the electrochemical generation of O₂^{•-} was achieved at -0.45 V. This potential is less than the O₂^{•-} generation potential in [MOEMPyrr⁺][PFTP⁻] that was achieved at -0.80 V. However, as the scan rate was stripped from 144 to 100, 81, 64, 36 and 9 mV/s, the reduction potential further reduced from -0.45 to -0.442, -0.440, -0.434, -0.430 and -0.419 V respectively (Figure 4.16a and Figure 4.16b). Following the same scan rate stripping, as shown in Figure 4.16b, the activation overpotential for O₂ reduction also decrease from -0.31 to -0.300, -0.292, -0.288, -0.283, and -0.279 V. These activations overpotential are far less than the ones observed for O₂ reduction in [MOEMPyrr⁺][PFTP⁻] (Figure 4.16c), which are -0.819, -0.815, -0.811, -0.789, -0.778 and -0.756 V for scan rate stripping from 144 to 9 mV/s respectively. These results showed that the Fe/Ru-SiMWCNT/[MOEMPyrr⁺][PFTP⁻] nanofluid could reduce the activation overpotential needed for O₂ reduction.

Also, the CV waves for O₂^{•-} detected in Fe/Ru-SiMWCNT/[MOEMPyrr⁺][PFTP⁻] nanofluid or [MOEMPyrr⁺][PFTP⁻] showed cathodic peak potential (E_{pC}) and the half peak potential (E_{pC}/2) that is not 56.5 mV. These indicate that the generation of O₂^{•-} in Fe/Ru-SiMWCNT/[MOEMPyrr⁺][PFTP⁻] nanofluid and [MOEMPyrr⁺][PFTP⁻] is irreversible (Bard et al., 1980; Hayyan et al., 2012; Hayyan et al., 2011; Richard S Nicholson, 1965). The irreversibility implies that O₂^{•-} is available for further utilization. In Figure 4.16a, the cathodic hump that appeared at -0.33 V is likely due to the IL's inactive impurity. This impurity could be prevalent even after N₂ based pretreatment or an O₂ environment. The cathodic hump might arise due to the IL's adsorption on the GC electrode surface, thereby resulting in an onset of micro electrochemical activity (Hayyan et al., 2012). The linearity of current densities to the square root of sweep rate for O₂^{•-} detected in Fe/Ru-SiMWCNT/[MOEMPyrr⁺][PFTP⁻]

nanofluid and [MOEMPyrr⁺][PFTP⁻], confirmed possible scenario of a diffusion-controlled process for the reduction of O₂ in the media (Figure E.1, Appendix E).

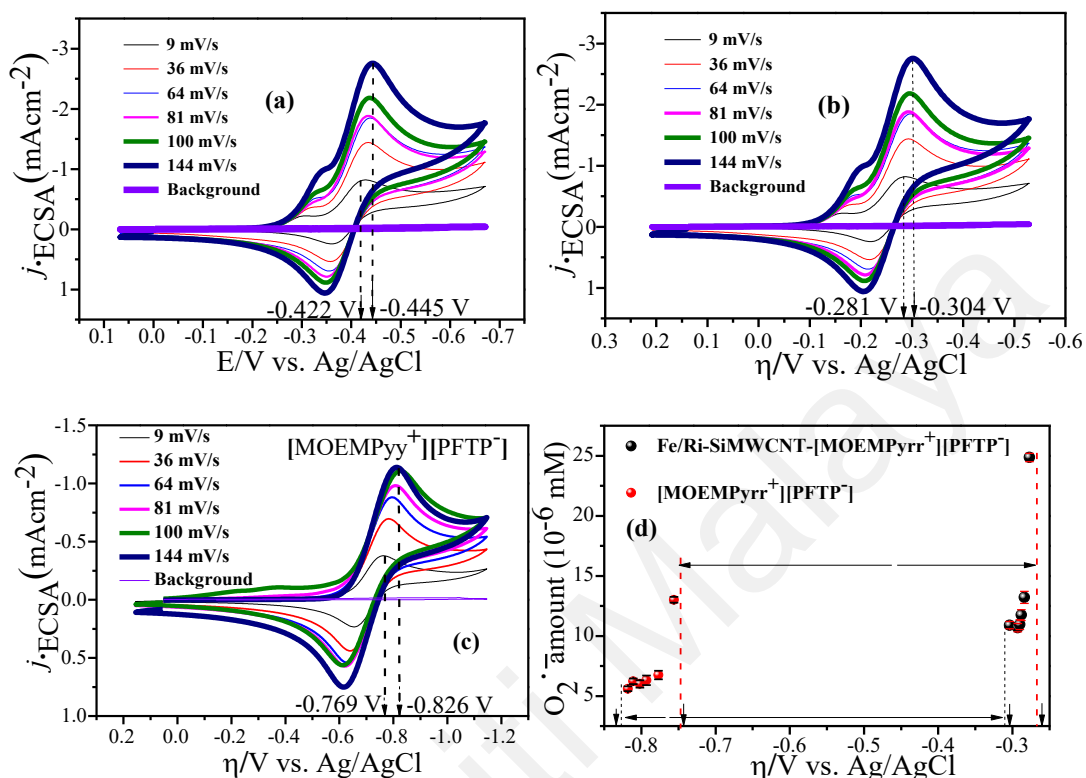


Figure 4.16: CVs of O₂^{•-} electrochemically generated in Fe/Ru-SiMWCNT/[MOEMPyrr⁺][PFTP⁻] nanofluid (a) In terms of applied potential (b) In terms of over-potential (c) Amount of O₂^{•-} in terms of activation overpotential. All measurements were done at 25 °C.

4.5.2.3 Mass transfer phenomena

It was found that the two mass transfer parameters (D_0 and C_0) are different in Fe/Ru-SiMWCNT/[MOEMPyrr⁺][PFTP⁻] nanofluid as compared to [MOEMPyrr⁺][PFTP⁻]. The diffusion coefficient (D_0) for O₂ in Fe/Ru-SiMWCNT/[MOEMPyrr⁺][PFTP⁻] nanofluid is 0.0064×10^{-10} m²/s and lower than [MOEMPyrr⁺][PFTP⁻] (0.5 m²/s). This result implies that O₂ transfer is limited in the nanofluid than the IL due to its high viscosity (106.23 mPa S). However, the solubility (C_0) of O₂ was high in Fe/Ru-SiMWCNT/[MOEMPyrr⁺][PFTP⁻] nanofluid ($C_0=74.16$

mM) as compared with ordinary [MOEMPyrr⁺][PFTP⁻] (C_o= 19.02 mM). This result is expected as Fe₃O₄ phases in the nanofluid is oxyphilic. Therefore, it can thereby boost the O₂ uptake in Fe/Ru-SiMWCNT/[MOEMPyrr⁺][PFTP⁻] nanofluid (Kepp, 2016; Pachecka et al., 2017; Y. Wang, Lafosse, & Jacobi, 2002).

4.5.2.4 Interfacial phenomena

The interfacial phenomena during detection of O₂^{•-}, expressed in terms of charge transfer coefficient (α) in the Fe/Ru-SiMWCNT/[MOEMPyrr⁺][PFTP⁻] nanofluid was ~0.64. This charge transfer coefficient is more significant than the one observed in [MOEMPyrr⁺][PFTP⁻] ($\alpha=0.499$). These values implied that more of the fraction of the interfacial potential at the GC-Fe/Ru-SiMWCNT/[MOEMPyrr⁺][PFTP⁻] nanofluid interface helps in lowering the free energy barrier for the one-electron O₂ reduction. This view is in cognisance with the one reported previously (Bard et al., 1980). Although this was estimated using CV, and O₂^{•-} residence time is usually shortly utilising this technique, transient amount of O₂^{•-} produced was evaluated in the nanofluid and compared with the IL using the stoichiometry of the one-electron reduction of O₂. Therefore, the quantification of O₂^{•-} was achieved directly by O₂ + e⁻ → O₂^{•-} through the variation of the amount of charge (Q = It, 1 electron = 96500 C/mole) supplied to the Fe/Ru-SiMWCNT/[MOEMPyrr⁺][PFTP⁻] nanofluid system. According to Figure 4.16d, ~24.846 × 10⁻⁶ mM of stable O₂^{•-} was momentarily produced at a much lower overpotential in the cell containing Fe/Ru-SiMWCNT/[MOEMPyrr⁺][PFTP⁻] nanofluid. When compared with ordinary [MOEMPyrr⁺][PFTP⁻], ~13.040 × 10⁻⁶ mM O₂^{•-} was produced at a much higher overpotential. These results confirmed higher charge transfer estimated in Fe/Ru-SiMWCNT/[MOEMPyrr⁺][PFTP⁻] nanofluid, and this consequently induces low over-potential for the O₂^{•-} electrochemical generation process.

4.5.2.5 Long-term stability of $O_2^{\bullet-}$

Since CV analysis could not assure the long-term stability of the $O_2^{\bullet-}$ in the Fe/Ru-SiMWCNT/[MOEMPyrr⁺][PFTP⁻] nanofluid, UV-Vis irradiation experiments were further used. UV-Vis irradiation analysis is essential, especially in cognisance to validating $O_2^{\bullet-}$ utilization in Fe/Ru-SiMWCNT/[MOEMPyrr⁺][PFTP⁻] nanofluid. Therefore, the $O_2^{\bullet-}$ was chemically generated and subjected to UV-Vis irradiation. This result is a comprehensive practice to measure any media's integrity capable of retaining $O_2^{\bullet-}$ (Hayyan et al., 2012). In the Fe/Ru-SiMWCNT/[MOEMPyrr⁺][PFTP⁻] nanofluid $O_2^{\bullet-}$ excitation wavelengths, according to Figure 4.17a, was found to be $\sim 258.2 \pm 0.01$ nm upon UV irradiation.

Compared with the ordinary [MOEMPyrr⁺][PFTP⁻], the excitation wavelength is $\sim 265.3 \pm 0.03$ nm. These experimental $O_2^{\bullet-}$ excitation wavelength values are consistent with the literature (Ahmed et al., 2015; Hayyan et al., 2012; Islam et al., 2009). The excitation wavelengths also influence understanding $O_2^{\bullet-}$ long-term stability in a medium of interest. Therefore, the kinetics of chemically generated $O_2^{\bullet-}$ was monitored in the Fe/Ru-SiMWCNT/[MOEMPyrr⁺][PFTP⁻] nanofluid for 2.0 days. After the first day, ~ 2.240 % total consumption of $O_2^{\bullet-}$ was observed (Figure 4.17b). The process follows pseudo-first-order with a rate constant of $0.423 \times 10^{-5} \text{ s}^{-1}$. Similarly, after 2.0 days, ~ 17.650 % total consumption of $O_2^{\bullet-}$ was observed. In this case, the process also followed pseudo-first-order with a rate constant of $3.792 \times 10^{-5} \text{ s}^{-1}$.

In comparison, after just 3.0 h, ~ 3.820 % total consumption of $O_2^{\bullet-}$ in [MOEMPyrr⁺][PFTP⁻] was observed. The kinetics of $O_2^{\bullet-}$ consumption in [MOEMPyrr⁺][PFTP⁻] also followed pseudo-first-order with a rate constant of $0.340 \times 10^{-5} \text{ s}^{-1}$. These result showed that $O_2^{\bullet-}$ can be sustained longer in Fe/Ru-SiMWCNT/[MOEMPyrr⁺][PFTP⁻] nanofluid than ordinary [MOEMPyrr⁺][PFTP⁻]. Overall, the parameters for the [MOEMPyrr⁺][PFTP⁻] is similar to $O_2^{\bullet-}$ consumption

other ILs reported previously (Hayyan et al., 2016; Hayyan et al., 2012; Schwenke et al., 2015). As for the $O_2^{\bullet-}$ consumption in the nanofluid, there is currently no study to compare with because this is the first study. However, the control experiments that were conducted so far are enough to validate the prowess of Fe/Ru-SiMWCNT/[MOEMPyrr⁺][PFTP⁻] nanofluid for $O_2^{\bullet-}$ based applications, for example, CO₂ conversion.

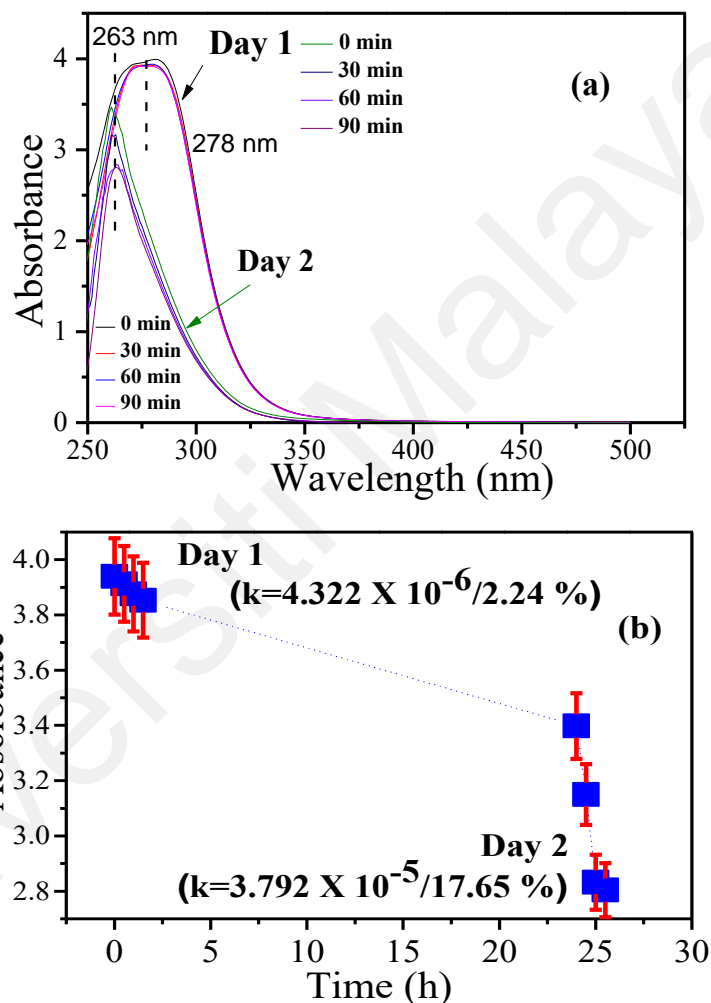


Figure 4.17: (a) Absorbance spectra of $O_2^{\bullet-}$ chemically generated and (b) Kinetics of $O_2^{\bullet-}$ decay in Fe/Ru-SiMWCNT/[MOEMPyrr⁺][PFTP⁻] nanofluid. Measurements and chemical generation of $O_2^{\bullet-}$ were achieved at room temperature.

4.5.2.6 Conversion of CO₂ to C₂O₆²⁻

Figure 4.18 shows the cyclic voltammograms (CVs) for successful CO₂ conversion (CO₂C) by $O_2^{\bullet-}$ in Fe/Ru-SiMWCNT/[MOEMPyrr⁺][PFTP⁻] nanofluid.

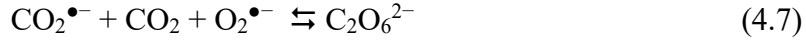
Figure 4.18a shows the CO₂C in terms of potential applied. Also, Figure 4.18b shows the CO₂C in terms of activation overpotential (η) required by the process. In Figure 4.18a, the CO₂C by O₂^{•-} detected in Fe/Ru-SiMWCNT/[MOEMPyrr⁺][PFTP⁻] nanofluid occurred at -0.596 V for 144 mV/s and -0.544 V for 9 mV/s CV scan rates. The corresponding activation overpotential (η) in Figure 4.17b for the CO₂C by O₂^{•-} is -0.281V for 144 mV/s and -0.304 V for 9 mV/s CV scan rates. Comparing the CO₂C in the ordinary [MOEMPyrr⁺][PFTP⁻] (Figure 4.18c), the activation overpotential (η) for CO₂C by O₂^{•-} occurred at -1.173 for 144 mV/s and -0.870 V for 9 mV/s. These results showed that the overpotential required for the O₂^{•-} mediated CO₂C is lower in Fe/Ru-SiMWCNT/[MOEMPyrr⁺][PFTP⁻] nanofluid than ordinary [MOEMPyrr⁺][PFTP⁻]. The decrease in activation over-potential arose due to three concerted phenomena outlined as follows:

- 1- The high CO₂ uptake by O₂Ru (P42/mm) phase in Fe/Ru-SiMWCNT/[MOEMPyrr⁺][PFTP⁻] nanofluid,
- 2- The low charge transfer resistance (R_{ct}) in CO₂ saturated Fe/Ru-SiMWCNT/[MOEMPyrr⁺][PFTP⁻] nanofluid (see Figure 4.13a),
- 3- Low Warburg impedance in CO₂ saturated Fe/Ru-SiMWCNT/[MOEMPyrr⁺][PFTP⁻] nanofluid (see Figure 4.13b).

The main product was C₂O₆²⁻ similar to the previous report considering the oxidative faradaic CV wave (AlNashef et al., 2002). The stoichiometry such as 2CO₂ + O₂^{•-} → C₂O₆²⁻, the C₂O₆²⁻ was quantified relative to the overpotential require for CO₂C in the two media (Figure 4.18c). It was found that ~12.86 × 10⁻⁶ mM of C₂O₆²⁻ was produced in Fe/Ru-SiMWCNT/[MOEMPyrr⁺][PFTP⁻] nanofluid at a lower overpotential of -0.392 V vs Ag/AgCl. In comparison, only ~7.71 × 10⁻⁶ mM of C₂O₆²⁻ was produced at a higher overpotential of -0.738 V in [MOEMPyrr⁺][PFTP⁻] (Figure 4.18 d). These results confirmed that the Fe/Ru-SiMWCNT/[MOEMPyrr⁺][PFTP⁻] nanofluid could

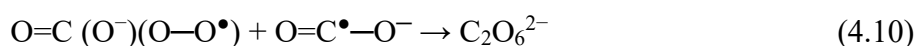
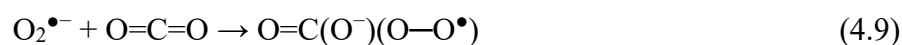
promote the energy-efficient generation of $C_2O_6^{2-}$ compared to ordinary [MOEMPyrr⁺][PFTP⁻].

Using a similar method for $O_2^{\bullet-}$ quantification but different stoichiometry such as $CO_2^{\bullet-} + CO_2 + O_2^{\bullet-} \rightarrow C_2O_6^{2-}$, the $C_2O_6^{2-}$ was estimated (Figure 4.18c). The formation of the $C_2O_6^{2-}$ is described in Eq. 4.7.

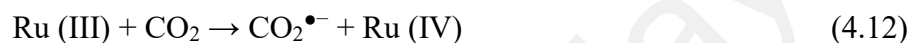


It was found that $\sim 12.86 \times 10^{-6}$ mM of $C_2O_6^{2-}$ was produced in Fe/Ru-SiMWCNT/[MOEMPyrr⁺][PFTP⁻] nanofluid at a lower overpotential of -0.392 V vs Ag/AgCl. In [MOEMPyrr⁺][PFTP⁻], $\sim 7.71 \times 10^{-6}$ mM of $C_2O_6^{2-}$ was produced at a higher overpotential of -0.738 V vs Ag/AgCl. This also implies that the Fe/Ru-SiMWCNT/[MOEMPyrr⁺][PFTP⁻] nanofluid promotes more efficient CO_2 reduction at a lower overpotential compared to the [MOEMPyrr⁺][PFTP⁻]. The energy efficiency (EE) associated with the CO_2 conversion by $O_2^{\bullet-}$ to $C_2O_6^{2-}$ in Fe/Ru-SiMWCNT/[MOEMPyrr⁺][PFTP⁻] nanofluid was higher than that observed in [MOEMPyrr⁺][PFTP⁻] as indicated in Figure 4.18e. This result implies that all the energy supplied to the reaction for the CO_2 conversion into $C_2O_6^{2-}$ by the $O_2^{\bullet-}$, in the Fe/Ru-SiMWCNT/[MOEMPyrr⁺][PFTP⁻] nanofluid was utilized. Typical EE values of 97.9 % and 50 % are observed for the Fe/Ru-SiMWCNT/[MOEMPyrr⁺][PFTP⁻] nanofluid and [MOEMPyrr⁺][PFTP⁻] respectively. This EE in these media are at GC/ -0.538 V vs. Ag/AgCl and GC/ -0.769 V vs Ag/AgCl respectively. These EE-values are higher than conventional electrochemical means of CO_2 conversion to oxocarbons. For instance, the production of CO from CO_2 using CN/MWCNT electrode was reported to have ~ 48 % energy efficiency at -1.46 V vs Ag/AgCl (Jhong et al., 2017). The mechanism of formation of the $C_2O_6^{2-}$ by the $CO_2 + O_2^{\bullet-}$ in the nanofluid can be described below:





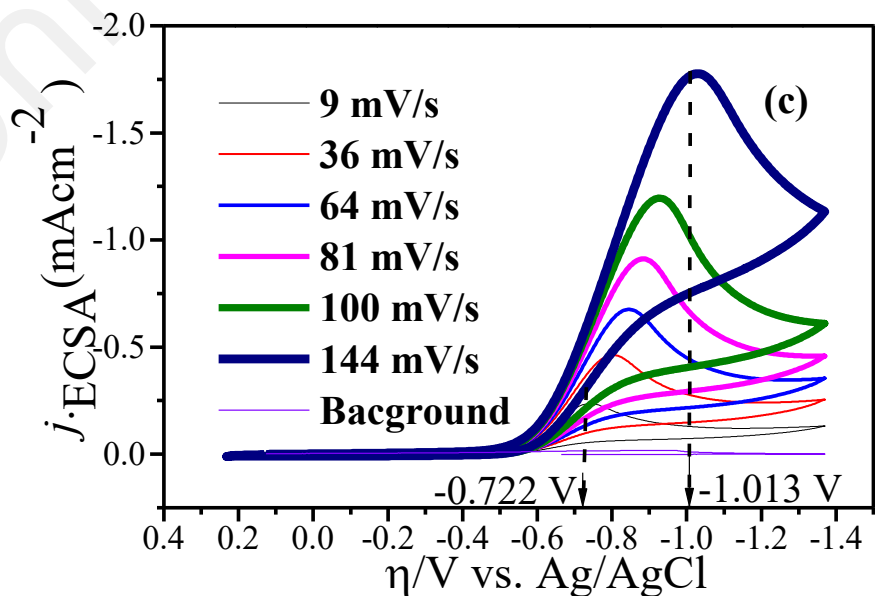
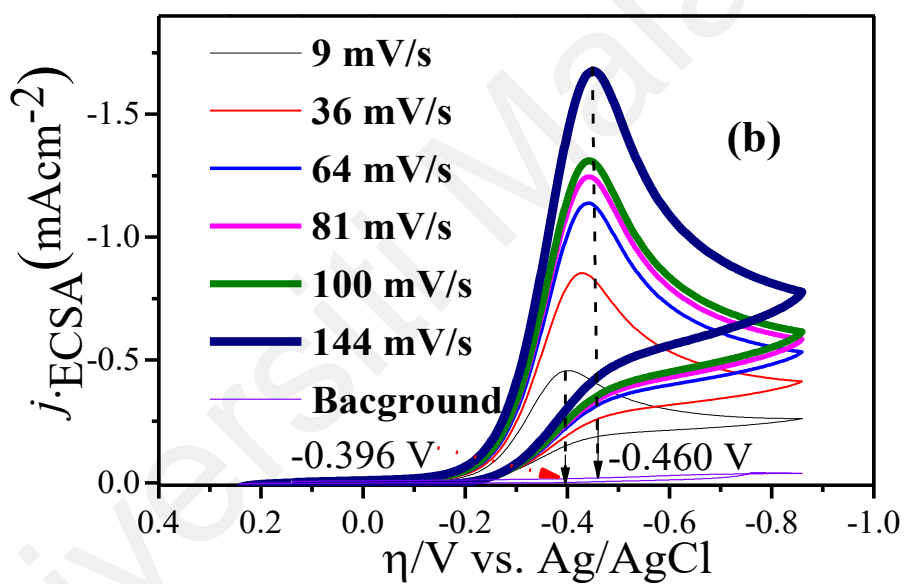
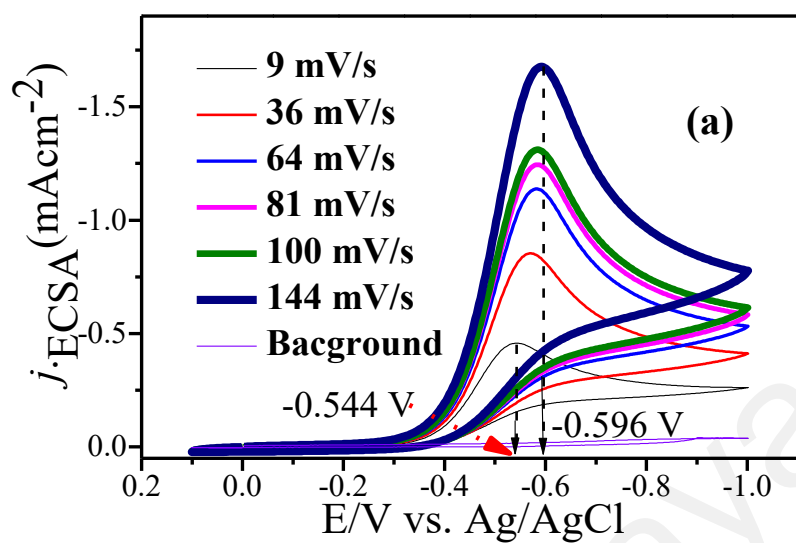
The formation of $\text{CO}_2^{\bullet-}$ in the nanofluid follows a similar mechanism described in Eqs. 4.3 to 4.6, which involves Fe (III) and Ru (IV) in the Fe/Ru-SiMWCNT as the mediator for the reduction of CO_2 into $\text{CO}_2^{\bullet-}$. These reactions are described by Eqs. 4.11 and 4.12.



This result accounts for the higher uptake of CO_2 by the nanofluid as described earlier. This information also accounts for the lower overpotential, higher $\text{C}_2\text{O}_6^{2-}$ product formation and higher energy efficiency in the Fe/Ru-SiMWCNT/[MOEMPyrr⁺][PFTP⁻] nanofluid compared to the [MOEMPyrr⁺][PFTP⁻]. As an additive effect, the $\text{O}_2^{\bullet-}$ also initiate the formation of the $\text{CO}_2^{\bullet-}$ by a simple electron transfer to the CO_2 .



The reaction described by Eq 4.13 is thermodynamically feasible as the electron in the $\text{CO}_2^{\bullet-}$ is delocalized over a wider distance at the two terminal oxygen atoms in the $\text{CO}_2^{\bullet-}$. This is also similar to the possibility of producing $\text{CO}_4^{\bullet-}$ from O_2 and $\text{CO}_2^{\bullet-}$. Both $\text{CO}_4^{\bullet-}$ and $\text{CO}_2^{\bullet-}$ contain π –electron that are delocalized over a wider distance. The mechanism is probable because CO_2 has the antibonding orbitals based on Hartree-Fock (HF) calculations and can facilitate interaction with superoxide to form an intermediate $\text{CO}_4^{\bullet-}$ which contain 1π –electron, or $\text{CO}_2^{\bullet-}$ which contain 2π – electrons. Both $\text{CO}_4^{\bullet-}$ and $\text{CO}_2^{\bullet-}$ have delocalized electrons.



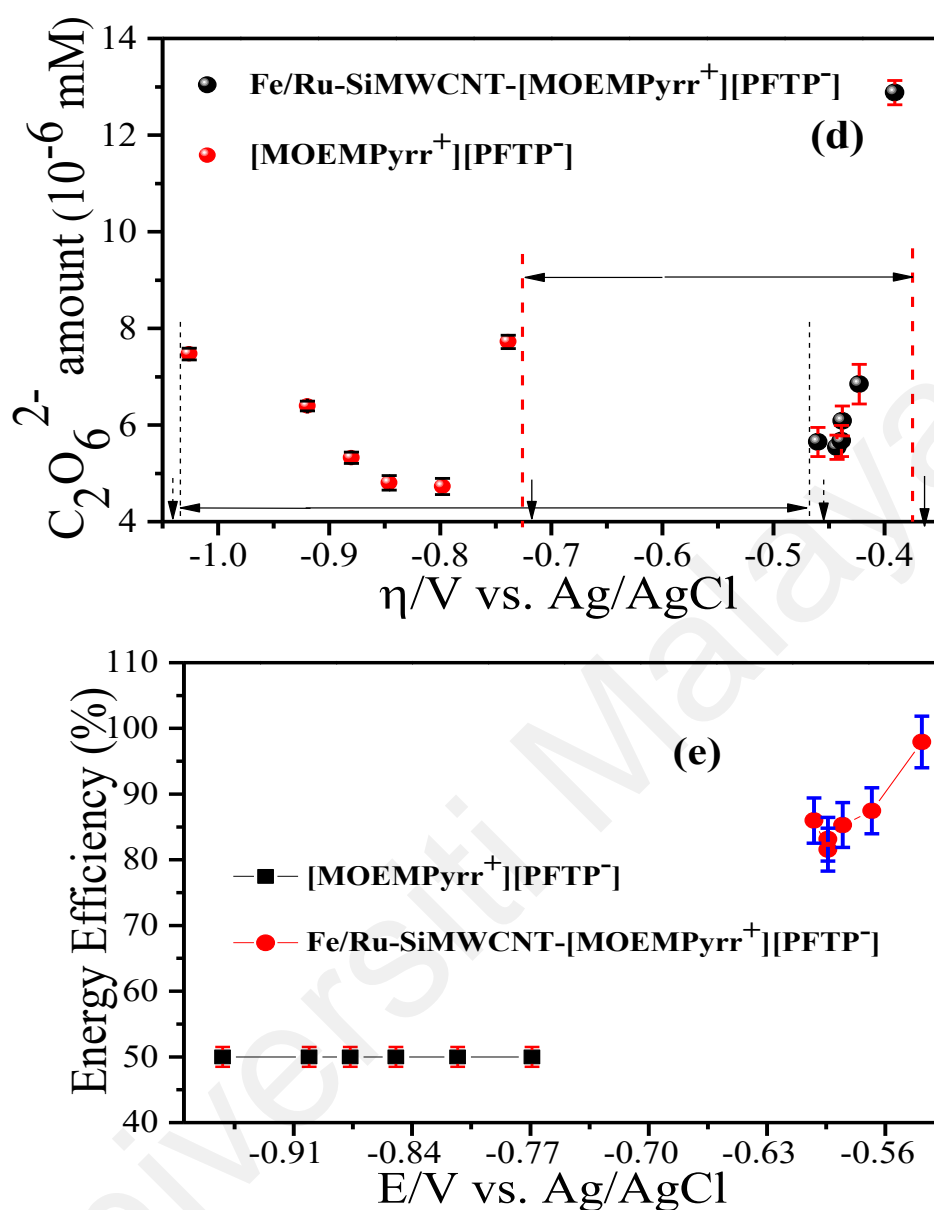


Figure 4.18: Cyclic voltammogram (CVs) of $C_2O_6^{2-}$ generation in Fe/Ru-SiMWCNT/[MOEMPyrr⁺][PFTP⁻] nanofluid (a) In terms of applied potential (b) In terms of activation overpotential (c) In terms of overpotential in [MOEMPyrr⁺][PFTP⁻] (d) Amount of $C_2O_6^{2-}$ detected in Fe/Ru-SiMWCNT/[MOEMPyrr⁺][PFTP⁻] nanofluid and [MOEMPyrr⁺][PFTP⁻] vs activation overpotential (e) Energy efficiency of CO_2 conversion to $C_2O_6^{2-}$ by $O_2^{\bullet-}$. Measurements were done at room temperature.

4.6 Carboxylation of Diethanolamine by $C_2O_6^{2-}$ to Carbamate

The carboxylation of diethanolamine from media containing $O_2^{\bullet-}/CO_2$ has been shown to produce carbamate (Casadei et al., 1997). Making carbamate through this means comes with the limitation that if an electron-withdrawing group activates the C-H adjacent to the N-H group, the C-H's competitive deprotonation can occur. Consequently, the carboxylation process due to the presence of strong electron-withdrawing nitrogen-based substituents is hampered. In retrospect, many reports suggested an aprotic medium to sustainably retain nucleophilic radicals for utilization in reactions (AlNashef et al., 2002; Maan Hayyan, Hashim, & AlNashef, 2016). For instance, the aprotic medium, which is renowned for being volatile, have been used for carbamate production mediated by $O_2^{\bullet-}/CO_2$ couples (Feroci et al., 2011; Feroci et al., 2000). Despite these advances, there are no reported electrolyte media that fulfil the criteria of using nanohybrid fluid to generate stable $O_2^{\bullet-}$ for CO_2 conversion to $C_2O_6^{2-}$. Also, the utilization of $C_2O_6^{2-}$ in the carboxylation of amines, especially nanofluid, is unfamiliar. Importantly it is promising if concerted procedures are adopted to develop a stable nanofluid as reported herewith.

In accordance, diethanolamine with very weak electron-withdrawing N-substituent was selected as a substrate. Therefore, to ascertain the feasibility of $O_2^{\bullet-}$ mediated CO_2 conversion in Fe/Ru-SiMWCNT/[MOEMPyrr⁺][PFTP⁻] nanofluid to $C_2O_6^{2-}$ and to investigate its applicability to the synthesis of organic carbamates, O_2/CO_2 -saturated Fe/Ru-SiMWCNT/[MOEMPyrr⁺][PFTP⁻] nanofluid containing diethanolamine was electrolysed using two different concepts as follows.

- 1- Electrolysis of O_2/CO_2 -saturated Fe/Ru-SiMWCNT/[MOEMPyrr⁺][PFTP⁻] nanofluid containing diethanolamine.
- 2- Electrolysis of O_2/CO_2 -saturated Fe/Ru-SiMWCNT/[MOEMPyrr⁺][PFTP⁻] nanofluid and after $C_2O_6^{2-}$ was generated, diethanolamine was added.

In the process, GC electrode was used as a working electrode at different control potentials such as -1.366 , -1.400 , -1.450 , -1.500 and -1.564 V vs Ag/AgCl. Recall as described in Figure 4.13, these control potential defined a trend using charge transfer resistance and Warburg impedance. The potentials herewith were selected and confirmed to be negative enough to allow the selective reduction of O_2 to $O_2^{\bullet-}$ but not negatively enough to promote diethanolamine's electro-reduction. This essence is to enable direct interaction of diethanolamine with $C_2O_6^{2-}$; fundamentally, $CO_2^{\bullet-}$ is released from $C_2O_6^{2-}$. However, in addition to the nanofluid, some ILs were also tested, and the sections are categorized into two sections; one involving using ILs as media and the other is using Fe/Ru-SiMWCNT/[MOEMPyrr⁺][PFTP⁻] nanofluid as media for CO_2 conversion by $O_2^{\bullet-}$. These scenarios are described in section 4.6.1 and 4.6.2.

4.6.1 Using ILs as media

4.6.1.1 Effect of time on product distribution

This section described the possible optimum time for the carboxylation reaction between diethanolamine and $C_2O_6^{2-}$. Accordingly, Table 4.12 shows the performance of $C_2O_6^{2-}$ towards carboxylation of diethanolamine at different electrolysis time. While the electrolysis reaction time was varied from 0.5, 1.0, 1.5, 2.0, 2.5, to 3.0 h, all other inputs variables such as initial concentration of liquid reactant; (0.2 mL of diethanolamine/1 mL IL), flow rate of gases; $CO_2 = 0.2$ mL/1 mL IL and $O_2 = 0.2$ mL/1 mL IL, reaction voltage (E_p) = -1.564 V, and [EDMPAm⁺][TFSI⁻] electrolyte were kept constant.

According to Table 4.12, there was no carbamate formed after 0.5 h of the electrolysis time. After 1 h of electrolysis time, ~93 % of methyl (2-hydroxyethyl) (methyl) carbamate was detected. It was found that the yield of the methyl isopropylcarbamate decreased to 52.07, 66.22, 56.06 and 71.17 % after 1.5, 2.0, 2.5 and 3 h electrolysis time. Besides, methyl isopropylcarbamate was produced after 1.5 h, and this particular carbamate was not observed after 2.0, 2.5 and 3.0 electrolysis time. Also,

other side products were kept throughout the electrolysis time. These results show that 1.0 h of electrolysis time is optimal to produce carbamate methyl (2-hydroxyethyl) (methyl) carbamate. This result indicates that as the electrolysis time proceeds after 1.0 h, the carbamate produced may become an *in-situ* feedstock for another consecutive reaction step that made other products at >1.0 h electrolysis time. This claim was confirmed from the production of methyl isopropylcarbamate after 1.5 h (see Table 4.13). Also, the production of 2, 3-dimethyl-1, 3-oxazinane, 4-ethylmorpholine, or 7-acetyl-2-methyl-2, 3-dihydrobenzo[b][1, 4] oxazepin-4(5H)-one at 1.5 h electrolysis time as shown in Table 4.12 is due to consecutive consumption of the methyl (2-hydroxyethyl) (methyl) carbamate as in-situ feedstock. These results are significant to indicate that 1.0h electrolysis time is suitable for the production of methyl (2-hydroxyethyl) (methyl) carbamate, and this electrolysis time is adopted throughout the reactions presented in other sections.

Table 4.12: Effect of time on carboxylation reaction between diethanolamine and $C_2O_6^{2-}$

Product distribution	Time/h					
	0.5	1.0	1.5	2.0	2.5	3.0
[a]	-	-	19.5	19.5	21.1	14.9
[b]	-	-	-	11.8	18.7	12.2
[c]	-	-	-	2.5	3.2	1.8
[d]	-	-	23.5	-	-	-
[e]	-	93	52.1	66.2	56.1	71.2
[f]	-	-	-	-	0.9	-
[g]	-	-	4.9	-	-	-

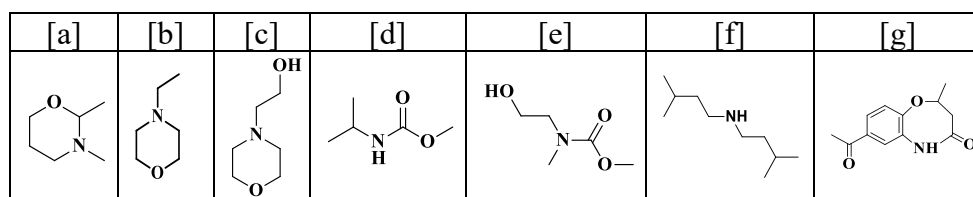


Table 4.13: Chemical symbols

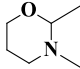
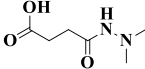
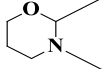
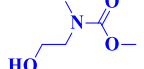
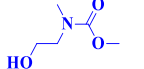
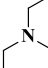
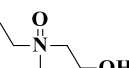
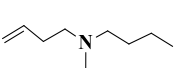
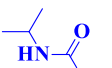
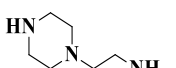
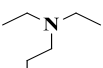
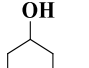
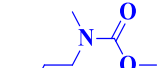
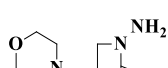
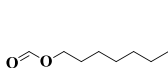
Chemical names:

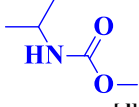
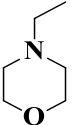
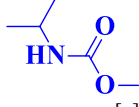
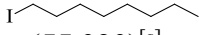
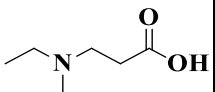
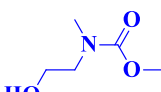
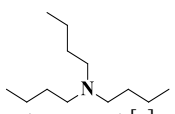
[a]; 2, 3-dimethyl-1, 3-oxazinane, [b]; 4-ethylmorpholine, [c]; 2-morpholinoethanol, [d]; methyl (2-hydroxyethyl) (methyl) carbamate, [e]; Methyl isopropylcarbamate, [f]; diisopentylamine, [g]; 7-acetyl-2-methyl-2, 3-dihydrobenzo [1, 4] oxazepin-4(5H)-one.

4.6.1.2 Effect of IL electrolyte on product distribution

Table 4.14 shows the effect of electrolytes such as [MOEMPyrr⁺][PFTP⁻] [EDMPAmm⁺][TFSI⁻], [TBMamm⁺][TFSI⁻], [BTMamm⁺][TFSI⁻] and [BMPip⁺][TFSI⁻] on the selectivity to carbamate. The product distribution presented in Tale 4.14 showed that some of the electrolyte can produce two different carbamates. For instance using [BTMamm⁺][TFSI⁻] and [BMPip⁺][TFSI⁻] electrolyte, methyl (2-hydroxyethyl) (methyl) carbamate and methyl isopropylcarbamate were detected. While in others ILs electrolyte such [MOEMPyrr⁺][PFTP⁻], [EDMPAmm⁺][TFSI⁻], [TBMamm⁺][TFSI⁻] only methyl (2-hydroxyethyl) (methyl) carbamate was detected. The production of methyl (2-hydroxyethyl) (methyl) carbamate was high in [MOEMPyrr⁺][PFTP⁻] (93.010 %), then BTMamm⁺][TFSI⁻] (15.540 %) and [BMPip⁺][TFSI⁻] (7.980 %). This screening was significant as [MOEMPyrr⁺][PFTP⁻] was selected for the subsequent electrolysis process.

Table 4.14: Effect of ILs electrolyte on product distribution

1	2	3	4	5
 (3.310) ^[a]	 (31.860) ^[f]	 (3.280) ^[k]	 (7.980) ^[p]	 (93.010) ^[t]
 (1.340) ^[b]	 (0.690) ^[g]	 (43.790) ^[l]	 (4.500) ^[q]	 (4.920) ^[u]
 (1.070) ^[c]	 (8.680) ^[h]	 (15.540) ^[m]	 (0.910) ^[r]	 (2.610) ^[v]

 (93.540) ^[d]	 (8.550) ^[i]	 (12.150) ^[n]	 (55.020) ^[s]	-
 (1.150) ^[e]	 (42.160) ^[j]	 (25.190) ^[o]	-	-

IL Electrolyte definitions; **1**=[EDMPAmm⁺][TFSI⁻], **2**=[TBMAmm⁺][TFSI⁻], **3**=[BTMAmm⁺][TFSI⁻], **4**=[BMPip⁺][TFSI⁻], **5**=[MOEMPyrr⁺][PFTP⁻].

*Chemical names:

[a]; 2, 3-dimethyl-1,3-oxazinane,

[b]; 4-ethylmorpholine,

[c]; 2-(diethylamino) ethanol,

[d]=[n]= [q]; methyl isopropylcarbamate,

[e]; 3-(diethylamino) propanoic acid,

[f]; 4-(2,2-dimethylhydrazinyl)-4-oxobutanoic acid,

[g]; N,N-diethyl-2-hydroxyethanamine oxide,

[h]; 1,2-oxazinan-4-ol,

[i]; 4-ethylmorpholine,

[j]=[m]=[p]; methyl (2-hydroxyethyl)(methyl)carbamate,

[k]; 2,3-dimethyl-1,3-oxazinane,

[l]; N-butyl-N-methylbut-3-en-1-amine,

[o]; Tributylamine,

[r]; 3-amino-5-(morpholinomethyl) oxazolidin-2-one,

[s]; 1-iodooctane,

[t]; Methyl (2-hydroxyethyl) (methyl) carbamate,

[u]; 4-(aminoethylpiperazine),

[v]; n-Heptyl methanoate.

Values in parenthesis are the isolated % yield of products. Reaction conditions: for details, see section 3.0. Pt as anode and GC electrode as a cathode, 1.0 h, -1.564 V, feedstock (DEA, CO₂, O₂ and ETI).

4.6.2 Using Fe/Ru-SiMWCNT/[MOEMPyrr⁺][PFTP⁻] nanofluid as media

4.6.2.1 Effect of an applied potential

Table 4.15 shows the result of carboxylation of diethanolamine from O₂^{•-}/CO₂ in Fe/Ru-SiMWCNT/[MOEMPyrr⁺][PFTP⁻] nanofluid. Here, the effect of different control potentials (-1.366, -1.400, -1.450, -1.500 and -1.564 V) was investigated. Through voltammetry analysis, these selected carboxylation potentials are negative enough to allow the selective reduction of O₂ to O₂^{•-} and subsequent CO₂ conversion, but not negative enough to promote electro-reduction of diethanolamine. This procedure is desired while investigating the impact of the *in-situ* generated C₂O₆²⁻ on the diethanolamine reactivity. Also, the carboxylation potentials are in range to which either Fe/Ru-SiMWCNT/[MOEMPyrr⁺][PFTP⁻] nanofluid or [MOEMPyrr⁺][PFTP⁻] are stable without showing any faradaic current (see Figure C.1c and C.1k, Appendix C). The data in Table 4.15, summarizes these two points:

- 1- Product distribution for the carboxylation of diethanolamine in Fe/Ru-SiMWCNT/[MOEMPyrr⁺][PFTP⁻] nanofluid is affected by the applied potential or activation over-potential.
- 2- The methyl (2-hydroxyethyl) (methyl) carbamate was produced as the main organic carbamate even though there are other side products.

These patterns also apply to the product distribution for the carboxylation of diethanolamine in [MOEMPyrr⁺][PFTP⁻] control shown in Table 4.16. In Fe/Ru-SiMWCNT/[MOEMPyrr⁺][PFTP⁻] nanofluid (Table 4.15 column 4, entry 5) and [MOEMPyrr⁺][PFTP⁻] (Table 4.16 column 4, entry 2) media, the carboxylation potential

of -1.564 V vs Ag/AgCl gave the best yield of methyl (2-hydroxyethyl) (methyl) carbamate. The starting material diethanolamine with a reaction temperature of 60 °C to strictly involves the C-N bond formation, produced a high yield of the methyl (2-hydroxyethyl) (methyl) carbamate after only 1.0 h. This was more rapid than using different starting materials such as phenylmethanamine, which was carboxylated to produce propyl benzylcarbamate after 3.0 h (Feroci et al., 2011). However, this comparison is on the assumption of neglecting the substituent's influence and focusing on the C-N bond formation, which is common, irrespective of the difference in the type of amine as starting material. It is suggested that the decrease in the carboxylation time is due to the significant halting of the nucleophilic susceptibility of the medium by using a non-imidazolium-based IL. This is because imidazolium-based IL media react with the $O_2^{\bullet-}$ to produce the corresponding 2-imidazolones (Feroci et al., 2011; Islam et al., 2009; AlNashef et al., 2010; Hayyan et al., 2013; Islam et al., 2008). In the viewpoint of the results in this study, the reaction in imidazolium based-IL media could increase the time required for the production of $C_2O_6^{2-}$.

The role of $C_2O_6^{2-}$ during the carboxylation of diethanolamine was verified previously from the CV analysis during CO_2 conversion by $O_2^{\bullet-}$ (Figure 4.18a and Figure 4.19a). To exclude the possibility of CO_2 influencing the carboxylation process, controlled electrolysis of O_2/CO_2 saturated Fe/Ru-SiMWCNT/[MOEMPyrr⁺][PFTP⁻] nanofluid at -1.564 V vs Ag/AgCl without diethanolamine was conducted (Figure 4.19b). After the electrolysis of O_2/CO_2 in Fe/Ru-SiMWCNT/[MOEMPyrr⁺][PFTP⁻] nanofluid, N_2 was sparged into the medium to eliminate any remnant CO_2 . The diethanolamine was then added to the catholyte medium, and eventually, methyl (2-hydroxyethyl) (methyl) carbamate was also isolated after the addition of EtI (Table 4.15 column 4, entry 5). This indicates the potential of $C_2O_6^{2-}$ in Fe/Ru-SiMWCNT/[MOEMPyrr⁺][PFTP⁻] nanofluid undergoing carboxylation reaction, which is unaffected by molecular CO_2 but associative

with cathodic reduction of O_2 to $O_2^{\bullet-}$. This observation also indicates $O_2^{\bullet-}$ mediated conversion of CO_2 to yield $C_2O_6^{2-}$ which eventually undergo carboxylation/deprotonation of diethanolamine. This kind of pattern has been observed before during carboxylation of phenylmethanamine in 1-Butyl-3-methylimidazolium tetrafluoroborate [BMIm⁺][BF₄⁻] to produce propyl benzyl carbamate (Feroci et al., 2011).

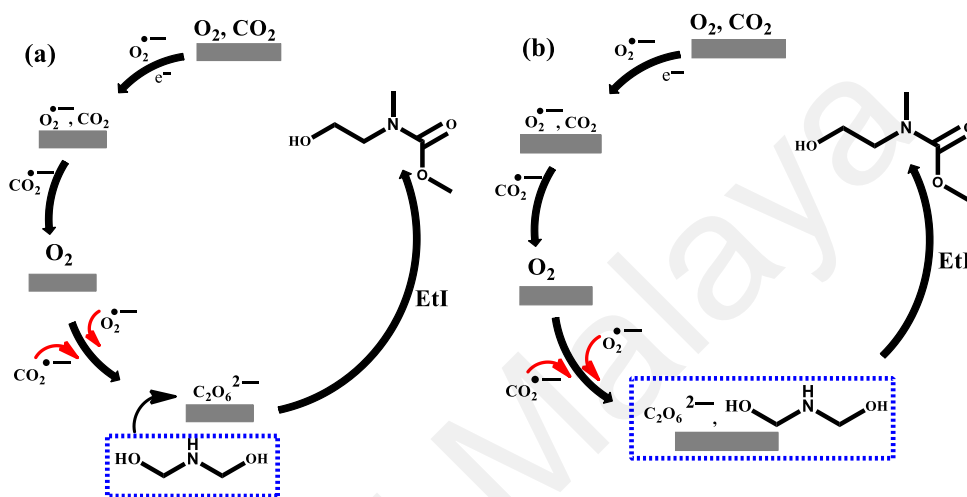


Figure 4.19: (a) Electrolysis of O_2/CO_2 in Fe/Ru-SiMWCNT/[MOEMPyrr⁺][PFTP⁻] nanofluid containing diethanolamine (b) Electrolysis of O_2/CO_2 in Fe/Ru-SiMWCNT/[MOEMPyrr⁺][PFTP⁻] nanofluid afterwards, Diethanolamine was added.

Table 4.15: Reactivity of electrogenerated $O_2^{\bullet-}$ in O_2/CO_2 -saturated Fe/Ru-SiMWCNT/[MOEMPyrr⁺][PFTP⁻] nanofluid containing 1.0 mM diethanolamine; effect of the over-potential on product distribution.

Entry	E/V	η/V	Yields ^[a] (%)				
			1a	2a	3a	4a	5a
1	-1.366	-1.160	33.82	1.74	-	13.2	51.9
2	-1.400	-1.194	63.01	1.80	-	-	-
3	-1.450	-1.244	73.01	1.82	-	-	-
4	-1.500	-1.294	83.01	2.10	-	-	-
5	-1.564	-1.244	93.01	4.92	2.61	-	-

^[a] Isolated % yields were computed based on the GCMS peak area: 1a; Methyl (2-hydroxyethyl) (methyl) carbamate, 2a; 4-(aminoethylpiperazine), 3a; n-Heptyl methanoate, 4a; 1-(4-Nitrobenzoyl) piperazine, 5a; 2-amino-2-methylpropane-1, 3-diol.

Table 4.16: Reactivity of electrogenerated $O_2^{\bullet-}$ in O_2/CO_2 -saturated [MOEMPyrr⁺][PFTP⁻] containing 1.0 mM diethanolamine; effect of over-potential on product distribution.

Entry	E/V	η/V	Yields ^[a] (%)	
			1a	2a
1	-1.366	-1.160	33.82±1.2	9.27±0.60
2	-1.400	-1.194	63.01±1.3	11.34±1.2
3	-1.450	-1.244	34.24±2.1	21.22±0.98
4	-1.500	-1.294	33.1±1.0	31.31±1.5
5	-1.564	-1.244	27.2 ±2.6	41.39±0.5

^[a]Isolated yields:

1a Methyl (2-hydroxyethyl) (methyl) carbamate,

2a N-(1-ethylazo) ethyl-1-piperidiamine.

This is a control experiment using [MOEMPyrr⁺][PFTP⁻], which is the base fluid of Ru/Fe-SiMWCNT/[MOEMPyrr⁺][PFTP⁻] nanofluid.

4.6.3 Proposed mechanism for methyl (2-hydroxyethyl) (methyl) carbamate formation

The proposed mechanism of methyl (2-hydroxyethyl) (methyl) carbamate formation from diethanolamine carboxylation using $C_2O_6^{2-}$ is shown in Figure 4.20. The necessary steps initially comprise of $CO_2^{\bullet-}$ release from $C_2O_6^{2-}$ especially in the vicinity of diethanolamine; hence, the subsequent steps involved are as follows;

1. The attack of the $CO_2^{\bullet-}$ on the nitrogen atom of diethanolamine.
2. The free radical quenching step by the second attack of the $CO_2^{\bullet-}$ on the nitrogen atom of diethanolamine.
3. The rearrangement into a pyrrole ring in the transition state accounts for the stability due to the aromatic ring with 6 electrons. The red lines represent the pyrrole ring in a two-dimensional plane. The blue-coloured atoms represent the atoms (the O^- of the carboxylate group) and the molecule (HCO_2^-) above the two-dimensional pyrrole plane. The dotted lines represent partial bond breaking and bond formation in the transition state.

4. The hydrogen donation and oxygen anion gain of the (blue arrows) HCO_2^- to release the $\text{C}_2\text{O}_6^{2-}$ to complete the formation of the methyl (2-hydroxyethyl) (methyl) carbamate.

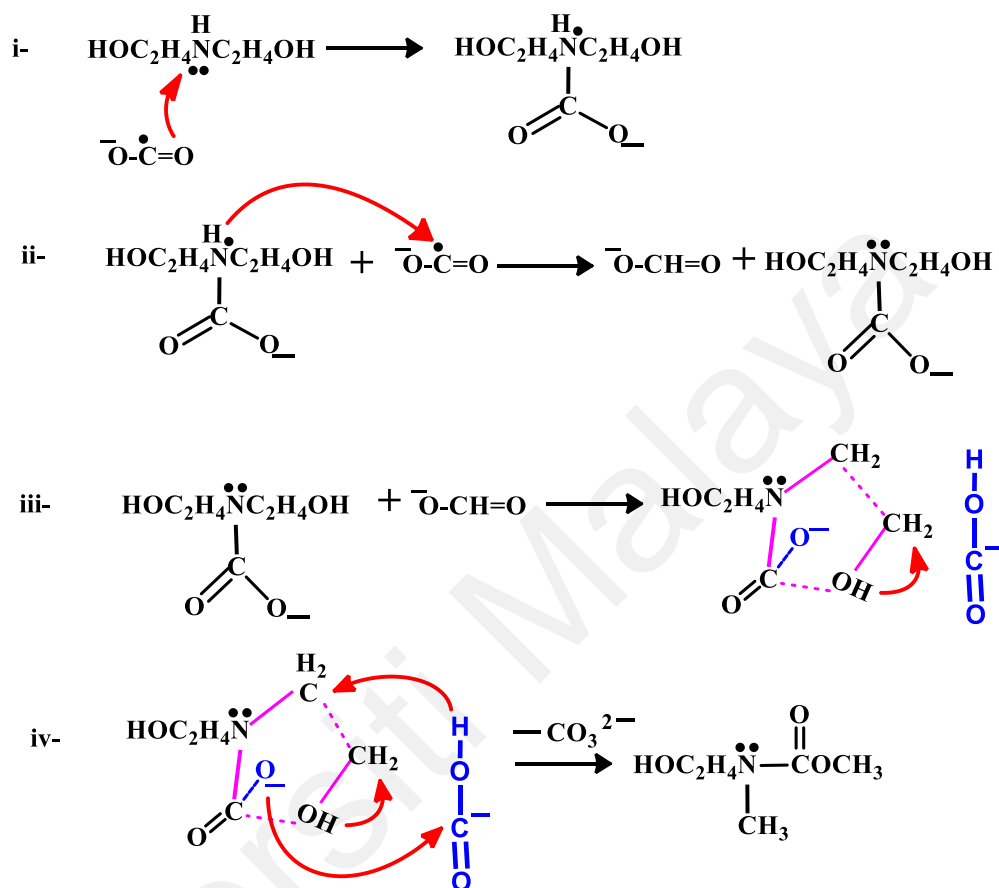


Figure 4.20: Summary of the proposed mechanism for the formation of methyl (2-hydroxyethyl) (methyl) carbamate.

4.6.3 GCMS analysis

To elucidate the major carboxylation products of diethanolamine in O_2/CO_2 saturated Ru/Fe-SiMWCNT/[MOEMPyrr⁺][PFTP⁻] nanofluid or [MOEMPyrr⁺][PFTP⁻] shown in Table 4.12 and Table 4.13, GCMS and NMR analysis was employed. The isolated product from the carboxylation reaction workup was identified as methyl (2-hydroxyethyl) (methyl) carbamate using GCMS analysis (Figure 4.21a). Using the temperature program from 40 °C to 350 °C at 10 °C/min and 5 min resting time, ethanol solvent, methyl (2-

hydroxyethyl) (methyl) carbamate can be detected at $\sim 8.58 \pm 0.23$ min retention time. The GCMS analysis MS pattern shown in Figure 4.21b accounted for the loss of $[\text{CH}_2\text{OH}^-]$ ($M/z=88$), $[\text{C}_5\text{H}_{10}\text{O}_2^+]$ ($M/z=102$) and $[\text{C}_6\text{H}_{12}\text{O}_2^+]$ ($M/z=115$), $[\text{C}_5\text{H}_{11}\text{O}_3^+]$ ($M/z=133$) from methyl (2-hydroxyethyl) (methyl) carbamate.

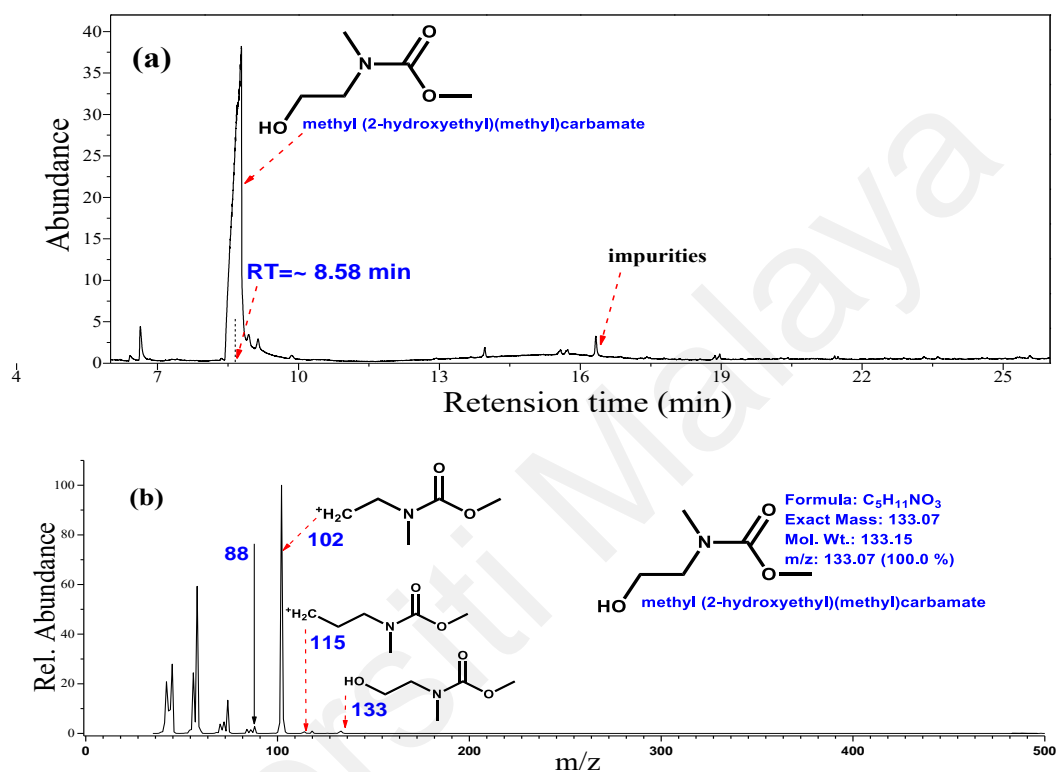


Figure 4.21: (a) GC chromatogram for methyl (2-hydroxyethyl) methylcarbamate as the product resulting from the reaction of $\text{C}_2\text{O}_6^{2-}$ and diethanolamine, (b) Mass spectrum for methyl (2-hydroxyethyl) methylcarbamate in Ru/Fe-SiMWCNT/[MOEMPyrr⁺][PFTP⁻] nanofluid.

4.6.4 NMR analysis

The NMR analysis of the methyl (2-hydroxyethyl) (methyl) carbamate was done in cognizance to previous another different carbamate that was reported (Feroci et al., 2011; Feroci et al., 2007; Inesi et al., 1998). The ^1H NMR spectrum analysis of isolated work-up of methyl (2-hydroxyethyl) (methyl) carbamate is shown in Figure 4.22a and Figure 4.22b. The singlet peaks (**1**, **3**) at 3.021 ppm and 3.332 ppm are due to the $-\text{CH}_3$

linked to oxygen and nitrogen on the methyl (2-hydroxyethyl) (methyl) carbamate, respectively. The triplet peaks (**a**) at 3.360 ppm is due to proton on the methylene linked to nitrogen (N-CH₂) linkage. The proton is coupled with two other neighbouring protons at 3.352 and 3.370 ppm chemical shifts, with j-coupling frequencies of 4.979 and 5.334 Hz, respectively. Also, the triplet peaks (**b**) at 3.456 is due to proton on the methylene linked to oxygen (O-CH₂) linkage. Similarly, the proton is coupled with two neighbouring protons at 3.448 and 3.464 ppm chemical shifts and a j-coupling frequency of 4.978 and 4.623 Hz.

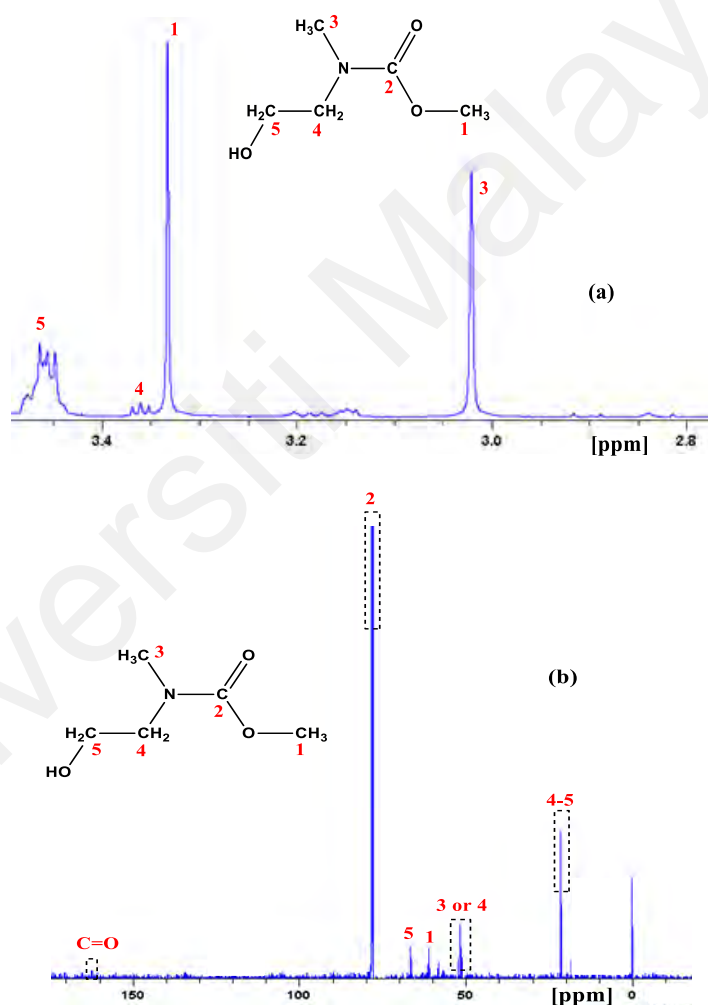


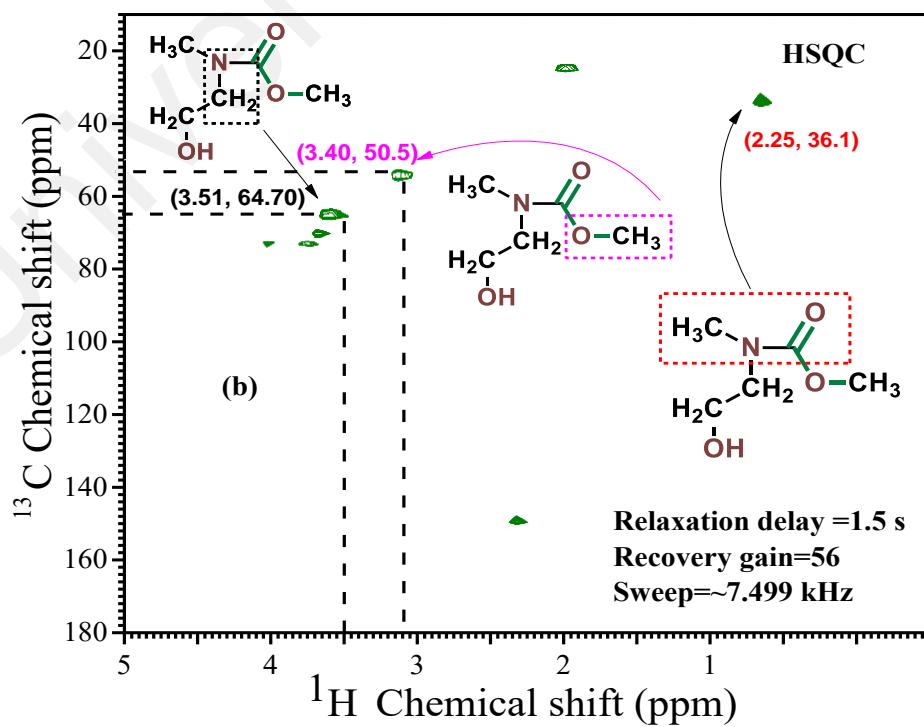
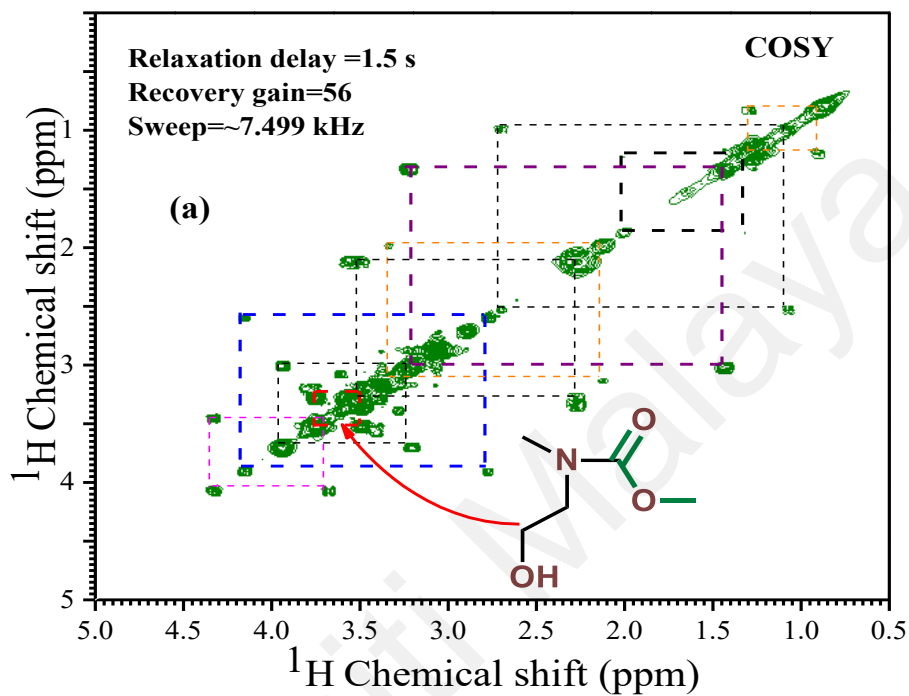
Figure 4.22: (a) ¹H NMR spectrum and (b) ¹³C H NMR spectrum of methyl 2-hydroxyethyl) (methyl) carbamate.

Given those mentioned above 1-D ¹H NMR analyses, the 2D ¹H/¹H COSY NMR shown in Figure 4.23a revealed a peak at the chemical shift of ~ 3.637 ppm coupled

with the peak at ~ 3.359 ppm. This confirmed the coupling of the triplets during the 1-D ^1H NMR analyses and indicated a compound with two distinct carbon atoms coordinated with different electronegative groups; most likely O and N. The result suggested that the ^1H -splitting revealed the two coupling peaks to be the triplets with three neighbouring protons for a $\text{R}^a\text{CH}_2\text{CH}_2\text{R}^b$ typical moiety construct in methyl (2-hydroxyethyl) (methyl) carbamate. The ^1H -splitting analysis in 2D $^1\text{H}/^1\text{H}$ COSY NMR also showed additional two singlets peaks at 3.10 ppm and 3.38 ppm with 3H integration, suggesting other structural constructs of R^cCH_3 or R^dCH_3 . It can be said that R^a or R^c groups can be indexed since they occurred more downfield the chemical shift than R^b or R^d such that in general, it can be postulated that $\text{R}^a=\text{R}^c=\text{Nitrogen}$ and $\text{R}^b=\text{R}^d=\text{Oxygen}$.

Through heteronuclear single quantum coherence spectroscopy (HSQC) shown in Figure 4.23b, there are correlations between ^1H at ~ 2.25 ppm, ~ 3.40 ppm, and ~ 3.51 ppm with ^{13}C , at ~ 151.1 ppm, ~ 50.5 ppm, and ~ 64.7 ppm, respectively. These $^1\text{H}/^{13}\text{C}$ couplings correspond to moieties such as $\text{H}_3\text{C}-\text{NC}$ (O), $\text{O}-\text{CH}_3$ and $\text{N}-\text{CH}_3$, respectively. The moieties are observable in the structural construct of methyl (2-hydroxyethyl) (methyl) carbamate. By implication, the HSQC ($^1\text{H}-^{13}\text{C}$) evaded the concern of signals splitting resulting from homonuclear $^{13}\text{C}/^{13}\text{C}$ J couplings, which usually reduce spectral resolutions to represent the $^1\text{H}/^{13}\text{C}$. To further confirm methyl (2-hydroxyethyl) (methyl) carbamate structure, a stronger correlation which is more than a bond away were investigated using heteronuclear multiple bond correlation spectroscopy (HMBC) analysis shown in Figure 4.23c in contours mode. The triplet proton at 3.360 ppm chemical shift is strongly correlated with the carbon at 159.5 ppm, which is three bonds away (entry 1 in Figure 4.23c). Similarly, the triplet proton at 3.456 ppm chemical shift is strongly correlated with the carbon at 50.5 ppm, which is also four bonds away (entry 2 in Figure 4.23c). Other correlations were observed at single bonds between the proton and carbon in methyl (2-hydroxyethyl) (methyl) carbamate. The triplet proton at 3.456

ppm chemical shift is correlated to carbon at a single bond (entry 3). Also, the proton at 3.02 ppm is correlated to the carbon at which is one bond away (entry 4). The proton at 3.02 ppm is correlated to the carbon at which is one bond away (entry 5).



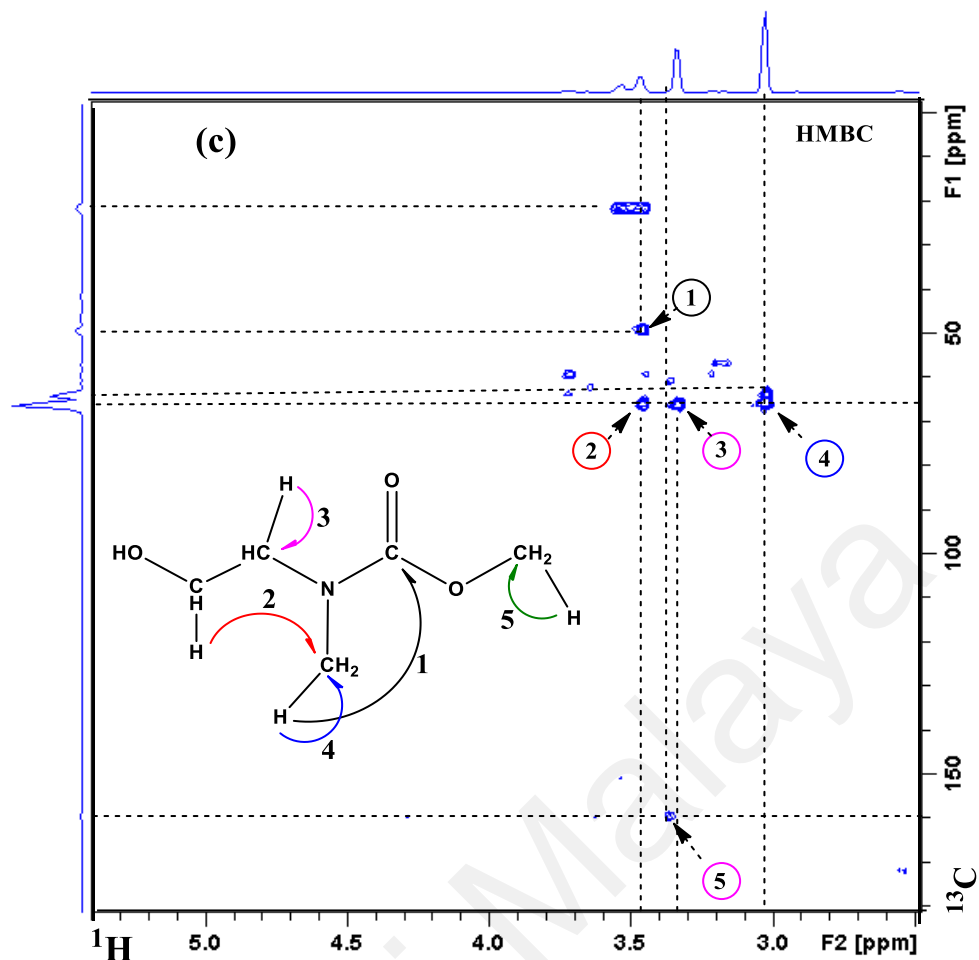


Figure 4.23: 2D-NMR analysis profiles for detected methyl (2-hydroxyethyl) (methyl) carbamate (a) COSY/400MHz, (b) HSQC/400mHz and (C) HMBC/600MHz

4.7 Dechlorination of CH_2Cl_2 and $\text{C}_6\text{H}_5\text{Cl}$ by $\text{O}_2^{\bullet-}$ in $[\text{BMPip}^+][\text{TFSI}^-]$

In retrospect, incineration technology is commonly used to remove chlorinated contaminants (Evans and Dellinger, 2005; Yang et al., 2017). Unfortunately, the incineration practice produces poisonous dioxins (Orloff et al., 2001; Xu et al., 2016). According to the 2015 World Health Organisation (WHO) report, eliminating dioxin toxicity is a significant public health priority for disease reduction. Consequently, the need to develop more effective technologies to destroy chlorinated contaminants without producing dioxin is necessary. Under this auspice, superoxide ion ($\text{O}_2^{\bullet-}$) in stable $[\text{BMPip}^+][\text{TFSI}^-]$ mediate the reductive dechlorination of $\text{C}_6\text{H}_5\text{Cl}$ and CH_2Cl_2 to non-dioxin oxygenates. This reaction is possible because the long-term stability of $\text{O}_2^{\bullet-}$ in

[BMPip⁺][TFSI⁻] is feasible (see Table 4.8 and Table 4.9). The long-term stability validates that 91.73 % of O₂^{•-} is available in [BMPip⁺][TFSI⁻] for any possible utilization. Moreover, DFT calculation further buttresses this capability through evident stability of [BMPip⁺] cation to the nucleophilic effect of O₂^{•-} as seen in the following subsection. Also, the COMOS-RS method was used to estimate the capacity of [BMPip⁺][TFSI⁻] to interact with C₆H₅Cl and CH₂Cl₂ model chlorinated compound during the conversion process. In section 4.7.1 Gaussian calculation will be discussed while section 4.7.2 describes the COSMOthermX calculation.

4.7.1 DFT frontier molecular orbital analysis

The evidence of [BMPip⁺][TFSI⁻] stability to nucleophilic susceptibility was determined using DFT calculation at the B3LYP/6-31G level of theory. Based on a molecular structure, the [BMPip⁺][TFSI⁻] does not contain a methoxy group on the piperidinium cation [BMPip⁺] (see Table 3.2).

In Figure 4.24a, from the optimized geometry of [BMPip⁺] cation, DFT calculation confirmed that the absence of methoxy functionality in the piperidinium cation determines why all its C(sp) contains negative Mulliken charges. These Mulliken atomic charges are significant properties that assure [BMPip⁺] cation's stability, especially to O₂^{•-} nucleophilic susceptibility (Fogarty et al., 2018; Griffith & Orgel, 1957).

Besides, the frontier molecular orbital (FMO) of C₆H₅Cl, CH₂Cl₂, O₂^{•-}, OH⁻ with [BMPip⁺] cation inclusive were estimated. The FMO theory, associated with the highest occupied molecular orbital (HOMO) and lowest unoccupied molecular orbital (LUMO), is one of the best approaches for explaining a molecule's chemical stability or reactivity (Dannenberg, 1999). In Figure 4.24b, the HOMO and LUMO for the [BMPip⁺] cation are in 3D renderings in terms of iso-valued surfaces. These HOMO (-3.482 eV) and LUMO (0.852 eV) energies represent the [BMPip⁺] cation potential energy required for

ionization and electron affinity, respectively. In accordance, high HOMO energy corresponds to a more reactive molecule with an electrophile, while low LUMO energy signifies less reactive molecular reaction with nucleophiles on non-exclusive terms (Fukui, 1982).

Comparing the HOMO of $O_2^{\bullet-}$ and $[BMPip^+]$ cation, the former was 5.230 eV and the latter is -3.482 eV. This result indicates that $O_2^{\bullet-}$ is extremely more reactive than $[BMPip^+]$ cation. Similarly, comparing the LUMO of $O_2^{\bullet-}$ and $[BMPip^+]$ -cation, the former was 4.803 eV, and the latter is -0.852 eV. This result also implies that $O_2^{\bullet-}$ has more electron affinity since it has lower LUMO energy than $[BMPip^+]$ -cation. On an exclusive term, the difference between the HOMO and LUMO energies represents the excitation energy ($E_{HOMO}-E_{LUMO} = E$), which dictates the chemical reactivity and kinetic stability of molecules (De Proft et al., 2007).

Further determination of the electrophilicity index showed that $[BMPip^+]$ -cation has an apparent positive character with an electrophilicity index of $\omega = 0.100$ eV at a DFT/3-21G level of theory. These results suggested that irrespective of the positive nature of $[BMPip^+]$ -cation, the negative Mulliken atomic charges of its C (sp) have to override possible nucleophilic attack by $O_2^{\bullet-}$. Contrarily, other methoxy functionalized piperidinium ILs such as 1-(3-methoxypropyl)-1-methylpiperidinium $[MOPMPip^+]$ (Hayyan et al., 2012), 1-(3-Methoxypropyl)-1-methylpiperidinium (Hayyan et al., 2017), or 1-(2-Methoxyethyl)-1-methylpiperidinium (Neale et al., 2016), contain at least a positive C (sp). At least one positive C (sp) presence in IL-cation is sufficient to boost its nucleophilic susceptibility. For example, $[MOPMPip^+]$ due to its positive carbon ($+0.234$ eV), it is nucleophilic susceptible to consuming $\sim 27\%$ $O_2^{\bullet-}$ after two hours (Hayyan et al., 2012). On the contrary, $[BMPip^+]$ consumes only $\sim 8.27\%$ of $O_2^{\bullet-}$ after three hours (see Table 4.9). Therefore, due to high $O_2^{\bullet-}$ consumption by methoxy functionalized ILs, they are not suitable for $O_2^{\bullet-}$ utilization if they are made of $[TFSI^-]$ anion, for instance,

in the dechlorination process. This is because the [MOPMPip⁺] contain [TFSI⁻] anion and consume a high amount of O₂^{•-} after 2h. Interestingly, the excitation energy (E) for [BMPip⁺]-cation (4.340 eV) is slightly greater than that for O₂^{•-} (0.430 eV). This result means that [BMPip⁺]-cation with large excitation energy (E) than O₂^{•-} is less polarizable and has high molecular stability.

Figure A.2a and Figure A.2b (Appendix A) show the HOMO energies of C₆H₅Cl and CH₂Cl₂. The DFT/6-31G level of theory estimates their HOMO energies to be -6.884 eV and -8.626 eV. This result shows that the polarization of CH₂Cl₂ is easier than C₆H₅Cl. In comparison with the HOMO energy of O₂^{•-}, it is apparent that the O₂^{•-} can mediate their polarization since the radical has higher HOMO (5.230 eV) energy than the chlorinated compounds.

Figure A.2c and Figure A.2d (Appendix A) shows the HOMO of O₂^{•-} and OH⁻ was estimated to be 3.586 eV and 11.319 eV, respectively. Delving to understand the reactivity of OH⁻ is important as it's the only contending radical to O₂^{•-}. It may arise if there is moisture so, evaluating its chemical reactivity in comparison to O₂^{•-} is necessary. Therefore, the result of comparing O₂^{•-} and OH⁻ indicates that OH⁻ is more reactive than O₂^{•-}. The high reactivity of OH⁻ is due to its high HOMO energy (11.319 eV). Despite this, O₂^{•-} have lower excitation energy. The HOMO orbital of O₂^{•-} is much closer to the LUMO orbital, and this makes it more readily available than OH⁻. By implication, for the kind of application in this present study, radical that is readily available is preferred and O₂^{•-} fulfils this criterion. Further determination of the electrophilicity index showed that O₂^{•-} has a more negative character with $\omega = -6.550$ eV than OH⁻ which has $\omega = -2.270$ eV.

Also, the positive character of C₆H₅Cl and CH₂Cl₂ is verified with an electrophilicity index of $\omega = 0.519$ eV and $\omega = 0.788$ eV respectively. These results indicate a higher positive character of C₆H₅Cl and CH₂Cl₂ than that of [BMPip⁺]-cation

($\omega = 0.100$ eV). In terms of competition, C_6H_5Cl and CH_2Cl_2 in $[BMPip^+][TFSI^-]$ will be consumed by $O_2^{\bullet-}$. Moreover, because $[BMPip^+]$ -cation has negative Mulliken atomic charges of its C (sp), the IL is not susceptible to nucleophilic attack by $O_2^{\bullet-}$. If water is used as a medium for the dechlorination process, the $O_2^{\bullet-}$ will disproportionate and the reaction will fail. Preferentially, $O_2^{\bullet-}$ interact with the C_6H_5Cl and CH_2Cl_2 during the dechlorination process. Although OH^- can react with C_6H_5Cl and CH_2Cl_2 , $O_2^{\bullet-}$ was selected because of its low excitation energy.

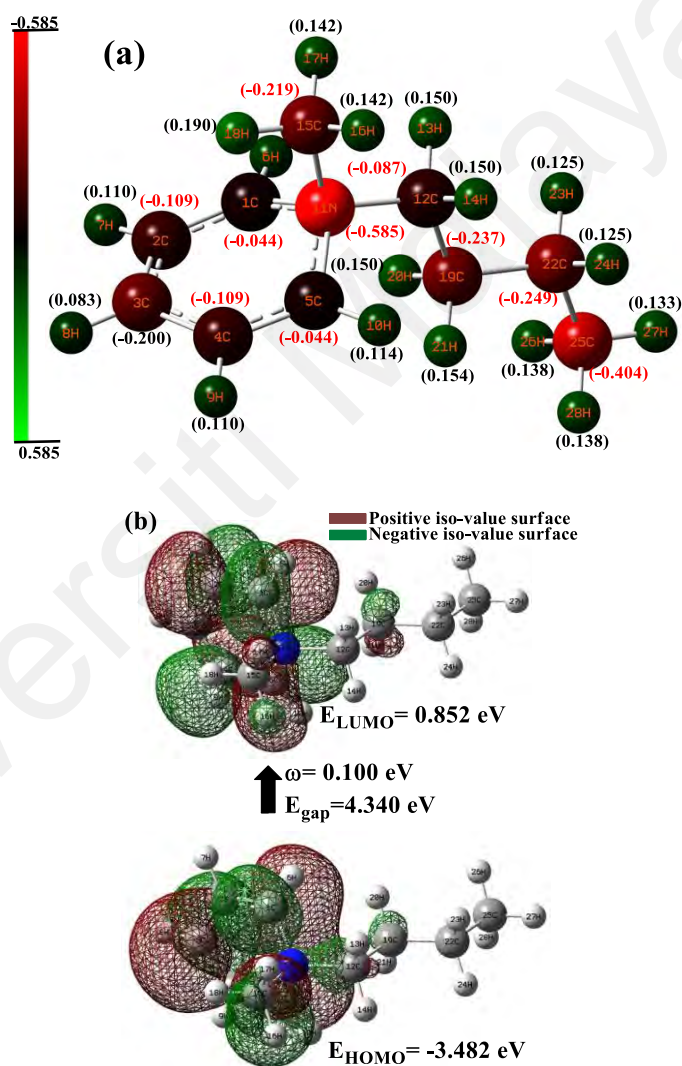


Figure 4.24: (a) Mulliken atomic charges on $[BMPip^+]$ -cation, (b) Frontier molecular orbital showing 3-D rendered iso-valued surfaces for $[BMPip^+]$ -cation. The green colour coding represents a negative iso-surface, while the brown colour coding signifies the positive iso-surface computed at the DFT/B3LYP/6-31G level of theory.

4.7.2 COSMO-RS benchmarking on dechlorination process

COSMO-RS technique was used as shown in Figure 4.25a and 4.25b to elucidate the solvent preference of [BMPip⁺][TFSI⁻] for C₆H₅Cl and CH₂Cl₂ dechlorination using O₂^{•-}. This is because of a likely argument of using H₂O as a solvent for C₆H₅Cl and CH₂Cl₂ dechlorination instead of ILs. OH⁻ from H₂O in normal hydro-dechlorination techniques potentially render chlorinated substance passive through the participation of the nascent proton from H₂O (Kopinke et al., 2016; Liu et al., 2018). Despite this suggestion, the chlorinated compound's solubility is another limitation that could limit the technique's viability. Especially with the philosophy of using O₂^{•-} for the dechlorination, H₂O will induce disproportionation of O₂^{•-}. Therefore, in Figure 4.25a and 4.25b, the realistic interaction of these moieties in the potential dechlorination process is shown.

Therefore, the σ -profile and σ -potential of [BMPip⁺][TFSI⁻], H₂O solvents, was calculated using the COSMO-RS method and compared with the σ -profile and σ -potential of the organic chlorides such as C₆H₅Cl and CH₂Cl₂ as shown in Figure 4.25a and 4.25b. The σ -profile and σ -potential histograms of these molecules measure the possible real interactions and their corresponding chemical potentials. The σ -profile and σ -potential histograms contain three central regions identified in Figure 4.25a and 4.25b and have been described in section 4.1.1. For a recap, the first region is where the σ values are less than -0.86 e/nm^2 . This region is associated with the hydrogen bond donor area (HBD). The second region is where σ values-centred between -0.86 e/nm^2 and $+0.86 \text{ e/nm}^2$; this defines the nonpolarized area. The third region is where σ values are higher than $+0.86 \text{ e/nm}^2$ and specify the hydrogen bond acceptor area (HBA).

However, σ -surface of H₂O in Figure 4.25a is dominated by the blue regions of strongly negative σ on the HBDs. The red areas of the oxygen-lone pairs are the HBA. These hydrogen bonding areas cause two almost symmetric peaks in the σ -profile of H₂O,

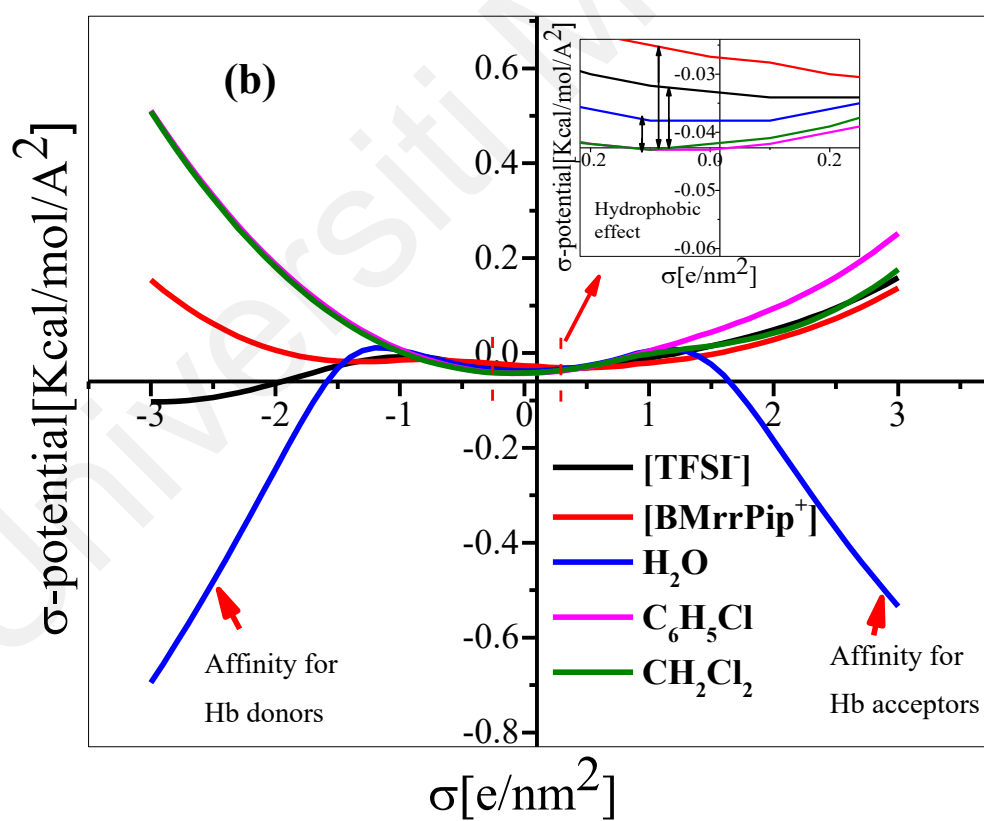
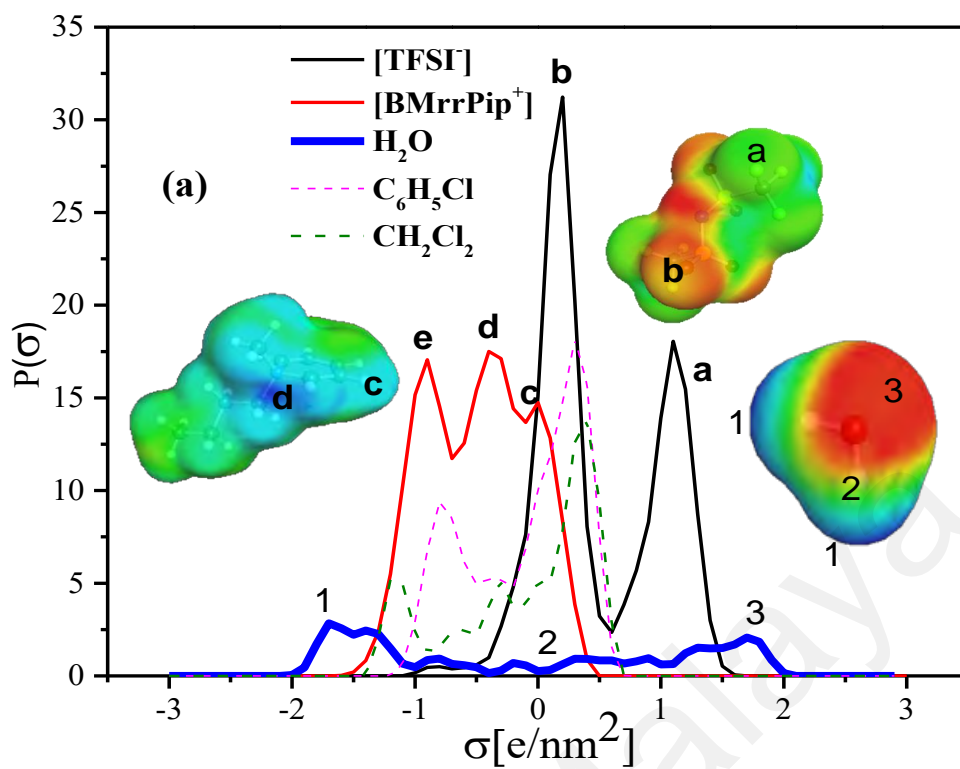
centred at $\pm 1.7 \text{ e/nm}^2$. This region dominates the σ -profile. Similarly, in Figure 4.25a, the σ -surface of $[\text{BMPip}^+][\text{TFSI}^-]$ is calculated precisely for the $[\text{BMPip}^+]$ and $[\text{TFSI}^-]$ ends. The σ -surface of $[\text{BMPip}^+][\text{TFSI}^-]$ is dominated by the blue regions of strongly negative σ (-0.921 e/nm^2) on the HBD coming from $[\text{BMPip}^+]$ contribution, and the red regions of the oxygen-lone pairs, which are HBA coming from $[\text{TFSI}^-]$ contribution with positive σ (1.108 e/nm^2). Generally, the $[\text{BMPip}^+][\text{TFSI}^-]$ or H_2O have both HBD and HBA capability.

There is a non-polar surface on CH_2Cl_2 , $\text{C}_6\text{H}_5\text{Cl}$, H_2O , and $[\text{BMPip}^+][\text{TFSI}^-]$. The non-polar surface on CH_2Cl_2 , $\text{C}_6\text{H}_5\text{Cl}$, $[\text{BMPip}^+]$, and $[\text{TFSI}^-]$ centered at $-0.273 \text{ e/nm}^2 < \sigma < 0.375 \text{ e/nm}^2$, $-0.797 \text{ e/nm}^2 < \sigma < 0.306 \text{ e/nm}^2$, $-0.383 \text{ e/nm}^2 < \sigma < 0.003 \text{ e/nm}^2$, and $\sigma = 0.196 \text{ e/nm}^2$ respectively. For H_2O solvent, the σ -profile has a relatively low portion of the non-polar surface area. This attribute is due to H_2O ability to provide the optimal partner of opposite polarity for all surface segments. Also, H_2O has a minimal concentration of suitable partner surfaces for non-polar, i.e. green surface segments of solutes. In Figure 4.25b, the polar range $-1.028 \text{ e/nm}^2 < \sigma < 1.081 \text{ e/nm}^2$, and H_2O has almost flat σ -potential with a minimal curvature. Essentially this corresponds to the electrostatic response of a strong dielectric medium. In the outer range of σ ($> \pm 1.0 \text{ e/nm}^2$), hydrogen bonding causes a strongly negative chemical potential for the HBD surface segment and HBA segment. Similarly, in the outer range, the polar range for $[\text{BMPip}^+][\text{TFSI}^-]$, hydrogen bonding causes a strongly positive chemical potential for the HBD surface segment and HBA segment. In comparison, the σ potential of CH_2Cl_2 and $\text{C}_6\text{H}_5\text{Cl}$ has a strong positive chemical potential similar to $[\text{BMPip}^+][\text{TFSI}^-]$ in the hydrogen bonding region (HBD or HBA). This attribute indicates a certain degree of repulsion of CH_2Cl_2 and $\text{C}_6\text{H}_5\text{Cl}$ from H_2O , particularly at the hydrogen bonding segment.

The hydrophobicity of CH_2Cl_2 and $\text{C}_6\text{H}_5\text{Cl}$ is also from the σ -potential centred in the range $-0.2 \text{ e/nm}^2 < \sigma < 0.2 \text{ e/nm}^2$ in the σ -potential. Meaning, a non-polar surface area

of C_6H_5Cl and CH_2Cl_2 prefers $[BMPip^+][TFSI^-]$ to H_2O . Mainly, the ambient condition can hardly break the strong hydrogen bond between the polar parts of H_2O or $[BMPip^+][TFSI^-]$. Hence only a small percentage of the non-polar (green) surface area of these solvents is available for non-polar molecular surface dissolving (Klamt, 2003). Water has less polar acceptor and less polar donor. Similarly, the TFSI has a slightly low polar donor and polar acceptor from the $[BMPip^+]$. However, C_6H_5Cl and CH_2Cl_2 show a certain degree of hydrophobicity but appear to interact more with $[BMPip^+][TFSI^-]$.

The composition dependence of the model chlorinated compounds (C_6H_5Cl , and CH_2Cl_2) to their activity coefficient (γ^∞) at infinite dilution in $[BMPip^+][TFSI^-]$ and H_2O is displayed in Figure 4.25(c-d). The COSMO-RS predicted values of γ^∞ at infinite dilution in H_2O as shown in Figure 4.25c while that in $[BMPip^+][TFSI^-]$ is shown in Figure 4.25d. The increase in γ^∞ with composition (moles) for the H_2O medium in Figure, 4.25c signifies escaping tendency of the constitutive molecules (C_6H_5Cl , or CH_2Cl_2). Moreover, the decrease in γ^∞ with an increase in composition (moles) for the $[BMPip^+][TFSI^-]$ medium in Figure 4.25d system signifies a strong attractive force between the constitutive molecules (C_6H_5Cl , or CH_2Cl_2). Therefore, apart from the fact that H_2O will disproportionate $O_2^{\bullet-}$ before mediating the dechlorination of C_6H_5Cl , and CH_2Cl_2 , the γ^∞ trend reveal H_2O to be less suitable as media unlike $[BMPip^+][TFSI^-]$. It is worth noticing that γ^∞ values in $[BMPip^+][TFSI^-]$ are lower than unity irrespective of variation in the composition while in H_2O they are greater than unity. These results mean that C_6H_5Cl or CH_2Cl_2 have strong attractive force with $[BMPip^+][TFSI^-]$ and repelling force in H_2O . The interpretation is in cognizance with previous studies though, different molecules were used and media (Putnam et al., 2003; Banerjee, T., & Khanna, A. 2006; Matheswaran et al., 2016).



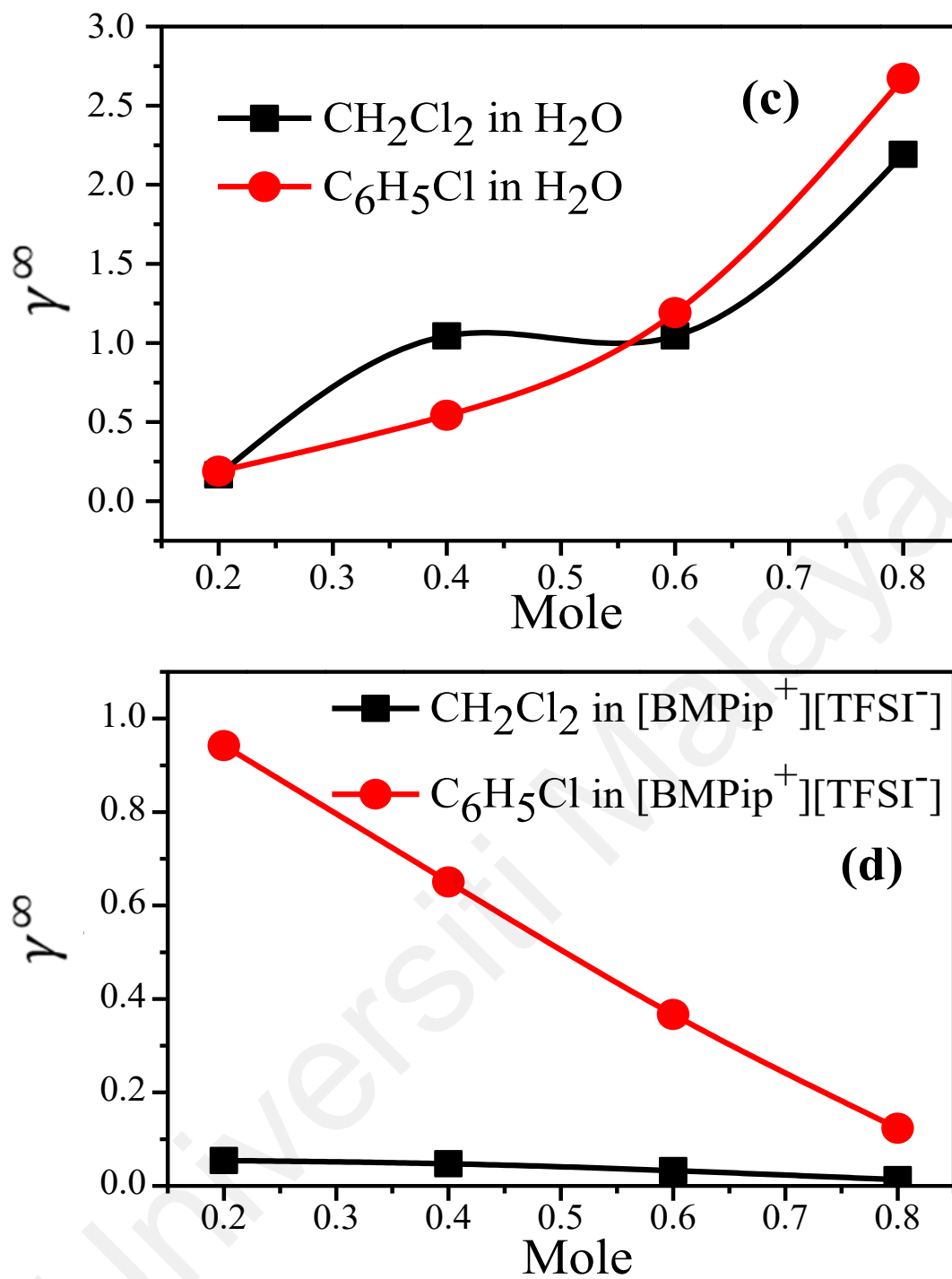


Figure 4.25: (a) σ -surface/ σ -profile of $[\text{BMPip}^+][\text{TFSI}^-]$ and H_2O in comparison with σ -profile of $\text{C}_6\text{H}_5\text{Cl}$ and CH_2Cl_2 , (b) σ -potential of $[\text{BMPip}^+][\text{TFSI}^-]$, H_2O , $\text{C}_6\text{H}_5\text{Cl}$, and CH_2Cl_2 , (c) Activity coefficient of $\text{C}_6\text{H}_5\text{Cl}$, or CH_2Cl_2 in H_2O , (d) Activity coefficient of $\text{C}_6\text{H}_5\text{Cl}$, or CH_2Cl_2 in $[\text{BMPip}^+][\text{TFSI}^-]$ at infinite dilution.

4.7.3 Electrochemical active surface area

The electrochemical active surface area (ECSA) of the GC electrode used in this study was determined to aid the normalization of subsequent current densities for $O_2^{\bullet-}$ generation and utilization.

To determine the ECSA, cyclic voltammetry (CV) was measured in a narrow potential range of -0.35 V to -0.8 mV range vs Ag/AgCl. The corresponding CV waves were measured in N_2 , and O_2 saturated [BMPip⁺][TFSI⁻], and [BMPip⁺][TFSI⁻] containing 2.5 mM CH_2Cl_2 or C_6H_5Cl respectively, as shown in Figure J.1 (a-f), (Appendix J). According to Figure J.1 (a-f), (Appendix J) the potential range has no faradaic current as expected from the criteria for the differential capacitance method (DCM) for estimating ECSA (Voiry et al., 2018).

Figure 4.26 (a-c) shows the capacitance (C_{DL}) and capacitance of an ideal flat surface (C_{DLRef}) in [BMPip⁺][TFSI⁻] and [BMPip⁺][TFSI⁻] containing 2.5 mM CH_2Cl_2 or C_6H_5Cl . The C_{DL} was determined directly in O_2 saturated [BMPip⁺][TFSI⁻] and [BMPip⁺][TFSI⁻] containing 2.5 mM CH_2Cl_2 or C_6H_5Cl . It was found to be influenced by the oxidation layer on an electrode's surface (Trasatti & Petrii, 1991). However, N_2 sterilization eliminates the fouling of electrodes from oxide layers prone to microscopic/nanoscale of scratches, bumps, and curves. Therefore, the C_{DLRef} was determined in N_2 saturated [BMPip⁺][TFSI⁻] and [BMPip⁺][TFSI⁻] containing 2.5 mM CH_2Cl_2 or C_6H_5Cl media. The values for C_{DLRef} as indicated in Figure 4.26 (a-c), the double-layer capacitance benchmark for ideal flat surfaces is in the range of 0.022 and 0.13 mC/cm² (McCrorry et al., 2013). This result shows that N_2 sterilization can estimate an ideal flat surface's capacitance. Therefore, by using Eq 3.6, the ECSA was calculated by taking the ratio of the C_{DL} to the C_{DLRef} relative to the geometric area (0.702 cm²) of the GC electrode. According to Figure 4.26d, the value of the ECSA of GC in O_2 -

saturated $[\text{BMPip}^+][\text{TFSI}^-]$, and $[\text{BMPip}^+][\text{TFSI}^-]$ containing 2.5 mM CH_2Cl_2 or $\text{C}_6\text{H}_5\text{Cl}$ is 0.827, 1.450 and 0.045 cm^2 , respectively. These results indicate that ECSA is dependent on the nature of the media in which an electrode is immersed.

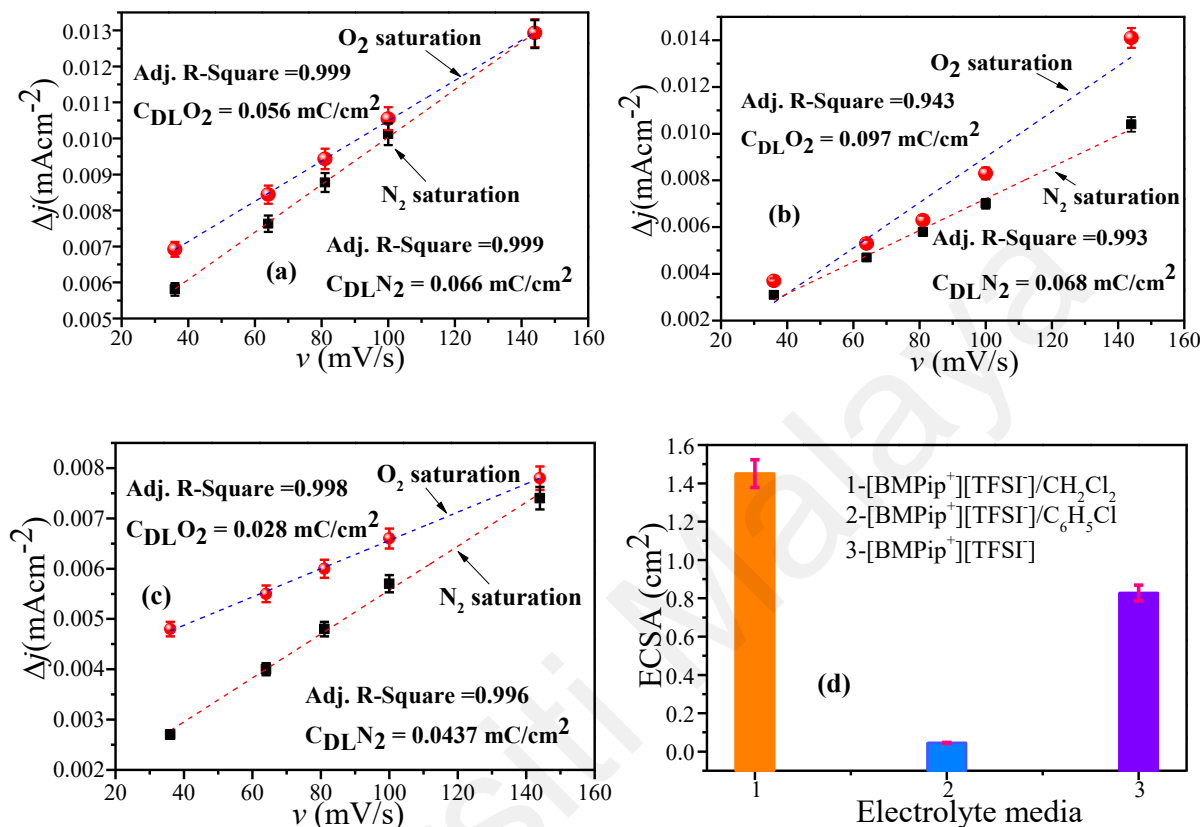


Figure 4.26: Charging difference (Δj) vs. scan rates stripping in N_2/O_2 saturated; (a) $[\text{BMPip}^+][\text{TFSI}^-]$, (b) $[\text{BMPip}^+][\text{TFSI}^-]/\text{CH}_2\text{Cl}_2$, (c) $[\text{BMPip}^+][\text{TFSI}^-]/\text{C}_6\text{H}_5\text{Cl}$, (d) Comparing the ECSA of GC electrode in O_2 saturated $[\text{BMPip}^+][\text{TFSI}^-]$, $[\text{BMPip}^+][\text{TFSI}^-]/\text{CH}_2\text{Cl}_2$, and $[\text{BMPip}^+][\text{TFSI}^-]/\text{C}_6\text{H}_5\text{Cl}$.

4.7.4 Evidence of $\text{O}_2^{\bullet-}$ in $[\text{BMPip}^+][\text{TFSI}^-]$ containing CH_2Cl_2 or $\text{C}_6\text{H}_5\text{Cl}$

The one-electron reduction of O_2 to $\text{O}_2^{\bullet-}$ was confirmed through cyclic voltammetry (CV) analysis in the three different media such as $[\text{BMPip}^+][\text{TFSI}^-]$, $[\text{BMPip}^+][\text{TFSI}^-]$ containing 2.5 mM of CH_2Cl_2 , and $[\text{BMPip}^+][\text{TFSI}^-]$ containing 2.5 mM of $\text{C}_6\text{H}_5\text{Cl}$. In Figure 4.27a, the CV waves corresponding to the generation of $\text{O}_2^{\bullet-}$ in the pure $[\text{BMPip}^+][\text{TFSI}^-]$ are shown in retrospect. In the presence of backward

oxidation CV waves, the $O_2^{\bullet-}$ was stable in $[BMPip^+][TFSI^-]$. Similarly, Figure 4.24a and 4.27b show the CV waves corresponding to the generation of $O_2^{\bullet-}$ in the $[BMPip^+][TFSI^-]$ containing 2.5 mM each of CH_2Cl_2 or C_6H_5Cl , respectively. Irrespective of the media, the reduction potential for O_2 to $O_2^{\bullet-}$ increased as the scan rate stripping increase (Figure 4.27a and 4.27b). These results implied that the process of O_2 electrochemical reduction to $O_2^{\bullet-}$ is time-dependent. For instance, at 9.0 mV/s, the reduction potential of O_2 to $O_2^{\bullet-}$ in $[BMPip^+][TFSI^-]$ occurred at -0.875 V. However, in $[BMPip^+][TFSI^-]$ containing 2.5 mM of CH_2Cl_2 or C_6H_5Cl , the reduction potential occurred at -0.742 V and -0.818 V respectively. The O_2 reduction potential in $[BMPip^+][TFSI^-]$ containing 2.5 mM of CH_2Cl_2 or C_6H_5Cl is slightly lower than the one observed in the ordinary $[BMPip^+][TFSI^-]$.

The interfacial charge transfer coefficient (α), the solubility of O_2 (C_o), and diffusion coefficient (D_o) of O_2 in $[BMPip^+][TFSI^-]$, and $[BMPip^+][TFSI^-]$ containing 2.5 mM of CH_2Cl_2 or C_6H_5Cl were determined using the equations 3.7, 3.8 and 3.9. In $[BMPip^+][TFSI^-]$, $\alpha = 0.535$, $D_o = 2.338 \times 10^{-10}$ m²/s. The D_o -value is smaller in magnitude to other ILs $[MOPMPip^+][TFSI^-]$ ($D_o = 1.00 \times 10^{-10}$ m²/s) (Hayyan et al., 2011). The solubility of O_2 in $[BMPip^+][TFSI^-]$ ($C_o = 4.231$ mM) smaller than the one observed in $[MOPMPip^+][TFSI^-]$ ($C_o = 14.300$ mM) (Hayyan et al., 2016; Hayyan et al., 2011). Similarly, in $[BMPip^+][TFSI^-]$ containing CH_2Cl_2 or C_6H_5Cl , the $\alpha = 0.324$ and $\alpha = 0.549$ respectively. These results showed that 2.5 mM of CH_2Cl_2 in 2 mL of $[BMPip^+][TFSI^-]$ reduced the α -value from 0.535 to 0.324. Similarly, the addition of 2.5 mM of C_6H_5Cl into 2.0 mL $[BMPip^+][TFSI^-]$ slightly increased the α -value from 0.535 to 0.549. By implication, the chlorinated compound's addition to the IL could increase or decrease the charge transfer's influence (Andrieux, Gallardo, & Saveant, 1989). These results confirmed that $O_2^{\bullet-}$ can be electrochemically generated in $[BMPip^+][TFSI^-]$ and especially $[BMPip^+][TFSI^-]$ containing 2.5 mM of CH_2Cl_2 or C_6H_5Cl . Ensuring the

generation of $\text{O}_2^{\bullet-}$ is an important criterion that should be established before estimating the exchange current density ($i_{o,\text{ECSA}}$) during reductive dechlorination of $\text{C}_6\text{H}_5\text{Cl}$, CH_2Cl_2 , or any other chlorinated pollutants.

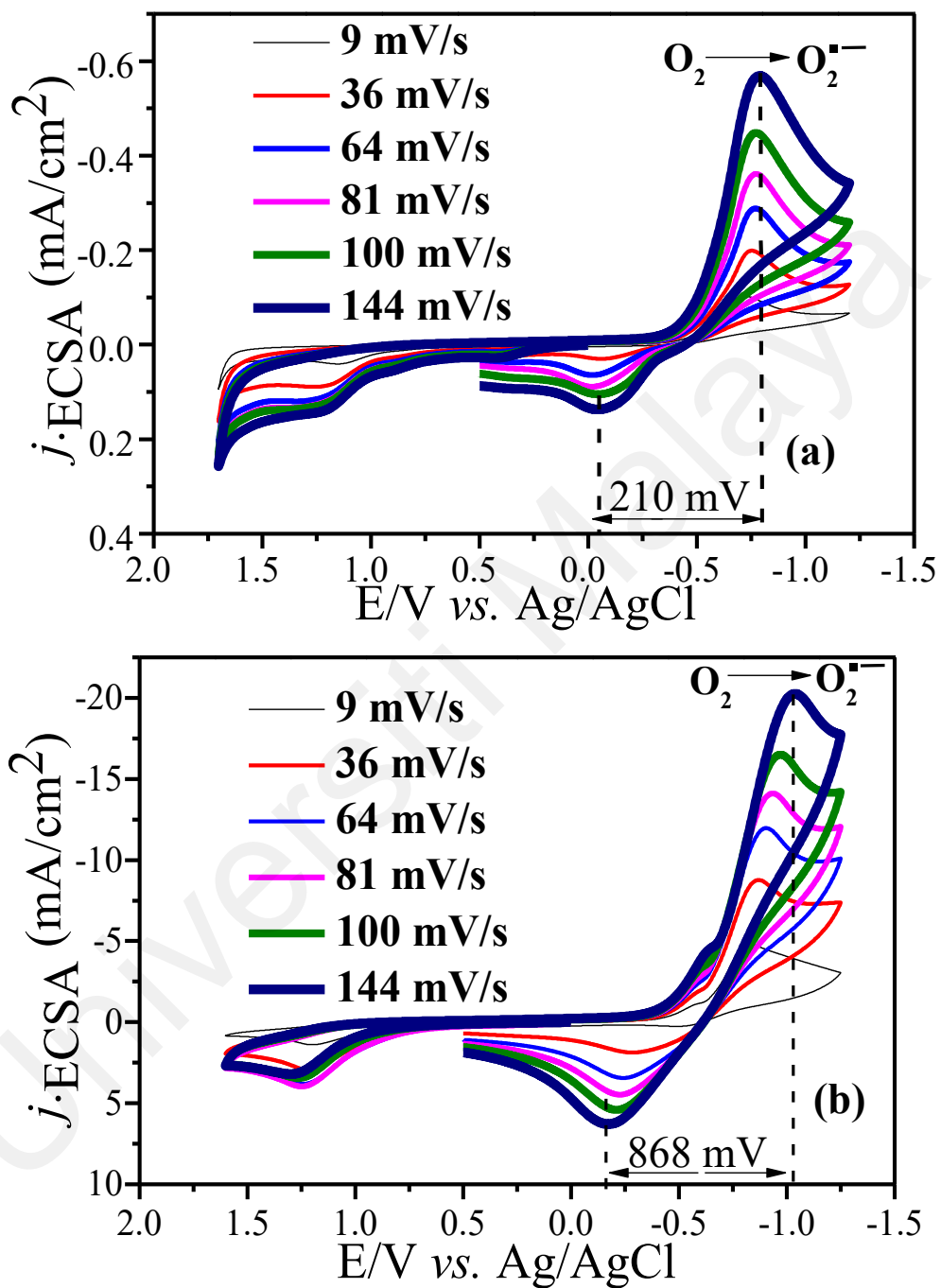


Figure 4.27: CV of $\text{O}_2^{\bullet-}$ generation in (a) $[\text{BMPip}^+][\text{TFSI}^-]$ containing 2.5 mM CH_2Cl_2 (b) $[\text{BMPip}^+][\text{TFSI}^-]$ containing 2.5 mM $\text{C}_6\text{H}_5\text{Cl}$.

4.7.5 Tafel analysis

The Tafel analysis associated with the generation of $\text{O}_2^{\bullet-}$ in $[\text{BMPip}^+][\text{TFSI}^-]$ and $[\text{BMPip}^+][\text{TFSI}^-]$ containing 2.5 mM of CH_2Cl_2 or $\text{C}_6\text{H}_5\text{Cl}$ was conducted using the Butler-Volmer equations (3.11-3.13).

In the Tafel plots (Figures 4.28a-c), measurements were conducted at three different temperatures, such as 25, 35, and 45 °C. In consideration, the absence of mass transfer limitation was assumed then 9 mV/s scan rate was maintained during the measurement for the proper exploration of the charge transfer kinetics. It was observed that the $\text{O}_2^{\bullet-}$ generation process occurred at an overpotential region where the Tafel plots are linear (Figures 4.28(a-c); linear Tafel regions). Therefore, Figures 4.28(d-f) show the corresponding Tafel slope associated with these linear Tafel regions. In $[\text{BMPip}^+][\text{TFSI}^-]$, the Tafel slopes at 25, 35, and 45 °C are 0.347 mV/dec, 0.267 mV/dec, and 0.207 mV/dec.

These changes in the Tafel slope with increasing temperature are mostly attributed to a change in the rate-determining step or the influence of temperature on the reaction's adsorption (Damjanovic, Genshaw, & Bockris, 1967). From an experimental point of view, this decrease in the Tafel slope trend in $[\text{BMPip}^+][\text{TFSI}^-]$ could be a consequence of an increase in the effective electrode surface area. Therefore, at 25 °C, the Tafel slope is higher because of the potential mass transfer limitations at higher overpotential. The larger Tafel slope also indicates greater polarization with increasing current density while the lower Tafel slope indicates an efficient electrocatalytic performance (Agbo & Danilovic, 2019; Y.-H. Fang & Liu, 2014). In comparison, the Tafel slope detected in $[\text{BMPip}^+][\text{TFSI}^-]$ (Figures 4.28d) and $[\text{BMPip}^+][\text{TFSI}^-]$ containing 2.5 mM of CH_2Cl_2 (Figures 4.28e) or $\text{C}_6\text{H}_5\text{Cl}$ (Figures 4.28f) at 35 °C indicated less mass transfer limitation. The Tafel slopes were 0.267 mV/dec, 0.045 mV/dec, 0.012 mV/dec for $[\text{BMPip}^+][\text{TFSI}^-]$

and [BMPip⁺][TFSI⁻] containing 2.5 mM of CH₂Cl₂ (Figures 4.28e) or C₆H₅Cl respectively.

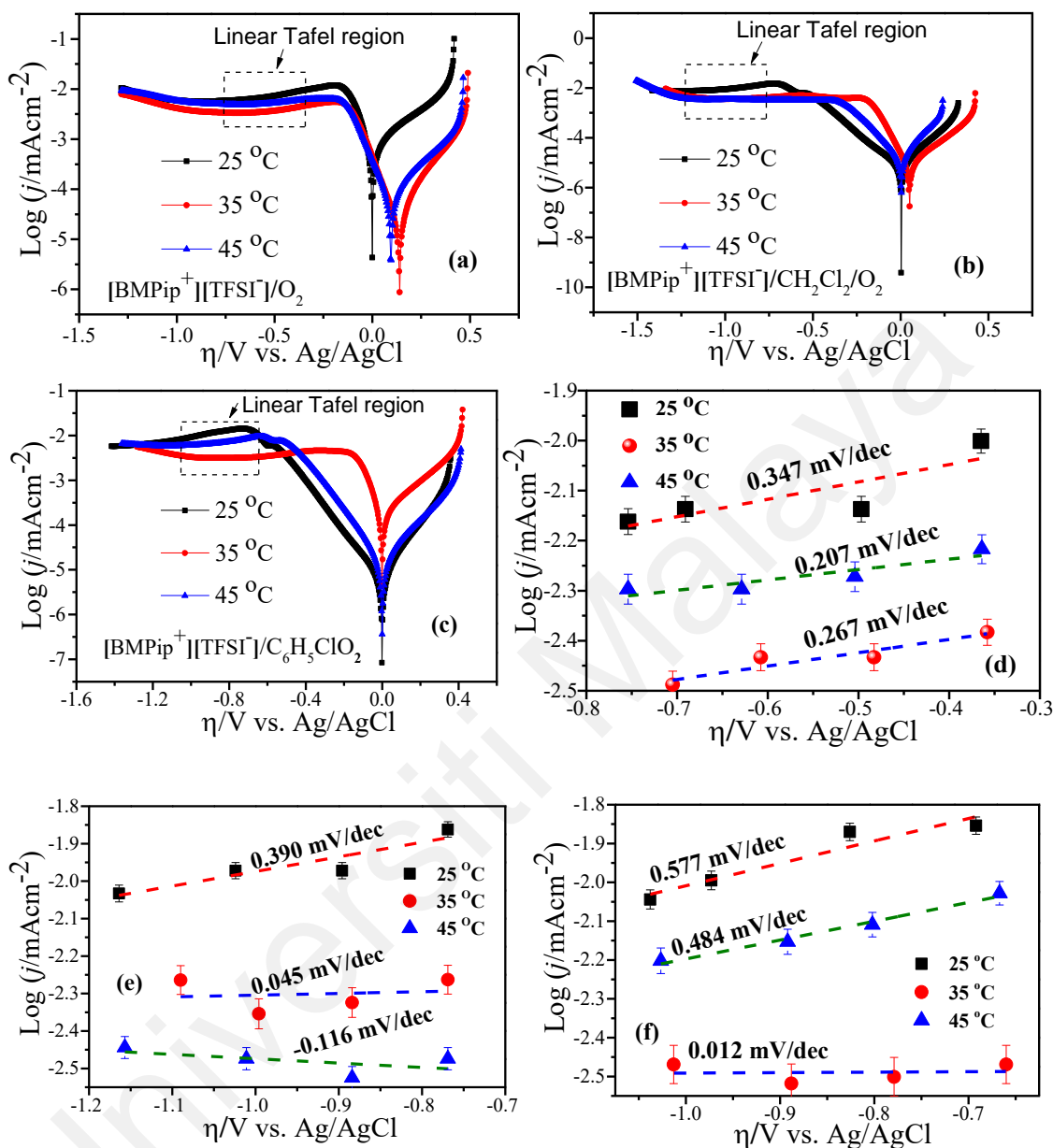


Figure 4.28: Tafel plot of $\text{Log}(j)$ versus overpotential (η) region in (a) O₂-saturated [BMPip⁺][TFSI⁻], (b) O₂-saturated [BMPip⁺][TFSI⁻] containing CH₂Cl₂ and (c) O₂-saturated [BMPip⁺][TFSI⁻] containing C₆H₅Cl. The scan rate was used at 9 mV/s. Linear Tafel plot detected in region in (d) O₂-saturated [BMPip⁺][TFSI⁻], (e) O₂-saturated [BMPip⁺][TFSI⁻] containing CH₂Cl₂ and (f) O₂-saturated [BMPip⁺][TFSI⁻] containing C₆H₅Cl.

4.7.6 Normalized exchange current density

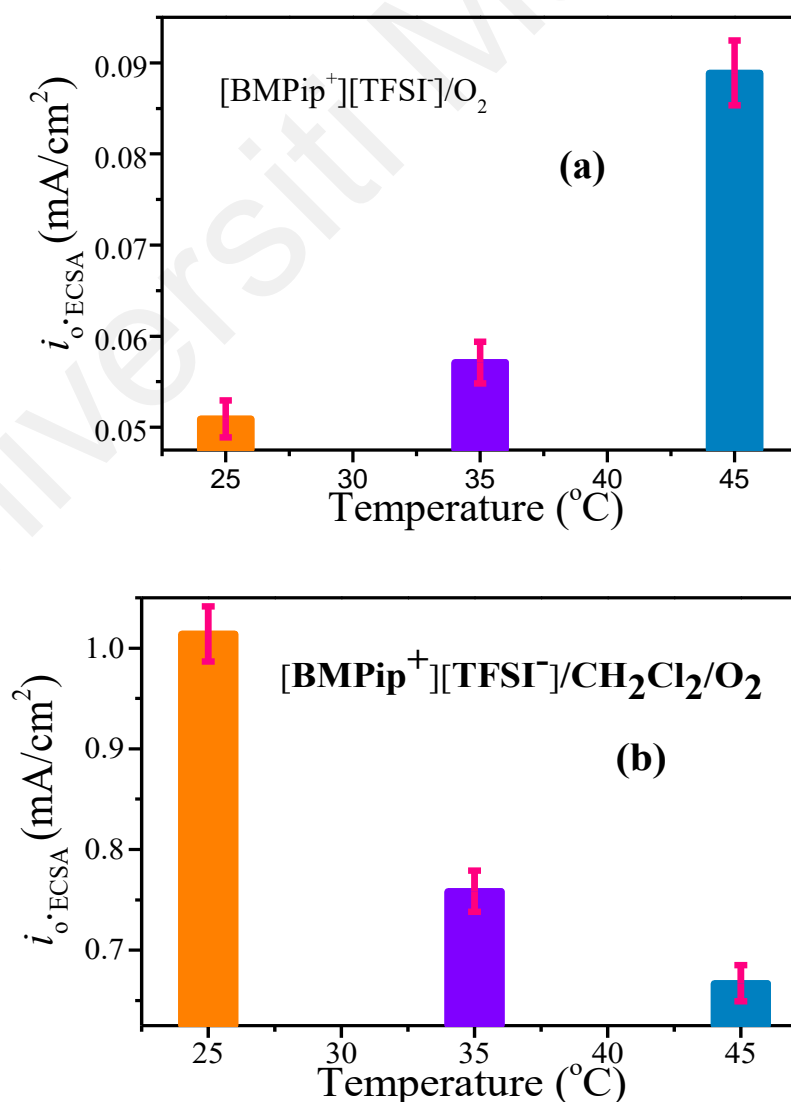
The normalized exchange current density ($i_{0.ECSA}$) was determined as a kinetic parameter for $O_2^{\bullet-}$ generation in $[BMPip^+][TFSI^-]$ and $[BMPip^+][TFSI^-]$ containing 2.5 mM of CH_2Cl_2 or C_6H_5Cl . Figure 4.29a-c show the dependence of $i_{0.ECSA}$ on temperature to estimate the activation energy for $O_2^{\bullet-}$ generation in the media. The $i_{0.ECSA}$ can provide the most discriminating means of assessment on the intrinsic electrochemical activity of $O_2^{\bullet-}$ for CH_2Cl_2 or C_6H_5Cl dechlorination.

Therefore, in Figure 4.29a for $[BMPip^+][TFSI^-]$, it was found that the $i_{0.ECSA}$ increases in the following order; 0.051, 0.047, and 0.089 mA/cm² as the temperature increases from 25, 35, and 45 °C. This confirms that the electron transfer rate from the GC electrode to O_2 , to mediate an electron reduction of O_2 to $O_2^{\bullet-}$ is more favoured at high temperatures. This result also suggests that it is improbable that the $[BMPip^+][TFSI^-]$ forms an IL layer on the GC electrode as the temperature increases.

However, Figure 4.29b and 4.29c show that the $i_{0.ECSA}$ decrease with an increase in temperature from 25, 35, and 45 °C for $[BMPip^+][TFSI^-]$ containing 2.5 mM of CH_2Cl_2 or C_6H_5Cl . This indicates the likelihood of CH_2Cl_2 or C_6H_5Cl binding on the GC electrode surface as the temperature increases. Consequently, this reduces the electron transfer rate from the GC electrode to the bulk analytes.

Moreover, Figure 4.29d show the Arrhenius plot for the temperature dependence of $i_{0.ECSA}$ detected in $[BMPip^+][TFSI^-]$ and $[BMPip^+][TFSI^-]$ containing 2.5 mM of CH_2Cl_2 or C_6H_5Cl . The Arrhenius plot was determined using the Arrhenius equation; $i_0 = A_0 \exp(-E_a/RT)$, where A_0 is the pre-exponential factor. The pre-exponential factor stipulates the maximum value of i_0 at infinite temperature or the collision frequency between reactant molecules at a standard concentration (Q. Li & Jun 2018). Also, the activation energy for O_2 reduction to $O_2^{\bullet-}$ in O_2 -saturated $[BMPip^+][TFSI^-]$ and O_2 -saturated $[BMPip^+][TFSI^-]$ containing CH_2Cl_2 and C_6H_5Cl is represented by E_a .

Therefore, from the $\ln(i_0)$ versus T^{-1} , the slopes and y-intercepts represent values of the A_0 and E_a . Analysis of the slope in $\ln(i_0)$ versus T^{-1} shows the different formal activation energy E_a detected in O_2 -saturated $[BMPip^+][TFSI^-]$, O_2 -saturated $[BMPip^+][TFSI^-]$ containing CH_2Cl_2 and C_6H_5Cl . The E_a for O_2 reduction to $O_2^{\bullet-}$ reduction in $[BMPip^+][TFSI^-]$ is 0.238 kcal/mol indicating that the reaction rate increases as the temperature increases. Differently, the E_a detected in $[BMPip^+][TFSI^-]$ containing 2.5 mM of CH_2Cl_2 or C_6H_5Cl are -0.098 kcal/mol and -0.198 kcal/mol. This result implies that the rate of O_2 reduction to $O_2^{\bullet-}$ reduction in $[BMPip^+][TFSI^-]$ containing 2.5 mM of CH_2Cl_2 or C_6H_5Cl decreases with increasing temperature. The negative E_a values may arise from the likely metathesis reaction mechanism between $O_2^{\bullet-}$ radical and CH_2Cl_2 or C_6H_5Cl (Benson & Dobis, 1998; Mozurkewich & Benson, 1984).



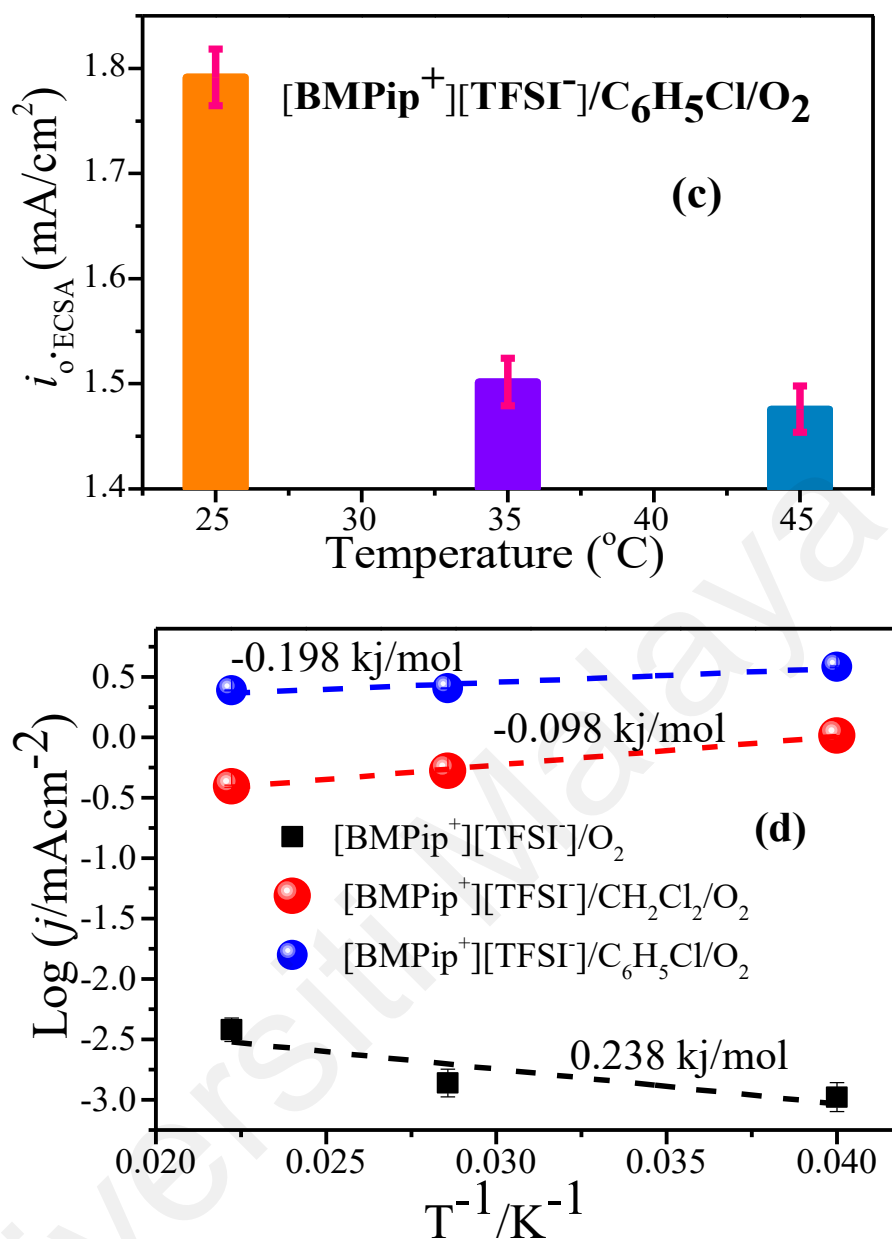


Figure 4.29: Normalized exchange current density ($i_{o,ECSA}$) for $\text{O}_2^{\bullet-}$ generation in (a) [BMPip⁺][TFSI⁻], (b) [BMPip⁺][TFSI⁻] containing CH_2Cl_2 and (c) [BMPip⁺][TFSI⁻] containing $\text{C}_6\text{H}_5\text{Cl}$. (d) The $\text{Ln}(i_0)$ versus T^{-1} for $\text{O}_2^{\bullet-}$ generation in [BMPip⁺][TFSI⁻], [BMPip⁺][TFSI⁻] containing CH_2Cl_2 , and [BMPip⁺][TFSI⁻] containing $\text{C}_6\text{H}_5\text{Cl}$.

4.7.7 Electrolytic dechlorination of CH_2Cl_2 and $\text{C}_6\text{H}_5\text{Cl}$ using $\text{O}_2^{\bullet-}$ in [BMPip⁺][TFSI⁻]

Figure 4.30 (a-c) shows the results for the dechlorination of 2.5 mM $\text{C}_6\text{H}_5\text{Cl}$ or CH_2Cl_2 in [BMPip⁺][TFSI⁻] using different electrolysis time such as 0.5, 1.0, 1.5 and 2.0

h at 35 °C. The temperature is suitable because the Tafel slope is low and different from that at 25 °C, whose Tafel slope is high and potentially inefficient for electrocatalytic performance (Agbo & Danilovic, 2019; Y.-H. Fang & Liu, 2014).

Figure 4.30a shows the conversion of C₆H₅Cl and CH₂Cl₂ in over 0.5, 1.0, 1.5, and 2.0 h electrolysis time. There were no remaining CH₂Cl₂ detected in the work-up solution after the first 0.5 h of reaction. These results show that the O₂^{•-} activity achieved a 100 % conversion of CH₂Cl₂. However, when the reaction proceeded for 1, 1.5, and 2 h electrolysis time, the work-up samples (raffinate) did not show CH₂Cl₂, indicating a 100 % conversion of CH₂Cl₂. Similarly, after 0.5 electrolysis time, C₆H₅Cl was detected, and O₂^{•-} achieved only 69.3 % conversion of C₆H₅Cl. Accordingly, the conversion of C₆H₅Cl by O₂^{•-} increased to 71.3, 77.3, and 100 % when the electrolysis time proceeded for another 1.0, 1.5, and 2 h, respectively. Hence, the product's selectivity from the O₂^{•-} conversion of CH₂Cl₂ or C₆H₅Cl in [BMPip⁺][TFSI⁻] is shown in Figure 4.30b and Figure 4.30c, respectively.

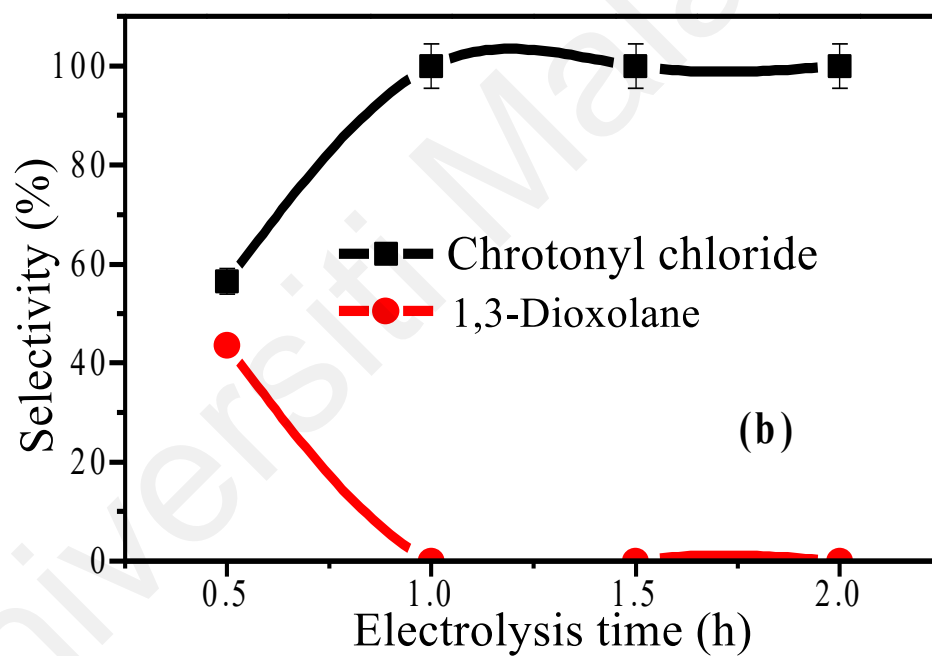
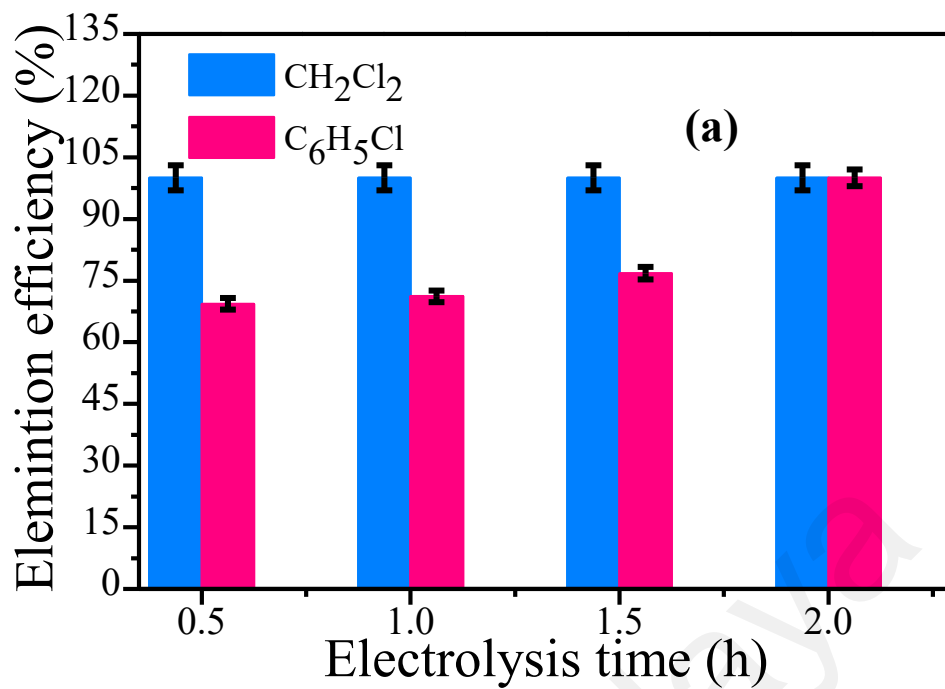
In Figure 4.30b, the selectivity to a crotonic acid chloride and 1, 3-Dioxolane was detected from CH₂Cl₂ dechlorination by O₂^{•-}. During the first 0.5 h electrolysis time, the reaction activity was 43.6 % and 56.84 % selective to crotonyl chloride and 1, 3-Dioxolane. For electrolysis at 1, 1.5, and 2 h, the reaction was 100 % selective to only crotonic acid chloride. The MS pattern associated with crotonyl chloride and 1, 3-Dioxolane is shown in Figure J1a and Figure J1b. In Figure J (a and b) the crotonyl chloride accounted for the loss of C₂HO (M/z = 41), C₂H₂ (M/z = 26), C₄H₃Cl (M/z = 86), C₄H₅O (M/z = 69), and C-H (M/z = 13) fragments confirming the formation of crotonyl chloride from dechlorination of CH₂Cl₂ by O₂^{•-}. In Figure J1a and Figure J1c, 1, 3-Dioxolane accounted for the loss of CH (M/z = 13), CH₃ (M/z = 15), CHO (M/z = 29), C₂H₄O (M/z = 44), and C₃H₅O₂ (M/z = 73) from dechlorination of CH₂Cl₂ by O₂^{•-}. Figure

4.30c, the product selectivity from the dechlorination of C₆H₅Cl by O₂^{•-} is cyclodihexyl-4-ethylbenzoate 2-oxo-2-phenylacetic acid. After the first 0.5 h, the product was 28.2 % and 71.6 % selective to cyclodihexyl-4-ethylbenzoate and 2-oxo-2-phenylacetic acid respectively. For electrolysis time at 1.0, 1.5, and 2.0 h, the product was 100 % selective to cyclodihexyl-4-ethylbenzoate. Figure J2 (a-c), shows that the MS pattern associated with the detection of cyclodihexyl-4-ethylbenzoate accounted for the loss of C₂H₃ (M/z = 27) C₃H₅ (M/z = 41), C₄H₇ (M/z = 55), C₅H₇ (M/z = 67), C₆H₅ (M/z = 79), C₆H₇O (M/z = 91), C₅H₉O₃ (M/z = 105), C₇H₃O₂ (M/z = 112), C₉H₁₃O (M/z = 133), C₁₀H₇O₂ (M/z = 151). Also, Figure J2 (a-d) shows that the MS pattern associated with the detection of 2-oxo-2-phenylacetic acid accounted for the loss of C₂H (M/z = 25), C₃H₂ (M/z = 38), C₉H₁₃O (M/z = 62).

Comparing these products with previous studies, O₂^{•-} is confirmed viable to dechlorinate organic chlorides. For instance, chlorobenzene has slow reactivity with O₂^{•-} (Roberts, Calderwood, & Sawyer, 1983) and extremely feasible with dichloromethane (Nanni et al., 1981). Surprisingly in this current study, cyclodihexyl-4-ethylbenzoate and 2-oxo-2-phenylacetic acid were produced from chlorobenzene dechlorination by O₂^{•-} in [BMPip⁺][TFSI⁻]. The use of [BMPip⁺][TFSI⁻], which is stable, could afford to retain the stoichiometric amount of O₂^{•-} for the dechlorination of chlorobenzene, unlike previous studies that used aprotic electrolytes. Producing cyclodihexyl-4-ethylbenzoate and 2-oxo-2-phenylacetic acid from chlorobenzene dechlorination by O₂^{•-} strongly suggests a possible metathesis reaction step. The metathesis reaction could be between two or more chlorobenzene molecule before the O₂^{•-} mediating the dechlorination in [BMPip⁺][TFSI⁻]. The metathesis reaction implied two or more chlorobenzene could form a C-Cl or C-C bond into a single hydrocarbon. However, for a higher number of chlorine substituents such as hexachlorobenzene, the dechlorination by O₂^{•-} yielded bicarbonate and chloride as the only produced (Sugimoto, Matsumoto, & Sawyer, 1988).

The degree of dechlorination (DD %) of CH_2Cl_2 or $\text{C}_6\text{H}_5\text{Cl}$ by $\text{O}_2^{\bullet-}$ during the electrolysis time is estimated. Analysis of the degree of dechlorination is necessary because chlorine substituents are known to mainly account for the level of organic chloride toxicity (W.-Y. Fang et al., 2019; Naumann, 2000). Figure 4.30d summarized the (DD %) of CH_2Cl_2 or $\text{C}_6\text{H}_5\text{Cl}$ by $\text{O}_2^{\bullet-}$. The DD % for CH_2Cl_2 was 100 % for all the electrolysis time intervals. However, the dechlorination of CH_2Cl_2 did not remove the chlorine substituent; hence, the DD % is not total. According to the crotonic acid chloride product obtained, there is still the presence of one chlorine substituent. The chlorine from crotonyl chloride might be challenging to dechlorinate because it is a resonance stabilized molecule considering its C (sp^2)-Cl moiety (Garifullina, Mahboob, & O'Reilly, 2016; Tian & Liu, 2014). Especially from the stereo-electronic effect perspective, C-centered radicals could be stabilized by the adjacent Cl-atom due to electron delocalization between non-bonding orbital and singly occupied molecular orbital (Tian & Liu, 2014).

As for $\text{C}_6\text{H}_5\text{Cl}$, DD % was found to increase with the increase in electrolysis time. During the first 0.5 h electrolysis time, DD % was 48.3 %. For an electrolysis time at 1.0, 1.5, and 2.0 h, the DD % increase to 77.7, 81.5, and 100 %, respectively. Considering the product distributions; cyclohexyl-4-ethylbenzoate and 2-oxo-2-phenylacetic acid, the DD % is the total dechlorination of $\text{C}_6\text{H}_5\text{Cl}$. This is because the products do not contain any chlorine atom as a substituent. Although DD % is total dechlorination, it requires a longer electrolysis time to reach 100 %. This is because the C (sp^2)-Cl in $\text{C}_6\text{H}_5\text{Cl}$ has a higher bond dissociation energy of 95.5 kcal/mol (Cioslowski, Liu, & Moncrieff, 1997), than the C(sp^3)-Cl bond dissociation energy of 82.8 kcal/mol in CH_2Cl_2 (Weissman & Benson, 1983), or C(sp^2)-Cl in crotonyl chloride. These results are significant by confirming that the hybridization state of carbon attached to the chlorine substituent control whether the dechlorination of chlorinated pollutant by $\text{O}_2^{\bullet-}$ will partially or totally remove the chlorine substituent.



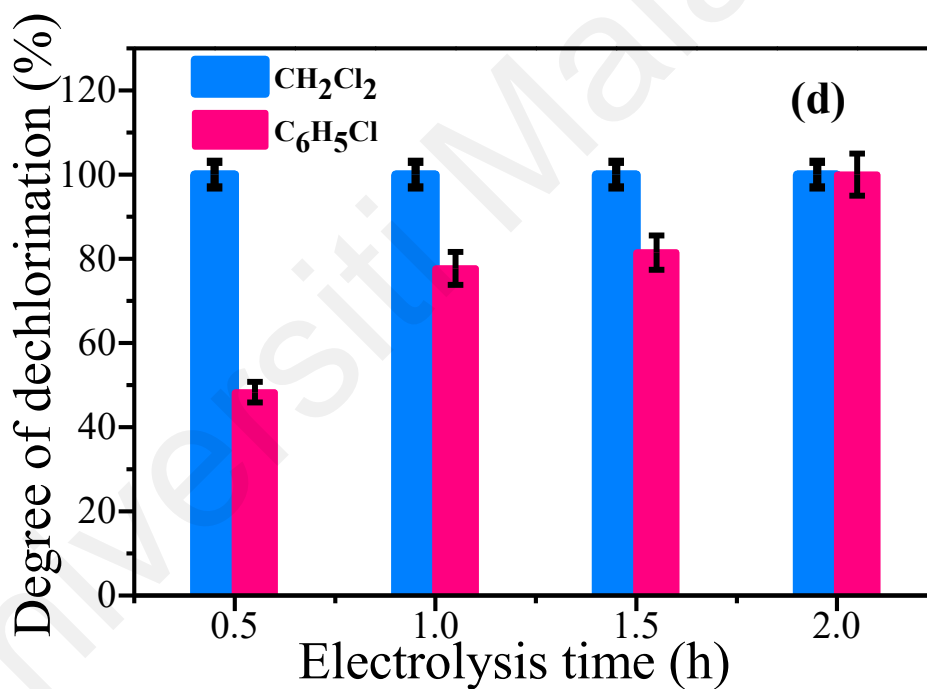
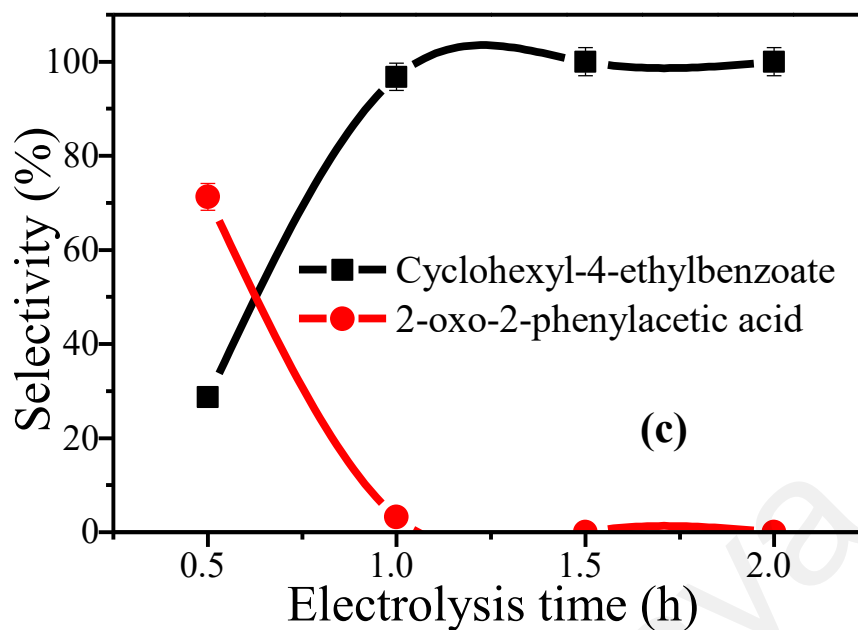


Figure 4.30: Dechlorination activity of C₆H₅Cl and CH₂Cl₂ by O₂^{•-} in [BMPip⁺][TFSI⁻]

(a) Conversion of C₆H₅Cl and CH₂Cl₂ by O₂^{•-} (b) Product selectivity from CH₂Cl₂ conversion by O₂^{•-} (c) Product selectivity from C₆H₅Cl conversion by O₂^{•-} and (d) Degree of dechlorination of CH₂Cl₂ or C₆H₅Cl by O₂^{•-}.

4.7.8 NMR analysis

Proton NMR analysis was further employed to elucidate some of the significant GCMS product distribution reported in Figure 4.30 (a-c). Firstly, the ¹H-NMR spectrum

of crotonic acid chloride is shown in Figure Ia. The doublet peak (1, 3) at a chemical shift of 2.974 ppm is due to the $-\text{CH}_3$ group linked to $-\text{CH}$ or $-\text{CH}$ linked to its counterpart $-\text{CH}$ in the crotonyl chloride structure. The proton is coupled with another neighbouring proton at 2.985 ppm chemical shift and a j -coupling frequency of 6.379 Hz. The quintet peak (2) at 1.833 ppm chemical shift is due to $-\text{CH}$ proton linked to CH and $-\text{CH}_3$. The proton is coupled with another neighbouring proton at 1.802, 1.789, 1.777, and 1.765 ppm chemical shift and a j -coupling frequency of 18.538, 27.748, 35.230, and 43.024 Hz, respectively. Considering 1, 3-dioxolane, the second product aside from crotonyl chloride, the singlet peak (a) at 3.075 ppm is due to Methylene. The triplet peak (b, c) at 3.229 ppm is due to proton on the methylene linked to oxygen ($\text{O}-\text{CH}_2$) linkage. The proton is coupled with another neighbouring proton at 3.215 ppm chemical shift and a j -coupling frequency of 10.025 Hz. The proton is also coupled with another adjacent proton at a 3.244 ppm chemical shift and a j -coupling frequency of 7.352 Hz.

From the work-up solution of $\text{C}_6\text{H}_5\text{Cl}$ dechlorination, the ^1H -NMR spectrum of cyclohexyl 4-ethylbenzoate, which is the primary product is shown in Figure Ib. The triplet Peak (3) at a chemical shift of 0.924 ppm is CH_3 linked to methylene in the cyclohexyl 4-ethylbenzoate. The proton is coupled with another two neighbouring protons at 0.935 ppm and 0.911 ppm, with a j -coupling frequency of 7.056 Hz, 7.599 Hz respectively. Similarly, the triplet peak (7, 3H, t) at 3.274 ppm is due to $\text{O}-\text{CH}$ linked to methylene. The proton is coupled with two other protons at 3.284 ppm and 3.264 ppm with the corresponding j -coupling frequency of 5.427 Hz and 6.161 Hz respectively. Otherwise, the Quintet Peak (7, 5H, q) at a chemical shift of 3.205 ppm is due to $-\text{O}-\text{CH}$ linked to two methylene in the cyclohexyl 4-ethylbenzoate structure. The proton is coupled with another two neighbouring protons at a lower chemical shift of 3.200 ppm and 3.193 ppm, with a j -coupling frequency of 8.029 Hz and 12.752 Hz respectively. The

proton is also coupled with additional two protons at a slightly higher chemical shift of 3.212 and 3.221 ppm with a *j*-coupling frequency of 0.956 and 4.437 Hz respectively.

The ¹H-NMR spectrum of 2-oxo-2-phenylacetic acid is shown in Figure Ib. The doublet peak (*x*₁ and *z*₁) at a chemical shift of 1.814 ppm was used to confirm the two –CH linkage's presence linked on the benzene ring of the 2-oxo-2-phenylacetic acid structure. The proton is coupled with another two neighbouring protons at a higher chemical shift of 1.822 ppm, with a *j*-coupling frequency of 5.146 Hz. There was another triplet peak (*x*, *y*, or *z*) at a chemical shift of 0.923 ppm used to confirm the proton at either *x*, *y*, and *z* position as shown in Figure Ib (Appendix I) positions in the 2-oxo-2-phenylacetic acid structure. The proton is coupled with another two neighbouring protons at 0.935 and 0.910 ppm with the corresponding *j*-coupling frequency of 7.177 and 7.626 Hz. Overall, the NMR interpretation is in line with previous literature (Lehtivarjo, Niemitz, & Korhonen, 2014; Wilkens et al., 2001).

CHAPTER 5: CONCLUSION AND RECOMMENDATION

5.1 Conclusions

In summary, two fundamental principles guided this work, 1) ILs electrophilicity index (positive character) influence the electrochemical generation, long-term stability and utilization of $O_2^{\bullet-}$, 2) The viability of a nanohybrid-IL (nanofluid) for $O_2^{\bullet-}$ generation and utilization depend on stable ILs as base fluids. Particularly using $O_2^{\bullet-}$ for conversion of CO_2 and chlorinated compounds, imidazolium-based cations are not suitable due to their tendency to be transformed into imidazolones. Thus, the ideal ILs for this kind of research should contain negatively charged carbon atoms in their cationic end. Therefore, the specific conclusions include the following.

- 1- Global electrophilicity indices (ω) can estimate the susceptibility of IL-cation, CO_2 , CH_2Cl_2 , C_6H_5Cl or any molecule to the nucleophilic effects of $O_2^{\bullet-}$. However, the global electrophilicity index as a chemical reactivity descriptor is sometimes not exclusive without corroborating it with the Mulliken atomic charge. Therefore, the ILs molecule with large negative iso-surfaces will have negative Mulliken charged atoms. Consequently, these negative Mulliken charged atoms could induce the ILs to be less susceptible to $O_2^{\bullet-}$ attack. In contrast, a molecule with large positive iso-surfaces will have a positive Mulliken charge for at least one atom in the ILs, CO_2 , CH_2Cl_2 , or C_6H_5Cl . So, this positive Mulliken charge could induce them to become more susceptible to $O_2^{\bullet-}$ attack. Overall, the reactivity parameter for properly evaluating molecules susceptibility to $O_2^{\bullet-}$ is the global electrophilicity index and Mulliken atomic charge. Noteworthy, the global electrophilicity index of $O_2^{\bullet-}$ is always negative while other molecular substrates like CO_2 , O_2 , CH_2Cl_2 , or C_6H_5Cl will be positive. Unless if the molecule is a radical then the global electrophilicity index will be negative too but with a different magnitude to $O_2^{\bullet-}$.

- 2- This study confirmed that transition metal phases could be hybridized onto carbon nanotube, forming novel Ru/Fe-SiMWCNT nanohybrid with unprecedented CO₂ and O₂ sorption and pseudocapacitive attributes. Based on XRD analysis, 97.8 % degree of crystallinity for the Ru/Fe-SiMWCNT nanohybrid treated at 600 °C was achieved. This is an indication that 600 °C is a suitable temperature to treat the nanohybrid to improve its crystallinity. Also, a 10.0kV electron beam can identify the Ru/Fe-SiMWCNT nanohybrid morphology through FESEM or HRTEM analysis. At this electron beam energy, the lattice image of MWCNT can be viewed, including the grain boundary with other phases (Fe₃O₄, RuO₂, and SiO₂). Furthermore, it is essential to confirm defects on MWCNT using Raman mapping analysis scanning across a wide area of the Fe/Ru-SiMWCNT nanohybrid to reveal its harmonic and defects.
- 3- Moreover, Fe₃O₄ is metastable which is desirable for pseudocapacitance; hence the absence of XPS satellite peak at ~718.800 eV binding energy confirms the lack of other iron oxide phases such as free γ -Fe₂O₃ hematite. A total absence of γ -Fe₂O₃ is required to assure the pseudocapacitive attribute in the context of the Fe₃O₄ phase. These collective attributes are necessary before approving Fe/Ru-SiMWCNT nanohybrid for the development of nanofluid.
- 4- In retrospect, there is no evidence on the generation and utilization of stable O₂^{•-} in a nanofluid until now. Therefore, this study pioneered the development of nanofluid for the synthesis and utilization of stable O₂^{•-}. As an instance, a novel Fe/Ru-SiMWCNT/[MOEMPyrr⁺][PFTP⁻] nanofluid was developed. Overall, the electrochemical potential window (ECW) of the ILs or Fe/Ru-SiMWCNT-IL media depends on the IL-cation and IL-anion end. For O₂^{•-} generation and application, the reductive window of (IL-cation end) must be > -1 vs Ag/AgCl, which is the conventional O₂^{•-} generation potential. Moreover, Fe/Ru-SiMWCNT

nanohybrid could influence the reductive window. For instance, reductive window of Fe/Ru-SiMWCNT hybridized [MTOAmm⁺][TFSI⁻], [EDMPAmm⁺][TFSI⁻], [BMAmm⁺][TFSI⁻], [TBMamm⁺][TFSI⁻], [MOEMPyrr⁺][PFTP⁻] and [MOEMMor⁺][TFSI⁻] nanofluid are -3.810, -3.600, -3.500, -3.100, -2.960, and -2.720 V vs Ag/AgCl respectively. These reductive windows are higher than their initial values of ordinary ILs. These ECW results implied that the nanofluid or ILs are viable as potential media for O₂^{•-} generation as their reductive window falls > -1.0 V vs Ag/AgCl. However, [PMIm⁺][TFSI⁻] and [BMIm⁺][TFSI⁻] have a low preference as media for O₂^{•-} since their reductive windows are low; -1.97 V vs Ag/AgCl and -1.99 V vs Ag/AgCl, respectively. Also, some ILs such as [BMIm⁺][TCM⁻] and [BMIm⁺][DCA⁻] have reductive window > -1.0 V vs Ag/AgCl but could not generate stable O₂^{•-}. However, ILs or ILs based nanofluid reductive windows do not exclusively determine the O₂^{•-} radical's stability. The instability of O₂^{•-} was due to the reaction of O₂^{•-} with the [BMIm⁺] cation, particularly via a possible attack on their positively charged carbon, and induced proton abstraction-like reaction. Similarly, O₂^{•-} instability could originate from the ILs decomposition product since their reductive window (negative limit) is close to the reduction voltage of O₂.

- 5- Due to the Fe₃O₄ and RuO₂ phase's pseudocapacitive attributes, there is capacitance increase in ILs base Fe/Ru-SiMWCNT nanohybrid from electrochemical impedance spectroscopic analysis. The capacitance in ordinary ILs is much lower than their Fe/Ru-SiMWCNT nanohybrid derived nanofluid. In terms of percentage, the improvements in capacitances are > 50 %. For instance, the percentage increase in capacitance in [EDMPAmm⁺][TFSI⁻], [BMPyrr⁺][TFSI⁻], [MOEMPyrr⁺][PFTP⁻], [BMIm⁺][TFSI⁻], [PMIm⁺][TFSI⁻], [TBMamm⁺][TFSI⁻], [BMAmm⁺][TFSI⁻], [MTOAmm⁺][TFSI⁻],

[BMPip⁺][TFSI⁻] are (69.09 %), (70.67 %), (50.56 %), (36.31 %), (53.14 %), (70.92 %), (71.69 %), (78.04 %) and (57.11 %) respectively. Irrespective, high capacitance only does not approve usage of the media for O₂^{•-} utilization. High capacitance indicate that the media could proffer low overpotential during the electrochemical process.

- 6- The electrochemical generation of stable O₂^{•-} in ILs or Fe/Ru-SiMWCNT-[MOEMPyrr⁺][PFTP⁻] nanofluid is characterized by asymmetrical voltammetry. Moreover, the asymmetrical voltammetry pattern appears in Fe/Ru-SiMWCNT-[MOEMPyrr⁺][PFTP⁻] nanofluid at lower activation overpotential and reduction potential. While in ordinary ILs, the asymmetrical voltammetry pattern appears at higher activation overpotential and reduction potential. In conclusion, the pseudocapacitive attributes in Fe/Ru-SiMWCNT-[MOEMPyrr⁺][PFTP⁻] nanofluid contributed to lowering the activation overpotential required for the process. This is also confirming that the potential for O₂^{•-} generation is constrained by the form of media. Moreover, the separation between the cathodic peak (E_p^c) and the half peak potential ($E_{p/2}^c$) in the ILs or Fe/Ru-SiMWCNT-[MOEMPyrr⁺][PFTP⁻] nanofluid was not a typical 56.5 mV of reversible system. The separation is not constant, and it changes when stripping the scan rate from 144 to 9 mV/s. This nature of E_p^c or $E_{p/2}^c$ separation indicated that the electrochemical generation of O₂^{•-} in the ILs or Fe/Ru-SiMWCNT-[MOEMPyrr⁺][PFTP⁻] nanofluid is irreversible. The irreversible nature of the process confirms O₂^{•-} availability for utilization in the conversion of CO₂, C₆H₅Cl and CH₂Cl₂.
- 7- The interfacial parameter such as charge transfer coefficient (α) detected in ILs was less than the one observed in Fe/Ru-SiMWCNT-[MOEMPyrr⁺][PFTP⁻] nanofluid. This result confirms that charge transfers faster in nanofluid than the

- ordinary ILs. Moreover, mass transfer parameter like O_2 solubility was high in $[MOEMPyrr^+][PFTP^-]$ to the tune of 19.020 mM. The selection of $[MOEMPyrr^+][PFTP^-]$ for nanofluid arises due to the high O_2 solubility therein.
- 8- The cyclic voltammetry could not validate the long-term stability of $O_2^{\bullet-}$ in ILs or nanofluid as the redox cycle only lasted for $\sim < 1$ min. Therefore, the chemical generation of $O_2^{\bullet-}$ by dissolving KO_2 in the ILs or Fe/Ru-SiMWCNT-IL validated the long-term stability of $O_2^{\bullet-}$. The $O_2^{\bullet-}$ was less stable in $[BMPyrr^+][TFSI^-]$, $[BMIm^+][TFSI^-]$, and $[PMIm^+][TFSI^-]$ ILs media as their ILs-cation have C (Sp²) positive Mulliken number that renders them more susceptible to attack by $O_2^{\bullet-}$. The percentage consumption of $O_2^{\bullet-}$ in $[BMPyrr^+][TFSI^-]$, $[BMIm^+][TFSI^-]$, and $[PMIm^+][TFSI^-]$ was 16.40, 18.10 and 47.92 %. This high percentage consumption of $O_2^{\bullet-}$ arises due to the reaction of $O_2^{\bullet-}$ with IL-cation. Using these media will be constrained by the competitive reaction between $O_2^{\bullet-}$ and the IL-cations. Moreover, percentage consumption of $O_2^{\bullet-}$ in $[EDMPAmm^+][TFSI^-]$, $[MOEMPyrr^+][PFTP^-]$, $[MOEMMor^+][TFSI^-]$, $[TBMAMm^+][TFSI^-]$, $[BMAMm^+][TFSI^-]$, and $[BMPip^+][TFSI^-]$ was low. These ILs are capable of serving as media for the conversion of CO_2 , C_6H_5Cl and CH_2Cl_2 using $O_2^{\bullet-}$.
- 9- The conversion of CO_2 by $O_2^{\bullet-}$ selectively produced peroxy-dicarbonate anion ($C_2O_6^{2-}$) in the ILs. The $C_2O_6^{2-}$ anion is detectable in IL using ATR-IR and can be computed using DFT-IR analysis. Since the $C_2O_6^{2-}$ anion is an asymmetric top molecule, i.e. the molecule that vibrates while rotating, the IR-peak will not be sharp as regular peaks but broad. The mechanism of $C_2O_6^{2-}$ production from $O_2^{\bullet-}$ utilization by CO_2 in ILs or nanohybrid-IL follow direct nucleophilic addition of $O_2^{\bullet-}$ to CO_2 . Intrinsically, the nucleophilic addition to produce $C_2O_6^{2-}$ could first produce $CO_2^{\bullet-}$ (containing π – electron) or $CO_4^{\bullet-}$ (containing 2π – electrons) as intermediate species. The pseudocapitance of Fe/Ru-

SiMWCNT/[MOEMPyrr⁺][PFTP⁻] nanofluid induced a lowering in the CO₂ conversion potential, activation overpotential and an increase in energy efficiency.

10- The C₂O₆²⁻ produced in either bare ILs or the Fe/Ru-SiMWCNT/[MOEMPyrr⁺][PFTP⁻] nanofluid can be utilized *in-situ* for carboxylation of amine (diethanolamine) to produce Methyl (2-hydroxyethyl) (methyl) carbamate. During this process, CO₂ could not influence the carboxylation process but C₂O₆²⁻ releasing CO₂^{•-} to facilitate the reaction. The optimum time of the carboxylation reaction was an hour. Different ILs have a unique capacity to produce carbamate with a distinctive structure. In producing methyl (2-hydroxyethyl) (methyl) carbamate, C₂O₆²⁻ first release CO₂^{•-} to attacked the nitrogen atom is diethanolamine substrate. Consequently, CO₂^{•-} re-attack the nitrogen atom in diethanolamine feedstock as a free radical quenching step forming pyrrole as transition state structure before producing the methyl (2-hydroxyethyl) (methyl) carbamate. The 1D ¹H NMR and ¹³CNMR, 2D NMR correlation spectroscopy (2D ¹H/¹H COSY NMR), heteronuclear single quantum coherence spectroscopy (HSQC) and heteronuclear multiple bond correlation (HMBC) could elucidate the structure of the carbamate. However, poor work-up of post-reaction medium could jeopardize the feasible realization of the structural elucidation. Hence, it is necessary to properly carry out the active component's separation using column chromatography.

11- The conversion of C₆H₅Cl or CH₂Cl₂ using O₂^{•-} in IL ([BMPip⁺][TFSI⁻]) is feasible, producing a non-dioxin product distribution. The normalized current density (*i*_{0,EC_{SA}}) detected in O₂ saturated [BMPip⁺][TFSI⁻] is dependent on temperature (25, 35, and 45 °C), suggesting that more of O₂^{•-} was produced and [BMPip⁺] cation is stable. Moreover, the normalized exchange current density

($i_{0,EC SA}$) detected in O_2 saturated [BMPip⁺][TFSI⁻] containing 2.5 mM of CH_2Cl_2 or C_6H_5Cl decreased with the temperature. This study proposed that a decrease in the $i_{0,EC SA}$ in [BMPip⁺][TFSI⁻] containing 2.5 mM of CH_2Cl_2 or C_6H_5Cl confirmed consumption of $O_2^{\bullet-}$ by the chlorinated pollutants.

12- The dynamic electrolysis of C_6H_5Cl or CH_2Cl_2 in [BMPip⁺][TFSI⁻] containing $O_2^{\bullet-}$ at -2.0 V vs Ag/AgCl, produced cyclohexyl 4-ethyl benzoate and 1, 3-dioxolane respectively, which are not toxic to the environment. The study also hypothesised that the hybridization state of (C)-Cl chlorinated pollutants determines their partial or total dechlorination by $O_2^{\bullet-}$ in ILs. Overall, [BMPip⁺][TFSI⁻] was selected for this purpose because all the carbon atoms in the [BMPip⁺] cation are negative. The negative carbon atomic charges make these particular IL less susceptible to $O_2^{\bullet-}$, and useful for electro-reductive dechlorination.

5.2 Recommendations

This research presents relevant advances and in-depth sceneries regarding $O_2^{\bullet-}$ generation and utilization in ILs. As a novel advance, the study also conceived the idea of producing new nanofluid media for $O_2^{\bullet-}$ generation and utilization. In either of the medium, Cyclic voltammetry was employed to detect the generation of $O_2^{\bullet-}$ throughout this study. However, because the $O_2^{\bullet-}$ has an unpaired electron that gives it additional property such as paramagnetic or spinning, it is recommended that the $O_2^{\bullet-}$ be investigated in these media using electron spin resonance (ESR) or electron paramagnetic resonance (EPR). The same family of IL but with a different substituent is recommended. This current study has established the effects of various types of IL-cation on the generation and utilization of $O_2^{\bullet-}$. This information will ascertain that there would not be competing with the IL-cation when the superoxide ion is generated and utilized. In

essence, the study rules out imidazolium IL but other ILs for a subsequent application similar to this study.

Considering that this study is the first to ever report the generation and utilization of $O_2^{\bullet-}$ in nanofluid, further research is necessary to examine various other transition metal nanohybrids with an affinity for O_2 , and CO_2 provide a level of catalytic effects. In doing so, concerted control experiments must be done when developing the nanohybrid or nanofluid for $O_2^{\bullet-}$ generation and utilization.

This study's technique can be improved into a pilot scale for electrolysis of CO_2 in nanofluid or electro-conductive dechlorination of chlorinated organics using $O_2^{\bullet-}$ in ILs while achieving an industrially scalable regeneration of the electrolyte media.

Universiti Malaysia

REFERENCES

- Afanasyev, I. B. (1991). *Superoxide ion: chemistry and biological implications* (Vol. 2): CRC press.
- Agbo, P., & Danilovic, N. (2019). An algorithm for the extraction of Tafel slopes. *Journal of Physical Chemistry*, 123(50), 30252-30264.
- Ahmed, O. U., Mjalli, F. S., Al-Wahaibi, T., Al-Wahaibi, Y., & AlNashef, I. M. (2015). Stability of superoxide ion in phosphonium-based ionic liquids. *Industrial & Engineering Chemistry Research*, 54(7), 2074-2080.
- Ahvenainen, P., Kontro, I., & Svedström, K. (2016). Comparison of sample crystallinity determination methods by X-ray diffraction for challenging cellulose materials. *Cellulose*, 23(2), 1073-1086.
- Alhafadhi, L., & Teh, J. (2020). Advances in reduction of total harmonic distortion in solar photovoltaic systems: A literature review. *International Journal of Energy Research*, 44(4), 2455-2470.
- Allen, M. (2009). Planetary boundaries: tangible targets are critical. *Nature Climate Change*, 3, 114-115.
- AlNashef, I. M., Hashim, M. A., Mjalli, F. S., Ali, M. Q. A.-h., & Hayyan, M. (2010). A novel method for the synthesis of 2-imidazolones. *Tetrahedron Letters*, 51(15), 1976-1978.
- AlNashef, I. M., Leonard, M. L., Kittle, M. C., Matthews, M. A., & Weidner, J. W. (2001). Electrochemical generation of superoxide in room-temperature ionic liquids. *Electrochemical and Solid-State Letters*, 4(11), 16-18.
- AlNashef, I. M., Leonard, M. L., Matthews, M. A., & Weidner, J. W. (2002). Superoxide electrochemistry in an ionic liquid. *Industrial & Engineering Chemistry Research*, 41(18), 4475-4478.
- AlSaleem, S. S., Zahid, W. M., Alnashef, I. M., & Haider, H. (2019). Destruction of environmentally hazardous halogenated hydrocarbons in stable ionic liquids with superoxide ion radical. *Separation and Purification Technology*, 215, 134-142.
- Aman, S., Khan, I., Ismail, Z., Salleh, M. Z., & Al-Mdallal, Q. M. (2017). Heat transfer enhancement in free convection flow of CNTs Maxwell nanofluids with four different types of molecular liquids. *Scientific Reports*, 7(1), 2445.
- Andanson, J. M., Meng, X., Traïkia, M., & Husson, P. (2016). Quantification of the impact of water as an impurity on standard physico-chemical properties of ionic liquids. *The Journal of Chemical Thermodynamics*, 94, 169-176.
- Andanson, J. M., Traïkia, M., & Husson, P. (2014). Ionic association and interactions in aqueous methylsulfate alkyl-imidazolium-based ionic liquids. *The Journal of Chemical Thermodynamics*, 77, 214-221.

- Andrieux, C. P., Gallardo, I., & Saveant, J. M. (1989). Outer-sphere electron-transfer reduction of alkyl halides. A source of alkyl radicals or of carbanions? Reduction of alkyl radicals. *Journal American Chemical Society*, *111*(5), 1620-1626.
- Andrieux, C. P., Hapiot, P., & Saveant, J. M. (1987). Mechanism of superoxide ion disproportionation in aprotic solvents. *Journal of the American Chemical Society*, *109*(12), 3768-3775.
- Aparicio, S., Atilhan, M., & Karadas, F. (2010). Thermophysical properties of pure ionic liquids: review of present situation. *Industrial & Engineering Chemistry Research*, *49*(20), 9580-9595.
- Aparicio, S., Atilhan, M., Khraisheh, M., Alcalde, R., & Fernández, J. (2011). Study on hydroxylammonium-based ionic liquids. II. Computational analysis of CO₂ absorption. *The Journal of Physical Chemistry B*, *115*(43), 12487-12498.
- Appel, A. M., & Helm, M. L. (2014). Determining the overpotential for a molecular electrocatalyst. *ACS Catalysis*, *4*(2), 630-633.
- Appel, A. M., Bercaw, J. E., Bocarsly, A. B., Dobbek, H., DuBois, D. L., Dupuis, M., ... & Waldrop, G. L. (2013). Frontiers, opportunities, and challenges in biochemical and chemical catalysis of CO₂ fixation. *Chemical Reviews*, *113*(8), 6621-6658.
- Artz, J., Iler, T. E., Thenert, K., Kleinekorte, J., Meys, R., Sternberg, A., . . . Leitner, W. (2018). Sustainable conversion of carbon dioxide: An integrated review of catalysis and life cycle assessment. *Chemical Reviews*, *118*(2), 434-504.
- Ashassi-Sorkhabi, H., Kazempour, A., & Salehi-Abar, P. (2018). A new insight into ionic liquid-water mixtures used as absorbent-refrigerant pairs: Theoretical and potentiometric aspects. *Journal of Molecular Liquids*, *251*, 190-200.
- Assadi, M. H. N., Gutierrez Moreno, J. J., & Fronzi, M. (2020). High-Performance Thermoelectric Oxides Based on Spinel Structure. *ACS Applied Energy Materials*.
- Avaca, L. A., Kaufmann, S., Kontturi, K., Murtoimäki, L., & Schiffrin, D. J. (1993). Theory of cyclic voltammetry for quasi-reversible electrodeposition reactions with insoluble products. *Berichte der Bunsengesellschaft für physikalische Chemie*, *97*(1), 70-76.
- Babamohammadi, S., Shamiri, A., & Aroua, M. K. (2015). A review of CO₂ capture by absorption in ionic liquid-based solvents. *Reviews in Chemical Engineering*, *31*(4), 383-412.
- Barai, D. P., Bhanvase, B. A., & Sonawane, S. H. (2020). A review on graphene derivatives-based nanofluids: Investigation on properties and heat transfer characteristics. *Industrial Engineering. Chemical Research*, *59*(22), 10231-10277.
- Barba, F., Batanero, B., & Barba, I. (2017). Electrogenerated superoxide anion: Hydroxylation of electroreducible substrates in aprotic solvent. *Journal of Electroanalytical Chemistry*, *793*, 66-69.

- Barbero, G., & Lelidis, I. (2017). Analysis of Warburg's impedance and its equivalent electric circuits. *Physical Chemistry Chemical Physics*, 19(36), 24934-24944.
- Bard, A. J., Faulkner, L. R., Leddy, J., & Zoski, C. G. (1980). *Electrochemical methods: fundamentals and applications* (Vol. 2): Wiley New York.
- Barlow, G. E., Bisby, R. H., & Cundall, R. B. (1979). Does disproportionation of superoxide produce singlet oxygen. *Radiation Physics and Chemistry*, 13(1-2), 73-75.
- Barnes, A. S., Rogers, E. I., Streeter, I., Aldous, L., Hardacre, C., Wildgoose, G. G., & Compton, R. G. (2008). Unusual voltammetry of the reduction of O₂ in [C₄dmim][N(Tf)₂] reveals a strong interaction of O₂^{•-} with the [C₄dmim]⁺ cation. *The Journal of Physical Chemistry C*, 112(35), 13709-13715.
- Banerjee, T., & Khanna, A. (2006). Infinite dilution activity coefficients for trihexyltetradecyl phosphonium ionic liquids: measurements and COSMO-RS prediction. *Journal of Chemical & Engineering Data*, 51(6), 2170-2177
- Bauer, G., Sersenová, D., Graves, D. B., & Machala, Z. (2019). Dynamics of singlet oxygen-triggered, RONS-based apoptosis induction after treatment of tumor cells with cold atmospheric plasma or plasma-activated medium. *Scientific Reports*, 9(1), 1-34.
- Becke, A. D. (1996). Density-functional thermochemistry. IV. a new dynamical correlation functional and implications for exact-exchange mixing. *Journal of Chemical Physics*, 104(3), 1040-1046.
- Benson, S. W., & Dobis, O. (1998). Existence of negative activation energies in simple bimolecular metathesis reactions and some observations on too-fast reactions. *Journal of Physical Chemistry*, 102(27), 5175-5181.
- Bhattacharjee, A., Coutinho, J. A., Freire, M. G., & Carvalho, P. J. (2015). Thermophysical properties of two ammonium-based protic ionic liquids. *Journal of solution chemistry*, 44(3-4), 703-717.
- Bielski, B. H. J., & Allen, A. O. (1977). Mechanism of the disproportionation of superoxide radicals. *The Journal of Physical Chemistry*, 81(11), 1048-1050.
- Bisquert, J. (2000). Influence of the boundaries in the impedance of porous film electrodes. *Physical Chemistry Chemical Physics*, 2(18), 4185-4192.
- Bisquert, J. (2002). Theory of the impedance of electron diffusion and recombination in a thin layer. *The Journal of Physical Chemistry B*, 106(2), 325-333.
- Bisquert, J., & Fabregat-Santiago, F. (2010). Impedance spectroscopy: a general introduction and application to dye-sensitized solar cells.
- Bittencourt, C., Navio, C., Nicolay, A., Ruelle, B., Godfroid, T., Snyders, R., . . . Ewels, C. P. (2011). Atomic oxygen functionalization of vertically aligned carbon nanotubes. *The Journal of Physical Chemistry C*, 115(42), 20412-20418.

- Boot-Handford, M. E., Abanades, J. C., Anthony, E. J., Blunt, M. J., Brandani, S., Mac Dowell, N., ... & Fennell, P. S. (2014). Carbon capture and storage update. *Energy & Environmental Science*, 7(1), 130-189
- Bolojan, L., Takács, I. M., Miclaus, V., & Damian, G. (2012). An EPR study of superoxide radicals from potassium superoxide solutions. *Applied Magnetic Resonance*, 42(3), 333-341.
- Bredar, A. R. C., Chown, A. L., Burton, A. R., & Farnum, B. H. (2020). Electrochemical impedance spectroscopy of metal oxide electrodes for energy applications. *ACS Applied Energy Materials*, 3(1), 66-98.
- Bryantsev, V. S., Giordani, V., Walker, W., Blanco, M., Zecevic, S., Sasaki, K., Chase, G. V. (2011). Predicting Solvent Stability in Aprotic Electrolyte Li-Air Batteries: Nucleophilic Substitution by the Superoxide Anion Radical ($O_2^{\cdot-}$). *The Journal of Physical Chemistry A*, 115(44), 12399-12409.
- Bunnett, J. F. (1963). Nucleophilic reactivity. *Annual Review of Physical Chemistry*, 14(1), 271-290.
- Burie, J.-R., Boullais, C., Nonella, M., Mioskowski, C., Nabedryk, E., & Breton, J. (1997). Importance of the conformation of methoxy groups on the vibrational and electrochemical properties of ubiquinones. *Journal of Physical Chemistry B*, 101(33), 6607-6617.
- Buzzeo, M. C., Evans, R. G., & Compton, R. G. (2004). Non-haloaluminate room-temperature ionic liquids in electrochemistry-a review. *ChemPhysChem*, 5(8), 1106-1120.
- Buzzeo, M. C., Klymenko, O. V., Wadhawan, J. D., Hardacre, C., Seddon, K. R., & Compton, R. G. (2003). Voltammetry of oxygen in the room-temperature ionic liquids 1-ethyl-3-methylimidazolium bis ((trifluoromethyl) sulfonyl) imide and hexyltriethylammonium bis ((trifluoromethyl) sulfonyl) imide: one-electron reduction to form superoxide. Steady-state and transient behavior in the same cyclic voltammogram resulting from widely different diffusion coefficients of oxygen and superoxide. *The Journal of Physical Chemistry A*, 107(42), 8872-8878.
- Buzzeo, M. C., Klymenko, O. V., Wadhawan, J. D., Hardacre, C., Seddon, K. R., & Compton, R. G. (2004). Kinetic analysis of the reaction between electrogenerated superoxide and carbon dioxide in the room temperature ionic liquids 1-ethyl-3-methylimidazolium bis (trifluoromethylsulfonyl) imide and hexyltriethylammonium bis (trifluoromethylsulfonyl) imide. *The Journal of Physical Chemistry B*, 108(12), 3947-3954.
- Caplow, M. (1968). Kinetics of carbamate formation and breakdown. *Journal of the American Chemical Society*, 90(24), 6795-6803.
- Carroll, L., Pattison, D. I., Davies, J. B., Anderson, R. F., Lopez-Alarcon, C., & Davies, M. J. (2018). Superoxide radicals react with peptide-derived tryptophan radicals with very high rate constants to give hydroperoxides as major products. *Free Radical Biology and Medicine*, 118, 126-136.

- Carsten, A. U. (2019). *Time-dependent density-functional theory: Concepts and applications*: Oxford University Press.
- Carter, M. T., Hussey, C. L., Strubinger, S. K. D., & Osteryoung, R. A. (1991). Electrochemical reduction of dioxygen in room-temperature imidazolium chloride-aluminum chloride molten salts. *Inorganic Chemistry*, 30(5), 1149-1151.
- Casadei, Maria A. (2001). Reactivity of the electrogenerated $O_2^{\cdot-}/CO_2$ system towards alcohols. *European Journal of Organic Chemistry*, 2001(9), 1689-1693.
- Casadei, M. A., Cesa, S., Feroci, M., Inesi, A., Rossi, L., & Moracci, F. M. (1997). The system as mild and safe carboxylating reagent synthesis of organic carbonates. *Tetrahedron*, 53(1), 167-176.
- Casadei, M. A., Cesa, S., Moracci, F. M., Inesi, A., & Feroci, M. (1996). Activation of carbon dioxide by electrogenerated superoxide ion: A new carboxylating reagent. *Journal Organic Chemistry*, 61(1), 380-383.
- Casadei, M. A., Moracci, F. M., Zappia, G., Inesi, A., & Rossi, L. (1997). Electrogenerated superoxide-activated carbon dioxide. A new mild and safe approach to organic carbamates. *Journal of Organic Chemistry*, 62(20), 6754-6759.
- Chatel, G., & MacFarlane, D. R. (2014). Ionic liquids and ultrasound in combination: synergies and challenges. *Chemical Society Reviews*, 43(23), 8132-8149.
- Chattaraj, P. K., Sarkar, U., & Roy, D. R. (2006). Electrophilicity Index. *Chemical Reviews*, 106(6), 2065-2091.
- Che, Y., Tsushima, M., Matsumoto, F., Okajima, T., Tokuda, K., & Ohsaka, T. (1996). Water-induced disproportionation of superoxide ion in aprotic solvents. *Journal of Physical Chemistry*, 100(51), 20134-20137.
- Chen, L.-J., Lin, C.-J., Zuo, J., Song, L.-C., & Huang, C.-M. (2004). First Spectroscopic Observation of Peroxocarbonate/Peroxodicarbonate in Molten Carbonate. *Journal of Physical Chemistry B*, 108(23), 7553-7556.
- Chen, L., Venkatram, S., Kim, C., Batra, R., Chandrasekaran, A., & Ramprasad, R. (2019). Electrochemical stability window of polymeric electrolytes. *Chemistry of Materials*, 31(12), 4598-4604.
- Chen, W., Qiu, L., Liang, S., Zheng, X., & Tang, D. (2013). Measurement of thermal conductivities of [mmim]DMP/CH₃OH and [mmim]DMP/H₂O by freestanding sensor-based 3ω technique. *Thermochimica Acta*, 560, 1-6.
- Chen, Y., Lai, Z., Zhang, X., Fan, Z., He, Q., Tan, C., & Zhang, H. (2020). Phase engineering of nanomaterials. *Nature Reviews Chemistry*, 4(5), 243-256.
- Chin, D. H., Chiericato, G., Nanni, E. J., & Sawyer, D. T. (1982). Proton-induced disproportionation of superoxide ion in aprotic media. *Journal of the American Chemical Society*, 104(5), 1296-1299.

- Chrobok, A., Baj, S., & Swadzba-Kwasny, M. (2007). Oxygen solubility in ionic liquids based on 1-alkyl-3-methylimidazolium cations. *Polish Journal of Chemistry*, 81(3), 337-344.
- Chuban, H., Dong, Z., & Shufang, W. (1991). Nucleophilic substitution of halogeno-nitrobenzenes by superoxide ions electrocatalyzed by metallo-porphyrins. *Journal of Applied Electrochemistry*, 21(8), 740-742.
- Cioslowski, J., Liu, G., & Moncrieff, D. (1997). Thermochemistry of homolytic C–C, C–H, and C–Cl bond dissociations in polychloroethanes: Benchmark electronic structure calculations. *Journal of American Chemical Society*, 119(47), 11452-11457.
- Compton, R. G., & Banks, C. E. (2018). *Understanding voltammetry*: World Scientific.
- Costentin, C., Robert, M., & Savéant, J.-M. (2003). Successive removal of chloride ions from organic polychloride pollutants. Mechanisms of reductive electrochemical elimination in aliphatic gem-polychlorides, α , β -polychloroalkenes, and α , β -polychloroalkanes in mildly protic medium. *Journal of American Chemical Society*, 125(35), 10729-10739.
- Cottrell, F. (1903). Residual current in galvanic polarization, regarded as a diffusion problem. *Zeitschrift für Physikalische Chemie*, 42, 385-431.
- Council, N. R. (2012). *Acute exposure guideline levels for selected airborne chemicals: Volume 12*. Washington, DC: The National Academies Press.
- Crooks, J. E., & Donnellan, J. P. (1989). Kinetics and mechanism of the reaction between carbon dioxide and amines in aqueous solution. *Journal of the Chemical Society, Perkin Transactions 2*(4), 331-333.
- Cui, X., Surkus, A.-E., Junge, K., Topf, C., Radnik, J., Kreyenschulte, C., & Beller, M. (2016). Highly selective hydrogenation of arenes using nanostructured ruthenium catalysts modified with a carbon–nitrogen matrix. *Nature Commun.*, 7(1), 11326.
- Cullinane, J. T., & Rochelle, G. T. (2006). Kinetics of carbon dioxide absorption into aqueous potassium carbonate and piperazine. *Industrial & Engineering Chemistry Research*, 45(8), 2531-2545.
- Damjanovic, A., Genshaw, M. A., & Bockris, J. O. M. (1967). The mechanism of oxygen reduction at platinum in alkaline solutions with special reference to H₂O₂. *Journal of Electrochemical Society*, 114(11), 1107.
- Dannenberg, J. J. (1999). Using perturbation and frontier molecular orbital theory to predict diastereofacial selectivity. *Chemical Review*, 99(5), 1225-1242.
- De Proft, F., Sablon, N., Tozer, D. J., & Geerlings, P. (2007). Calculation of negative electron affinity and aqueous anion hardness using Kohn–Sham HOMO and LUMO energies. *Faraday discussions*, 135, 151-159.
- De Simone, G., Angeli, A., Bozdog, M., Supuran, C. T., Winum, J.-Y., Monti, S. M., & Alterio, V. (2018). Inhibition of carbonic anhydrases by a substrate analog: benzyl

carbamate directly coordinates the catalytic zinc ion mimicking bicarbonate binding. *Chemical Communications*, 54(73), 10312-10315.

Dennington, R., Keith, T., & Millam, J. (2009). GaussView, Version 5.

Dhattarwal, H. S., Remsing, R. C., & Kashyap, H. K. (2020). How flexibility of the nanoscale solvophobic confining material promotes capillary evaporation of ionic liquids. *The Journal of Physical Chemistry C*, 124(8), 4899-4906.

Dickinson, B. C., & Chang, C. J. (2011). Chemistry and biology of reactive oxygen species in signaling or stress responses. *Nature Chemical Biology*, 7(8), 504-511.

Ding, H. L., Zhang, Y. X., Wang, S., Xu, J. M., Xu, S. C., & Li, G. H. (2012). Fe₃O₄@SiO₂ core/shell nanoparticles: The silica coating regulations with a single core for different core sizes and shell thicknesses. *Chem. Mater.*, 24(23), 4572-4580.

Doblinger, S., Lee, J., & Silvester, D. S. (2019). Effect of ionic liquid structure on the oxygen reduction reaction under humidified conditions. *The Journal of Physical Chemistry C*, 123(17), 10727-10737.

Dong, K., Liu, X., Dong, H., Zhang, X., & Zhang, S. (2017). Multiscale studies on ionic liquids. *Chemical Reviews*, 117(10), 6636-6695.

Dong, Y., Luo, J., Li, S., & Liang, C. (2020). CeO₂ decorated Au/CNT catalyst with constructed Au-CeO₂ interfaces for benzyl alcohol oxidation. *Catalysis Communications*, 133, 105843.

Dresselhaus, M. S., Jorio, A., Hofmann, M., Dresselhaus, G., & Saito, R. (2010). Perspectives on carbon nanotubes and graphene raman spectroscopy. *Nano Letters*, 10(3), 751-758.

Duc Chinh, V., Speranza, G., Migliaresi, C., Van Chuc, N., Minh Tan, V., & Phuong, N.-T. (2019). Synthesis of gold nanoparticles decorated with multiwalled carbon nanotubes (Au-MWCNTs) via cysteaminium chloride functionalization. *Sci. Rep.*, 9(1), 5667.

Dutta, B., Deb, D., & Bhattacharya, S. (2018). Ionic liquid-SnO₂ nanoparticle hybrid electrolytes for secondary charge storage devices: Physicochemical and electrochemical studies. *International Journal of Hydrogen Energy*, 43(8), 4081-4089.

Earle, M. J., & Seddon, K. R. (2000). Ionic liquids. green solvents for the future. *Pure and applied chemistry*, 72(7), 1391-1398.

Eckert, F., & Klamt, A. (2013). COSMOtherm. *Version C2, 1*.

Edwards, J. O., & Pearson, R. G. (1962). The Factors Determining Nucleophilic Reactivities. *Journal of the American Chemical Society*, 84(1), 16-24.

- Elgrishi, N., Rountree, K. J., McCarthy, B. D., Rountree, E. S., Eisenhart, T. T., & Dempsey, J. L. (2018). A practical beginner's guide to cyclic voltammetry. *Journal of Chemical Education*, 95(2), 197-206.
- Espinoza, E. M., Clark, J. A., Soliman, J., Derr, J. B., Morales, M., & Vullev, V. I. (2019). Practical aspects of cyclic voltammetry: How to estimate reduction potentials when irreversibility prevails. *Journal of The Electrochemical Society*, 166(5), H3175.
- Evans, C. S., & Dellinger, B. (2005). Mechanisms of dioxin formation from the high-temperature oxidation of 2-chlorophenol. *Environmental Science & Technology*, 39(1), 122-127.
- Evans, R. G., Klymenko, O. V., Hardacre, C., Seddon, K. R., & Compton, R. G. (2003). Oxidation of N, N, N', N'-tetraalkyl-para-phenylenediamines in a series of room temperature ionic liquids incorporating the bis (trifluoromethylsulfonyl) imide anion. *Journal of Electroanalytical Chemistry*, 556, 179-188.
- Evans, R. G., Klymenko, O. V., Saddoughi, S. A., Hardacre, C., & Compton, R. G. (2004). Electroreduction of oxygen in a series of room temperature ionic liquids composed of group 15-centered cations and anions. *The Journal of Physical Chemistry B*, 108(23), 7878-7886.
- Fal, J., Barylyak, A., Besaha, K., Bobitski, Y. V., Cholewa, M., Zawlik, I., Żyła, G. (2016). Experimental investigation of electrical conductivity and permittivity of SC-TiO₂-EG nanofluids. *Nanoscale Research Letters*, 11(1), 375-375.
- Fal, J., Wanic, M., Budzik, G., Oleksy, M., & Żyła, G. (2019). Electrical conductivity and dielectric properties of ethylene glycol-based nanofluids containing silicon oxide-lignin hybrid particles. *Nanomaterials*, 9(7), 1008.
- Fang, W.-Y., Ravindar, L., Rakesh, K. P., Manukumar, H. M., Shantharam, C. S., Alharbi, N. S., & Qin, H.-L. (2019). Synthetic approaches and pharmaceutical applications of chloro-containing molecules for drug discovery: A critical review. *European Journal of Medicinal Chemistry*, 173, 117-153.
- Fang, Y.-H., & Liu, Z.-P. (2014). Tafel kinetics of electrocatalytic reactions: From experiment to first-principles. *ACS Catalysis*, 4(12), 4364-4376.
- Feroci, M., Chiarotto, I., Orsini, M., Sotgiu, G., & Inesi, A. (2011). Carbon dioxide as carbon source: Activation via electrogenerated O₂⁻ in ionic liquids. *Electrochimica Acta*, 56(16), 5823-5827.
- Feroci, M., Inesi, A., & Rossi, L. (2000). The reaction of amines with an electrogenerated base. Improved synthesis of arylcarbamic esters. *Tetrahedron Letters*, 41(6), 963-966.
- Feroci, M., Orsini, M., Rossi, L., Sotgiu, G., & Inesi, A. (2007). Electrochemically promoted C-N bond formation from amines and CO₂ in ionic liquid BMIm-BF₄: Synthesis of carbamates. *The Journal of Organic Chemistry*, 72(1), 200-203.

- Feroci, M., Orsini, M., Sotgiu, G., Rossi, L., & Inesi, A. (2005). Electrochemically promoted C–N bond formation from acetylenic amines and CO₂. Synthesis of 5-Methylene-1,3-oxazolidin-2-ones. *The Journal of Organic Chemistry*, 70(19), 7795-7798.
- Field, J. A., & Sierra-Alvarez, R. (2008). Microbial degradation of chlorinated dioxins. *Chemosphere*, 71(6), 1005-1018.
- Fogarty, R. M., Matthews, R. P., Ashworth, C. R., Brandt-Talbot, A., Palgrave, R. G., Bourne, R. A., ... & Lovelock, K. R. (2018). Experimental validation of calculated atomic charges in ionic liquids. *The Journal of Chemical Physics*, 148(19), 193817.
- Frisch, M., Trucks, G., Schlegel, H., Scuseria, G., Robb, M., Cheeseman, J., Petersson, G. (2009). Gaussian 09, Rev. E. 01.
- Fukui, K. (1982). Role of frontier orbitals in chemical reactions. *Science*, 218(4574), 747-754.
- Gabrielli, C., Grand, P., Lasia, A., & Perrot, H. (2004). Investigation of hydrogen adsorption and absorption in palladium thin films: III. Impedance spectroscopy. *Journal of Electrochemical Society*, 151(11), A1943.
- Gaciño, F. M., Regueira, T., Lugo, L., Comuñas, M. J. P., & Fernández, J. (2011). Influence of molecular structure on densities and viscosities of several ionic liquids. *Journal of Chemical & Engineering Data*, 56(12), 4984-4999.
- Gadewar, S. B., Malone, M. F., & Doherty, M. F. (2000). Selectivity targets for batch reactive distillation. *Industrial Engineering Chemical Research*, 39(6), 1565-1575.
- Galamba, N., Paiva, A., Barreiros, S., & Simões, P. (2019). Solubility of Polar and Nonpolar Aromatic Molecules in Subcritical Water: The Role of the Dielectric Constant. *Journal of Chemical Theory and Computation*, 15(11), 6277-6293.
- Gan, Q., Rooney, D., & Zou, Y. (2006). Supported ionic liquid membranes in nanopore structure for gas separation and transport studies. *Desalination*, 199(1-3), 535-537.
- Gao, J. J., Xu, K. H., Tang, B., Yin, L. L., Yang, G. W., & An, L. G. (2007). Selective detection of superoxide anion radicals generated from macrophages by using a novel fluorescent probe. *The FEBS journal*, 274(7), 1725-1733.
- Garifullina, A., Mahboob, A., & O'Reilly, R. J. (2016). A dataset of homolytic C–Cl bond dissociation energies obtained by means of W1w theory. *Chem. Data Collect.*, 3-4, 21-25.
- Gaussian 09, R. A. (2009). M. J. Frisch, G. W. Trucks, H. B. Schlegel, G. E. Scuseria, M. A. Robb, J. R. Cheeseman, G. Scalmani, V. Barone, G. A. Petersson, H. Nakatsuji, X. Li, M. Caricato, A. Marenich, J. Bloino, B. G. Janesko, R. Gomperts, B. Mennucci, H. P. Hratchian, J. V. Ortiz, A. F. Izmaylov, J. L. Sonnenberg, D. Williams-Young, F. Ding, F. Lipparini, F. Egidi, J. Goings, B. Peng, A. Petrone,

T. Henderson, D. Ranasinghe, V. G. Zakrzewski, J. Gao, N. Rega, G. Zheng, W. Liang, M. Hada, M. Ehara, K. Toyota, R. Fukuda, J. Hasegawa, M. Ishida, T. Nakajima, Y. Honda, O. Kitao, H. Nakai, T. Vreven, K. Throssell, J. A. Montgomery, Jr., J. E. Peralta, F. Ogliaro, M. Bearpark, J. J. Heyd, E. Brothers, K. N. Kudin, V. N. Staroverov, T. Keith, R. Kobayashi, J. Normand, K. Raghavachari, A. Rendell, J. C. Burant, S. S. Iyengar, J. Tomasi, M. Cossi, J. M. Millam, M. Klene, C. Adamo, R. Cammi, J. W. Ochterski, R. L. Martin, K. Morokuma, O. Farkas, J. B. Foresman, and D. J. Fox., *Inc., Wallingford CT.*

- Ge, R., Hardacre, C., Nancarrow, P., & Rooney, D. W. (2007). Thermal conductivities of ionic liquids over the temperature range from 293 K to 353 K. *Journal of Chemical & Engineering Data*, 52(5), 1819-1823.
- Ghosh, A. K., & Brindisi, M. (2015). Organic carbamates in drug design and medicinal chemistry. *Journal of medicinal chemistry*, 58(7), 2895-2940.
- Gibian, M. J., Sawyer, D. T., Ungermann, T., Tangpoonpholvivat, R., & Morrison, M. M. (1979). Reactivity of superoxide ion with carbonyl compounds in aprotic solvents. *Journal of the American Chemical Society*, 101(3), 640-644.
- Giguère, P. A., & Lemaire, D. (1972). Etude Spectroscopique des dérivés du Peroxyde d'hydrogène. V. Les Percarbonates KHCO_4 et $\text{K}_2\text{C}_2\text{O}_6$. *Canadian Journal of Chemistry*, 50(10), 1472-1477.
- Gordon, C. M. (2001). New developments in catalysis using ionic liquids. *Applied Catalysis A: General*, 222(1-2), 101-117.
- Goullé, J.-P., Lacroix, C., Vaz, E., Rouvier, P., & Proust, B. (1999). Fatal case of dichloromethane poisoning. *Journal Analytical Toxicology*, 23(5), 380-383.
- Griffith, J. S., & Orgel, L. E. (1957). Ligand-field theory. *Quarterly Reviews Chemical Society*, 11(4), 381-393.
- Gu, Y., Zhang, Q., Duan, Z., Zhang, J., Zhang, S., & Deng, Y. (2005). Ionic liquid as an efficient promoting medium for fixation of carbon dioxide: A clean method for the Synthesis of 5-Methylene-1,3-oxazolidin-2-ones from Propargylic Alcohols, Amines, and Carbon Dioxide catalyzed by Cu(I) under mild conditions. *The Journal of Organic Chemistry*, 70(18), 7376-7380.
- Guengerich, F. P., Kim, D. H., & Iwasaki, M. (1991). Role of human cytochrome P-450 IIE1 in the oxidation of many low molecular weight cancer suspects. *Chemical Research in Toxicology*, 4(2), 168-179.
- Guidelli, R., Compton, R. G., Feliu, J. M., Gileadi, E., Lipkowsky, J., Schmickler, W., & Trasatti, S. (2014). Defining the transfer coefficient in electrochemistry: An assessment (IUPAC Technical Report). *Pure Applied Chemistry*, 86(2), 245-258.
- Guo, L., Li, J., Cui, Y., Kosol, R., Zeng, Y., Liu, G., Tsubaki, N. (2020). Spinel-structure catalyst catalyzing CO_2 hydrogenation to full spectrum alkenes with an ultra-high yield. *Chemical Communical*, 56(65), 9372-9375.

- Gurkan, B. E., de la Fuente, J. C., Mindrup, E. M., Ficke, L. E., Goodrich, B. F., Price, E. A., Brennecke, J. F. (2010). Equimolar CO₂ absorption by anion-functionalized ionic liquids. *Journal of the American Chemical Society*, 132(7), 2116-2117.
- Gut, I., Nedelcheva, V., Soucek, P., Stopka, P., & Tichavská, B. (1996). Cytochromes P450 in benzene metabolism and involvement of their metabolites and reactive oxygen species in toxicity. *Environ Health Perspect.*, 104 Suppl 6(Suppl 6), 1211-1218.
- Hallett, J. P., & Welton, T. (2011). Room-temperature ionic liquids: Solvents for synthesis and catalysis. *Chemical Reviews*, 111(5), 3508-3576.
- Hayyan, M., Alakrach, A. M., Hayyan, A., Hashim, M. A., & Hizaddin, H. F. (2017). Superoxide ion as oxidative desulfurizing agent for aromatic sulfur compounds in ionic liquid media. *ACS Sustainable Chemistry and Engineering*, 5(2), 1854-1863.
- Hayyan, M., Hashim, M. A., & AlNashef, I. M. (2014). Kinetics of superoxide ion in dimethyl sulfoxide containing ionic liquids. *Ionics*, 21(3), 719-728.
- Hayyan, M., Hashim, M. A., & AlNashef, I. M. (2016a). Superoxide ion: generation and chemical implications. *Chemical Reviews*, 116(5), 3029-3085.
- Hayyan, M., Ibrahim, M., Hayyan, A., & Hashim, M. A. (2017). Investigating the long-term stability and kinetics of superoxide ion in dimethyl sulfoxide containing ionic liquids and the application of thiophene destruction. *Brazilian Journal of Chemical Engineering*, 34(1), 227-239.
- Hayyan, M., Ibrahim, M. H., Hayyan, A., AlNashef, I. M., Alakrach, A. M., & Hashim, M. A. (2015). Facile route for fuel desulfurization using generated superoxide ion in ionic liquids. *Industrial & Engineering Chemistry Research*, 54(49), 12263-12269.
- Hayyan, M., Ibrahim, M. H., Hayyan, A., & Hashim, M. A. (2017). Investigating the Long-Term Stability and Kinetics of Superoxide Ion in Dimethyl Sulfoxide Containing Ionic Liquids and the Application of Thiophene Destruction. *Brazilian Journal of Chemical Engineering*, 34(1), 227-239.
- Hayyan, M., Mjalli, F. S., AlNashef, I. M., & Hashim, M. A. (2012). Chemical and electrochemical generation of superoxide ion in 1-butyl-1-methylpyrrolidinium bis (trifluoromethylsulfonyl) imide. *Internationa Journal of Electrochemical Science*, 7, 8116-8127.
- Hayyan, M., Mjalli, F. S., AlNashef, I. M., & Hashim, M. A. (2012). Generation and stability of superoxide ion in tris(pentafluoroethyl)trifluorophosphate anion-based ionic liquids. *J. Fluorine Chemistry*, 142, 83-89.
- Hayyan, M., Mjalli, F. S., Hashim, M., AlNashef, I. M., Tan, X., & Chooi, K. (2010). Generation of superoxide ion in trihexyl (tetradecyl) phosphonium bis (trifluoromethylsulfonyl) imide room temperature ionic liquid. *Journal of Applied Sciences*, 10(12), 1176-1180.

- Hayyan, M., Mjalli, F. S., Hashim, M. A., & AlNashef, I. M. (2011, February). Electrochemical Generation of Superoxide Ion in Ionic Liquid 1-(3-Methoxypropyl)-1-Methylpiperidinium Bis (Trifluoromethylsulfonyl) Imide. In *IOP Conference Series: Materials Science and Engineering* (Vol. 17, No. 1, p. 012028). IOP Publishing.
- Hayyan, M., Mjalli, F. S., Hashim, M. A., & AlNashef, I. M. (2012). Generation of superoxide ion in pyridinium, morpholinium, ammonium, and sulfonium-based ionic liquids and the application in the destruction of toxic chlorinated phenols. *Industrial & Engineering Chemistry Research*, 51(32), 10546-10556.
- Hayyan, M., Mjalli, F. S., Hashim, M. A., & AlNashef, I. M. (2013). An investigation of the reaction between 1-butyl-3-methylimidazolium trifluoromethanesulfonate and superoxide ion. *Journal of Molecular Liquid*, 181, 44-50.
- Hayyan, M., Mjalli, F. S., Hashim, M. A., AlNashef, I. M., Al-Zahrani, S. M., & Chooi, K. L. (2012). Long term stability of superoxide ion in piperidinium, pyrrolidinium and phosphonium cations-based ionic liquids and its utilization in the destruction of chlorobenzenes. *Journal Electroanalytical Chemistry*, 664, 26-32.
- Hayyan, M., Mjalli, F. S., Hashim, M. A., AlNashef, I. M., & Mei, T. X. (2013). Investigating the electrochemical windows of ionic liquids. *Industrial & Engineering Chemistry Research*, 19(1), 106-112.
- Hayyan, M., Mjalli, F. S., Hashim, M. A., AlNashef, I. M., & Tan, X. M. (2011a). Electrochemical reduction of dioxygen in Bis (trifluoromethylsulfonyl) imide based ionic liquids. *Journal of Electroanalytical Chemistry*, 657(1-2), 150-157.
- He, R., Chen, S., Yang, F., & Wu, B. (2006). Dynamic diffuse double-layer model for the electrochemistry of nanometer-sized electrodes. *Journal of Physical Chemistry B*, 110(7), 3262-3270.
- Hegeland, F., Rasmussen, F., & Brodersen, S. (1973). The selection rules and the transition moment for rotation-vibrational transitions in axial molecules. *Journal of Raman Spectroscopy*, 1(5), 433-453.
- Hensen, B., Wei Huang, W., Yang, C.-H., Wai Chan, K., Yoneda, J., Tantt, T., Dzurak, A. S. (2020). A silicon quantum-dot-coupled nuclear spin qubit. *Nature Nanotechnology*, 15(1), 13-17.
- Heyn, R. H., Jacobs, I., & Carr, R. H. (2014). Synthesis of aromatic carbamates from CO₂: implications for the polyurethane industry. In *Advances in Inorganic Chemistry* (Vol. 66, pp. 83-115): Elsevier.
- Honda, M., Sonehara, S., Yasuda, H., Nakagawa, Y., & Tomishige, K. (2011). Heterogeneous CeO₂ catalyst for the one-pot synthesis of organic carbamates from amines, CO₂ and alcohols. *Green Chemistry*, 13(12), 3406-3413.
- Hoz, S., & Buncl, E. (1985). The α -Effect: A critical examination of the phenomenon and its origin. *Israel Journal of Chemistry*, 26(4), 313-319.

- H.-R.M. Jhong, C.E. Tornow, B. Smid, A.A. Gewirth, S.M. Lyth, P.J.A. Kenis, A Nitrogen-doped carbon catalyst for electrochemical CO₂ conversion to CO with high selectivity and current density, *ChemSusChem*, 10 (2017) 1094-1099.
- Huang, B., Isse, A. A., Durante, C., Wei, C., & Gennaro, A. (2012). Electrocatalytic properties of transition metals toward reductive dechlorination of polychloroethanes. *Electrochimica Acta*, 70, 50-61.
- Huang, Q., Luo, Q., Chen, Z., Yao, L., Fu, P., & Lin, Z. (2018). The effect of electrolyte concentration on electrochemical impedance for evaluating polysulfone membranes. *Environmental Science: Water Research & Technology*, 4(8), 1145-1151.
- Huang, X., Zhu, J., Ge, B., Deng, K., Wu, X., Xiao, T., Wang, Z. (2019). Understanding Fe₃O₄ nanocube assembly with reconstruction of a consistent superlattice phase diagram. *Journal of the American Chemical Society*, 141(7), 3198-3206.
- Huang, Y.-Q., Song, H.-J., Liu, Y.-X., & Wang, Q.-M. (2018). Dehydrogenation of N-heterocycles by superoxide ion generated through single-electron transfer. *Chemistry – A European Journal*, 24(9), 2065-2069.
- Hunt, A. J., Sin, E. H., Marriott, R., & Clark, J. H. (2010). Generation, capture, and utilization of industrial carbon dioxide. *ChemSusChem: Chemistry & Sustainability Energy & Materials*, 3(3), 306-322
- Ibrahim, M. H., Hayyan, M., Hashim, M. A., Hayyan, A., & Hadj-Kali, M. K. (2016). Physicochemical properties of piperidinium, ammonium, pyrrolidinium and morpholinium cations based ionic liquids paired with bis(trifluoromethylsulfonyl)imide anion. *Fluid Phase Equilibria*, 427, 18-26.
- Ikeuchi, H. (2005). Accuracy of theoretical equations for diffusion currents at a disk electrode. *Journal of Electroanalytical Chemistry*, 577(1), 55-58.
- Inesi, A., Mucciante, V., & Rossi, L. (1998). A convenient method for the synthesis of carbamate esters from amines and tetraethylammonium hydrogen carbonate. *The Journal of Organic Chemistry*, 63(4), 1337-1338.
- Ion, A., Doorslaer, C. V., Parvulescu, V., Jacobs, P., & Vos, D. D. (2008). Green synthesis of carbamates from CO₂, amines and alcohols. *Green Chemistry*, 10(1), 111-116.
- Islam, M. M., Imase, T., Okajima, T., Takahashi, M., Niikura, Y., Kawashima, N., Ohsaka, T. (2009b). Stability of superoxide ion in imidazolium cation-based room-temperature ionic liquids. *The Journal of Physical Chemistry A*, 113(5), 912-916.
- Islam, M. M., Saha, M. S., Okajima, T., & Ohsaka, T. (2005). Current oscillatory phenomena based on electrogenerated superoxide ion at the HMDE in dimethylsulfoxide. *Journal Electroanalytical Chemistry*, 577(1), 145-154.
- Jansch, T., Wallauer, J., & Roling, B. (2015). Influence of electrode roughness on double layer formation in ionic liquids. *The Journal of Physical Chemistry C*, 119(9), 4620-4626.

- Jarosik, A., Krajewski, S. R., Lewandowski, A., & Radzimski, P. (2006). Conductivity of ionic liquids in mixtures. *Journal of Molecular Liquids*, 123(1), 43-50.
- Jeschke, P. (2010). The unique role of halogen substituents in the design of modern agrochemicals. *Pest Management Science.*, 66(1), 10-27.
- Jiang, S., Dai, L., Qin, Y., Xiong, L., & Sun, Q. (2016). Preparation and characterization of octenyl succinic anhydride modified taro starch nanoparticles. *PloS one*, 11(2), 0150043.
- Johnson, R. A., Nidy, E. G., & Merritt, M. V. (1978). Superoxide chemistry. Reactions of superoxide with alkyl halides and alkyl sulfonate esters. *Journal of the Chemical Society*, 100(25), 7960-7966.
- Jones, D. P., & Griffith, W. P. (1980a). Alkali-metal peroxocarbonates, $M_2[CO_3] \cdot nH_2O_2$, $M_2[C_2O_6]$, $M[HCO_4] \cdot nH_2O$, and $Li_2[CO_4] \cdot H_2O$. *Journal of the Chemical Society, Dalton Transactions*(12), 2526-2532.
- Jupp, A. R., Johnstone, T. C., & Stephan, D. W. (2018). The global electrophilicity index as a metric for Lewis acidity. *Dalton Transactions*, 47(20), 7029-7035.
- Kai, T., Zhou, M., Johnson, S., Ahn, H. S., & Bard, A. J. (2018). Direct observation of $C_2O_4^{\cdot -}$ and $CO_2^{\cdot -}$ by oxidation of oxalate within nanogap of scanning electrochemical microscope. *Journal of the Chemical Society*, 140(47), 16178-16183.
- Karimi Darvanjooghi, M. H., Pahlevaninezhad, M., Abdollahi, A., & Davoodi, S. M. (2017). Investigation of the effect of magnetic field on mass transfer parameters of CO_2 absorption using Fe_3O_4 -water nanofluid. *AIChE Journal*, 63(6), 2176-2186.
- Katayama, Y., Onodera, H., Yamagata, M., & Miura, T. (2004). Electrochemical reduction of oxygen in some hydrophobic room-temperature molten salt systems. *Journal of Electrochemical Society*, 151(1), 59-63.
- Kazemiabnavi, S., Zhang, Z., Thornton, K., & Banerjee, S. (2016). Electrochemical stability window of imidazolium-based ionic liquids as electrolytes for lithium batteries. *Journal of Physical Chemistry B*, 120(25), 5691-5702.
- Kepp, K. P. (2016). A quantitative scale of oxophilicity and thiophilicity. *Inorganic Chemistry*, 55(18), 9461-9470.
- Keppler, F., Borchers, R., Pracht, J., Rheinberger, S., & Schöler, H. F. (2002). Natural formation of vinyl chloride in the terrestrial environment. *Environmental Science and Technology*, 36(11), 2479-2483.
- Khan, N. A., Hasan, Z., & Jhung, S. H. (2014). Ionic liquids supported on metal-organic frameworks: Remarkable adsorbents for adsorptive desulfurization. *Chemistry – A European Journal*, 20(2), 376-380.

- Klamt, A., Eckert, F., & Arlt, W. (2010). COSMO-RS: An alternative to simulation for calculating thermodynamic properties of liquid mixtures. *Annual Review of Chemical and Biomolecular Engineering*, 1, 101-122.
- Kleij, A. W. (2019). CO₂ catalysis: Mature and multifaceted. *Advanced Synthesis & Catalysis*, 361(2), 221-222.
- Kletetschka, G., Inoue, Y., Lindauer, J., & Hülka, Z. (2019). Magnetic tunneling with CNT-based metamaterial. *Sci. Rep.*, 9(1), 2551.
- Klymenko, O. V., Evans, R. G., Hardacre, C., Svir, I. B., & Compton, R. G. (2004). Double potential step chronoamperometry at microdisk electrodes: simulating the case of unequal diffusion coefficients. *Journal of Electroanalytical Chemistry*, 571(2), 211-221.
- Kuhns, R. J., & Shaw, G. H. (2018). The carbon dioxide problem and solution. In *Navigating the Energy Maze* (pp. 99-115): Springer.
- Kumar, S., & Dhaliwal, A. (2020). Cyclic voltammetry synthesis of polyaniline as supercapacitors electrode. *Materials Today: Proceedings*, 21, 1833-1839.
- Kumar, A., & Sevilla, M. D. (2018). SOMO–HOMO Level Inversion in Biologically Important Radicals. *The Journal of Physical Chemistry B*, 122(1), 98-105.
- Kumelan, J., Kamps, Á. P.-S., Urukova, I., Tuma, D., & Maurer, G. (2005). Solubility of oxygen in the ionic liquid [bmim][PF₆]: Experimental and molecular simulation results. *Journal of Chemical Thermodynamic*, 37(6), 595-602.
- Lackner, K., Ziock, H. J., & Grimes, P. (1999). *Carbon dioxide extraction from air: Is it an option?* (No. LA-UR-99-583). Los Alamos National Lab., NM (US).
- Larkin, P. (2017). *Infrared and raman spectroscopy: principles and spectral interpretation*: Elsevier.
- Lates, V., Falch, A., Jordaan, A., Peach, R., & Kriek, R. J. (2014). An electrochemical study of carbon dioxide electroreduction on gold-based nanoparticle catalysts. *Electrochimica Acta*, 128, 75-84.
- Le Minh, C., Jones, R. A., Craven, I. E., & Brown, T. C. (1997). Temperature-programmed oxidation of coke deposited on cracking catalysts: Combustion mechanism dependence. *Energy & Fuels*, 11(2), 463-469.
- Lee, Y.-S., & Ryu, K.-S. (2017). Study of the lithium diffusion properties and high rate performance of TiNb₆O₁₇ as an anode in lithium secondary battery. *Scientific Reports*, 7(1), 16617.
- Lehtivarjo, J., Niemitz, M., & Korhonen, S.-P. (2014). Universal J-coupling prediction. *Journal of Chemical Information Modelling*, 54(3), 810-817.
- Lei, C., Liang, F., Li, J., Chen, W., & Huang, B. (2019). Electrochemical reductive dechlorination of chlorinated volatile organic compounds (Cl-VOCs): Effects of

molecular structure on the dehalogenation reactivity and mechanisms. *Chemical Engineering Journal*, 358, 1054-1064.

Lei, Z., Chen, B., Koo, Y. M., & MacFarlane, D. R. (2017). Introduction: ionic liquids. *Chemical Reviews*, 117(10), 6633-6635.

Lerch, S., & Strassner, T. (2019). Expanding the electrochemical window: new tunable aryl alkyl ionic liquids (TAAILs) with dicyanamide anions. *Chemistry – A European Journal*, 25(71), 16251-16256.

Li, C. C., Zhang, W., Ang, H., Yu, H., Xia, B. Y., Wang, X., Yan, Q. (2014). Compressed hydrogen gas-induced synthesis of Au–Pt core–shell nanoparticle chains towards high-performance catalysts for Li–O₂ batteries. *Journal of Material Chemistry A*, 2(27), 10676-10681.

Li, Q., & Jun, Y.-S. (2018). The apparent activation energy and pre-exponential kinetic factor for heterogeneous calcium carbonate nucleation on quartz. *Communication Chemistry*, 1(1), 56.

Li, X.-R., Wang, B., Xu, J.-J., & Chen, H.-Y. (2011). In vitro detection of superoxide anions released from cancer cells based on potassium-doped carbon nanotubes–ionic liquid composite gels. *Nanoscale*, 3(12), 5026-5033.

Liedtke, T., Hilche, T., Klare, S., & Gansäuer, A. (2019). Condition screening for sustainable catalysis in single-electron steps by cyclic voltammetry: additives and solvents. *ChemSusChem*, 12(13), 3166-3171.

Liu, S., Xiao, J., Lu, X. F., Wang, J., Wang, X., & Lou, X. W. (2019). Efficient electrochemical reduction of CO₂ to HCOOH over Sub-2 nm SnO₂ quantum wires with exposed grain boundaries. *Angewandte Chemie International Edition*, 58(25), 8499-8503.

Liu, S., Mei, L., Liang, X., Liao, L., Lv, G., Ma, S., . . . Xi, K. (2018). Anchoring Fe₃O₄ nanoparticles on carbon nanotubes for microwave-induced catalytic degradation of antibiotics. *ACS Appl. Mater. & Inter.*, 10(35), 29467-29475.

Lu, W., Sculley, J. P., Yuan, D., Krishna, R., Wei, Z., & Zhou, H. C. (2012). Polyamine-tethered porous polymer networks for carbon dioxide capture from flue gas. *Angewandte Chemie International Edition*, 51(30), 7480-7484.

Lu, W., Sculley, J. P., Yuan, D., Krishna, R., & Zhou, H.-C. (2013). Carbon dioxide capture from air using amine-grafted porous polymer networks. *The Journal of Physical Chemistry C*, 117(8), 4057-4061.

Lucio, A. J., Shaw, S. K., Zhang, J., & Bond, A. M. (2018). Double-layer capacitance at ionic liquid–boron-doped diamond electrode interfaces studied by fourier transformed alternating current voltammetry. *The Journal of Physical Chemistry C*, 122(22), 11777-11788.

Lundgren, C. A. K., Sjöstrand, D., Biner, O., Bennett, M., Rudling, A., Johansson, A.-L., . . . Högbom, M. (2018). Scavenging of superoxide by a membrane-bound superoxide oxidase. *Nature Chemical Biology*, 14(8), 788-793.

- Magherusan, A. M., Zhou, A., Farquhar, E. R., García-Melchor, M., Twamley, B., Que Jr., L., & McDonald, A. R. (2018). Mimicking class I b Mn²⁺-ribonucleotide reductase: A MnII₂ complex and its reaction with superoxide. *Angewandte Chemie International Edition*, 57(4), 918-922.
- Mai, N. L., & Koo, Y.-M. (2016). Computer-Aided Design of Ionic Liquids for High Cellulose Dissolution. *ACS Sustainable Chemistry & Engineering*, 4(2), 541-547.
- Mann, M. A., Helfrick, J. C., & Bottomley, L. A. (2014). Diagnostic criteria for the characterization of quasireversible electron transfer reactions by cyclic square wave voltammetry. *Analytical Chemistry*, 86(16), 8183-8191.
- Mao, Q., Krewer, U., & Hanke-Rauschenbach, R. (2010). Total harmonic distortion analysis for direct methanol fuel cell anode. *Electrochemistry Communications*, 12(11), 1517-1519.
- Mar, S. Y., Chen, C. S., Huang, Y. S., & Tiong, K. K. (1995). Characterization of RuO₂ thin films by raman spectroscopy. *Applied Surface Science*, 90(4), 497-504.
- Marciniak, A., & Wlazło, M. (2012). Activity coefficients at infinite dilution and physicochemical properties for organic solutes and water in the ionic liquid 4-(2-methoxyethyl)-4-methylmorpholinium bis(trifluoromethylsulfonyl)-amide. *The Journal of Chemical Thermodynamics*, 47, 382-388.
- Maricle, D., & Hodgson, W. (1965). Reduction of oxygen to superoxide anion in aprotic solvents. *Analytical Chemistry*, 37(12), 1562-1565.
- Markewitz, P., Kuckshinrichs, W., Leitner, W., Linssen, J., Zapp, P., Bongartz, R., & er, T. E. (2012). Worldwide innovations in the development of carbon capture technologies and the utilization of CO₂. *Energy & environmental science*, 5(6), 7281-7305.
- Martin, E. T., McGuire, C. M., Mubarak, M. S., & Peters, D. G. (2016). Electroreductive remediation of halogenated environmental pollutants. *Chemical Review*, 116(24), 15198-15234.
- Matheswaran, P., Wilfred, C. D., Kurnia, K. A., & Ramli, A. (2016). Overview of activity coefficient of thiophene at infinite dilution in ionic liquids and their modeling using COSMO-RS. *Industrial & Engineering Chemistry Research*, 55(3), 788-797.
- Mathias, J.-D., Anderies, J. M., & Janssen, M. A. (2017). On our rapidly shrinking capacity to comply with the planetary boundaries on climate change. *Scientific Reports*, 7, 42061.
- McCann, N., Phan, D., Wang, X., Conway, W., Burns, R., Attalla, M., Maeder, M. (2009). Kinetics and mechanism of carbamate formation from CO₂(aq), carbonate species, and monoethanolamine in aqueous solution. *The Journal of Physical Chemistry A*, 113(17), 5022-5029.

- McCrory, C. C. L., Jung, S., Peters, J. C., & Jaramillo, T. F. (2013). Benchmarking heterogeneous electrocatalysts for the oxygen evolution reaction. *Journal of the American Chemical Society*, 135(45), 16977-16987.
- McKay, G. (2002). Dioxin characterisation, formation and minimisation during municipal solid waste (MSW) incineration: Review. *Chemical Engineering Journal*, 86(3), 343-368.
- Mei, B.-A., Munteshari, O., Lau, J., Dunn, B., & Pilon, L. (2018). Physical interpretations of nyquist plots for EDLC electrodes and devices. *The Journal of Physical Chemistry C*, 122(1), 194-206.
- Memming, R. (2015). *Semiconductor electrochemistry*: John Wiley & Sons.
- Merritt, M. V., & Sawyer, D. T. (1970). Electrochemical studies of the reactivity of superoxide ion with several alkyl halides in dimethyl sulfoxide. *The Journal of Organic Chemistry*, 35(7), 2157-2159.
- Miao, L., Basak, R., Ran, S., Xu, Y., Kotta, E., He, H., Xu, Z. (2019). High temperature singlet-based magnetism from Hund's rule correlations. *Nature communications*, 10(1), 644.
- Mills, I. M. (1964). Raman selection rules for vibration-rotation transitions in symmetric top molecules. *Molecular Physics*, 8(4), 363-373.
- Miyake, Y., Tokumura, M., Wang, Q., Amagai, T., Horii, Y., & Kannan, K. (2017). Mechanism of formation of chlorinated pyrene during combustion of polyvinyl chloride. *Environmental Science and Technology*, 51(24), 14100-14106.
- Mohammad, M., Khan, A. Y., Subhani, M. S., Bibi, N., Ahmad, S., & Saleemi, S. (2001). Kinetics and electrochemical studies on superoxide. *Research on Chemical Intermediates*, 27(3), 259-267.
- Mohan, A., K.V, N., & C, J. (2017). Removal of chlorobenzene and 1,4-dichlorobenzene using novel poly-o-toluidine zirconium(IV) phosphotellurite exchanger. *Resource-Efficient Techn.*, 3(3), 317-328.
- Molina, A., González, J., Laborda, E., & Compton, R. G. (2013). On the meaning of the diffusion layer thickness for slow electrode reactions. *Physical Chemistry Chemical Physics*, 15(7), 2381-2388.
- Mondragón, R., Juliá, J. E., Cabedo, L., & Navarrete, N. (2018). On the relationship between the specific heat enhancement of salt-based nanofluids and the ionic exchange capacity of nanoparticles. *Scientific Report*, 8(1), 7532.
- Monti, M., Santos, B., Mascaraque, A., de la Fuente, O. R., Niño, M. A., Menteş, T. O., . . . de La Figuera, J. (2012). Magnetism in nanometer-thick magnetite. *Physical Review B*, 85(2), 020404.
- Moosavi, M., Khashei, F., Sharifi, A., & Mirzaei, M. (2016). Transport properties of short alkyl chain length dicationic ionic liquids—The effects of alkyl chain length and temperature. *Industrial & Engineering Chemistry Research*, 55(33), 9087-9099.

- Morgan, D. J. (2015). Resolving ruthenium: XPS studies of common ruthenium materials. *Surface and Interface Analysis*, 47(11), 1072-1079.
- Motobayashi, K., Shibamura, Y., & Ikeda, K. (2020). Origin of a high overpotential of co electrodeposition in a room-temperature ionic liquid. *Journal of Physical Chemistry Letters*, 8697-8702.
- Mozurkewich, M., & Benson, S. W. (1984). Negative activation energies and curved Arrhenius plots. 1. Theory of reactions over potential wells. *Journal of Physical Chemistry*, 88(25), 6429-6435.
- Muller, P. (1994). Glossary of terms used in physical organic chemistry (IUPAC Recommendations 1994). In *Pure and applied chemistry* (Vol. 66, pp. 1077).
- Muñoz-Rugeles, L., Galano, A., & Alvarez-Idaboy, J. R. (2018). The other side of the superoxide radical anion: its ability to chemically repair DNA oxidized sites. *Chemical Communications*, 54(97), 13710-13713.
- Menzel, T., Afanas'ev, I. B., Kleschyov, A. L., & Harrison, D. G. (2002). Detection of superoxide in vascular tissue. *Arteriosclerosis, thrombosis, and vascular biology*, 22(11), 1761-1768.
- Myland, J. C., & Oldham, K. B. (2005). Quasireversible cyclic voltammetry of a surface confined redox system: a mathematical treatment. *Electrochemistry Communications*, 7(3), 282-287.
- Nanni, E. J., Angelis, C. T., Dickson, J., & Sawyer, D. T. (1981). Oxygen activation by radical coupling between superoxide ion and reduced methyl viologen. *Journal of the American Chemical Society*, 103(14), 4268-4270.
- Naumann, K. (2000). Influence of chlorine substituents on biological activity of chemicals: a review. *Pest Management Science*, 56(1), 3-21.
- Nauseef, W. M. (2014). Detection of superoxide anion and hydrogen peroxide production by cellular NADPH oxidases. *Biochimica et biophysica Acta (BBA)-general subjects*, 1840(2), 757-767.
- Neale, A. R., Li, P., Jacquemin, J., Goodrich, P., Ball, S. C., Compton, R. G., & Hardacre, C. (2016b). Effect of cation structure on the oxygen solubility and diffusivity in a range of bis{(trifluoromethyl)sulfonyl}imide anion based ionic liquids for lithium-air battery electrolytes. *Physical Chemistry Chemical Physics*, 18(16), 11251-11262.
- Neese, F., Atanasov, M., Bistoni, G., Maganas, D., & Ye, S. (2019). Chemistry and quantum mechanics in 2019: Give us insight and numbers. *Journal of the American Chemical Society*, 141(7), 2814-2824.
- Newton, T. A., & Warren, H. W. (1980). Nucleophilic substitution reactions: Modifications and an extension. *Journal of Chemical Education*, 57(10), 747.
- Ni, Y., Chen, Z., Fu, Y., Liu, Y., Zhu, W., & Liu, Z. (2018a). Selective conversion of CO₂ and H₂ into aromatics. *Nature communications*, 9(1), 3457.

- Ni, Y., Chen, Z., Fu, Y., Liu, Y., Zhu, W., & Liu, Z. (2018b). Selective conversion of CO₂ and H₂ into aromatics. *Nature communications*, 9(1), 3457.
- Nicholson, R. S. (1965). Theory and application of cyclic voltammetry for measurement of electrode reaction kinetics. *Analytical Chemistry*, 37(11), 1351-1355.
- Nicholson, R. S., & Shain, I. (1965). Theory of stationary electrode polarography for a chemical reaction coupled between two charge transfers. *Analytical Chemistry*, 37(2), 178-190.
- Nkurikiyimfura, I., Wang, Y., Safari, B., & Nshingabigwi, E. (2020). Temperature-dependent magnetic properties of magnetite nanoparticles synthesized via coprecipitation method. *Journal of Alloys and Compounds*, 846, 156344.
- O'Toole, S., Pentlavalli, S., & Doherty, A. P. (2007). Behavior of electrogenerated bases in room-temperature ionic liquids. *The Journal of Physical Chemistry B*, 111(31), 9281-9287.
- O'Mahony, A. M., Silvester, D. S., Aldous, L., Hardacre, C., & Compton, R. G. (2008). Effect of water on the electrochemical window and potential limits of room-temperature ionic liquids. *Journal of Chemical & Engineering Data*, 53(12), 2884-2891.
- Oh, Y., & Hu, X. (2015). Ionic liquids enhance the electrochemical CO₂ reduction catalyzed by MoO₂. *Chemical Communication*, 51(71), 13698-13701.
- Oke, J. A., Idisi, D. O., Sarma, S., Moloi, S. J., Ray, S. C., Chen, K. H., Pong, W. F. (2019). Electronic, electrical, and magnetic behavioral change of SiO₂-NP-decorated MWCNTs. *ACS Omega*, 4(11), 14589-14598.
- Orazem, M. E., & Tribollet, B. (2011). *Electrochemical Impedance Spectroscopy* (Vol. 48): John Wiley & Sons.
- Orloff, K. G., Hewitt, D., Metcalf, S., Kathman, S., Lewin, M., & Turner, W. (2001). Dioxin exposure in a residential community. *Journal of Exposure. Science and Environmental Epidemiology*, 11(5), 352-358.
- Ozawa, T., & Hanaki, A. (1977). On a spectrally well-defined and stable source of superoxide ion, O₂⁻. *FEBS Letters*, 74(1), 99-102.
- Pachecka, M., Sturm, J. M., Lee, C. J., & Bijkerk, F. (2017a). Adsorption and dissociation of CO₂ on Ru(0001). *Journal of Physical Chemistry C*, 121(12), 6729-6735.
- Paddon, C. A., Silvester, D. S., Bhatti, F. L., Donohoe, T. J., & Compton, R. G. (2007). Coulometry on the voltammetric timescale: Microdisk potential-step chronoamperometry in aprotic solvents reliably measures the number of electrons transferred in an electrode process simultaneously with the diffusion coefficients of the electroactive species. *Electroanalysis: An International Journal Devoted to Fundamental and Practical Aspects of Electroanalysis*, 19(1), 11-22.
- Padmanabhan, J., Parthasarathi, R., Elango, M., Subramanian, V., Krishnamoorthy, B. S., Gutierrez-Oliva, S., . . . Chattaraj, P. K. (2007). Multiphilic descriptor for

chemical reactivity and selectivity. *The Journal of Physical Chemistry A*, 111(37), 9130-9138.

- Pan, L., Ai, M., Huang, C., Yin, L., Liu, X., Zhang, R., Mi, W. (2020). Manipulating spin polarization of titanium dioxide for efficient photocatalysis. *Nature communications*, 11(1), 418.
- Pandolfi, F., Chiarotto, I., Rocco, D., & Feroci, M. (2017). Electrogenerated superoxide anion induced oxidative amidation of benzoin. *Electrochimica Acta*, 254, 358-367.
- Parr, R. G. (1982). Density functional theory. In *Electron distributions and the chemical bond* (pp. 95-100): Springer.
- Paschoal, V. H., Faria, L. F. O., & Ribeiro, M. C. C. (2017). Vibrational spectroscopy of ionic liquids. *Chemical Reviews*, 117(10), 7053-7112.
- Peover, M., & White, B. (1966). Electrolytic reduction of oxygen in aprotic solvents: The superoxide ion. *Electrochimica Acta*, 11(8), 1061-1067.
- Perakis, F., De Marco, L., Shalit, A., Tang, F., Kann, Z. R., , T. D., Nagata, Y. (2016). Vibrational Spectroscopy and Dynamics of Water. *Chemical Review*, 116(13), 7590-7607.
- Perdew, J. P. (1986). Density-functional approximation for the correlation energy of the inhomogeneous electron gas. *Physical Reviews B*, 33(12), 8822.
- Periana, R. A., Taube, D. J., Evitt, E. R., Löffler, D. G., Wentreck, P. R., Voss, G., & Masuda, T. (1994). A novel, high yield system for the oxidation of methane to methanol. In H. E. Curry-Hyde & R. F. Howe (Eds.), *Studies in Surface Science and Catalysis* (Vol. 81, pp. 533-544): Elsevier.
- Pike, S. J., Hutchinson, J. J., & Hunter, C. A. (2017). H-Bond Acceptor Parameters for Anions. *Journal of the American Chemical Society*, 139(19), 6700-6706.
- Pozo-Gonzalo, C., Kar, M., Jónsson, E., Howlett, P. C., MacFarlane, D. R., & Forsyth, M. (2016). Reduction of oxygen in a trialkoxy ammonium-based ionic liquid and the role of water. *Electrochimica Acta*, 196, 727-734.
- Purvis, G. D., 3rd. (1991). On the use of isovalued surfaces to determine molecule shape and reaction pathways. *Journal of Computer-Aided Molecular Design*, 5(1), 55-80.
- Puthongkham, P., & Venton, B. J. (2020). Recent advances in fast-scan cyclic voltammetry. *Analyst*, 145(4), 1087-1102.
- Putnam, R., Taylor, R., Klamt, A., Eckert, F., & Schiller, M. (2003). Prediction of infinite dilution activity coefficients using COSMO-RS. *Industrial & engineering chemistry research*, 42(15), 3635-3641.
- Qian, W., Texter, J., & Yan, F. (2017). Frontiers in poly(ionic liquid)s: syntheses and applications. *Chemical Society Reviews*, 46(4), 1124-1159.

- Ramdin, M., de Loos, T. W., & Vlugt, T. J. (2012). State-of-the-art of CO₂ capture with ionic liquids. *Industrial & Engineering Chemistry Research*, 51(24), 8149-8177.
- Randström, S., Appetecchi, G. B., Lagergren, C., Moreno, A., & Passerini, S. (2007). The influence of air and its components on the cathodic stability of N-butyl-N-methylpyrrolidinium bis (trifluoromethanesulfonyl) imide. *Electrochimica Acta*, 53(4), 1837-1842.
- Randström, S., Appetecchi, G. B., Lagergren, C., Moreno, A., & Passerini, S. (2007). The influence of air and its components on the cathodic stability of N-butyl-N-methylpyrrolidinium bis(trifluoromethanesulfonyl)imide. *Electrochimica Acta*, 53(4), 1837-1842.
- Řehák, K., Morávek, P., & Strejc, M. (2012). Determination of mutual solubilities of ionic liquids and water. *Fluid Phase Equilibria*, 316, 17-25.
- René, A., Hauchard, D., Lagrost, C., & Hapiot, P. (2009). Superoxide protonation by weak acids in imidazolium based ionic liquids. *The Journal of Physical Chemistry B*, 113(9), 2826-2831.
- Rigo, A., Argese, E., Orsega, E. F., & Viglino, P. (1979). Detection of superoxide ion in aqueous media by N-halopiperidines. *Inorganica Chimica Acta*, 35, 161-164.
- Rilo, E., Vila, J., Pico, J., García-Garabal, S., Segade, L., Varela, L. M., & Cabeza, O. (2010). Electrical conductivity and viscosity of aqueous binary mixtures of 1-Alkyl-3-methyl Imidazolium tetrafluoroborate at four temperatures. *Journal of Chemical & Engineering Data*, 55(2), 639-644.
- Roberts, J. L., Calderwood, T. S., & Sawyer, D. T. (1983). Oxygenation by superoxide ion of tetrachloromethane, trichlorofluoromethane, trichloromethane, p,p'-DDT and related trichloromethyl substrates (RCCl₃) in aprotic solvents. *Journal of American Chemical Society*, 105(26), 7691-7696.
- Roberts, J. L., Calderwood, T. S., & Sawyer, D. T. (1984). Nucleophilic oxygenation of carbon dioxide by superoxide ion in aprotic media to form the peroxydicarbonate (2-) ion species. *Journal of American Chemical Society*, 106(17), 4667-4670.
- Roberts Jr., J. L., & Sawyer, D. T. (1983). Activation of superoxide ion by reactions with protons, electrophiles, secondary amines, radicals, and reduced metal ions. *Israel Journal of Chemistry* . 23(4), 430-438.
- Rogers, E. I., Huang, X.-J., Dickinson, E. J., Hardacre, C., & Compton, R. G. (2009). Investigating the mechanism and electrode kinetics of the oxygen|superoxide (O₂|O₂^{•-}) couple in various room-temperature ionic liquids at gold and platinum electrodes in the temperature range 298–318 K. *The Journal of Physical Chemistry C*, 113(41), 17811-17823.
- Rogers, E. I., Šljukić, B., Hardacre, C., & Compton, R. G. (2009). Electrochemistry in room-temperature ionic liquids: Potential windows at mercury electrodes. *Journal of Chemical & Engineering Data*, 54(7), 2049-2053.

- Rohe, S., Révol, G., Marmin, T., Barriault, D., & Barriault, L. (2020). Single-Electron Transfer from Dimsyl Anion in the Alkylation of Phenols. *The Journal of Organic Chemistry*, 85(4), 2806-2813.
- Rojas, M. F., Bernard, F. L., Aquino, A., Borges, J., Vecchia, F. D., Menezes, S., Einloft, S. (2014). Poly(ionic liquid)s as efficient catalyst in transformation of CO₂ to cyclic carbonate. *Journal of Molecular Catalysis A: Chemical*, 392, 83-88.
- Ruckart, K. N., O'Brien, R. A., Woodard, S. M., West, K. N., & Glover, T. G. (2015). Porous solids impregnated with task-specific ionic liquids as composite sorbents. *The Journal of Physical Chemistry C*, 119(35), 20681-20697.
- Rudolph, M., & Ratcliff, E. L. (2017). Normal and inverted regimes of charge transfer controlled by density of states at polymer electrodes. *Nature Communication*, 8(1), 1048.
- Runge, E., & Gross, E. K. (1984). Density-functional theory for time-dependent systems. *Physical Review Letter*, 52(12), 997.
- Ryding, M. J., Debnárová, A., Fernández, I., & Uggerud, E. (2015a). Nucleophilic Substitution in Reactions between Partially Hydrated Superoxide Anions and Alkyl Halides. *The Journal Organic Chemistry*, 80(12), 6133-6142.
- Ryding, M. J., Debnárová, A., Fernández, I., & Uggerud, E. (2015b). Nucleophilic Substitution in Reactions between Partially Hydrated Superoxide Anions and Alkyl Halides. *The Journal of Organic Chemistry*, 80(12), 6133-6142.
- Ryding, M. J., Fernández, I., & Uggerud, E. (2016). Oxidation of NO[•] by small oxygen species HO₂⁻ and O₂^{•-}: the role of negative charge, electronic spin and water solvation. *Physical Chemistry Chemical Physics*, 18(14), 9524-9536.
- Sadeghpour, M., Yusoff, R., & Aroua Mohamed, K. (2017). Polymeric ionic liquids (PILs) for CO₂ capture. In *Reviews in Chemical Engineering* (Vol. 33, pp. 183).
- Saidi, M. (2020). CO₂ absorption intensification using novel DEAB amine-based nanofluids of CNT and SiO₂ in membrane contactor. *Chemical Engineering and Processing*, 149, 107848.
- Salazar, P. F., Chan, K. J., Stephens, S. T., & Cola, B. A. (2014). Enhanced electrical conductivity of imidazolium-based ionic liquids mixed with carbon nanotubes: A spectroscopic study. *Journal of The Electrochemical Society*, 161(9), 481-486.
- Samadi, Z., Haghshenasfard, M., & Moheb, A. (2014). CO₂ absorption using nanofluids in a wetted-wall column with external magnetic field. *Chemical Engineering Technology*, 37(3), 462-470.
- San Filippo, J., Chern, C.-I., & Valentine, J. S. (1975). Reaction of superoxide with alkyl halides and tosylates. *The Journal of Organic Chemistry*, 40(11), 1678-1680.
- Santos, D., Santos, M., Franceschi, E., Dariva, C., Barison, A., & Mattedi, S. (2016). Experimental density of ionic liquids and thermodynamic modeling with group

- contribution equation of state based on the lattice fluid theory. *Journal of Chemical & Engineering Data*, 61(1), 348-353.
- Sanz-Pérez, E. S., Murdock, C. R., Didas, S. A., & Jones, C. W. (2016). Direct capture of CO₂ from ambient air. *Chemical Reviews*, 116(19), 11840-11876.
- Sas, O. G., Ivaniš, G. R., Kijevčanin, M. L., González, B., Domínguez, A., & Radović, I. R. (2018). Densities and derived volumetric properties of ionic liquids with [Nf₂] and [NTf₂] anions at high pressures. *Journal of Chemical & Engineering Data*, 63(4), 954-964.
- Sathyanarayana, D. N. (2015). *Vibrational spectroscopy: theory and applications*: New Age International.
- Sawyer, D., Roberts, J., JL, Calderwood, T., Sugimoto, H., & McDowell, M. (1985). Reactivity and activation of dioxygen-derived species in aprotic media (a model matrix for biomembranes). *Philosophical Transactions of the Royal Society of London. B, Biological Sciences*, 311(1152), 483-503.
- Sawyer, D. T., Chiericato Jr, G., & Tsuchiya, T. (1982). Oxidation of ascorbic acid and dehydroascorbic acid by superoxide ion in aprotic media. *Journal of the American Chemical Society*, 104(23), 6273-6278.
- Sawyer, D. T., Sobkowiak, A., & Roberts, J. L. (1995). *Electrochemistry for chemists*: Wiley.
- Sawyer, D. T., & Valentine, J. S. (1981). How super is superoxide? *Accounts of Chemical Research*, 14(12), 393-400.
- Schäfer, A., Huber, C., & Ahlrichs, R. (1994). Fully optimized contracted Gaussian basis sets of triple zeta valence quality for atoms Li to Kr. *Journal of Chemical Physics*, 100(8), 5829-5835.
- Schlosser, P. M., Bale, A. S., Gibbons, C. F., Wilkins, A., & Cooper, G. S. (2015). Human health effects of dichloromethane: key findings and scientific issues. *Environ. Health Perspect.*, 123(2), 114-119.
- Schröder, U., Wadhawan, J. D., Compton, R. G., Marken, F., Suarez, P. A. Z., Consorti, C. S., Dupont, J. (2000). Water-induced accelerated ion diffusion: voltammetric studies in 1-methyl-3-[2,6-(S)-dimethylocten-2-yl]imidazolium tetrafluoroborate, 1-butyl-3-methylimidazolium tetrafluoroborate and hexafluorophosphate ionic liquids. *New Journal of Chemistry*, 24(12), 1009-1015.
- Schwenke, K. U., Herranz, J., Gasteiger, H. A., & Piana, M. (2015). Reactivity of the ionic liquid Pyr₁₄TFSI with superoxide radicals generated from KO₂ or by contact of O₂ with Li₇Ti₅O₁₂. *Journal of Electrochemical Society*, 162(6), 905-914.
- Schwöbel, J., Ebert, R.-U., , R., & Sc nn, G. (2009). Prediction of the Intrinsic Hydrogen Bond Acceptor Strength of Organic Compounds by Local Molecular Parameters. *Journal of Chemical Information and Modeling*, 49(4), 956-962.

- Scovazzo, P., Havard, D., McShea, M., Mixon, S., & Morgan, D. (2009). Long-term, continuous mixed-gas dry fed CO₂/CH₄ and CO₂/N₂ separation performance and selectivities for room temperature ionic liquid membranes. *Journal of Membrane Science*, 327(1), 41-48.
- Seki, S., Kobayashi, T., Kobayashi, Y., Takei, K., Miyashiro, H., Hayamizu, K., Umebayashi, Y. (2010). Effects of cation and anion on physical properties of room-temperature ionic liquids. *Journal of Molecular Liquids*, 152(1), 9-13.
- Sessler, C. D., Rahm, M., Becker, S., Goldberg, J. M., Wang, F., & Lippard, S. J. (2017). CF₂H₂, a Hydrogen Bond Donor. *Journal of the American Chemical Society*, 139(27), 9325-9332.
- Sethupathy, P., Alnashef, I. M., Monnier, J. R., Matthews, M. A., & Weidner, J. W. (2012). Synthesis of carbonyl compounds from alcohols using electrochemically generated superoxide ions in RTILs. *Synthetic Communications*, 42(24), 3632-3647.
- Shebanova, O. N., & Lazor, P. (2003). Raman study of magnetite (Fe₃O₄): laser-induced thermal effects and oxidation. *Journal of Raman Spectroscopy*, 34(11), 845-852.
- Shoup, D., & Szabo, A. (1982). Chronoamperometric current at finite disk electrodes. *Journal of Electroanalytical Chemistry and Interfacial Electrochemistry*, 140(2), 237-245.
- Singh, M., Singh, K. N., Dwivedi, S., & Misra, R. A. (1991). Superoxide (O₂^{•-}) - initiated oxidation of primary alcohols to carboxylic acids. *Synthesis*, 1991(04), 291-293.
- Singh, P. S., & Evans, D. H. (2006). Study of the electrochemical reduction of dioxygen in acetonitrile in the presence of weak acids. *The Journal of Physical Chemistry B*, 110(1), 637-644.
- Smith, M. R., & Myers, S. S. (2018). Impact of anthropogenic CO₂ emissions on global human nutrition. *Nature Climate Change*(8), 834-839.
- Steffen, C., Thomas, K., Huniar, U., Hellweg, A., Rubner, O., & Schroer, A. (2010). TmoleX—a graphical user interface for Turbomole. *Journal of Computer Chemistry*, 31(16), 2967-2970.
- Sugimoto, H., Matsumoto, S., & Sawyer, D. T. (1988). Degradation and dehalogenation of polychlorobiphenyls and halogenated aromatic molecules by superoxide ion and by electrolytic reduction. *Environmental Science & Technology*, 22(10), 1182-1186.
- Sun, J., Forsyth, M., & Macfarlane, D. R. (1998). Room-temperature molten salts based on the quaternary ammonium ion. *The Journal of Physical Chemistry B*, 102(44), 8858-8864.
- Sundar, L. S., Singh, M. K., Ramana, E. V., Singh, B., Grácio, J., & Sousa, A. C. M. (2014). Enhanced thermal conductivity and viscosity of nanodiamond-nickel nanocomposite nanofluids. *Scientific Report*, 4(1), 4039.

- Switzer, E. E., Zeller, R., Chen, Q., Sieradzki, K., Buttry, D. A., & Friesen, C. (2013). Oxygen reduction reaction in ionic liquids: The addition of protic species. *The Journal of Physical Chemistry C*, 117(17), 8683-8690.
- Takei, T., Dong, Q., Yonesaki, Y., Kumada, N., & Kinomura, N. (2010). Preparation of ultrafine magnetite and its oxygen adsorption. *Materials Science and Engineering: B*, 173(1), 84-88.
- Tang, S. Y., Bourne, R. A., Smith, R. L., & Poliakoff, M. (2008). The 24 principles of green engineering and green chemistry: "Improvements Productively". *Green Chemical*, 10(3), 268-269.
- Thomas, W. C., Brooks, F. P., Burnim, A. A., Bacik, J.-P., Stubbe, J., Kaelber, J. T., Ando, N. (2019). Convergent allostery in ribonucleotide reductase. *Nature communications*, 10(1), 2653.
- Tian, Y., & Liu, Z.-Q. (2014). Metal-free radical cascade dichloromethylation of activated alkenes using CH₂Cl₂: highly selective activation of the C–H bond. *RSC Advances*, 4(110), 64855-64859.
- Tokuda, H., Hayamizu, K., Ishii, K., Susan, M. A. B. H., & Watanabe, M. (2005). Physicochemical properties and structures of room temperature ionic liquids. 2. Variation of alkyl chain length in imidazolium cation. *The Journal of Physical Chemistry B*, 109(13), 6103-6110.
- Tomida, D. (2018). Thermal conductivity of ionic liquids. *Impact of thermal conductivity on energy technologies*, 17.
- Tomida, D., Kenmochi, S., Qiao, K., Tsukada, T., & Yokoyama, C. (2013). Densities and thermal conductivities of N-alkylpyridinium tetrafluoroborates at high pressure. *Fluid Phase Equilibria*, 340, 31-36.
- Tomida, D., Kenmochi, S., Tsukada, T., Qiao, K., & Yokoyama, C. (2007). Thermal conductivities of [bmim][PF₆], [hmim][PF₆], and [omim][PF₆] from 294 to 335 K at pressures up to 20 MPa. *International Journal of Thermophysics*, 28(4), 1147-1160.
- Tomkiewicz, A. C., Cress, C. D., & Landi, B. J. (2020). Enhanced saltwater stability of CNT wires under electrical bias. *Carbon*, 168, 180-192.
- Torralba-Calleja, E., Skinner, J., & Gutiérrez-Tauste, D. (2013). CO₂ capture in ionic liquids: a review of solubilities and experimental methods. *Journal of Chemistry*, 2013.
- Torres Pineda, I., Lee, J. W., Jung, I., & Kang, Y. T. (2012). CO₂ absorption enhancement by methanol-based Al₂O₃ and SiO₂ nanofluids in a tray column absorber. *International Journal Refrigeration*, 35(5), 1402-1409.
- Torresi, R. M., Lodovico, L., Benedetti, T. M., Alcântara, M. R., Debiemme-Chouvy, C., & Deslouis, C. (2013). Convective mass transport in ionic liquids studied by electrochemical and electrohydrodynamic impedance spectroscopy. *Electrochimica Acta*, 93, 32-43.

- Trasatti, S., & Petrii, O. A. (1991). Real surface area measurements in electrochemistry. *Pure and Applied Chemistry*, 63(5), 711.
- Tu, J., Yuan, Y., Zhan, P., Jiao, H., Wang, X., Zhu, H., & Jiao, S. (2014). Straightforward approach toward SiO₂ nanospheres and their superior lithium storage performance. *The Journal of Physical Chemistry C*, 118(14), 7357-7362.
- Urita, K., Ide, N., Isobe, K., Furukawa, H., & Moriguchi, I. (2014). Enhanced electric double-layer capacitance by desolvation of lithium ions in confined nanopores of microporous carbon. *ACS Nano*, 8(4), 3614-3619.
- Ussiri, D. A., & Lal, R. (2017). Introduction to global carbon cycling: an overview of the global carbon cycle. In *Carbon sequestration for climate change mitigation and adaptation* (pp. 61-76): Springer.
- Valkenburg, M. E. V., Vaughn, R. L., Williams, M., & Wilkes, J. S. (2005). Thermochemistry of ionic liquid heat-transfer fluids. *Thermochimica Acta*, 425(1), 181-188.
- van Ruijven, B. J., De Cian, E., & Sue Wing, I. (2019). Amplification of future energy demand growth due to climate change. *Nature communications*, 10(1), 2762.
- Vander Hoogerstraete, T., Jamar, S., Wellens, S., & Binnemans, K. (2014). Determination of halide impurities in ionic liquids by total reflection x-ray fluorescence spectrometry. *Analytical Chemistry*, 86(8), 3931-3938.
- Vanneman, M., & Dranoff, G. (2012). Combining immunotherapy and targeted therapies in cancer treatment. *Nature reviews cancer*, 12(4), 237.
- Vicent-Luna, J. M., Gutiérrez-Sevillano, J. J., Anta, J. A., & Calero, S. (2013). Effect of room-temperature ionic liquids on CO₂ separation by a Cu-BTC metal-organic framework. *The Journal of Physical Chemistry C*, 117(40), 20762-20768.
- Villagrán, C., Aldous, L., Lagunas, M. C., Compton, R. G., & Hardacre, C. (2006). Electrochemistry of phenol in bis{(trifluoromethyl)sulfonyl}amide ([NTf₂]⁻) based ionic liquids. *Journal of Electroanalytical Chemistry*, 588(1), 27-31.
- Vogt, C., Monai, M., Kramer, G. J., & Weckhuysen, B. M. (2019). The renaissance of the Sabatier reaction and its applications on Earth and in space. *Nature Catalysis*, 2(3), 188-197.
- Voiry, D., Chhowalla, M., Gogotsi, Y., Kotov, N. A., Li, Y., Penner, R. M., Weiss, P. S. (2018). Best practices for reporting electrocatalytic performance of nanomaterials. *ACS Nano*, 12(10), 9635-9638.
- Vuković, M., Valla, T., & Milun, M. (1993). Electron spectroscopy characterization of an activated ruthenium electrode. *Journal of Electroanalytical Chemistry*, 356(1), 81-91.
- Wang, L., Drahushuk, L. W., Cantley, L., Koenig, S. P., Liu, X., Pellegrino, J., Scott Bunch, J. (2015). Molecular valves for controlling gas phase transport made from

- discrete ångström-sized pores in graphene. *Nature Nanotechnology*, 10(9), 785-790.
- Wang, R., Zhang, S., Su, Y., Liu, J., Ying, Y., Wang, F., & Cao, X. (2017). Semi-solid state electrochromic device based on deep eutectic solvent gel electrolyte and transparent au modified FTO electrode. *Electrochimical Acta*, 258, 328-335.
- Wang, Y. L., Li, B., Sarman, S., Mocci, F., Lu, Z. Y., Yuan, J., & Fayer, M. D. (2020). Microstructural and dynamical heterogeneities in ionic liquids. *Chemical Reviews*, 120(13), 5798-5877.
- Wang, Y., Lafosse, A., & Jacobi, K. (2002). Adsorption and reaction of CO₂ on the RuO₂ (110) surface. *The Journal of Physical Chemistry B*, 106(21), 5476-5482.
- Wang, Y., Nie, J., Lu, C., Wang, F., Ma, C., Chen, Z., & Yang, G. (2020). Imidazolium-based polymeric ionic liquids for heterogeneous catalytic conversion of CO₂ into cyclic carbonates. *Microporous and Mesoporous Materials*, 292, 109751.
- Weber, J., Fluekiger, P., Morgantini, P. Y., Schaad, O., Goursoot, A., & Daul, C. (1988). The modelling of nucleophilic and electrophilic additions to organometallic complexes using molecular graphics techniques. *Journal Computer-Aided Molecular Design*, 2(3), 235-253.
- Weissman, M., & Benson, S. W. (1983). Heat of formation of the CHCl₂ radical. Bond dissociation energies in chloromethanes and chloroethanes. *The Journal Physical Chemistry*, 87(2), 243-244.
- Weng, X., Cui, Y., Shaikhutdinov, S., & Freund, H.-J. (2019). CO₂ Adsorption on CaO(001): Temperature-programmed desorption and infrared study. *The Journal of Physical Chemistry C*, 123(3), 1880-1887.
- Wickramanayake, S., Hopkinson, D., Myers, C., Hong, L., Feng, J., Seol, Y., Luebke, D. (2014). Mechanically robust hollow fiber supported ionic liquid membranes for CO₂ separation applications. *Journal of Membrane Science*, 470, 52-59.
- Wilamowska, M., Graczyk-Zajac, M., & Riedel, R. (2013). Composite materials based on polymer-derived SiCN ceramic and disordered hard carbons as anodes for lithium-ion batteries. *Journal of power sources*, 244, 80-86.
- Wilcken, R., Zimmermann, M. O., Lange, A., Joerger, A. C., & Boeckler, F. M. (2013). Principles and applications of halogen bonding in medicinal chemistry and chemical biology. *Journal Medinal Chemical*, 56(4), 1363-1388.
- Wilkens, S. J., Westler, W. M., Markley, J. L., & Weinhold, F. (2001). Natural J-coupling analysis: Interpretation of scalar j-couplings in terms of natural bond orbitals. *Journal of Ammerican Chemical Society*, 123(48), 12026-12036.
- Winterbourn, C. C. (2020). Biological chemistry of superoxide radicals. *ChemTexts*, 6(1), 7.
- Wu, C., Hou, X., Zheng, Y., Li, P., & Lu, D. (2017). Electrophilicity and nucleophilicity of boryl radicals. *Journal of Organic Chemistry*, 82(6), 2898-2905.

- Xiao, Y., Wang, Y., Bo, S.-H., Kim, J. C., Miara, L. J., & Ceder, G. (2020). Understanding interface stability in solid-state batteries. *Nature Reviews Materials*, 5(2), 105-126.
- Xiong, Y., Luo, H., Nie, Y., Chen, F., Dai, W., Wang, X., Gong, R. (2019). Synergistic effect of silica coated porous rodlike nickel ferrite and multiwalled carbon nanotube with improved electromagnetic wave absorption performance. *Journal of Alloys and Compounds*, 802, 364-372.
- Xu, J., Ye, Y., Huang, F., Chen, H., Wu, H., Huang, J., Wu, Y. (2016). Association between dioxin and cancer incidence and mortality: a meta-analysis. *Scientific Report*, 6(1), 38012.
- Yang, D., Zhu, Q., Chen, C., Liu, H., Liu, Z., Zhao, Z., Han, B. (2019). Selective electroreduction of carbon dioxide to methanol on copper selenide nanocatalysts. *Nature Communications*, 10(1), 677
- Yang, L., Liu, G., Zheng, M., Zhao, Y., Jin, R., Wu, X., & Xu, Y. (2017). Molecular mechanism of dioxin formation from chlorophenol based on electron paramagnetic resonance spectroscopy. *Environmental Science & Technology*, 51(9), 4999-5007.
- Yang, N. (2014). Dichloromethane. In P. Wexler (Ed.), *Encyclopedia of Toxicology (Third Edition)* (pp. 99-101). Oxford: Academic Press.
- Yao, C., & Anderson, J. L. (2009). Retention characteristics of organic compounds on molten salt and ionic liquid-based gas chromatography stationary phases. *Journal of Chromatography A*, 1216(10), 1658-1712.
- Ye, Q., Xu, H., Wang, Q., Huo, X., Wang, Y., Huang, X., Zhang, J. (2021). New insights into the mechanisms of tartaric acid enhancing homogeneous and heterogeneous copper-catalyzed Fenton-like systems. *Journal of Hazardous Materials*, 407, 124351.
- Yennie, C. J., Hopson, R., & Hess, K. M. (2017). Quantifying the Product Distribution of a Chemical Reaction by ¹H NMR Spectroscopy: A Cooperative Learning Approach for the Undergraduate Organic Chemistry Laboratory. *Journal of Chemical Education*, 94(9), 1383-1387.
- Yoon, D.-W., Gross, D. E., Lynch, V. M., Sessler, J. L., Hay, B. P., & Lee, C.-H. (2008). Benzene-, Pyrrole-, and Furan-Containing Diametrically Strapped Calix[4]pyrroles—An Experimental and Theoretical Study of Hydrogen-Bonding Effects in Chloride Anion Recognition. *Angewandte Chemie International Edition*, 47(27), 5038-5042.
- Yoshimura, M., Honda, K., Kondo, T., Uchikado, R., Einaga, Y., Rao, T. N., . . . Fujishima, A. (2002). Factors controlling the electrochemical potential window for diamond electrodes in non-aqueous electrolytes. *Diamond and Related Materials*, 11(1), 67-74.

- Yoshinaga, T., Yamaye, M., Kito, T., Ichiki, T., Ogata, M., Chen, J., Yamanobe, T. (2004). Alkaline dechlorination of poly(vinyl chloride) in organic solvents under mild conditions. *Polymer Degradation Stability*, 86(3), 541-547.
- Yu, G., Zhao, D., Wen, L., Yang, S., & Chen, X. (2012). Viscosity of ionic liquids: Database, observation, and quantitative structure-property relationship analysis. *AIChE Journal*, 58(9), 2885-2899.
- Zabik, N. L., Anwar, S., Ziu, I., & Martic-Milne, S. (2019). Electrochemical reactivity of bulky-phenols with superoxide anion radical. *Electrochimica Acta*, 296, 174-180.
- Zağli, E., & Falconer, J. L. (1981). Carbon dioxide adsorption and methanation on ruthenium. *Journal of Catalysis*, 69(1), 1-8.
- Zaichenko, A., Schröder, D., Janek, J., & Mollenhauer, D. (2020). Pathways to triplet or singlet oxygen during the dissociation of alkali metal superoxides: Insights by multireference calculations of molecular model systems. *Chemistry.– A European Journal*, 26(11), 2395-2404.
- Zawrah, M. F., Khattab, R. M., Girgis, L. G., El Daidamony, H., & Abdel Aziz, R. E. (2016). Stability and electrical conductivity of water-base Al₂O₃ nanofluids for different applications. *HBRC Journal*, 12(3), 227-234.
- Zeng, S., Zhang, X., Bai, L., Zhang, X., Wang, H., Wang, J., Zhang, S. (2017). Ionic-liquid-based CO₂ capture systems: structure, interaction and process. *Chemical Reviews*, 117(14), 9625-9673.
- Zhang, J., Sun, B., Zhao, Y., Tkacheva, A., Liu, Z., Yan, K., Wang, G. (2019). A versatile functionalized ionic liquid to boost the solution-mediated performances of lithium-oxygen batteries. *Nature Communication*, 10(1), 602.
- Zhang, Q., Li, Q., Liu, D., Zhang, X., & Lang, X. (2018). Density, dynamic viscosity, electrical conductivity, electrochemical potential window, and excess properties of ionic liquid N-butyl-pyridinium dicyanamide and binary system with propylene carbonate. *Journal of Molecular Liquids*, 249, 1097-1106.
- Zhang, T.-F., Li, Z.-P., Wang, J.-Z., Kong, W.-Y., Wu, G.-A., Zheng, Y.-Z., Luo, L.-B. (2016). Broadband photodetector based on carbon nanotube thin film/single layer graphene Schottky junction. *Scientific Reports*, 6(1), 38569.
- Zhang, Y., Zhang, J., Son, H., Kong, J., & Liu, Z. (2005). Substrate-induced raman frequency variation for single-walled carbon nanotubes. *Journal of the American Chemical Society*, 127(49), 17156-17157.
- Zhao, Y., Yu, B., Yang, Z., Zhang, H., Hao, L., Gao, X., & Liu, Z. (2014). A protic ionic liquid catalyzes CO₂ conversion at atmospheric pressure and room temperature: Synthesis of quinazoline-2,4(1H,3H)-diones. *Angewandte Chemie*, 53(23), 5922-5925.
- Zheng, K., Song, Y., Wang, X., Li, X., Mao, X., & Wang, D. (2019). Understanding the electrode reaction process of dechlorination of 2, 4-dichlorophenol over Ni/Fe

nanoparticles: Effect of pH and 2, 4-dichlorophenol concentration. *Journal Environmental Science*, 84, 13-20.

Zhigang Lei Orcid, B. C., Yoon-Mo Koo, and Douglas R. MacFarlane. (2017). Introduction: Ionic Liquids. *Chemical Review*, 117(10), 6633-6635.

Zigah, D., Ghilane, J., Lagrost, C., & Hapiot, P. (2008). Variations of diffusion coefficients of redox-active molecules in room temperature ionic liquids upon electron transfer. *The Journal of Physical Chemistry B*, 112(47), 14952-14958.

Zimmerman, J. B., Anastas, P. T., Erythropel, H. C., & Leitner, W. (2020). Designing for a green chemistry future. *Science*, 367(6476), 397-400.

Universiti Malaysia